DISS. ETH NO. 22136

Thermo-Mechanical Lifetime Assessment of Components for 700°C Steam Turbine Applications

A thesis submitted to attain the degree of

DOCTOR OF SCIENCES of ETH ZURICH
(Dr. sc. ETH Zurich)

presented by

FRANK EHRHARDT

Dipl.-Ing., TU Dresden

born on 27.06.1980

citizen of Germany

accepted on the recommendation of

Prof. Dr. Edoardo Mazza, *examiner*
Prof. Dr.-Ing. habil. Karl Maile, *co-examiner*
Dr. Stuart Holdsworth, *co-examiner*

2014

Acknowledgement

The present dissertation is the result of an intensive and interesting research activity on a collaborative project between the industrial partner Alstom and the High Temperature Integrity Group at the Swiss Federal Laboratories for Materials Science and Technology Empa in Dübendorf. The work would not have been possible without the help and support of many people I want to express my deep gratitude to at this point.

My sincere thanks deserve my supervisors Prof. Dr. E. Mazza and Dr. S. R. Holdsworth who have guided and supported me throughout my PhD with their sound experience and knowledge. I want to express my gratitude especially to Stuart for his patience and commitment to this work and the many fruitful and encouraging discussions. Moreover I want to thank Prof. Dr. K. Maile for the interest in the present work and the acceptance of co-examination.

Particular gratitude is due to Dr. A. Pirscher, Mr. L. Ripamonti, Dr. P. Walker and Dr. M. Sell from Alstom Switzerland Ltd. for enabling the collaborative research project and the financial support, which is greatly acknowledged. Additionally I am grateful to Dr. M. Reigl, Dr. I. Kühn, Dr. J. Chen and Dr. B. Masserey for the help and support as well as profound guidance coming from Alstom Steam Turbines Research and Development department. Furthermore the professional support and advice of Dr. R. B. Scarlin and Mr. S. Keller and his colleagues during manufacturing of the dissimilar metal welded joints and guidance on Alstom welding technology is acknowledged.

Many thanks also go to my colleagues at the Laboratory of Mechanics for Modelling and Simulation at Empa for enabling a nice atmosphere and the countless talking, not entirely related to professional discussions. The demanding time of the PhD was made considerably more bearable by the enjoyable lunch and coffee breaks shared with them. In particular the invaluable help and support of the laboratory technician Mr. F. Bürki should be emphasised.

Finally I want express my sincere gratitude to my family and friends, without their continuous support the present dissertation would be hardly imaginable. To my parents I owe the opportunity of my education, without their moral and financial support my studies would have not been possible. Also I want to acknowledge the support of my friends and colleagues who contributed to the success of the present work with their appreciation and patience during all the years.

The most gratitude I want to express to my girlfriend Stefanie for her love, help and patience during the time of the doctorate, which on many occasions was characterised by private restrictions.

Contents

Nomenclature **vii**

Summary **xi**

Zusammenfassung **xv**

1 Introduction and Research Objective **1**

2 State of Knowledge **5**
- 2.1 High-Temperature Mechanical Behaviour . . . 6
  - 2.1.1 Microstructural Fundamentals and Strength of Metals . . . 6
  - 2.1.2 Behaviour under Static Loading . . . 14
  - 2.1.3 Cyclic Loading Conditions . . . 23
  - 2.1.4 Multiaxial Stress State . . . 32
- 2.2 Damage and Lifetime Assessment . . . 34
  - 2.2.1 Creep Damage . . . 34
  - 2.2.2 Fatigue Damage . . . 36
  - 2.2.3 Creep-Fatigue Interaction . . . 40
- 2.3 Nickel-base Materials . . . 44
  - 2.3.1 Phases and Hardening Mechanisms . . . 45
  - 2.3.2 Alloy 617 . . . 47
- 2.4 Heat Resistant Steels and their Weldments . . . 49
  - 2.4.1 Heat Resistant Steels . . . 49
  - 2.4.2 High Temperature Weldments . . . 55

3 Materials and Testing Procedure **63**
- 3.1 Materials . . . 64
  - 3.1.1 Alloy 617 . . . 64
  - 3.1.2 Dissimilar Metal Welded Joints . . . 65
- 3.2 Testing Procedure . . . 66
  - 3.2.1 LCF/TMF Testing . . . 66
  - 3.2.2 Creep Rupture Testing . . . 69

4 High Temperature Mechanical Behaviour of Alloy 617 71
4.1 Experimental Determination of Material Behaviour 72
4.1.1 Tensile Properties 72
4.1.2 Creep 73
4.1.3 Low Cycle Fatigue 76
4.1.4 Creep-Fatigue 78
4.2 Modelling of Material Behaviour 81
4.2.1 Cyclic Plasticity 81
4.2.2 Creep 85
4.2.3 Creep-Fatigue Interaction 89
4.3 Lifetime Assessment of Alloy 617 Rotor Features 97
4.3.1 Thermo-mechanical Cycle Definition 97
4.3.2 Service Cycle TMF Testing 100

5 High Temperature Behaviour of Dissimilar Metal Welded Joints 105
5.1 Experimental Determination of Material Behaviour 106
5.1.1 Creep 106
5.1.2 Low Cycle Fatigue 112
5.1.3 Creep-Fatigue 117
5.2 Modelling of Material Behaviour 126
5.2.1 Creep Rupture Strength 126
5.2.2 Fatigue Endurance 128
5.2.3 Creep-Fatigue Interaction 130
5.2.4 Maximum Application Temperatures 134

6 Conclusion and Outlook 135

Appendix 139
A Specimen Geometries 139
B Alloy 617 - Creep Model Parameters 140

Curriculum Vitae 157

Nomenclature

Abbrevations

AD700	”Advanced 700°C pulverised coal-fired power plants“ project
bcc	body-centred cubic
BM	Base material
CF	Creep-fatigue
CGHAZ	Coarse-grained heat affected zone
CNRT	Circumferential notched round tensile
CR	Creep rupture
CSS	Cyclic stress-strain
DMW	Dissimilar metal weldment
ESR	Electro-slag remelting
fcc	Face-centred cubic
FEM	Finite element method
FGHAZ	Fine-grained heat affected zone
FL	Fusion line
GCP	Geometrically closed packed
HAGB	High angle grain boundary
HAZ	Heat affected zone
HCF	High cycle fatigue
HCP	Hexagonal closed packed
HP	High pressure
ICHAZ	Intercritical heat affected zone
IP	Intermediate pressure
LAGB	Low-angle grain boundary
LCF	Low cycle fatigue
PM	Parent material
PSB	Persistent slip band
PWHT	Post weld heat treatment
SEM	Scanning electron microscope
SMW	Similar metal weldment
TCP	Topologically closed packed
TEM	Transmission electron microscope
TF	Thermal fatigue

TIG	Tungsten inert gas - welding technology
TMF	Thermo-mechanical fatigue
VIM	Vacuum induction melting
WM	Weld metal
WSF	Weld strength factor
WSRF	Weld strength reduction factor

Arabic Symbols

A	Norton parameter for minimum creep strain rate
A_u	Fracture deformation strain
b	Burgers vector
C_i	Kinematic hardening parameter for ith backstress
D	Total combined damage
D_c	Total creep damage
D_f	Total fatigue damage
E	Elastic modulus
F	Constant in time-dependent creep term
G	Shear modulus
H	Multiaxiality factor
m	Exponent in time-dependent creep term
N	Number of cycles
n	Stress exponent for minimum creep strain rate
N_f	Number of cycles to failure
p	Equivalent accumulated plastic strain
$P(T,t)$	Time-temperature parameter
Q	Saturation stress in isotropic hardening evolution rule
Q_c	Activation energy for creep
R	Isotropic hardening stress
$R_{\varepsilon/t/T}$	Creep strain strength to achieve ε at time t and temperature T
R_m	Tensile strength
$R_{p\varepsilon}$	Proof strength for non-proportional strain ε
$R_{u/t/T}$	Creep rupture strength at time t and temperature T
T	Temperature
t	Time
T_M	Melting temperature (or solidus temperature in alloys)
t_σ	Triaxiality factor
T_{Dam}	Damage temperature
t_h	Duration of hold period
t_u	Rupture time
$W_{c,crit}$	Critical dissipated creep energy
W_c	Dissipated creep energy
$W_{pl,crit}$	Critical dissipated plastic energy
W_{pl}	Dissipated plastic energy

Z_c'	Factor in Graham-Walles creep law to account for prior plastic strain accumulation
Z_u	Reduction of area at rupture

Greek Symbols

δ	Lattice misfit parameter
$\dot{\varepsilon}_{c,min}$	Minimum creep strain rate
$\varepsilon_{c,e}$	Equivalent (uniaxial) creep strain
ε_{c1}	Primary creep strain
ε_{c2}	Secondary creep strain
ε_{c3}	Tertiary creep strain
ε_c	Creep strain
ε_{Dc}	Creep ductility
ε_{el}	Elastic strain
ε_m	Mechanical strain
ε_{pl}	Plastic strain
ε_{th}	Thermal strain
ε_t	Total strain
ε_u	Creep rupture strain
γ_i	Dynamic recovery parameter for ith backstress
λ	Lame's constant
ν	Poisson's ratio
σ	Stress
σ_e	von Mises effective stress
σ_y	Yield stress
$\sigma_{1,2,3}$	Principal stress Max, Med, Min

Vectors, Tensors

$\mathbf{C}$	Elasticity tensor C_{ijkl}
$\mathbf{D}$	Damage tensor D_{ij}
$\boldsymbol{\varepsilon}$	Strain tensor ε_{ij}
$\boldsymbol{\varepsilon}^{el}$	Elastic strain tensor ε_{ij}^{el}
$\boldsymbol{\varepsilon}^{pl}$	Plastic strain tensor ε_{ij}^{pl}
$\boldsymbol{\sigma}$	Stress tensor σ_{ij}
$\mathbf{s}$	Deviatoric stress tensor s_{ij}
$\mathbf{X}$	Backstress tensor X_{ij}
$\mathbf{X}'$	Backstress tensor X_{ij}'

Summary

In order to increase the thermal efficiency and to reduce resource exploitation, recent development of advanced steam turbine technology has been targeted to steam inlet temperatures above 700°C and corresponding steam pressures exceeding 350 bar. These temperature levels are not sustainable for heat resistant steals and alternatively the much more expensive nickel- and cobalt based alloys have to be exploited. Previous European collaborative research and development activities between turbine manufacturers, forgemasters and research centres have identified candidate Ni-base alloys as suitable forgable high pressure steam turbine rotor materials and have also comprised welding procedure development for joints between Ni-base alloys and low as well as high alloyed ferritic steels. Due to economical reasons it is desired to replace the expensive Ni-base alloys with conventional heat resistant steels in these regions of the steam turbine rotor that are operating below ~500-550°C. Since a welded rotor design is favoured, dissimilar metal weldments are required.

The presented research work is aimed at the development of thermo-mechanical lifetime assessment methodologies for the evaluation of 700°C steam turbine components involving the formulation of advanced constitutive deformation and damage model equations. The first main objective was the development and verification of the effectiveness of advanced creep-fatigue lifetime assessment methodologies and determination of the required material input parameters for the accurate and reliable evaluation of Alloy 617 steam turbine rotor features at maximum application temperatures. To achieve the appointed objectives an extensive material testing campaign was required. For the characterisation of the material behaviour under static loading conditions creep rupture experiments for medium and target application temperatures have been conducted in order to investigate the influence of ageing treatment of Alloy 617. Taking into account material property data from previous research activity a constitutive creep deformation equation was developed on the basis of a modified Graham-Walles law, which well represents the mean creep behaviour of the investigated and reviewed Alloy 617 heats. In order to determine the time-independent plastic flow as well as the fatigue endurance characteristics, continuous cycling LCF experiments have been performed for the entire temperature range. On this basis a constitutive plasticity model of Chaboche type have been developed, which accurately describes the observed material response under cyclic loading. Furthermore cyclic/hold experiments have been conducted on Alloy 617 in order to investigate the occurring creep-fatigue damage mechanism and to determine the CF endurance characteristics. Thereby a modification on the creep law was introduced for description of the materials decreased creep resistance under combined creep-fatigue loading. For the assessment of creep and fatigue damage fractions a very promising approach considering plastic and creep dissipated energy as failure criterion was developed. The effectiveness of this energy exhaustion method was verified with the calculation of endurance curves for continuous cycling LCF and cyclic/hold conditions over a broad range of temperatures, strain ranges and hold periods. The effectiveness of the developed constitutive deformation model was further verified on a service-type TMF experiment, which cycle definition was determined from a life-limiting location in a 700°C high-pressure steam turbine rotor under realistic loading conditions while featuring significantly different strain ranges within an anisothermal cycle. The developed creep-fatigue lifetime assessment methodology for Alloy 617 was verified with the help of post test microstructural investigations, where the accordant damage appearances could reliably be represented.

For further characterization of Alloy 617 and accordant verification of applicability of the material in future steam turbine technology, with particular respect to the planned long-term operation in steam turbine rotors, additional creep-rupture experiments are necessary for a reliable creep rupture strength prediction. Additionally creep-fatigue experiments, preferably also thermomechanical experiments, with representative strain ranges and sufficiently long hold durations are to be performed to further investigate the apparent creep-fatigue damage mechanism. The post-test metallographic investigation on the TMF test conducted within the present work have revealed, despite the comparable large strain range of the experiment, extensive creep damage development under the imposed thermomechanical cycle.

The second main objective of the present research work was the identification of the maximum application temperatures of dissimilar metal welded joints between the Ni-base Alloy 617 and a 1% CrMoV low alloy bainitic rotor steel as well as a higher alloyed 10% Cr martensitic rotor steel, with respect to their creep rupture and fatigue properties. A testing procedure for the static creep and cyclic testing of the DMW joints was developed and a extensive testing campaign was conducted comprising creep rupture, continuous cycling LCF as well as CF cyclic/hold experiments for target temperatures defined on experience with accordant similar metal weldments. Based on the experimental results the fatigue and creep-fatigue endurance characteristics have been determined and corresponding models have been developed for their description. Accordingly the creep rupture strength curves have been determined, whereas CR strength extrapolation were only possible to maximum rupture times of 30 kh, due to the limited test duration of available DMW joint creep data. On this basis information could be obtained on the maximum achievable application temperatures of the investigated DMW joints. Post-test metallographic investigations revealed Type IV creep damage in the FGHAZ of the steels, which constitutes the main creep failure observed during creep loading of similar metal weldments. Additionally fusion line cracking associated with a Type I precipitate condition at the interface between Alloy 617 weld metal and the steel HAZ was observed in the investigated Alloy 617 - 1% CrMoV and Alloy 617 - 10% Cr DMW joints. Whereas the Type I carbide layer was apparent in Alloy 617 - 1% CrMoV DMW joint specimens even after short duration high temperature exposure, the situation was not clearly visible within the Alloy 617 - 10% Cr DMW joint. One major reason for the development of these Type I precipitates are the cross fusion line chemical composition gradients, mainly for the constituents C and Cr, which are obviously larger for the low alloyed 1% CrMoV steel compared to the 10% Cr steel with respect to the chemical composition of Alloy 617. For long-term creep loading conditions, representative of service condition existing in steam turbine rotors, the predominant failure mechanism for both DMW joints appeared to be FL cracking associated with the Type I precipitate condition. Since additional element diffusion is to be expected during long-term high temperature exposure, the experimental verification of long-term creep rupture strength is absolutely essential in order to guarantee the safe operation of the dissimilar metal weldments under service conditions. Additionally it should be noted that the presented experimental results have been obtained by uniaxial loaded cross-weld specimens with relatively small cross-sections that have been extracted from the weldments. On the one hand possible welding residual stresses have been reduced by the cutting out of the specimens and on the other hand no experience has been obtained on the effect of multiaxial stress states on the creep behaviour of the investigated DMW joints.

Zusammenfassung

Für die Steigerung des thermischen Wirkungsgrades sowie die Senkung des Rohstoffverbrauches zielen aktuelle Entwicklungen von fortschrittlicher Dampfturbinentechnologie auf Dampfeintrittstemperaturen von über 700°C und entsprechenden Dampfeintrittsdrücken von über 350 bar ab. Diese Temperaturbereiche sind für herkömmliche hochwarmfeste Stähle nicht erreichbar, weswegen der Einsatz der sehr viel teureren Nickel- bzw. Kobaltbasislegierungen notwendig wird. In vorangegangenen Europäischen Forschungs- und Entwicklungsvorhaben zwischen Herstellern von Kraftwerkstechnik, Lieferanten von Schmiedeteilen sowie Forschungseinrichtungen konnten geeignete Nickelbasislegierungen für den Einsatz als schmiedbare Rotorwerkstoffe für Hochdruckdampfturbinen identifiziert werden. Diese Aktivitäten beinhalteten auch die Entwicklung von Schweissverfahren für Verbindungen zwischen den Nickelbasislegierungen und herkömmlichen hochwarmfesten niedrig- und hochlegierten ferritischen Stählen. Aus ökonomischen Gründen wird ein Ersatz der teuren Nickelbasislegierungen durch konventionelle hochwarmfeste Stähle in Bereichen der Dampfturbinenrotoren angestrebt, deren Temperaturen im Betrieb ∼500-550°C nicht überschreiten. Da eine geschweisste Ausführung bevorzugt wird, sind artungleiche Schweissverbindungen notwendig.

Das vorliegende Forschungsvorhaben zielt auf die Entwicklung von Methoden für die thermomechanische Lebensdauerabschätzung von 700°C Dampfturbinenkomponenten ab und beinhaltet die Formulierung von fortschrittlichen konstitutiven Deformations- und Schädigungsgleichungen. Die erste Zielsetzung der vorliegenden Arbeit beinhaltet die Entwicklung und Verifikation der Anwendbarkeit von Methoden der Kriechermüdungslebensdauerabschätzung sowie die Ermittlung der benötigten Werkstoffparameter für die zuverlässige Beurteilung von Dampfturbinenrotoren aus der Nickelbasislegierung Alloy 617 unter maximalen Einsatztemperaturen. Für die Erfüllung der Forschungsziele war eine umfangreiche Prüfkampagne durchzuführen. Für die Charakterisierung des Werkstoffverhaltens unter statischer Beanspruchung wurden Kriechexperimente unter mittleren sowie maximalen Einsatztemperaturen durchgeführt, um den Einfluss von Glühbehandlungen von Alloy 617 zu untersuchen. Unter Berücksichtigung von Werkstoffdaten aus früheren Forschungsvorhaben konnte eine konstitutive Kriechverformungsgleichung auf der Basis einer modifizierten Graham-Walles-Gleichung entwickelt werden, welche das mittlere Kriechverhalten der untersuchten sowie überprüften Alloy 617 Chargen sehr gut beschreibt. Für die Bestimmung des zeitunabhängigen plastischen Fliessverhaltens und der Ermüdungsfestigkeit wurden für den gesamten Temperaturbereich LCF-Experimente ohne Haltezeit durchgeführt. Anschliessend wurde ein konstitutives Plastizitätsmodell nach Chaboche entwickelt und an die Messergebnisse angepasst, welches die ermittelte Werkstoffantwort unter zyklischer Beanspruchung sehr zufriedenstellend beschreibt. Darüberhinaus wurden für Alloy 617 LCF-Experimente mit Haltezeit durchgeführt, um die auftretenden Schädigungsmechanismen sowie die erträglichen Schwingspielzahlen unter Kriechermüdung zu untersuchen. Für die Beschreibung der auftretenden Verringerung der Kriechfestigkeit unter kombinierter Kriechermüdungsbeanspruchung von Alloy 617 wurde eine Modifikation der Kriechgleichung eingeführt. Ein sehr vielversprechender Ansatz für die Bestimmung der Kriech- und Ermüdungsschadensanteile unter Berücksichtigung der dissipierten Energien wurde entwickelt. Die Effektivität dieses Energieerschöpfungsverfahrens wurde anhand der Ermüdungskurven von LCF-Experimenten ohne sowie mit verschiedenen Haltezeiten in einem breiten Temperaturbereich verifiziert. Darüberhinaus konnte das entwickelte konstitutive Verformungsmodell anhand eines betriebsähnlichen TMF-Experimentes verifiziert werden. Der Beanspruchungszyklus des TMF-Experimentes wurde bestimmt durch die errechneten Belastungen an einer Lebensdauer begrenzenden Position eines 700°C Hochdruckdampfturbinenrotors unter realistischen Betriebsbeanspruchungen. Das entwickelte Verfahren zur Bestimmung der Kriechermüdungslebensdauer für Alloy 617 wurde anhand von mikrostrukturellen Untersuchungen geprüfter Proben verifiziert, wobei die aufgetretenen Schädigungsbilder verlässlich repräsentiert werden konnten.

Für eine erweiterte Beschreibung des Werkstoffverhaltens und Verifizierung der Anwendbarkeit von Alloy 617 in zukünftigen Dampfturbinentechnologien sind zusätzliche Kriechexperimente für eine zuverlässige Voraussage der Kriechfestigkeit notwendig, was besonders für die geplanten Einsatzzeiten für Dampfturbinenrotoren gilt. Weitere Kriechermüdungsexperimente, bevorzugt auch anisotherme TMF-Experimente, mit repräsentativen Dehnungsschwingbreiten und ausreichend langen Haltezeiten sollten durchgeführt werden, um den auftretenden Schadensmechanismus unter Kriechermüdung noch eingehender zu untersuchen. Die mikrostrukturellen Untersuchungen der TMF-Probe der vorliegenden Arbeit zeigten eine erhebliche Kriechschädigung für den beaufschlagten thermomechanischen Zyklus mit vergleichbar grosser Dehnschwingbreite.

Die zweite Zielstellung der vorliegenden Forschungsarbeit war die Bestimmung der maximalen Einsatztemperaturen von artungleichen Schweissverbindungen zwischen der Nickelbasislegierung Alloy 617 und einem niedriglegierten bainitischen 1% CrMoV-Stahl sowie einem hochlegierten martensitischen 10% Cr-Stahl, in Bezug auf deren Kriech- und Ermüdungsfestigkeiten. Im Rahmen dieser Arbeit wurde ein Testverfahren für Kriech- sowie LCF-Experimente von artungleichen Schweissverbindungen (DMW) entwickelt und ein umfangreiches Testprogramm durchgeführt, welches LCF-Experimente mit und ohne Haltezeit sowie Kriechexperimente

für Zieltemperaturen beinhaltete, welche basierend auf Erfahrungen mit vergleichbaren artgleichen Schweissverbindungen festgelegt wurden. Mithilfe der experimentellen Ergebnisse konnten die Ermüdungs- und Kriechermüdungsfestigkeiten der DMW bestimmt werden. Entsprechend konnten für beide Schweissverbindungen die Kriechfestigkeiten bestimmt werden, wobei Extrapolationen aufgrund begrenzter experimenteller Prüfzeiten nur bis zu Kriechbruchzeiten von 30 kh möglich waren. Basierend auf den ermittelten Kriech- und Kriechermüdungsergebnissen konnten für die untersuchten artungleichen Schweissverbindungen die maximal möglichen Einsatztemperaturen festgelegt werden. Mikrostrukturelle Untersuchungen der DMW zeigten Kriechschädigung vom Typ IV in der FGHAZ der Stähle, was auch für das hauptsächliche Kriechversagen von artgleichen Schweissverbindungen verantwortlich ist. Zusätzlich wurde Kriechbruch an der Schmelzlinie beobachtet, welcher mit Typ I Ausscheidungen an der Grenzfläche zwischen Alloy 617 Schweissgut und der Wärmeeinflusszone der Stähle in Verbindung gebracht werden konnte. Während die Typ I Karbidschicht bei Proben der Alloy 617 - 1% CrMoV DMW schon bei kurzen Einsätzen unter hohen Temperaturen deutlich sichtbar war, konnte dies für die Alloy 617 - 10% Cr DMW nicht bestätigt werden. Einer der Haupteinflussfaktoren für die Bildung der Typ I Ausscheidungen ist der Gradient der chemischen Elementzusammensetzungen entlang der Schmelzlinie, wobei im wesentlichen C und Cr von Interesse sind. Dieser Gradient ist für den 1% CrMoV-Stahl klar grösser als für den 10% Cr-Stahl im Vergleich zu Alloy 617. Unter Langzeitkriechbeanspruchung der Schweissverbindungen, welche charakteristisch für den Betriebseinsatz von Dampfturbinenrotoren ist, kann der vorherrschende Schadensmechanismus der DMW als Kriechbruch entlang der Schmelzlinie, hervorgerufen durch die Typ I Ausscheidungen, angenommen werden. Da während der Langzeitbeanspruchung zusätzliche Elementdiffusionen erwartet werden können, stellt die Verifikation der Kriechfestigkeit der DMW eine essentielle Notwendigkeit für deren sicheren Betrieb in Dampfturbinenkomponenten dar. Darüberhinaus sollte erwähnt werden, dass die experimentellen Ergebnisse für einachsig beanspruchte Proben mit relativ kleinen Probenquerschnitten erzeugt wurden. Während auf der einen Seite mögliche Schweisseigenspannungen durch die Entnahme der Proben aus der Schweissnaht verringert wurden, konnten zu den untersuchten artungleichen Schweissverbindungen keinerlei Erkenntnisse zum Einfluss von mehrachsigen Spannungszuständen gewonnen werden.

Chapter 1

Introduction and Research Objective

The future provision of stable and affordable energy can be described as one of the major actual challenges since with increasing industrialisation in the developing countries the global energy consumption is going to rise. Factors like the environmental emission regulations, unstable political situations and the availability of energy reserves and other scarce resources will influence the composition of future energy production. While renewable energies like wind, solar and hydropower will have a rising contribution to power production, a safe and reliable base load energy supply can only be ensured with conventional energy production. The heavy reliance of power generation on fossil fuels will continue in the decades to come, all the more as the amount of nuclear power generation is reduced. Because the amount of commercially exploitable oil and natural gas reserves is unlikely to be sufficient to cover the projected increasing power demand, coal may be the only fuel available in substantial quantities in many regions around the world to span the time until introduction of further advanced renewable energies.

One of the most common large scale energy conversion devices from thermal to electrical energy is the steam power plant exploiting the thermodynamics of the steam-water cycle in utilising a steam generator (heating device), a steam turbine, condenser and finally a generator for the generation of electrical energy. With actual applications in nuclear and fossil power plants as well as in high efficient combined cycle gas turbine plants, steam turbine technology is also going to be adapted in future renewable energy technologies like geothermal, concentrated solar power or biomass power plants. For this reason one main point of interest is to increase the thermal efficiency of fossil fired steam power plants which can be mainly achieved by increasing the steam inlet parameters, e.g. steam inlet pressure and temperature. For the ecological and economical optimisation of the operation of the power plant, which can last 300.000 operating hours, materials are required with very good long term mechanical behaviour under high temperature loading. Especially highly loaded components like turbine rotors, valve and turbine casings play a key role in further development of steam turbine technology, since their massive dimensions require additional manufacturing properties.

During the last 25 years intensive effort has been spent in the development of high temperature resistant ferritic-martensitic 9-12% CrMo(W)VNbN steels in order to increase the steam inlet temperature and pressure of fossil fired power plants to 600-625°C / 300 bar with simultaneous thermal efficiencies exceeding 45-47% [44, 84]. In order to increase the thermal efficiency further achieving 50-55%, steam inlet parameters of 700-720°C / 375 bar are targeted in advanced coal fired steam power plants with a long-term goal of 750°C steam temperature. These temperature levels are not sustainable for heat resistant steels and alternatively the much more expensive nickel- and cobalt-based alloys have to be exploited. During the European collaborative research and development project "Advanced 700°C pulverized coal-fired power plants" (AD700), including contributions from turbine manufacturers, forgemasters and research centres, properties of candidate Ni-base alloys and product forms for advanced 700°C steam turbine technology have been investigated and demonstrated [99, 100]. The start of similar projects in the USA and Japan indicates the great potential and attraction of the advanced 700°C steam turbine technology [12].

The broad spectrum of relevant material properties for the use in steam turbine components comprises high strength and ductility both under short- and long-term conditions, sufficient oxidation resistance as well as good production and processing properties, including formability and hardenability of large components, weldability for production and repair purposes. Furthermore turbine components are subject to strict safety regulations since a possible failure would lead to catastrophic damage. Therefore ultrasonic inspectability of the material for even large wall thicknesses is required to ensure a defect free production or to guarantee the non-destructive testing of the accordant components. One central problem is the selection of a suitable forgable steam turbine rotor material. The R&D activity within the AD700 project included the manufacture of full-scale prototypes for Ni-base alloy forgings required for High Pressure (HP) and Intermediate Pressure (IP) steam turbine rotors and welding procedure development for joints in cast Ni-base alloys and for dissimilar metal welded joints. Due to economical reasons it is desired to replace the expensive Ni-base alloys with conventional 9-12% CrMo(W)VNbN or low alloy 1-2% CrMoV steels in these regions of the steam turbine rotors that are operating below approximately 500-550°C. This implies the requirement of dissimilar metal weldments between rotor discs made of Ni-base alloy and conventional steels since a welded design of the rotor is favoured.

During operation steam turbine components are subject to intense thermo-mechanical loading, especially during start-up and shut-down phases when large thermal strains and stresses are induced due to thermal transients. This can cause low cycle fatigue damage in local high loaded regions mainly as the result of material deterioration. Additionally the primary loading, mainly centrifugal body forces and pressure loads, during long-term stationary operation can cause significant creep damage and hence limits the achievable component lifetime. In order to exploit the materials strength ability optimally and to reduce any avoidable conservatism in the design of advanced steam turbine technology, the knowledge of the thermo-mechanical material behaviour, e.g. the constitutive deformation and damage models, are absolutely necessary. Therefore the knowledge of the major damage mechanisms during long-term exposure to temperature, corrosion and thermomechanical loadings are essential to accurately predict the lifetime of the component and ensure the safe operation of the power plant.

The present thesis documents work conducted in a collaborative research project between ALSTOM Power Switzerland and the Swiss Federal Laboratories for Materials Science and Technology EMPA, as part of the ETH Zurich research domain. It is the continuation of two former research collaborations between the High Temperature Integrity Group of EMPA / ETH and the Mechanical Integrity department of ALSTOM Power Steam Turbine R&D in Baden, Switzerland. The project is aimed at the development of thermo-mechanical lifetime assessment methodologies for the evaluation of 700°C steam turbine components involving the formulation of advanced constitutive deformation and damage model equations. The *main objectives* of the present research work include the following:

- *Development and verification of the effectiveness of advanced creep-fatigue lifetime assessment methodologies and determination of the required material input parameters for the accurate and reliable evaluation of Alloy 617 steam turbine rotor features at maximum steam turbine application temperatures.*

- *Identification of the maximum application temperatures of dissimilar metal welded joints between the Ni-base Alloy 617 and a 1% CrMoV low alloy bainitic rotor steel as well as a higher alloyed 10% Cr martensitic rotor steel with respect to both their creep and creep-fatigue properties.*

In order to achieve the appointed objectives an extensive testing campaign was necessary to investigate the material behaviour during long-term loading both under static and cyclic conditions covering a broad temperature and stress field. For ensuring the applicability of the generated results to the assessment of industrial turbine components, Alloy 617 test material was available in the right product form, originating from the prototype rotor forging from the AD700 project. The Alloy 617 - 1% CrMoV dissimilar metal welded joint test material was sourced from a second generation full-production ring weldment manufactured within an ALSTOM internal R&D activity where sections of the ring-weld were available to the present project. For the Alloy 617 - 10% Cr DMW joint parts from an existing full-size ring weldment had to be extracted and rewelded using the company specific weld geometry, welding procedure and heat treatment to ensure optimal transferability and applicability of the determined results. In order to exploit the greatest potential material knowledge data basis, access to confidential ALSTOM own material data and test results was granted to the present project as well as important information on specific testing procedures and design methods. For protection of the interest of the company not all the available data is published in the present documentation.

The *content* of the present thesis can be subdivided into the following chapters:

Chapter 2 provides an overview about the basic knowledge of the mechanical behaviour of heat resistant steels and Ni-base alloys and its weldments under high-temperature loading. The general deformation and damage mechanisms of crystalline materials are introduced, both under static and cyclic loading, and accordant damage assessment methodologies are compared to determine combined damage due to creep-fatigue interaction.

Chapter 3 presents details on the testing material and the experimental testing procedures applied within this thesis.

Chapter 4 summarises the work on the development of advanced creep-fatigue lifetime assessment methodologies of Alloy 617 at maximum steam turbine application temperatures. The chapter covers the experimental determination and the constitutive modelling of the material behaviour and presents results from post test metallurgical investigations to underpin an accordant damage model.

Chapter 5 provides documentation of the work performed on the identification of the maximum application temperatures of dissimilar welded joints between the Ni-base Alloy 617 and a 1% CrMoV low alloy bainitic rotor steel as well as a higher alloyed 10% Cr martensitic rotor steel with respect to both their creep and creep-fatigue properties.

Chapter 6 finally concludes the presented work and gives an outlook for further research and development activity.

Chapter 2

State of Knowledge

For the safe operation of materials under high thermo-mechanical loading the knowledge of the material deformation and deterioration characteristics is indispensable. The material properties primarily depend on the predominant microstructure of the material that is determined by the alloy composition, heat treatment and the degree of deformation. At high temperatures a number of thermally activated microstructural changes occur depending on temperature, mechanical loading and time. From the microstructural investigation of the prevailing material deterioration and damage mechanisms, accurate deformation models and damage assessment methodologies can be established which allow for a safe and highly efficient design of future technology. The thermo-mechanical loading leads to time- and rate dependent, diffusion-controlled deformations which are decreasing the strength and limiting the long-term operation of the material [10].

This chapter aims at reviewing the current state of knowledge with respect to the high-temperature behaviour of modern heat-resistant steels and Ni-base alloys. The basic strengthening mechanisms at elevated temperatures are summarised as well as the material characteristics observed under static and cyclic loading conditions. The basic fundamentals are given on constitutive modelling of the materials deformation and strength behaviour as well as on the concepts of consideration of multiaxial and non-uniform service cycle loading. The following chapter also introduces into the various damage mechanisms prevailing in materials under high temperature loading and reviews the relevant damage and lifetime assessment methodologies, with particular respect to creep-fatigue interaction under cyclic thermo-mechanical loading. Finally the current state of research on high-temperature similar and dissimilar welded joints is presented, covering the typical microstructural features of welded structures as well as the behaviour under high-temperature static and cyclic loading.

2.1 High-Temperature Mechanical Behaviour

2.1.1 Microstructural Fundamentals and Strength of Metals

Deformation of crystalline materials is perceived to be linked to the movement of crystal defects, so called dislocations, and its resistance to this movement arising from microstructural obstacles as well as to their rearrangement to form substructures. Conventional metallic materials feature a crystalline structure characterised by a regular arrangement of atoms within the closest neighbourhood of an atom in the crystal lattice. The most common lattice characteristics are as shown in Fig. 2.1 the body-centred cubic (bcc) structure, distinguished by a lattice unit-cube occupied by atoms at the corners and the centre, and the face-centred cubic (fcc) structure, identified by corner and cube face centre occupation. Heat resistant steels may have ferritic, martensitic or austenitic matrix structures. Whereas both ferritic and martensitic steels exhibit a bcc lattice structure (α-lattice), austenitic steels as well as Ni-base alloys have fcc lattice (γ-lattice) characteristics. Because of the lower diffusion coefficient of the closer packed fcc crystal lattice, austenitic steels are superior to ferritic steels with respect to their long-term creep strength. The decisive disadvantages of austenitic alloys are the lower heat conductivity and higher thermal expansion coefficients respectively, which penalize austenitic steels for their use in large turbine components because of increased induced thermal strains during temperature transients.

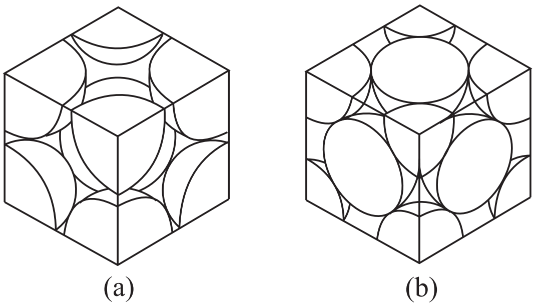
(a) (b)

Figure 2.1: Unit cell for (a) bcc and (b) fcc crystal lattice structure

While an infinite 3-dimensional recurrence of the above described unit cube would mean the perfect crystal lattice, real crystalline materials contain imperfections or lattice defects. In these locations the inter-atomic distances are disturbed from their equilibrium condition in perfect crystals. Irregularities within the lattice can also be present as point defects, e.g. interstitial atoms and vacancy defects. Plastic deformations and random misorientations during the crystal growth stage cause the formation of dislocations, characterised by disturbed interplanar spacings between two adjacent lattice planes and linear extension, i.e. they constitute line defects. Stacking faults within the lattice or grain boundaries in polycrystals constitute planar defects, whereas impurities, precipitates and voids can be denoted as bulk defects.

Polycrystalline materials consist of randomly oriented grains characterised by a macroscopically isotropic arrangement, whereas single crystal materials exhibit elastic anisotropy depending on the structure of the unit cell. These grain boundaries have an important influence on the thermo-mechanical behaviour of materials since they act as obstacles to impede long-range dislocation motion. The two basic types of disruptions in crystalline metals are represented in Fig. 2.2. Edge dislocations are extra planes of atoms in the crystal lattice, whereas screw dislocations are characterised by lattice planes spiralling around the dislocation line. In reality the dislocation lines are mostly curved indicating both edge and screw dislocation character [38, 61, 91]. Apart from the fact that a stress free perfect crystal would exhibit no dislocations, the dislocation density in well-annealed crystals can reach about $10^{10}\,\mathrm{m}^{-2}$, whereas during large deformations the dislocation density can be 10^{14} to $10^{15}\,\mathrm{m}^{-2}$. The increase of the dislocation density due to plastic straining results in work hardening because the further movement of dislocations is mutually obstructed.

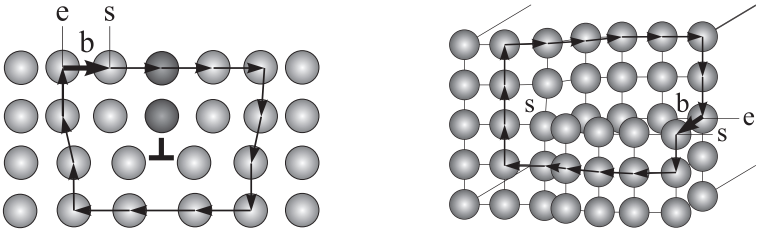

(a) Edge dislocation

(b) Screw dislocation

Figure 2.2: Dislocations as disruptions of the crystal lattice, after [61]

Above homologous temperatures of approximately $0.4\,\mathrm{T_M}$, a gradually change from time-independent to time-dependent material strength and deformation can be observed since the loading conditions allow for thermal activated processes like dislocation climb or lattice diffusion of point defects. In order to achieve a thermodynamic equilibrium condition the minimum overall strain energy resulting from the lattice disturbance is sought. As soon as the activation energy for diffusion or dislocation slide or climb is attained, dislocation movement is possible and will lead to a rearrangement of the dislocation network. The thermodynamic potential to achieve minimum lattice disturbance leads to the annihilation of dislocations of unequal sign within the crystal or to the formation of low-angle grain boundary (LAGB) configurations, that are characterised by a stacking of equal sign edge dislocations. Boundaries within the crystals constitute an important microstructural feature since they influence the deformation behaviour and the recovery, recrystallisation and grain growth processes [10].

The fundamental changes of the microstructure due to thermal activated diffusion processes and the rearrangement of the dislocation structure during recovery and recrystallisation processes is schematically shown in Fig. 2.3. Plastic deformation of the crystal results in stretching of the grains, forming a texture in the deformation direction, and a substantial increase of the dislocation density. Especially the movement of screw dislocations leads to enhanced vacancy formation in the lattice. During the process of recovery, the dislocation structure is rearranged, forming an energetically more favourable lattice configuration featuring LAGBs with small angle misorientations of the grain regions adjacent to the boundary. The high-angle grain boundaries (HAGB) are not shifted during the recovery processes and hence the deformed grain structure is attained. One distinguishes between static recovery of the material without the presence of mechanical loadings and dynamic recovery due to simultaneous mechanical straining. Generally recovery results in a reduced strength but increased ductility of the material, which is practically used in annealing processes.

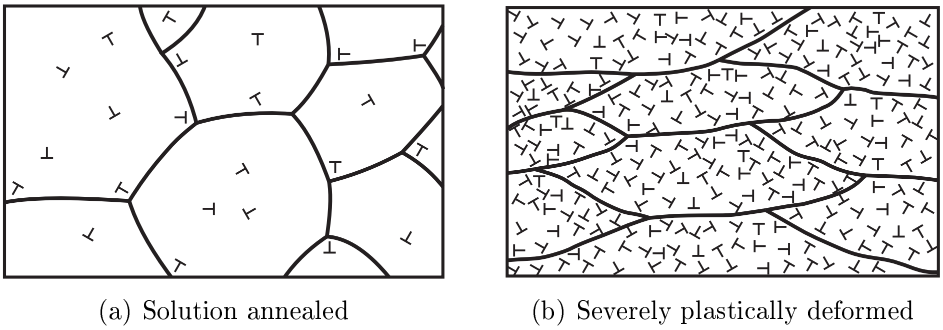

(a) Solution annealed

(b) Severely plastically deformed

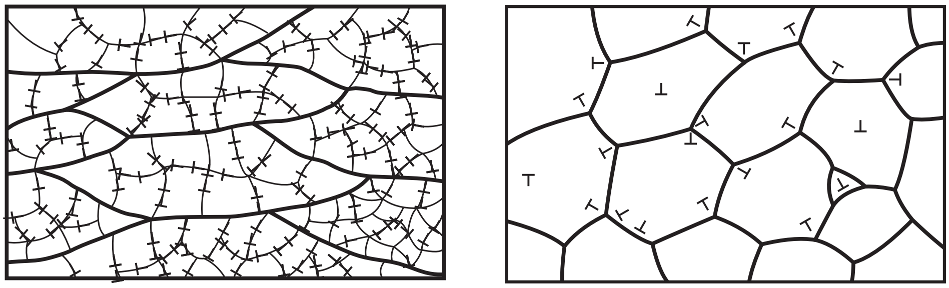

(c) Recovery

(d) Complete recrystallisation

Figure 2.3: Schematic microstructural alteration during recovery and recrystallisation with respect to grain shape and size as well as to the dislocation arrangement and density, after [10]

At higher annealing temperatures eventually recrystallisation occurs resulting in complete grain reformation and hence is linked to the movement of both LAGBs and HAGBs. A solution annealed grain structure emerges, exhibiting mostly globular grains with substantially reduced dislocation densities compared to recovery processes. The process of recrystallisation is chronologically separated into an incubation phase, when nucleation of new grains takes place, and a growth phase of the recrystallisation nuclei until the whole grain structure is exhausted. The kinetics of the recrystallisation process are influenced by the duration and temperature as well as the grain structure, e.g. degree of plastic deformation and initial grain size. Also the amount of alloying elements and precipitated phases or dispersed particles have considerable influence on the movement of grain boundaries as well as nucleation and grain growth during recrystallisation.

During recrystallisation the lattice distortion enthalpy is reduced to very low levels. The new formed HAGBs contain yet the chemical energy stored in the grain boundaries. Hence there is a potential to reduce this grain boundary enthalpy, which is not very high compared to that of recrystallisation. After primary recrystallisation during annealing the new grains, at sufficiently high temperatures, tend to minimize the remaining grain boundary enthalpy by coarsening. Thereby larger grains grow at the expense of smaller grains by moving of grain boundaries, e.g. detaching atoms from the shrinking grain and attaching to the growing grain. Situations when only a few grains grow very large lead to an unequal grain size distribution, i.e. a bimodal grain structure. This so called secondary recrystallisation principally occurs in alloys, where a equal continuous grain growth is prevented due to precipitations.

Deformation mechanisms

At temperatures below approximately $0.5\,\mathrm{T_M}$ the propagation of dislocations in the lattice results in a slip of one segment of the lattice relative to another lattice segment. This so called dislocation slip or glide mechanism is restricted to slip planes consisting of the closest packed planes of the crystal. It is important to note that the two mentioned crystal lattice structures differ in the amount of slip systems, with bcc-lattices exhibiting a larger number of slip planes compared to fcc crystal lattices. If the shear stress acting in the slip plane exceeds a critical value, e.g. the critical resolved shear stress, plastic deformation will occur. This resistance during dislocation slip in a defect-free crystal is called Peierls-Nabarro stress. As indicated in Fig. 2.2, edge dislocations move parallel to their Burgers vector b, screw dislocations perpendicularly. Unlike edge dislocations, screw dislocations can change the slip plane they are moving on, facilitated by the intersection of slip planes along a certain crystal direction. The presence of cross-slip is often featured by wavy or ill-defined dislocation substructures in bcc-crystals.

In the course of minimising the lattice distortion enthalpy, it might be more favourable for the dislocation to split into two partial dislocations. Since the elastic energy of a lattice dislocation is proportional to the square of the Burgers vector, splitting into two dislocations with smaller Burgers vectors results in less stacking-fault energy than the movement of the dislocation by one full lattice length, as it is true for a perfect dislocation. Materials with bcc-lattice structure exhibit high stacking-fault energies and feature spatial or wavy dislocation arrangement, whereas in fcc-crystals with lower stacking-fault energy planar dislocation structures have been observed [38].

The second important lattice deformation mechanism after dislocation slip at lower temperatures is deformation twinning. As shown in Fig. 2.4, a region within the crystal lattice is reoriented as the atoms between the twin planes are rotated about an axis. The twinning event occurs very rapidly involving only small plastic deformation. The stress required for the nucleation of the twin is thereby much larger than the one needed for twin propagation. Consequently the nucleation is responsible for a sudden load drop causing serrations on the yield curve. Twinning formation generally is observed in crystals with restricted slip systems at lower temperature levels and comparatively high strain rates [61, 91].

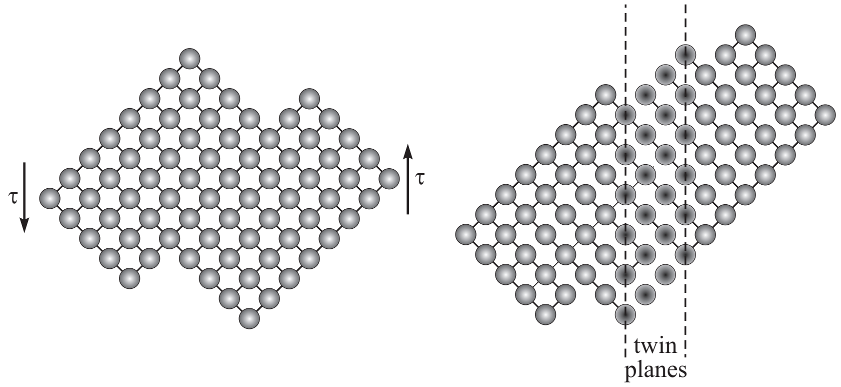

Figure 2.4: Twin formation in a crystal, after [61, 91]

The above mentioned deformation mechanisms are already active at low temperatures of approximately 0.15-0.2 T_M. The minimum amount of stress to overcome the lattice friction, caused by the break up of the atomic bonding along the dislocation line during glide, is achieved by thermal activation even at low temperatures. At higher temperatures diffusion controlled processes activate the dislocation climb mechanism, characterised by vacancy mechanism causing the diffusion of atoms and vacancies to or away from the site of the dislocation. Hence edge locations are than able to move out of their slip plane. The dislocation climb mechanism facilitates the recovery processes like dislocation annihilation, the rearrangement of the dislocation network forming LAGB and the ability of edge dislocations to climb over obstacles in their slip plane. Additionally the ability of screw dislocations to slip is enhanced at higher temperatures. In general the thermodynamic potential for dislocation climb increases with increasing temperature, whereas the potential for dislocation slip is decreasing. [10].

Strengthening mechanisms

The strengthening mechanisms for ambient to medium temperature levels are not suitable since an efficient blockage of dislocation movements is impeded due to thermal activated processes like lattice diffusion, grain recovery and grain growth mechanisms, grain boundary sliding and recrystallisation. High-temperature strength materials hence have to exhibit microstructural strengthening mechanisms that are sufficiently effective also at elevated temperature operation. These strengthening mechanisms are mainly constituted by obstacles to dislocation movement on different scales, including grains, second phases, precipitates and substitutional or interstitial atoms. Obstacles on the atomic scale are represented by point defects including vacancies, interstitial and substitutional atoms. As shown in Fig. 2.5 point defects cause a local distortion to the crystal lattice, which results in an interaction with the stress field of near dislocations. This method is used as the basis for solid solution hardening, where the solute obstacles affect the propagation of edge and screw dislocations effectively. A solid solution is a mixture of elements which do not have a strong affinity to each other. If the solute and the solvent atoms are of the same size, the solute atoms occupy solvent lattice positions as a substitutional atom, solute atoms of much smaller size an the other side will occupy interstitial places in the lattice. The introduction of solute atoms into a solvent atomic lattice hence produces a stronger alloy than the pure metal. However, only a small number of alloy systems exist permitting an extensive solid solubility between two or more elements. Furthermore the strengthening effect of solid solution hardening decreases with increasing temperature due to the enhanced thermal fluctuation of the atoms.

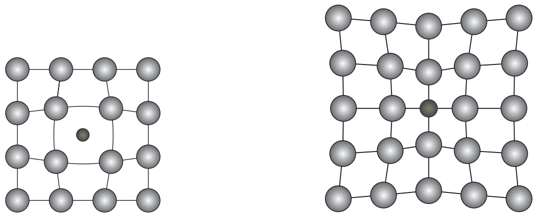

(a) Interstitial atom (b) Substitutional atom

Figure 2.5: Solid solution hardening leading to a distortion of the lattice by interstitial and substitutional atoms, after [61]

Solute obstacles strongly influence the propagation of both edge and screw dislocations due to their distortion of the crystal lattice and results in paraelastic dislocation interactions, as shown in Fig. 2.6. At enhanced temperatures, when the point defects are sufficiently mobile, the attractive interaction of dislocations can lead to diffusion of point defects into the dislocation core region. Thereby dislocations might be pinned by the solute atmosphere or the precipitates along the core. At certain temperature and deformation rate conditions the enhanced

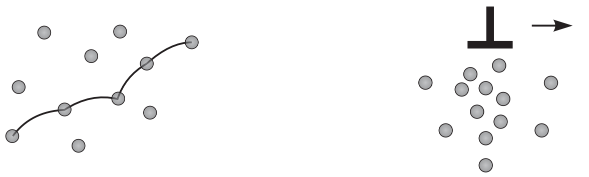

(a) Paraelastic dislocation interactions in solid solution hardened alloys

(b) Accumulation of interstitial atoms at dislocations at high temperatures

Figure 2.6: Interaction of point defects and dislocations in solid solution strengthened alloys, after [61]

solute mobility can cause the repeated pinning and unpinning of dislocations from point defects or precipitates during straining, which is resulting in the macroscopic observation of serrated yield phenomena, i.e. dynamic strain ageing or Portevin-LeChatelier effect [38, 61].

Solution annealed alloys which pass through a multi-phase region during cooling, caused by the limited solubility of the alloying elements, show second phase precipitation in the supersaturated solid solution matrix. Usually the formation of a phase equilibrium is suppressed by a suitable fast cooling, and the coordinated precipitation is conducted during subsequent heat treatments. The precipitation process is divided into the nucleation and growth of these precipitated particles and is characterised by the volume fraction of the precipitates and their average size. Precipitated second phase particles are important obstacles to dislocation movement and there are various precipitation hardening mechanisms involved. The particle hardening effect is primarily caused by coherency strengthening, resulting from the introduction of a strain field in the matrix around the precipitates due to a mismatch of the lattice parameters. Secondarily stacking-fault strengthening, caused by interaction forces due to different stacking-fault energies of the matrix and the precipitate, and chemical strengthening, associated with an increase of

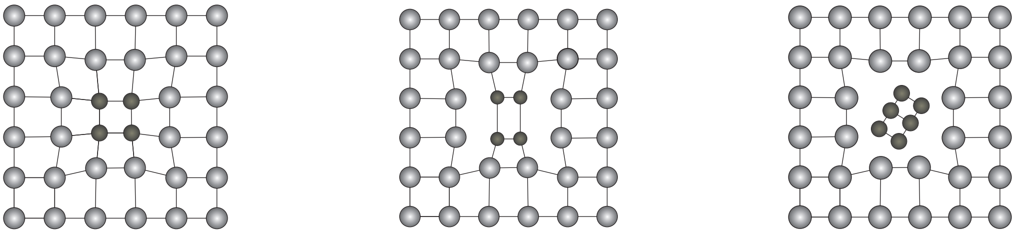

(a) Coherent particle

(b) Semi-coherent particle

(c) Incoherent particle

Figure 2.7: Coherent, semi-coherent and incoherent interfaces between precipitated particles and surrounding matrix, after [61]

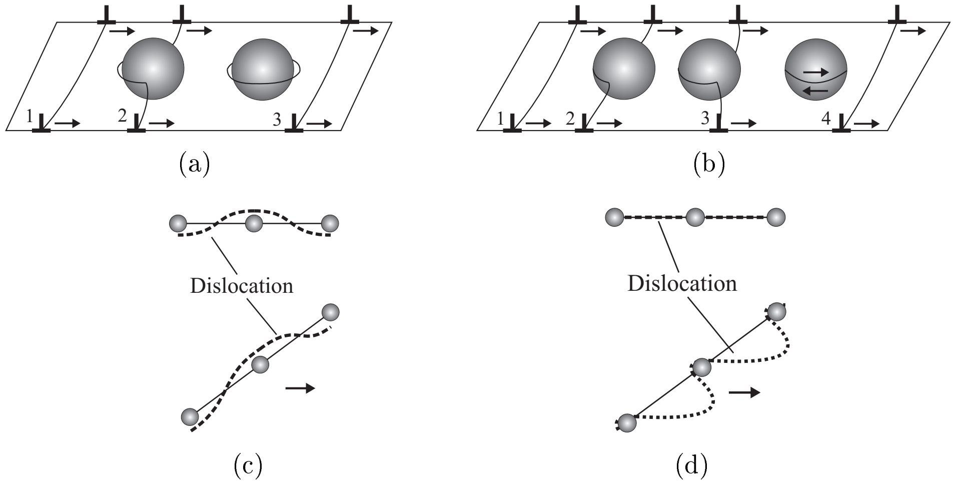

(a) (b)

(c) (d)

Figure 2.8: Schematic representation of the interaction mechanism of dislocations passing through precipitated particles: (a) Orowan mechanism, (b) Srolovitz mechanism, (c) general climb and (d) local climb, after [2]

energy due to the formation of new boundaries during coherent particle cutting, are active. The strongest precipitation hardening effect is normally obtained by a fine dispersion of coherent and semi-coherent particles [61].

Depending on the misfit-parameter δ, defined by the difference of the lattice parameter of matrix and precipitate, one distinguishes coherent, semi-coherent and incoherent particles, see Fig. 2.7. The precipitated particles provide beneficial obstacles that dislocations must either cut, climb over or move between. Under any circumstances a higher stress is necessary to move the dislocation through a lattice containing precipitates. The dislocation is pinned to the particle until the shear stress is sufficient to invoke climbing and looping of the dislocation or precipitate shearing. The interaction between precipitates and dislocations can cause macroscopic hardening or softening of the material depending on the involved microstructural deformation mechanism. Strain hardening of the material is constituted by the looping mechanism proposed by OROWAN [71], as shown in Fig. 2.8, and the assumption that dislocations bend and form loops around the precipitate. The remaining dislocation ring increases the resistance to motion of further dislocations. This effect can macroscopically be observed as strain-hardening behaviour in cyclic stress-strain curves of materials. The propagation of dislocations through crystal lattices containing precipitated particles causes the formation of a back stress in the opposite direction of the dislocation propagation. This back stress results from dislocation pileups and hence exhibits orientation-dependent hardening characteristics which must be represented by a tensorial description. If the shear stress is sufficiently large, coherent and semi-coherent precipitated particles can be sheared by dislocations. This shear or Srolovitz mechanism results in dislocation glide on a slip plane through the particle, displacing the precipitate lattice on one side of the slip plane relative to the other. Repeated shearing of the particle can lead to precipitate cutting into subparticles. This shearing mechanism leads to softening of the material [91].

Whereas at low temperatures the precipitation strengthening effect may be accounted for by introducing a threshold stress below which no dislocation slip is possible, high temperature exposure allow the thermal activation of diffusion controlled dislocation climb mechanisms. This constitutes a temperature and strain rate dependent component to the threshold stress for dislocation climb and plays an substantial role in controlling the creep rate during static high-temperature loading.

A dislocation strengthening effect results from the interaction of dislocations on various intersecting slip planes with increasing dislocation density during mechanical straining. The increasing number of activated slip systems and mutual dislocation interactions lead to an enhancement of the flow stress, e.g. work or strain hardening. In a homogeneous polycrystal material with sufficient small grain sizes this hardening effect can be regarded as isotropic. However the assumption of randomly distributed dislocations is critical, since in most materials the dislocations tend to form heterogeneous dislocation substructures during monotonic or cyclic loading conditions.

2.1.2 Behaviour under Static Loading

The long-term high-temperature operation of materials is limited by the continuous deterioration of the microstructure due to deformation, damage processes or corrosive influences. A reliable design, operation and monitoring of high temperature components require the knowledge of the time-dependent constitutive deformation behaviour and strength properties of the used material.

Above $0.4\,\mathrm{T_M}$ possible time-dependent processes do not take excessive long durations without practical relevance, but the thermal activation of dislocation climb processes induces inelastic time-dependent deformation of the material, e.g. creep deformation. The macroscopically observable creep strain results basically from transcrystalline deformation processes like dislocation propagation and the diffusion of lattice point defects, but also intercrystalline processes featuring grain boundary sliding and diffusion contribute as well. During creep the material microstructure is subject to an equilibrium state between the formation of new dislocations in order to accommodate for the plastic deformation and to recovery processes, characterised by the annihilation of dislocations and the formation of dislocation substructures [10].

At high stress levels the plastic deformation is substantially based on dislocation slip, which causes transgranular fracture after extensive plastic loading. At decreased stress levels or higher temperatures mainly diffusion-controlled microstructural processes are dominant and the deformation behaviour is constituted by the time-, stress- and temperature-dependent dislocation creep process. Dislocation creep is characterised by the presence of diffusion and dislocation climb processes. In Fig. 2.9 the dominant deformation and fracture mechanism maps depending on stress and temperature are shown for polycrystalline materials. At very high temperatures above approximately 0.6 T_M, or low stresses accordingly, creep deformation is essentially caused by diffusion processes in the crystal. Coble creep characterises the diffusion process along the grain boundaries at sufficient low stresses and temperatures below 0.7 T_M, whereas above this temperature diffusion takes place in the whole crystal lattice, i.e. Nabarro-Herring creep. At these temperatures temperature resistant materials can no longer be used since the dominating diffusion processes have such an high influence on dislocation propagation, that obstacles are easily bypassed and the strengthening mechanisms are no longer effective. [10, 2, 70]

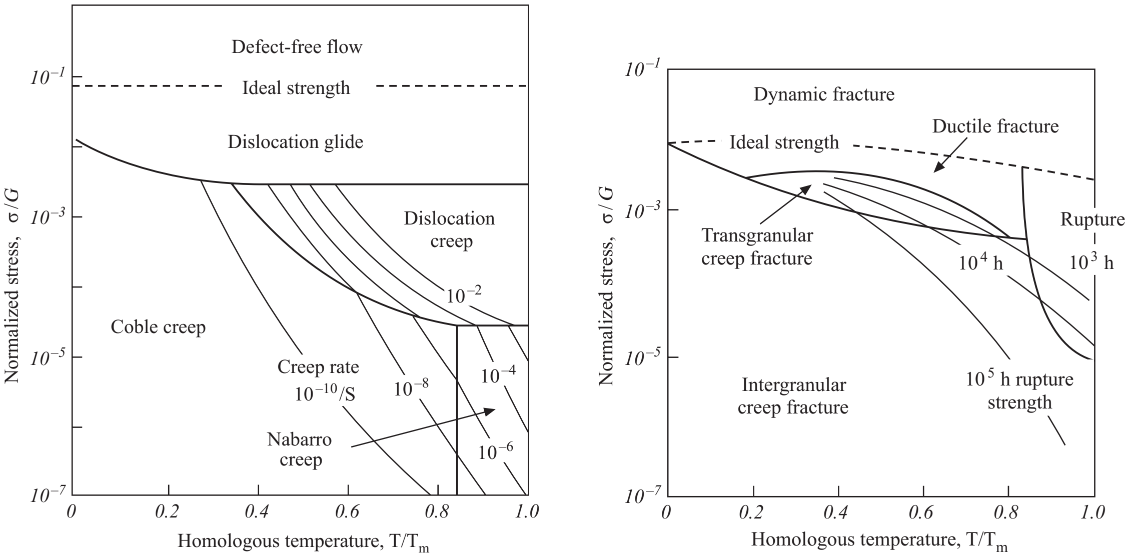

(a) Deformation mechanism map showing the dominant deformation mechanism

(b) Fracture mechanism map indicating the damage processes and fracture appearance

Figure 2.9: Schematic deformation and fracture mechanism maps with contours of constant creep strain rate and constant time to creep rupture for polycrystalline materials for normalised stress and homologous temperature, after [2]

In particular the HAGBs act as an important feature during dislocation creep, since the increased dislocation density around these lattice distortions facilitates enhanced diffusion and to a disadvantageous coarsening of the grain boundary strengthening precipitates. HAGBs, and with increasing diffusional character also

LAGBs, are vulnerable to long-term creep loading since they feature the formation of voids and micro-cracks which results in intergranular creep fracture.

Since the thermal activated microstructural deformation mechanisms are present at basically all stress levels, the knowledge of the material creep deformation characteristics is essential for the safe operation of high-temperature components. The material creep behaviour can be experimentally determined by creep rupture tests, where the strain of a specimen is measured under constant load conditions. Usual representations are the variations of the creep strain $\varepsilon_c(t)$ and the derived creep strain rate $\dot{\varepsilon}_c(t)$, as shown in Fig. 2.9. The total observable strain ε_t can be divided into an instantaneous part ε_0, that may be subdivided into an elastic ε_e and plastic ε_p contribution, and into the time-dependent creep strain ε_c:

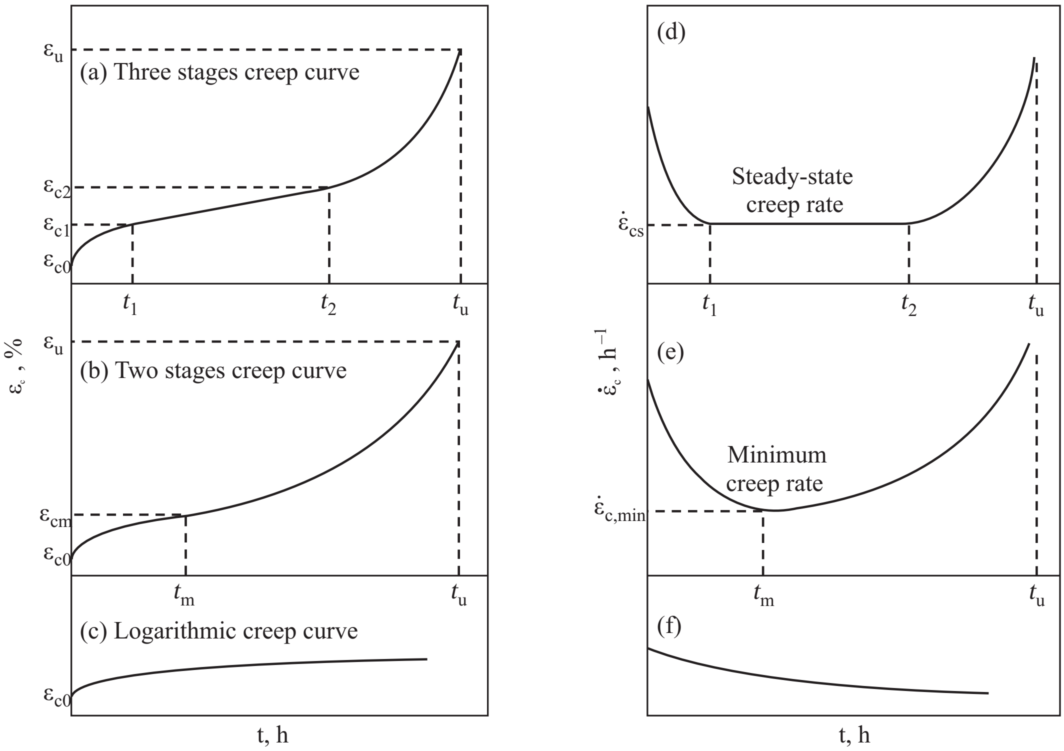

Figure 2.10: Schematic representation of the creep behaviour under monotonic tensile load for different engineering alloys: (a)-(c) creep strain, (d)-(f) creep strain rate as a function of time, after [2]

$$\varepsilon_t = \varepsilon_{el} + \varepsilon_{pl} + \varepsilon_c \tag{2.1}$$

The profile of the creep strain curve in most metals and alloys is characterised by three stages, consisting of a primary, a secondary or steady-state and a tertiary creep stage until creep fracture. In the primary creep stage $\dot{\varepsilon}_c$ decreases to a steady-state creep strain rate $\dot{\varepsilon}_s$, attributed to strain hardening and to a decrease of mobile dislocations. Fig. 2.11 schematically shows the evolution of the dislocation substructures during the first creep stages. During primary creep deformation a subgrain structure develops from an initial random dislocation distribution.

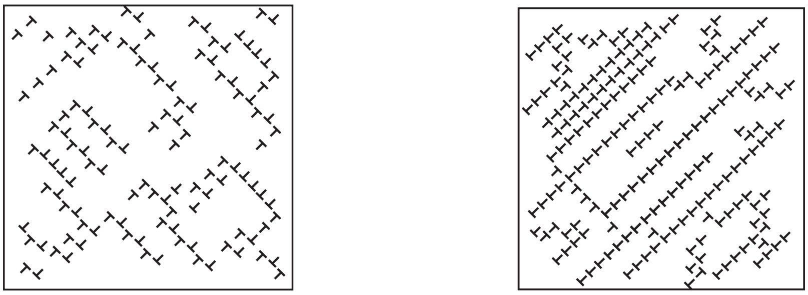

(a) Random dislocation distribution at the beginning of primary creep

(b) Beginning formation of LAGBs in advanced primary creep stage

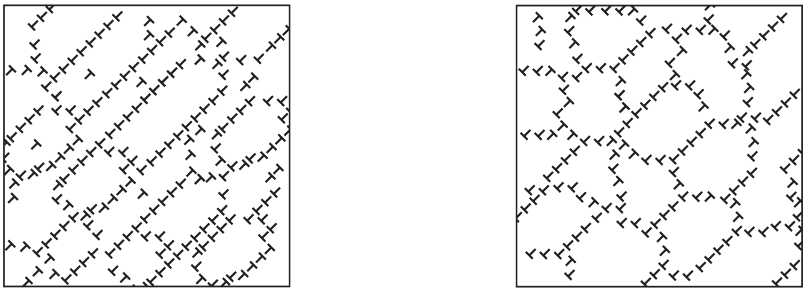

(c) Pronounced formation of LAGBs at the end of primary creep

(d) Completed subgrain formation during secondary creep stage

Figure 2.11: Schematic representation of the evolution of dislocation substructures during creep deformation, after [10]

The secondary creep stage features a constant $\dot{\varepsilon}_c$, where a state of balance between the rate of formation and annihilation of dislocations is present and the subgrain diameter remains approximately constant. Under certain conditions a steady-state creep stage might be absent and only a minimum creep strain rate $\dot{\varepsilon}_{c,min}$ is observable. Finally tertiary or accelerated creep is initiated, characterised by incipient formation of transgranular or intergranular creep damage induced voids leading to increasing $\dot{\varepsilon}_c$ and macroscopic creep cracking until final fracture at the creep rupture time t_u and creep rupture strain ε_u. The fracture mechanism map, as shown for fcc-metals in Fig. 2.9, provides important information about the dominant damage and fracture mechanisms, resulting in fracture in a shorter time than any other simultaneously prevailing mechanism. This is especially useful for the determination of guidelines for assessment of damage evaluation and remaining life estimation of components operating under high thermo-mechanical loading conditions [2].

Creep deformation modelling

Simple phenomenological descriptions of the creep deformation in form of equations are mostly given for constant stress σ and temperature T conditions. Constitutive equations that couple evolutionary deformation modelling, whether the material exhibits strain hardening or softening behaviour, with the occurring material deterioration or damage are the most universal means, but demand extensive testing effort in order to determine the required material properties. Phenomenological equations are, depending on their extension, able to describe the three technical creep stages, e.g. primary, secondary and tertiary creep deformation contributions.

The most important parameter is the minimum or steady-state creep strain rate, that can be represented by a power function of the stress:

$$\dot{\varepsilon}_c = f(\sigma) = A \cdot \sigma^n \tag{2.2}$$

In this equation, also referred to as Norton law, A is a material constant depending on temperature and microstructural properties, whereas the stress exponent n indicates the dominant deformation mechanism. Usually the temperature-dependence is incorporated by a Arrhenius exponential function and the minimum creep rate can be given as:

$$\dot{\varepsilon}_c = f(\sigma) \cdot f(T) = A \cdot \sigma^n \cdot e^{-Q_c/RT} \tag{2.3}$$

where Q_c represents the activation energy for the creep deformation mechanism and R the gas constant. For many materials the minimum creep rate is inversely proportional to the creep rupture time, which is usually referred to as the Monkman-Grant relationship:

$$\dot{\varepsilon}_c = \frac{C}{(t_r)^m} = A \cdot \sigma^n \cdot e^{-Q_c/RT} \tag{2.4}$$

where C is a constant depending on total elongation during creep and m is a constant often nearly equal to 1.

The stress exponent indicates the creep deformation mechanism, with n=4-7 for dislocation creep and n=1-2 for creep-induced grain boundary gliding. Under very low loading and creep rates stress exponents of approximately n=1 can arise, which is caused by dominant diffusion-controlled creep deformation. Fig. 2.12 shows the correlation between the activation energy for high-temperature creep and lattice self diffusion for pure metals [70, 84]. In the stress region, where dislocation creep is the dominant deformation mechanism, higher n are observed. Fig. 2.13 shows the minimum creep rates for heat-resistant solid-solution and precipitation strengthened steels compared to not alloyed iron. The effect of these strengthening mechanisms are effectively described by an internal friction stress, which is constituted by the stress field interactions of these obstacles and moving dislocations.

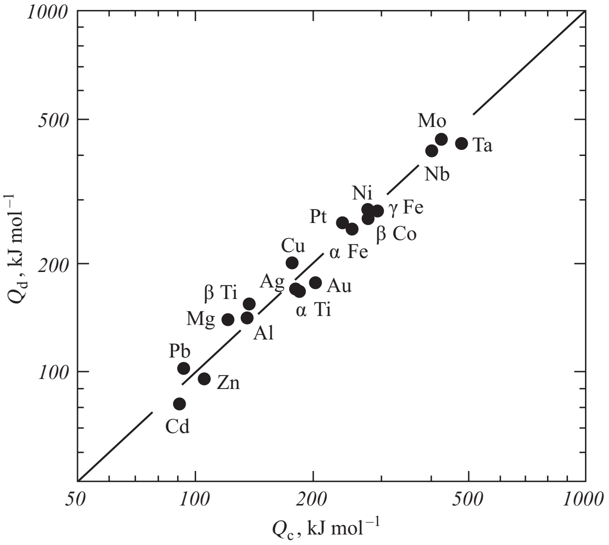

Figure 2.12: Correlation between activation energies for high-temperature diffusion-creep, Q_c, and lattice self diffusion, Q_d, in pure metals, after [70]

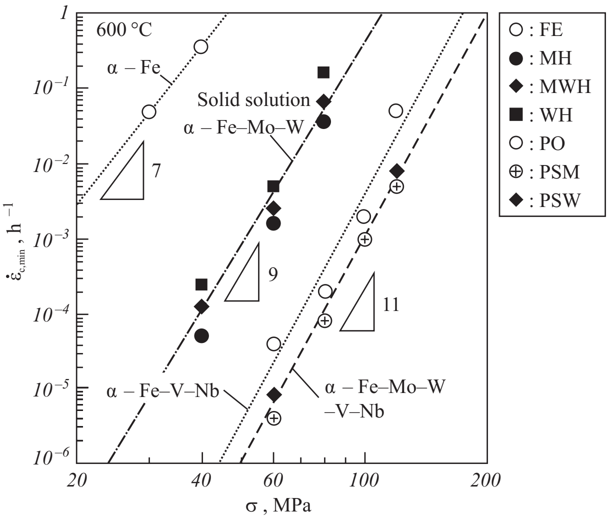

Figure 2.13: Minimum creep rate of α-Fe and solid-solution α-Fe-Mo-W alloys with ferritic matrix and precipitation hardened α-Fe-C-Mo-W-V-Nb alloys at 600°C. MH: Fe-0.12Mo, MWH: Fe-0.34Mo-1.63W, WH: Fe-2.27W, PO: Fe-0.06C-0.2V-0.08Nb, PSM: Fe-0.06C-0.51Mo-0.2V-0.08Nb, PSW: Fe-0.06C-0.15Mo-0.7W-0.2V-0.08Nb, Fe is pure iron, (mass%), after [2]

In order to integrate the modelling capability to describe the creep deformation behaviour more accurately within the technical important creep strain region, i.e. primary and secondary creep, extensions of the stress-dependent term $f(\sigma)$ with a time-dependent term $f(t)$ have been proposed. Common approaches are the one from BAILEY [7] in form of a power-law:

$$f(t) = F \cdot t^m \tag{2.5}$$

or the one from GAROFALO [28] as exponential function:

$$f(t) = \Phi_1(1 - e^{-\Phi_2 t}) + \dot{\varepsilon}_s \cdot t \tag{2.6}$$

On the basis of these temperature, stress and time-dependent terms appropriate combined approaches have been developed, the most popular is the Norton-Bailey equation, as a combination of 2.2 and 2.5:

$$\varepsilon_c = K \cdot \sigma^n \cdot t^m \tag{2.7}$$

Restrictions of the above mentioned creep deformation equations within time, temperature and stress lead to a development of more advanced equation sets, for example the Θ-projection method, which is an extension of the Garofalo equation sets [25, 84]:

$$\varepsilon_c = \varepsilon_1 + \Theta_1\big(1 - e^{\Theta_2 \cdot t}\big) + \Theta_3\big(1 - e^{\Theta_4 \cdot t}\big) \tag{2.8}$$

The parameters Θ_i at the same time are temperature and stress dependent functions, that might contain up to 20 parameters. Also the modified Garofalo equation, which has been developed in German and European research projects, has found broad industrial application. Based on 2.6 an additional term is added to account for the tertiary creep regime similar to 2.8. The primary, secondary and tertiary creep strain contributions are determined as follows:

$$\begin{aligned} \varepsilon_c &= \varepsilon_{c1} + \varepsilon_{c2} + \varepsilon_{f3} \\ &= \varepsilon_{c1max} \cdot \left(1 - e^{-g_1 (t/t_{12})^u}\right) + \dot{\varepsilon}_{cmin} \cdot t + C_{23} \cdot (t/t_{23})^f \end{aligned} \tag{2.9}$$

Herein D, u, C_{23} and f are constants and the transition times t_{12} and t_{23} as well as the maximum primary creep strain ε_{c1max} and the minimum creep rate $\dot{\varepsilon}_{cmin}$ are temperature and stress dependent [37, 84].

An alternative approach to describe creep deformation, covering all three creep stages, is the one proposed by GRAHAM and WALLES [31]:

$$\dot{\varepsilon}_c = A_1 \sigma^{n_1} \varepsilon_c^{m_1} + A_2 \sigma^{n_2} \varepsilon_c^{m_2} + A_3 \sigma^{n_3} \varepsilon_c^{m_3} \,. \tag{2.10}$$

An advantage of this model is the incorporation of the strain hardening rule, which allows a better description of load level changes, as are existing even under simple stress relaxation conditions, than the time hardening assumption. In a modified version of the creep law (2.10) the tertiary creep behaviour was represented by an effective stress concept, see equation (2.32) in section 2.2.1, with a damage parameter D:

$$\dot{\varepsilon}_c = A_1 \left(\frac{\sigma_e}{1 - D}\right)^{n_1} \varepsilon_{c,e}^{m_1} + A_2 \left(\frac{\sigma_e}{1 - D}\right)^{n_2} \varepsilon_{c,e}^{m_2} \,. \tag{2.11}$$

Here the damage evolution equation $\dot{D}$ is to be determined as described in section 2.2.1, equations (2.33) or (2.34). Additionally expressions of the creep damage variable depending also on the multiaxiality of the stress state can be incorporated [55].

Determination of long-term creep strength

The determination of the materials long-term properties, e.g. the creep rupture strength $R_{u/t/T}$ and the creep strain strength $R_{\varepsilon/t/T}$, is a fundamental for the design of steam-turbine components. Most common is the description of the mean material properties, since different heats of nominally the same material scatter in terms of strength properties due to slight variations of the chemical composition, product form and heat treatment.

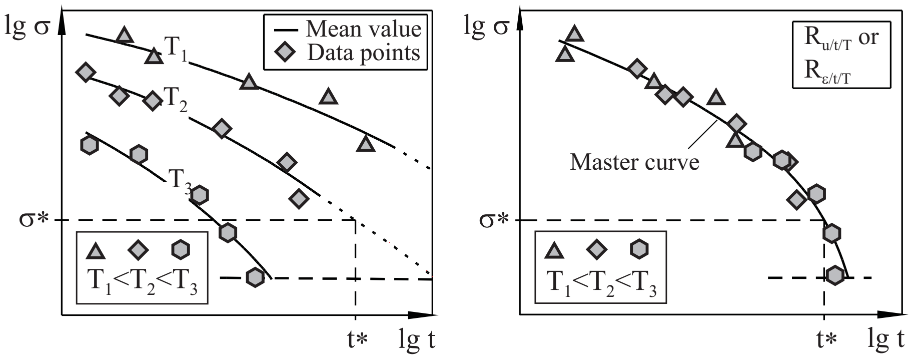

Figure 2.14: Scatterband analysis using time-temperature parameter and prediction of the rupture time and time to datum strain at constant stress

One practically important method is the introduction of a time-temperature parameter $P(T,t)$ for the evaluation of $R_{u/t/T}$ and $R_{\varepsilon/t/T}$ for multiple heats of a material. Thereby the isothermal $R_{u/t/T}$- and $R_{\varepsilon/t/T}$-curves are each combined into one characteristic master curve $P(\sigma)$, with the assumption that the thermal activated microstructural processes are occurring at a faster rate at higher temperatures. The main interest here is a extrapolation of long-term creep strength properties on the basis of shorter testing results. Fig. 2.14 shows the scatterband analysis using a time-temperature parameter and the prediction of the rupture time and time to datum strain at constant stress for three different temperatures.

One of the most common time-temperature parameters is the one proposed by Larson and Miller [49] with the material specific constant C:

$$\mathrm{P_{LM}} = \mathrm{T(C + \log\, t)}\,. \tag{2.12}$$

For certain materials better fitting results on experimental creep rupture data have been accomplished by the relationship proposed by Manson and Haferd [57]:

$$\mathrm{P_{MH}} = \frac{\log \mathrm{t} - \log \mathrm{t_a}}{\mathrm{T} - \mathrm{T_a}}\,. \tag{2.13}$$

The time-temperature parameters differentiate by the trend of the isostats, i.e. curves of constant stress, in the time-temperature plot. The master curve is defined by a model function, whose parameters are determined by regression analysis. The model function is usually a polynomial of the stress function $f(\sigma)$, e.g. $\log \sigma$ or σ^m. Resolving for $\log t$ gives the following regression equation:

$$\log \mathrm{t} = \mathrm{B}_0 + \frac{1}{\tau} \cdot \sum_{\mathrm{j}=1}^{\mathrm{M}} \mathrm{B}_{\mathrm{j}} \cdot (\mathrm{f}(\sigma))^{\mathrm{j}-1} \tag{2.14}$$

where the parameters B_j have to be determined depending on the polynomial order M. A broad overview about most widely used time-temperature parametric equations as well as algebraic equations in creep rupture data assessments is given in [36].

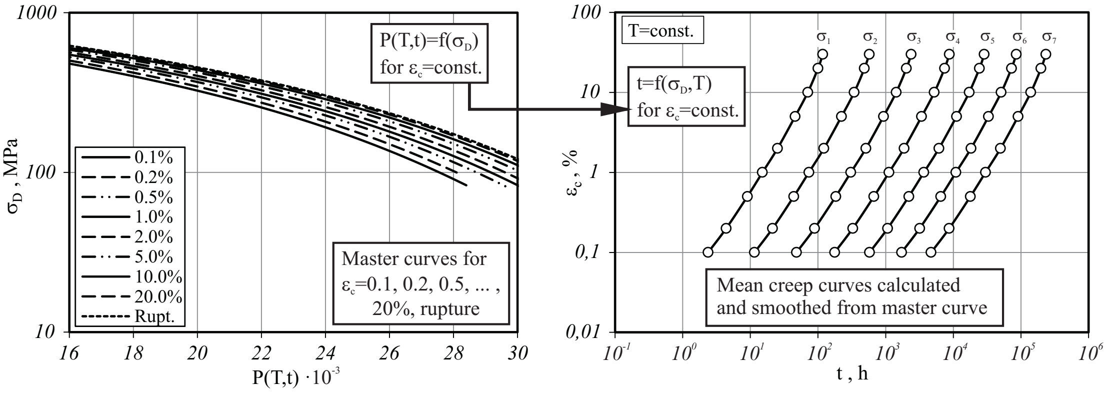

Figure 2.15: Master curve families for creep strain strength $R_{\varepsilon/P(T,t)}$ and creep rupture strength $R_{u/P(T,t)}$ (a) and mean creep curves based on optimised master curves (b)

For sufficient large creep rupture datasets master curve families of $R_{u/P(T,t)}$ and $R_{\varepsilon/P(T,t)}$can be determined and mean creep curves can be constructed, as shown in Fig. 2.15. These mean creep curves form the basis for heat specific modelling of the creep deformation behaviour of high-temperature materials [84].

2.1.3 Cyclic Loading Conditions

Cyclic loading comprise the variation of stress or temperature with time, contrary to monotonic static loading conditions. Primarily high-temperature components are charged to their static creep loading during steady-state operation, but additionally thermal loading during the temperature transients induce considerable strains and stresses, e.g. the secondary cyclic loading. The material damage resulting from the cyclic loading is called fatigue, characterised by the formation of fatigue cracks and subsequent crack growth.

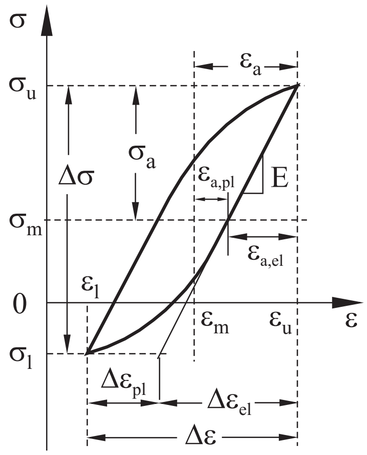

Figure 2.16: Closed σ-ε-hysteresis loop with arbitrary position and designations of important measures

Under high temperature loading the fatigue endurance region can be divided, depending on the number of cycles to failure, into a low cycle fatigue (LCF) and a high cycle fatigue (HCF) portion. LCF leads to fatigue crack initiation at numbers of cycles N_f typically less than 10^4 - 10^5, fatigue endurances above this transition limit are considered as HCF. Historically LCF was introduced as the simulation of thermal fatigue (TF) of thermal loaded components, but in order to simplify the laboratory testing conditions isothermal testing is conducted for standard LCF material testing. Anisothermal testing of materials can be subdivided into thermal fatigue, with rapidly changing temperature and hence thermal induced stresses and strains during thermal shock testing, and thermo-mechanical fatigue (TMF) with variable temperature and mechanical loading profiles [10, 50]. Fig. 2.16 shows the variations of stress and strain for a closed hysteresis cycle, as it is observed under low and high temperature LCF testing when the material response is time-independent or the testing frequency is sufficiently high. Due to the considerable plastic strain contributions during LCF testing, uniaxial strain controlled testing is adapted in standard high temperature material testing, with variable strain amplitudes and strain rates in order to account for the time-dependent flow characteristics [6, 40]. Generally these testing conditions represent TF more realistically, because strains are the decisive feature for thermal fatigue damage. In constant strain amplitude tests the stress response of the material indicates the relevant hardening characteristics during plastic deformation, as is schematically shown in Fig. 2.17 for a cyclically softening and hardening material respectively. Ferritic and martensitic steels offer a cyclic softening stress response under strain-controlled loading, whereas austenitic steels and Ni-base alloys exhibit cyclic hardening characteristics. The balance between the predominant hardening and softening mechanisms in the material constitutes the characteristic stress-strain

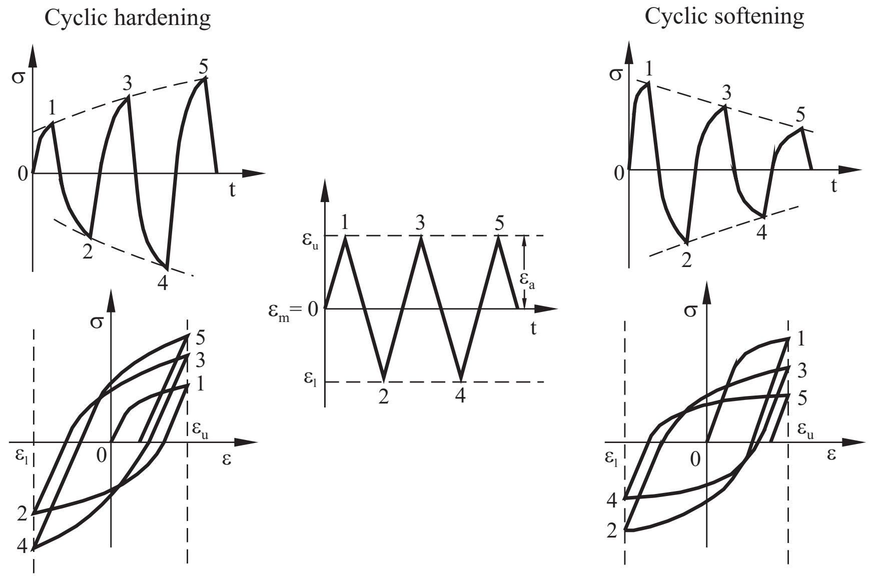

Figure 2.17: Cyclic softening and hardening material response during strain controlled testing with zero mean strain

relationship. At straining of a material above the elastic limit of proportionality, macroscopic strain hardening arises through the increase of the dislocation density and mutual dislocation interactions, that requires a higher applied stress to maintain an imposed deformation. During monotonic tensile deformation the plastic straining causes the flow stress to increase due to dislocation multiplication, especially when tested from solution-annealed initial state. With substantially increased internal energy, which is stored in the dense dislocation pile-ups and generally all lattice distortions, the rate of recovery is increasing such that LAGBs and subgrains are formed. The formation of low-energy dislocation arrangements by thermal activated dislocation climb and cross-slip processes constitute macroscopic softening of the accordant material, which opposes the hardening mechanisms. Generally the continuous change of the microstructural features and its influence on dislocation motion results in a history dependence of the material behaviour, e.g. different internal states due to the transforming microstructure [10, 61, 91].

One major restriction of the laboratory testing procedure, in order to achieve realistic testing times, is the accelerated strain rate adopted for LCF testing in the range of 0.5 - 20 %/min, which is remarkably above the strain rates of large steam turbine components under service-type operation. The same applies for the length of possible hold times in the tensile or compressive peaks, which might be introduced in order to account for creep deformation effects. Standard strain controlled LCF tests with symmetric or asymmetric hold periods in tension or compression peak strain are common testing practice and the effects of hold time duration, strain rate and damage temperature have been widely investigated for modern heat resistant low alloy 1-2% CrMoV and advanced 9-12% CrMo(W)VNbN steam turbine rotor steels [8, 32, 78].

Next to the deformation characteristics of the material under cyclic loading, standard LCF test results provide information on the fatigue endurance behaviour. Strain localisations and the formation of persistent slip bands (PSBs) under progressive cyclic plastic deformation lead to an irreversible dislocation rearrangement and hence to a microstructural alteration. Mostly at surfaces these PSBs cause protrusion profiles, which are resulting from different plastic deformation within the PSBs during alternating plastic shearing. The extrusions and intrusions at these characteristic slip steps often place the origin of fatigue micro-cracks, whose progressive accelerating growth finally leads to fracture at cycle N_f. The accordant damage mechanisms leading to fatigue crack initiation in metals are explained in detail in chapter 2.2.2. During strain controlled testing crack initiation is marked by a stress drop in σ_a and a reduction of the stress range $\Delta\sigma$. Fig. 2.18 shows the evolution of the stress response of a cyclic softening steel during strain-controlled LCF testing and the respective hysteresis loops at start, mid-life condition and at the end of life, characterised by a deformation of the compressive part of the hysteresis due to crack closure effects. In the terminal stage until final fracture indefinite deformation conditions prevail, caused by the geometry of the macroscopic crack and the affected deformation resistance to the imposed strain. Hence the number of cycles to crack initiation is defined as a x% stress drop below a certain reference level, that is either defined by a saturated plateau or a linear softening curve typical for ferritic or martensitic steels as shown in Fig. 2.18. The percentage x is application specific and typically in the range of 1 - 5 % [83, 84].

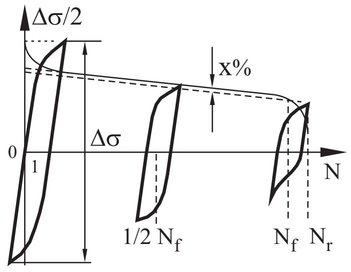

Figure 2.18: Reduction of $\Delta\sigma$ in ε-controlled LCF tests for a cyclic softening material and definition of numbers of cycles to crack initiation

As a fundamental LCF test result the fatigue endurance characteristics $\Delta\varepsilon = f(N_f)$ are commonly determined. Next to standard continuous cycling LCF experiments, LCF tests with hold time are conducted, whereas with increasing duration of the hold period the endurance is decreasing. One of the most common approaches for the parametric description of the fatigue endurance curve originally proposed for low temperatures is the one proposed by Coffin [19] and Manson [18], where the fatigue endurance curve is represented as the sum of an elastic and a plastic contribution:

$$\Delta\varepsilon = \Delta\varepsilon_{el} + \Delta\varepsilon_{pl} = C_1 \cdot N_f^{-\beta_1} + C_2 \cdot N_f^{-\beta_2} \,. \tag{2.15}$$

In a double logarithmic plot this represents elastic and plastic asymptotic lines as indicated in Fig. 2.19, which represents the schematic Coffin-Manson endurance characteristics of a metal under high temperature continuous cycling. Thereby the

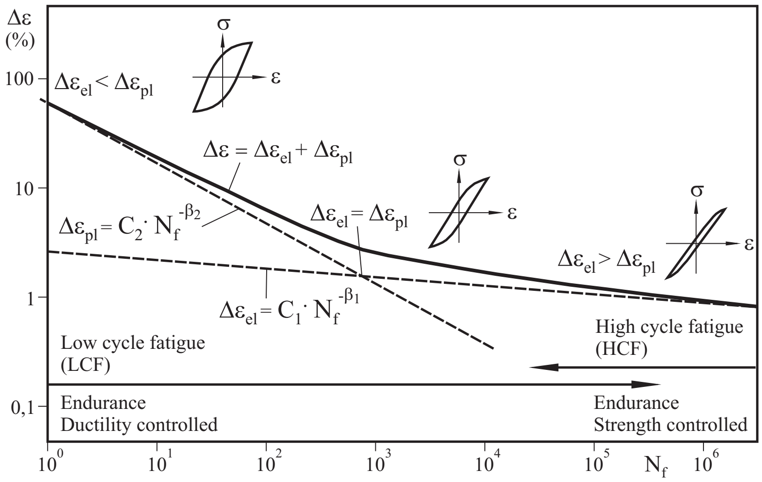

Figure 2.19: Schematic partition of the endurance curve into an elastic and plastic distribution for low and high cycle fatigue, after [19, 84]

coefficients C_1, C_2, β_1 and β_2 are material and temperature specific parameters. The assumption in eqn. (2.15) is that the material endurance during high strain amplitude cycling is mainly defined by its ductility properties, whereas the HCF endurance is controlled by the strength of the material. With increasing temperature the creep strain contribution becomes increasingly dominant, the deformation time-dependent and hence the fatigue endurance is strain rate dependent under high temperature loading [10, 19, 83, 84].

Next to the fatigue endurance data the static flow and cyclic stress-strain characteristics of the material are important input parameters for the design of high-temperature components. During initial loading, e.g. tensile testing under suitable strain rates, the static flow curve of the material is revealed, indicating strain hardening during plastic deformation. For description of the cyclic stress-strain (CSS) characteristics usually the cyclic flow curve at mid-life condition $N_f/2$ is generated. For this purpose the peak stresses σ_a at the reversal points at peak strain ε_a are plotted for selected number of cycles N/N_f. For cyclic softening materials the CSS curve is below the initial loading curve, which is schematically shown in Fig. 2.20. Additionally the influence of hold periods at peak strain is indicated, where the recovery processes during the stress relaxation phases lead to progressive softening. The recovery processes, mainly based on dislocation creep in these stress regions, are strongly temperature dependent and below a specific transition temperature no effect of hold periods can be observed. For description of the static flow and CSS characteristics usually the total strain is separated into an elastic portion $\varepsilon_{el} = \sigma/E$ and a plastic contribution ε_{pl}, which can be expressed as a power law function as proposed by Ramberg and Osgood [80]:

$$\varepsilon = \varepsilon_{\mathrm{el}} + \varepsilon_{\mathrm{pl}} = \frac{\sigma}{\mathrm{E}} + \left(\frac{\sigma}{\mathrm{K}'}\right)^{1/\mathrm{n}'} . \tag{2.16}$$

The cyclic hardening exponent n' and the cyclic hardening coefficient K' therein depend on N/N_f, $\dot{\varepsilon}$, T and are material specific.

One of the most efficient experimental methods to determine the CSS characteristics of a material is the incremental step test. During the test the plastic strain amplitude varies linearly between two limits, which features an important fact, because the rearrangement of the dislocation substructures during testing is independent to a specific ε_a and hence the loading is random-like. More importantly, the incremental step test offers the capability to approximately determine the fatigue endurance characteristics if there is only insubstantial knowledge of the material. Another experimental method for the approximate determination of the CSS curve with one single test offers the multiple-step test, featuring blocks of incremented plastic strain limits in which the material is cycled until stabilised hysteresis loops result. This process is continued until the entire CSS curve is generated. For each specific strain amplitude however the material response was due to a dislocation substructure developed specifically under the accordant ε_a, which is contrary to the incremental step test exhibiting microstructural features resulting from a random loading history, which in principle correspond to service-type loading conditions to a much greater extend. Experiments on materials with bcc as well as fcc lattice structures have revealed that the dislocation substructures developed as a response to low plastic strain amplitude cycling show loose dislocation veins or bundles, whereas with increasing ε_a the formation of PSBs is observed. With extended plastic straining dislocation rearrangement and multiple-slip mechanisms result in the development of labyrinth or cell substructures [16, 69].

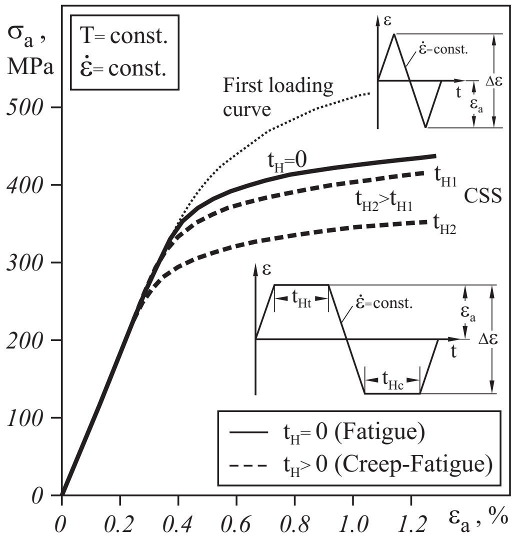

Figure 2.20: Schematic representation of the static flow and cyclic stress-strain curves at mid-life condition of standard LCF experiments with and without hold periods at peak strain

Constitutive modelling of plasticity

The deformation of crystalline materials can be divided into an elastic and a plastic or irreversible portion. The assumption of small strain plasticity allows the additive decomposition of the total strain tensor into an elastic component ε^{el} and a plastic contribution ε^{pl}:

$$\varepsilon = \varepsilon^{el} + \varepsilon^{pl}\,. \tag{2.17}$$

For isotropic, linear elastic materials the 4th order elasticity tensor $\mathbf{C}$ reduces to the following expression with the shear modulus G and Lame's coefficient λ:

$$\begin{gathered}\sigma = \mathbf{C}\,\varepsilon^{el}\\ \sigma_{ij} = \lambda\,\varepsilon_{kk}\delta_{ij} + 2G\,\varepsilon_{ij} \qquad (2.18)\\ \text{with}\quad G = \frac{E}{2(1+\nu)} \quad\text{and}\quad \lambda = \frac{\nu E}{(1+\nu)(1-2\nu)}\end{gathered}$$

as well as E being the elastic modulus and ν the Poisson's ratio of the material. With $\sigma_H{=}1/3\,\sigma_{kk}$ equals the hydrostatic or spherical stress, the deviatoric stress tensor $\mathbf{s}$ can be expressed:

$$s_{ij} = \sigma_{ij} - \frac{1}{3}\sigma_{kk}\delta_{ij}\,. \tag{2.19}$$

The deviatoric stress component is primarily associated to cause plastic flow, because plastic deformation is assumed to be incompressible and hence must be independent on the hydrostatic stress tensor components. For isotropic metallic materials, where the yield stress is not orientation-dependent, a commonly used approach for a yield function f depending on the second invariant J_2 of the stress tensor is the one proposed by von Mises:

$$f = \sqrt{3J_2} - \sigma_y = 0 \quad\text{with}\quad J_2 = \frac{1}{2}s_{ij}:s_{ij} = \frac{1}{2}\Big(\sigma_{ii}^2 - \sigma_{ij}\sigma_{ij}\Big)\,. \tag{2.20}$$

Thereby σ_y denotes the yield stress of the material and $\sigma_e = \sqrt{3J_2}$ represents the von Mises effective stress, which generally transfers a multiaxial stress state into an equivalent uniaxial quantity. The effective stress can also be expressed in terms of the principle stresses:

$$f = \sqrt{\frac{1}{2}\Big((\sigma_1{-}\sigma_2)^2 + (\sigma_2{-}\sigma_3)^2 + (\sigma_3{-}\sigma_1)^2\Big)} - \sigma_y = 0\,. \tag{2.21}$$

It should be remembered that the material state in the stress tensor is clearly defined either by the three stress invariants J_1, J_2, J_3 or the three principle stresses σ_1, σ_2, σ_3. The expression of the yield function in (2.21) represents a cylinder of the radius σ_y along the hydrostatic axis in the principle stress space, where at the surface ($f{=}0$) plastic flow occurs and the interior of the cylinder constitutes the elastic region ($f{<}0$).

In order to model the experimentally observed strain hardening behaviour, adequate hardening rules have to be provided. Strain hardening constitutes itself in a change of the yield surface in the stress space, whereas two different types of hardening have been observed, i.e. isotropic and kinematic hardening. Isotropic hardening represents itself in a shrinkage or an expansion of the elasticity domain for cyclic softening and hardening materials respectively. As indicated in Fig. 2.21a isotropic hardening can be included by the consideration of an additional hardening term R, which itself typically depends on an internal state variable. Common approaches use the accumulated plastic strain p or the dissipated plastic energy W_{pl}, which are defined as follows:

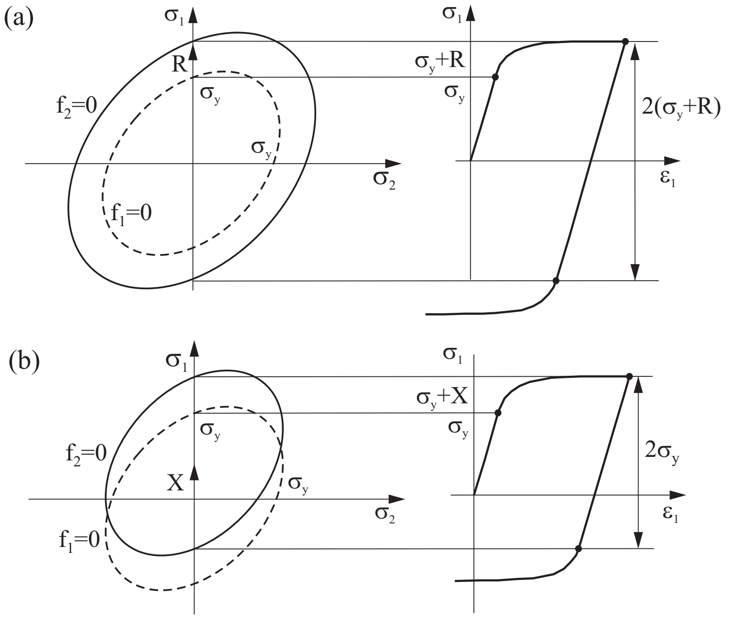

Figure 2.21: Schematic representation of (a) isotropic hardening and (b) kinematic hardening

$$p = \int \left(\frac{2}{3} \dot{\varepsilon}^{pl} : \dot{\varepsilon}^{pl} \right)^{1/2} dt \,, \quad W_{pl} = \int \sigma : \dot{\varepsilon}^{pl} \, dt \,. \tag{2.22}$$

A common approach to model the isotropic hardening evolution-dependent is the one proposed by Chaboche [14]:

$$\dot{R} = b\,(Q - R)\,\dot{p} \,, \tag{2.23}$$

where Q denotes a saturation value of the isotropic hardening stress, which is negative ($Q < 0$) in the case of cyclic softening and positive ($Q > 0$) for cyclic hardening, and b the rate at which R is changing. During reversed loading conditions however the isotropic hardening model predicts an unreasonably large elastic domain $2(\sigma_y + R)$, as indicated in Fig. 2.21a. The increase of the flow stress is not exclusively explainable with the increase of dislocation density, but additionally by the orientation dependent mutual blocking and interaction mechanisms between dislocations and lattice obstacles, e.g. dislocation pile-ups at LAGBs and HAGBs as well as in the range of precipitated phases and particles. Such a behaviour is more appropriately modelled by kinematic hardening, which corresponds to a translation of the flow surface in the stress space, as shown in Fig. 2.21b. In order to facilitate this translation a backstress tensor $\mathbf{X}$ is introduced, whose deviatoric component $\mathbf{X}'$ is used to express the flow function:

$$f = \sqrt{\frac{3}{2}\Big((\mathbf{s}-\mathbf{X}'):(\mathbf{s}-\mathbf{X}')\Big)} - \sigma_y = 0\,. \tag{2.24}$$

The simplest form of linear kinematic hardening, originating to PRAGER [75], is accomplished by a backstress formulation $\mathbf{X} = 2/3\, C\varepsilon^{pl}$, where C is the hardening constant in the resulting bilinear elastic-plastic behaviour. Extensions to this linear approach by the introduction of a dynamic recovery term $\gamma\mathbf{X}\dot{p}$ have been proposed by ARMSTRONG and FREDERICK [4] by the following evolution equation for the backstress:

$$\dot{\mathbf{X}} = \frac{2}{3}C\dot{\varepsilon}^{pl} - \gamma\mathbf{X}\dot{p}\,, \tag{2.25}$$

where γ is the recovery constant. For the anisothermal case the evolution equation for the backstress has to be extended by a term exhibiting the partial derivatives of the temperature dependent parameters [14]:

$$\dot{\mathbf{X}} = \frac{2}{3}C\dot{\varepsilon}^{pl} - \gamma\mathbf{X}\dot{p} + \frac{1}{C(T)}\frac{\partial C}{\partial T}\mathbf{X}\dot{T}\,. \tag{2.26}$$

Assuming isothermal deformation eqn. (2.25) can be analytically integrated to yield for the uniaxial case:

$$X = \kappa\,\frac{C}{\gamma}\Big(1 - e^{-\kappa\gamma(p-p_0)}\Big) + X_0\, e^{-\kappa\gamma(p-p_0)}\,. \tag{2.27}$$

Therein $\kappa \pm 1$ constitutes the flow direction for tension or compression in the particular loading branch and X_0 and p_0 represent the initial values for the backstress and the accumulated plastic strain at the load reversal points during any random cyclic loading. For large accumulated plastic strains p the back stress X is saturating at a value C/γ, whereas γ controls the hardening rate.

In order to improve the description of the non-linear hardening characteristics, multiple backstress approaches have been proposed by CHABOCHE ET. AL. [15], suggesting the linear superposition of individual backstresses:

$$\mathbf{X} = \sum_{i=1}^{M}\mathbf{X}_i(C_i, \gamma_i)\,. \tag{2.28}$$

$$\dot{\mathbf{X}}_i = \frac{2}{3} C_i \dot{\varepsilon}^{pl} - \gamma_i \mathbf{X}_i \dot{p}$$

$$\text{for} \quad i = 1, 2, 3$$

$$\dot{\mathbf{X}}_4 = \frac{2}{3} C_4 \dot{\varepsilon}^{pl}$$

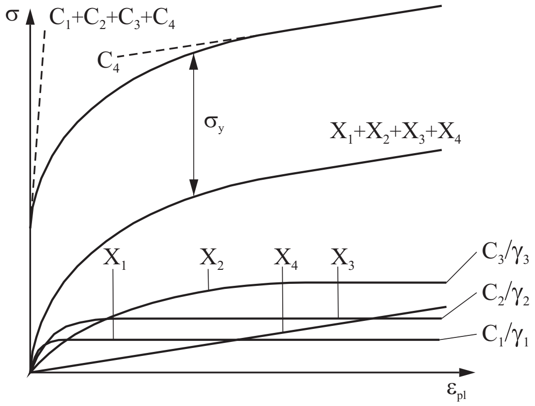

Figure 2.22: Schematic representation of the superposition of several linear and nonlinear backstresses

Especially the transition between elastic and plastic behaviour enacts a problem, since the hardening constant would need to be infinite to allow a smooth transition. Therefore at least one of the parameters C_i should be of high value to satisfy this drawback. As it can be seen from eqn. (2.27) the backstresses saturate to C/γ for a sufficient high accumulation of plastic strain. A exemplary sketch of the backstress evolutions of a combination of three nonlinear and one linear kinematic hardening terms is given in Fig. 2.22. The linear hardening term is implemented for the description of non-saturating strain hardening behaviour with a tangent modulus of C_4, whereas the three nonlinear backstress terms are adjusted to represent optimally the hardening characteristics over the entire strain range [15, 50, 14].

With the assumption of a symmetric stress cycle and sufficient stabilised cyclic hardening or softening effects the CSS relationship of a combined hardening model, including nonlinear kinematic backstress terms and isotropic hardening, can be identified as [50]:

$$\frac{\Delta\sigma}{2} = \sum_{i=1}^{M} \frac{C_i}{\gamma_i} \tanh\Big(\gamma_i \frac{\Delta\varepsilon_{pl}}{2}\Big) + \sigma_y + R\,. \tag{2.29}$$

2.1.4 Multiaxial Stress State

Creep rupture and LCF tests are typically performed under uniaxial loading on smooth specimens. The material properties established under these uniaxial conditions, where the stress is homogeneously constant within the specimen cross section, have to be transferred to a general multiaxial stress state. Components may globally be subject to multiaxial loading or may exhibit necessary design features like grooves and notches, which act as stress concentrations and where locally a multiaxial stress state with inhomogeneous stress distributions prevails.

A commonly adapted approach for experimental simulation of a multiaxial stress-strain state is the use of circumferentially notched round tensile (CNRT) specimens, which is schematically shown in Fig. 2.23. The deformation constraint leads to a multiaxial stress state, where the axial stress σ_a and the tangential stress σ_t exhibit their maximum values at the surface of the notch ground. The radial stress on the other hand shows its maximum in a region below the notch ground surface, which is constituted by a plane stress state. For the evaluation of the multiaxial stress state commonly the multiaxiality factor H is determined, which can be expressed as the ratio of the hydrostatic stress and the von Mises equivalent stress:

$$H = \frac{3\,\sigma_H}{\sigma_e}\,. \tag{2.30}$$

Due to the strain constraint at the notched region a triaxial stress state prevails, resulting in maximum values of H for the region below the notch ground. During investigations on CNRT specimen under creep rupture conditions creep embrittlement at the notch region has been observed for certain materials, leading to an substantial drop of the creep ductility properties due to the deformation constraint and a remarkable decrease of the creep rupture strength of notched compared to smooth specimen geometries [59, 60]. Knowledge on the multiaxial behaviour of modern heat resistant steam turbine rotor steels have been gathered by the work of Schwienheer [84] and Radosavljevic [78] based on material originating from an 2%CrMoV bainitic and two 9-10%CrMo(Co)VNbN(B) martensitic rotor steel forgings. Creep rupture experi-

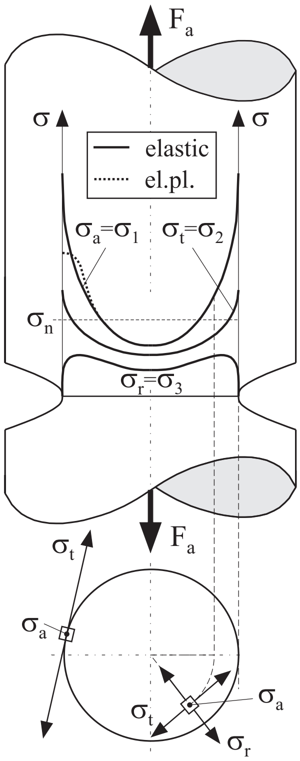

Figure 2.23: Multiaxial stress state in a circumferentially notched specimen showing the principle stress distributions in the notched cross section for elastic and elastic-plastic material response

ments for a range of standard notch geometries have revealed notch-hardening both for the cast and forged product form of the 10%CrMoVNbN steel, i.e. increasing creep rupture strength $R_{u/t/T}$ with increasing notch factor $K_t = \sigma_{e,max}/\sigma_n$. The comparatively small influence of the notch effect on $R_{u/t/T}$ is mainly explained by the large creep rupture strain or ductility A_u of this martensitic steel. The distinct primary creep strain formation observed for the steel leads to an early redistribution of the stress field around the notch and hence the geometrical notch effect is markedly reduced [84].

2.2 Damage and Lifetime Assessment

2.2.1 Creep Damage

During creep deformation various microstructural processes, i.e. the change of dislocation substructure, lead to an increase of the creep strain rate. Damage induced by creep deformation in form of cavities or creep cracking most usually is only measurable during the tertiary creep stage of a creep rupture test. On the microstructural level however creep cavity formation can be detected often in the early stages of lifetime and hence the formal understanding of the according creep damage characteristics plays an important role in damage assessment and lifetime prediction methodologies.

As indicated in the fracture mechanism map (Fig. 2.9) at high stress creep deformation predominantly transgranular creep damage is observed, resulting in transgranular ductile fracture, which is the transition to conventional tensile testing at elevated temperatures. The accumulation of dislocations at obstacles and the associated stress concentrations lead to interface cracking, which finally results in the characteristic dimples at the fracture surface.

During long-term creep loading on the other side creep damage is usually intergranular, characterised by wedge-type cracks at grain boundary triple points or cavity-type voids at the grain boundaries of polycrystalline materials. In the very early stages of creep life crack nucleation occurs at the grain boundaries mainly caused by grain boundary sliding of adjacent grains relative to each other. Grain boundary sliding causes stress concentrations at singular points like triple edges or precipitates at the grain boundary. The creep crack nuclei grow further to individual creep voids, that can be detected with the accordant expenditure. These cavities might arise to cavity chains along the grain boundaries, which than form into micro-cracks. Creep induced cracking mechanisms lead to an increasing creep rate, which can be explained by the reduction of the effective cross section due to void and crack formation, the increase of the material volume and hence length increase due to excessive void formation and finally the necking of the failing cross section for creep ductile materials [10, 43]. Fig. 2.24 shows a schematic representation of the creep damage evolution with increasing creep strain and time. Generally the microstructural processes during primary and secondary creep are considered as reversible, i.e. they can be reversed by an appropriate heat treatment. The creep damage induced in form of cavities and micro-cracks on the other side is irreversible [84].

On the basis of the correlation between the characteristic creep curve and the macroscopically observable creep damage, standard assessment rules have been established, where the creep cavity and micro-crack distribution of service loaded

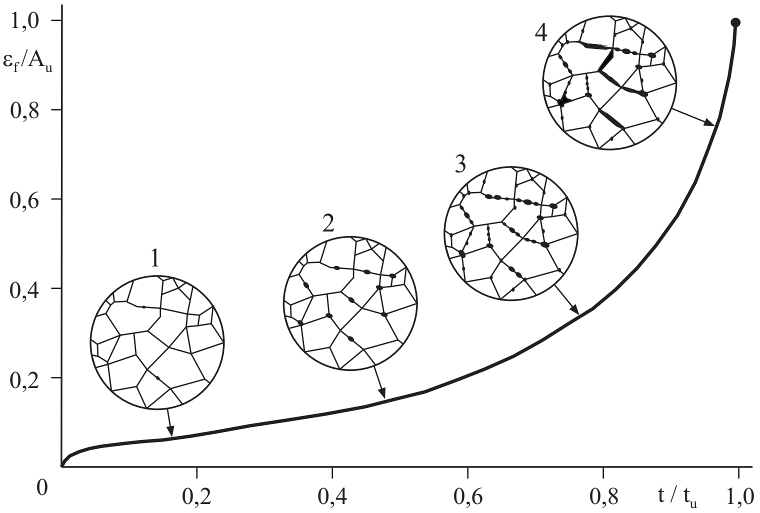

Figure 2.24: Schematic representation of the evolution of creep damage during monotonic creep rupture testing. 1: Nucleation, damage not detectable. 2: Single micro voids / cavities. 3: Micro void chains, distinctly detectable. 4: Micro cracking and final rupture due to macro cracks

components is determined with replica footprints from the component surface [101]. Various creep damage models use a damage variable D, which is defined by the ratio of the damaged area A_D and the nominal cross section A of a material volume element:

$$D = \frac{A_D}{A} \,. \tag{2.31}$$

Thereby it is assumed that these grain boundaries, which are damaged by creep cavities or cracks, only partially transfer the force. The effective stress acting in the damaged cross section can be described for the uniaxial case by:

$$\sigma_{eff} = \frac{\sigma}{1-D} \,. \tag{2.32}$$

For the description of creep damage Kachanov [42] suggested the following differential equation:

$$\dot{D} = \Big(\frac{\sigma_e}{A_0(1-D)}\Big)^r \,, \tag{2.33}$$

where A_0 and r are material specific parameters. An extension of the approach of Kachanov is the creep damage law proposed by Rabotnov [77]:

$$\dot{D} = \frac{(\sigma_e/A_0)^r}{(1-D)^\phi} \,, \tag{2.34}$$

where ϕ is a further temperature and material specific exponent introduced in order to describe the nonlinear increase of creep damage evolution.

The above introduction of a scalar damage variable D assumes isotropic damage, which does not depend on any orientation. In the case of non-isotropic damage due to micro-cracking approximately perpendicular to the maximum principal stress, a tensorial damage variable might be defined, considering the surface orientation of micro-defects [51].

2.2.2 Fatigue Damage

The most conclusive results of fatigue deformation and damage initiation mechanisms have been obtained with high purity single crystals of fcc metals. In commercial alloys the microstructural complexities mostly preclude an clear investigation of the fatigue mechanisms. One of the most visible features during saturated cyclic loading is the formation of localized slip bands, which can be observed on the free surface of a cycled specimen and which often place the origin of fatigue crack initiation. During cyclic loading with low plastic strain amplitudes exclusively single slip systems are activated and hence edge dislocation movement is dominating since screw dislocations can easily annihilate due to their cross-slip capabilities. The edge dislocations form substructures, like clusters, veins or persistent slip bands (PSB). Fig. 2.25a shows the schematic representation of the matrix with the

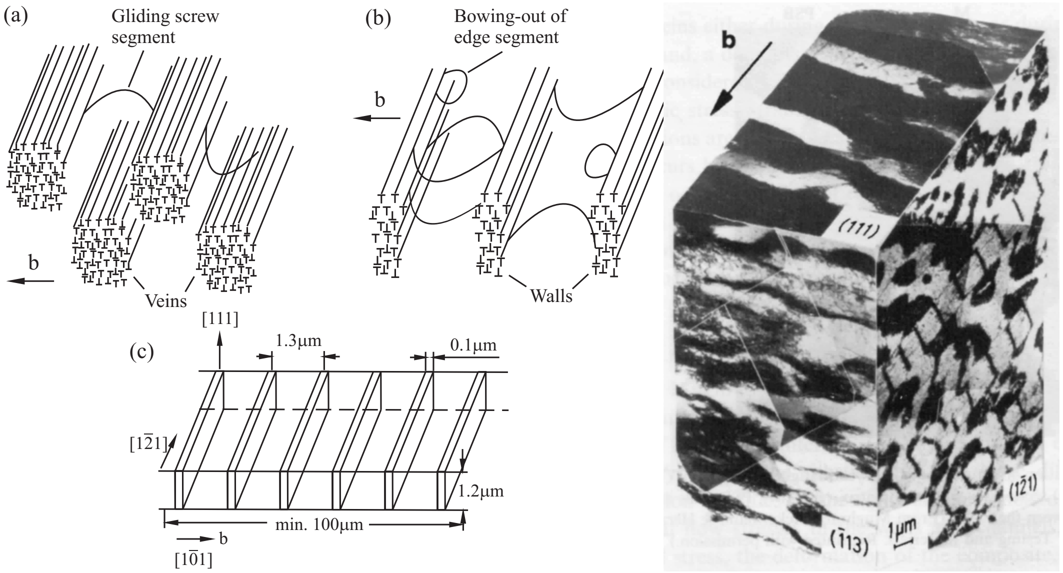

(a) Dislocation substructures in a plane perpendicular to the sliding plane. (a) Vein structure in the matrix. (b) Enlarged view on the bipolar walls and dislocation debris within a PSB. (c) A three-dimensional sketch of a PSB configuration, after [92]

(b) A three-dimensional construction of TEM images of the matrix vein and PSB configuration in Cu cycled to saturation at 20°C at $\gamma_{pl} = 1.5 \cdot 10^{-3}$, reprinted with permission from [64]

Figure 2.25: Dislocation substructures in cyclic loaded fcc metals and the formation of persistent slip bands

veins or walls, consisting of a dense array of edge dislocations, and channels. The channels in between the walls exhibit comparatively low dislocation densities, and the plastic deformation in them occurs mainly by the glide of screw dislocations. The PSB structure is generated by a mutual blocking of glide dislocations and the formation of a ladder structure of parallel walls, that are positioned normal to the Burgers vector *b*. Fig. 2.25b is an arrangement of several TEM micrographs showing the three-dimensional configuration of the matrix veins and PSB structures in a Cu single crystal cycled to saturation at 20°C. The $(1\bar{2}1)$ plane parallel to *b* clearly shows the ladder-like arrangement of the walls in the PSBs [17, 64, 92].

Whereas the veins of the matrix undergo only micro-yielding, the PSBs accommodate high plastic shear strains and exhibit macro-yielding. During alternating plastic deformation dislocations are continuously generated and annihilated in the PSB, whereas the annihilation of dislocation dipoles lead to vacancy generation. At a free crystal surface material can emanate and form the characteristic slip lines. Fig. 2.26a shows the formation of a protrusion profile with characteristic extrusions and intrusions along the PSB due to the enhanced slip activity. This surface roughness leads to stress concentrations, where fatigue micro-cracks might initiate preferably at intrusions in the vicinity of the interface between protrusion and surrounding matrix [54]. The grain structure of polycrystalline materials with random orientation towards the primary loading direction causes the activation of multiple-slip systems and grain specific dislocation substructure arrangements. At free surfaces the intense plastic straining related to PSBs can be accommodated by protrusion slide mechanisms, whereas the occurrence probability of PSBs in constrained grains is much smaller, see Fig. 2.26b. In regions within a grain dominated by single-slip ladder-type PSB substructures occur, whereas in regions

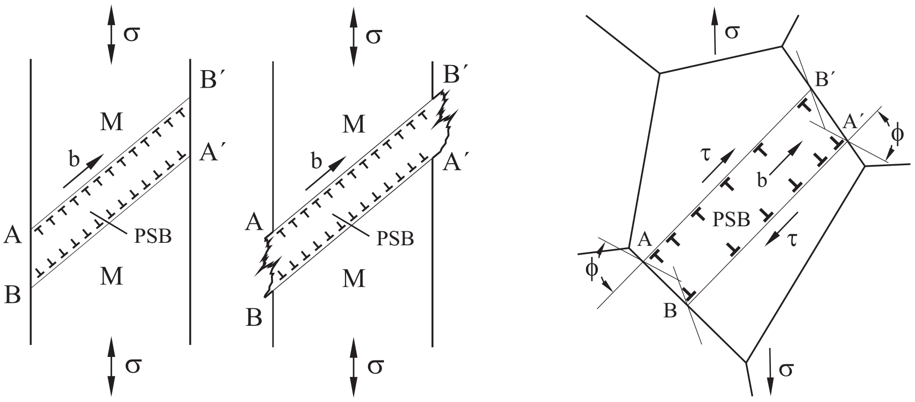

(a) Formation of a protrusion profile with characteristic extrusions and intrusions along a PSB at the specimen surface

(b) Schematic sketch of the interaction of a PSB and a grain boundary

Figure 2.26: Fatigue crack initiation due to persistent slip bands at surfaces of crystals or at grain boundaries of polycrystalline materials, after [54, 63]

characterised by multiple-slip systems labyrinth structures might develop. With increasing plastic strain amplitude multiple-slip processes lead to cell substructure configurations during saturated cycling, where the prevailing mean dislocation cell size can be correlated to the plastic strain amplitude [17]. Fig. 2.27 contains SEM micrographs of transcrystalline and intercrystalline fatigue crack initiation due to PSBs in plastically cycled polycrystalline Cu. The dislocation structure shown schematically in Fig. 2.26b leads to a stress localisation due to a dislocation accumulation in the PSB adjacent to the grain boundary. The induced tensile stresses are large enough to break the grain boundary and lead to intercrystalline crack initiation. Additionally LAGBs or twinning grain boundaries, due to their elastic anisotropy and the resulting stress concentrations, can support the initiation of cracks [54, 92].

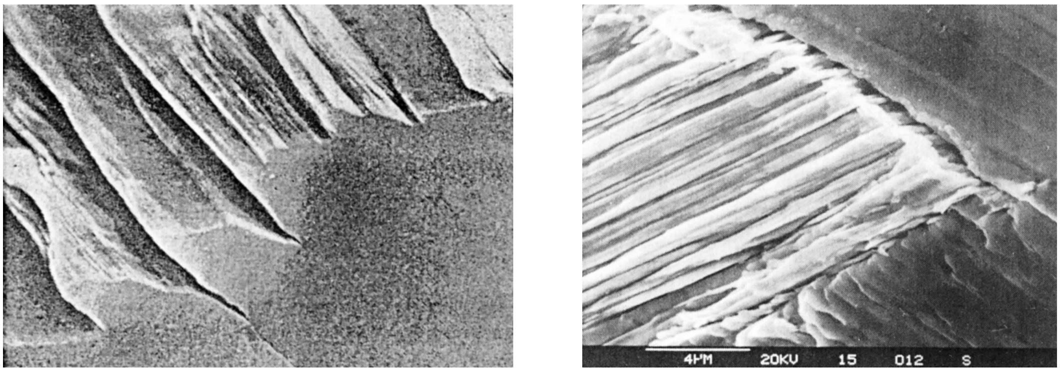

(a) Detail of a protrusion profile of a PSB at the surface of a cyclically deformed Cu specimen showing crack initiation at an intrusion

(b) Intercrystalline crack initiation in polycrystalline Cu due to interaction of PSBs and grain boundaries

Figure 2.27: Fatigue crack initiation due to persistent slip bands at free surface grains or at grain boundaries of polycrystalline Cu, reprinted with permission from [39]

For the fatigue crack initiation processes in precipitation hardened alloys the shear strain localization in PSBs plays an important role. If the precipitates are sufficiently coherent with respect to the surrounding matrix and allow the dislocations to cut through the precipitate, a strain localisation in planar slip bands is often observed. In γ'-hardened Ni-base superalloys the cutting through the precipitated phase particle results in the formation of extreme narrow slip bands. Broader PSBs can even lead to an repeated cutting of the precipitates and their final dissolution. Fig. 2.28 indicates schematically the cutting mechanism of precipitates due to PSBs for constrained interior grains and surface grains respectively. Fatigue crack initiation is in general influenced by a variation of parameters. For example a reduction of the grain size usually leads to an increasing fatigue strength, since the slip length is drastically reduced. One major influencing parameter on the fatigue crack initiation and propagation is constituted by the ambient atmosphere.

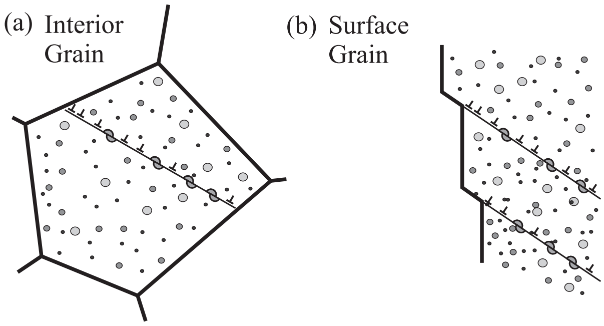

Figure 2.28: Strain localisation in PSBs in precipitation hardened alloys and formation of slip steps in surface grains, after [54]

Oxygen or any other corrosive medium will cover the free surfaces of the slip steps and might even be transported inside the material under alternating deformation. In certain materials the protective surface oxide layer can be demolished caused by the extruding slip steps, which results in incipient interaction of fatigue and corrosive damage mechanisms and substantially reduced cyclic lifetime until fatigue crack initiation [10, 24, 54].

As already mentioned the fatigue endurance characteristics are commonly determined as the total strain range of a LCF experiment versus the number of cycles to crack initiation $\Delta\varepsilon = f(N_f)$. The determination of the fatigue damage resulting from load spectra with variable strain ranges and temperatures is conducted on the basis of damage accumulation hypothesis, where the most common is the Miner law assuming the linear accumulation of cycle ratios N_i/N_{fi} and hence the amount of fatigue damage can be given as:

$$D_f = \sum_i N_i/N_{fi}\,, \tag{2.35}$$

where the achievement of the relevant failure criterion is predicted when D_f reaches unity. The index i in eqn. (2.35) represents the numerator for each identifiable cycle within the load spectrum.

Following earlier work Skelton [87] proposed a general formulation of the fatigue criterion based on the dissipated energy during cyclic loading which depend on the deformation history including the combination of stress and strain values at all points in the stabilised hysteresis loop. The dissipated energy can be formulated as:

$$W_{pl} = \int \sigma d\varepsilon_{pl}\,. \tag{2.36}$$

For a range of different materials, e.g. a martensitic 9%Cr steel, the austenitic steel AISI 316L and the Ni-base alloy Nimonic 101 it was observed, that the cumulative energy expended during cyclic loading per volume until fatigue failure is a material and temperature specific constant, independent of the applied strain range. Furthermore it was found, that the dissipated energy is also a appropriate measure to describe the cyclic hardening or softening characteristics of the material. Additional work by SKELTON ET. AL. [88] showed, that the dissipated energy criterion is a preferable approach in assessing damage summation of block loading tests with variable strain ranges.

More recent work performed by GOCMEZ ET. AL. [29] aimed at applying the dissipated energy criterion to both isothermal LCF and out-of-phase thermomechanical loading conditions and resulted in considerable prediction capabilities. Additionally KORSUNSKY ET. AL. [48] compared the dissipated energy approach to other well-established fatigue assessment methodologies and demonstrated both the reliability and accuracy of the energy-based fatigue failure criterion.

MACHA ET. AL. [53] reviewed energy-based criteria of multiaxial fatigue. Generally, depending on the ductility of the material and the associated failure and damage processes under multiaxial fatigue, the use of energy-based criterion poses no difficulty, concluding that the most promising results are obtained by the consideration of only the component connected with the critical fracture plane. It has to be mentioned here, that the concept of the equivalent strain or stress measure in order to assess multiaxial loading states is formulated on the basis of an equal energy approach and hence the usage of dissipated energy fatigue failure criterion is the stringent continuation. In fact also the damage summation hypothesis of Miner (2.35) assumes the existence of a critical dissipated energy $W_{pl,crit}$, which generally is identified with the cycle number to fatigue failure [87, 88]. The fatigue damage fraction can hence be formulated by:

$$D_f = \sum_i W_{pl,i}/W_{pl,crit,i} \,. \tag{2.37}$$

2.2.3 Creep-Fatigue Interaction

In the course of the development of modern fossil power generation plants as well as modern nuclear power plants, failure due to creep-fatigue interaction is receiving increasing interest, since the efforts for enhanced operation flexibility results in an increased number of start-up and shut-down cycles. Increasing the operation temperatures not only results in enhanced creep loading during steady-state operation but additionally imposes considerable thermal stresses in large components during temperature transients. Such situations have prompted investigations on creep-fatigue interaction mechanisms for various materials and the development of approaches for evaluating creep-fatigue damage processes in design and remaining life assessments. One of the fundamental elements of the assessment of the structural integrity of components is the fatigue or creep-fatigue analysis, e.g. the proof of a sufficient lifetime of the component until reaching a critical damage due to cyclic loading. MANSON ET. AL. [58] proposed the *Strain range partitioning* method, where the accumulation of fatigue and creep damage fractions is conducted directly from the analysis of the accordant hysteresis loop with up to four inelastic strain components ($\Delta\varepsilon_{pp}$, $\Delta\varepsilon_{pc}$, $\Delta\varepsilon_{cp}$, $\Delta\varepsilon_{cc}$). The method is based on the fundamental concepts of micro-damage mechanisms during fatigue and creep-fatigue loading conditions, as shown schematically in Fig. 2.29 and requires an extensive testing scope in order to determine the related endurance components, which is the main reason why the method has not found wide application. Hence conventional approaches were favoured, applicable to creep-fatigue life estimation with a minimum requirement of input data from pure-fatigue and pure-creep experiments. The damage fractions due to fatigue D_f and creep D_c are calculated separately and a linear damage summation is conducted, where failure is conceded when the sum of D_f and D_c reaches a specified failure criterion. The fraction of fatigue damage is commonly determined by the total strain range $\Delta\varepsilon$ or the plastic strain range $\Delta\varepsilon_{pl}$, or alternatively by the dissipated energy per cycle W_{pl}, and estimations from fatigue endurance curves based on LCF experiments as mentioned in 2.2.2.

Conventional approaches for determination of the creep damage during creep-fatigue loading on the other side encompass methods based on the prevailing stress or strain measures. The first method proposed for the prediction of creep damage under variable loading conditions is the *Time fraction* approach [82], assuming the stress to be the governing parameter for creep rupture life:

$$D_c = N \int_0^{t_h} \frac{dt}{t_u(\sigma, T)} \, . \tag{2.38}$$

Hence the determination of creep damage using the *Time fraction* approach is based on material data derived from monotonic creep rupture tests, e.g. the creep rupture strength evolution. The evaluation of creep damage based on strain measures is incorporated in the *Ductility exhaustion* approach [34, 76], where the inelastic creep strain is regarded as the principal parameter controlling creep damage:

$$D_c = N \int_0^{t_h} \frac{\dot{\varepsilon}_c}{\varepsilon_{Dc}(\dot{\varepsilon}_c, T)} dt \, , \tag{2.39}$$

where ε_{Dc} represents the creep ductility or creep strain limit of the material derived from monotonic creep rupture experiments.

Based on the above mentioned approaches for determination of creep damage, a number of design codes and creep-fatigue assessment procedures have been developed, i.e. the *Time fraction* approach is incorporated into the ASME III [5] and RCC-MR [3] procedures, whereas the R5 procedure [11] is based on the *Ductility exhaustion* approach.

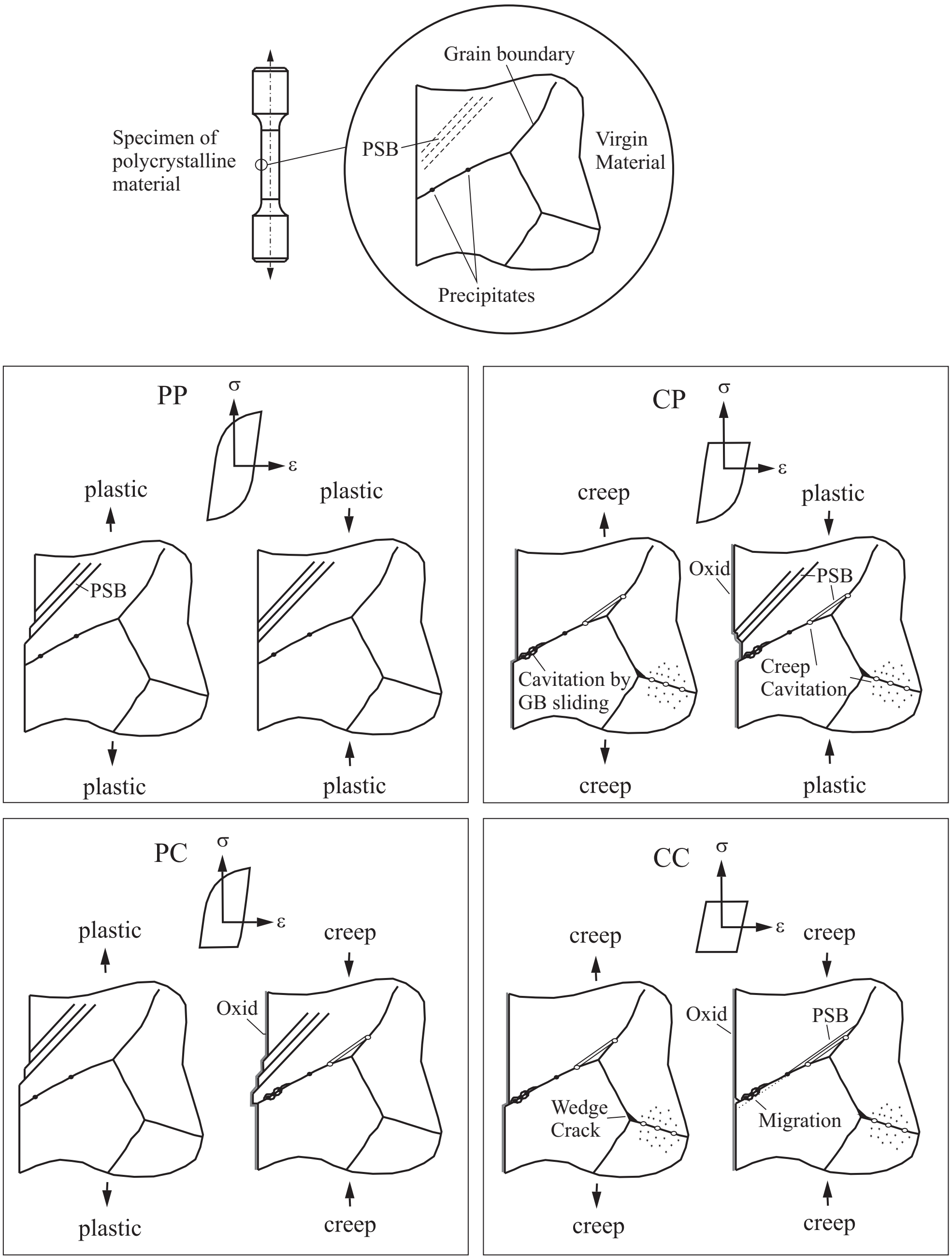
Grain boundary
Specimen of polycrystalline material
PSB
Virgin Material
Precipitates
PP
σ
ε
plastic
plastic
PSB
plastic
plastic
CP
σ
ε
creep
plastic
Oxid
PSB
Cavitation by GB sliding
Creep Cavitation
creep
plastic
PC
σ
ε
plastic
creep
Oxid
plastic
creep
CC
σ
ε
creep
creep
Oxid
PSB
Wedge Crack
Migration
creep
creep

Figure 2.29: Schematic representation of micro-damage mechanisms due to fatigue and creep-fatigue loading according to the method of strain range partitioning, after [58, 84]

More recent work by various researchers have revealed, that the prediction of creep damage in creep-fatigue tests is considerably improved by the formulation of the creep ductility depending on stress, creep strain rate and temperature and the so called *Stress modified ductility exhaustion* approach has been introduced by

Spindler [89]:

$$D_c = \int \frac{\dot{\varepsilon}_c}{\varepsilon_{Dc}(\sigma, \dot{\varepsilon}_c, T)} dt\,. \tag{2.40}$$

The approach has been validated for uniaxial and multiaxial stress states for the austenitic Type 304 stainless steel, whereas its functional form is motivated by simple mechanistic models of creep cavity nucleation and growth [89].

In analogy to the energy based approaches to assess fatigue damage, Payten et.al. [74] and Takahashi et.al. [96] proposed a *Strain energy exhaustion* approach, where the creep damage is determined by the ratio of dissipated creep strain energy during creep-fatigue loading $W_c = \sigma\, d\varepsilon_c$ and the dissipated energy expended to cause failure in monotonic creep rupture experiments $W_{c,crit}$:

$$D_c = \int \frac{\dot{W}_c}{W_{c,crit}(\dot{W}_c, T)} dt\,. \tag{2.41}$$

In [96] Takahashi et.al. evaluated and compared representative approaches for the prediction of failure life under creep-fatigue conditions, by systematically applying the above mentioned methods to available test data for a wide range of different materials, e.g. low alloy ferritic CrMoV steels, higher alloyed martensitic 9-12%Cr steels, Type 304 and Type 316 austenitic steels and various Ni-base alloys used in power generation industry. The extensive comparison revealed the tendency of the *Time fraction* approach to non-conservative predictions of creep damage in general, especially for small strain ranges. Furthermore the classical *Ductility exhaustion* approach showed a common tendency to be overly conservative in many situations. For the *Stress modified ductility exhaustion* method to assess creep-fatigue damage interaction an improved predictability was observed with an slightly non-conservative tendency, whereas the *Strain energy exhaustion* approach offered the best accuracy of life prediction among the tested procedures. Considering the relatively small strain range in operating components, the *Time fraction* and classical *Ductility exhaustion* approach were seen not to give a reliable assessment of creep damage and failure life, because of the non-conservative tendency of the former and the excessively conservative tendency of the latter. The energy-based approach (2.41) was concluded to give the most promising predictions for all the considered materials [96].

2.3 Nickel-base Materials

The driving force for the development of Ni-base alloys is constituted by the gas turbine industry, were the thermal efficiency has been improved by enhanced combustion and material temperatures. Ni-base alloys feature a favourable combination of superior strength and oxidation resistance up to very high temperatures and a good processability. Furthermore Ni-base alloys exhibit a complete fcc lattice over the entire temperature range, which features an inherent low diffusion coefficient compared to the bcc lattice structure of conventional steels and hence results in considerably improved creep deformation properties at high temperature loading. In addition, the base element Ni allows for a wide range of alloy measures resulting in substantial strengthening mechanisms due to solid solution and precipitation hardening with very high volume fractions of precipitated phases. Also sufficiently high Cr and Al contents are feasible in order to guaranty enhanced corrosion protection under very high temperature operation [10].

Ni-base alloys are differentiated by the effects of the various alloying elements on the dominant strengthening mechanism, e.g. *solid solution hardening*, *precipitation hardening* or *dispersion hardening*. Beyond that, Ni-base materials are divided by its main constituents, were the major industrially relevant Ni-base alloy classes are: Ni-Fe, Ni-Cr, Ni-Cr-Fe, Ni-Cr-Co and Ni-Cr-Mo. Table 2.1 gives an overview about some industrially relevant Ni-base alloys based on their chemical compositions.

		Chemical Composition in mass %							
Type	Alloy	Fe	Cr	Co	Mo	W	Nb	Al	Ti
Ni-Fe	Alloy 706	37.0	16.0	-	-	-	2.9	0.2	1.8
Ni-Fe	Alloy 718	18.5	19.0	-	3.0	-	5.1	0.5	1.0
Ni-Cr	Nimonic 80	-	19.5	-	-	-	-	1.4	2.3
Ni-Cr	Alloy 702	2.0	16.0	-	-	-	-	3.0	-
Ni-Cr-Co	Alloy 617	-	22.0	12.5	9.0	-	-	1.0	0.3
Ni-Cr-Co	Nimonic 263	-	20.0	20.0	5.9	-	-	0.4	2.1
Ni-Cr-Co	Udimet 500	-	18.0	19.0	4.2	-	-	3.0	3.0
Ni-Cr-Co	Udimet 720	-	18.0	14.5	3.0	1.3	-	0.4	5.0
Ni-Cr-Co	Waspaloy	-	19.5	13.5	4.3	-	-	1.3	3.0
Ni-Cr-Fe	Alloy 600	8.0	15.5	-	-	-	-	0.2	0.2
Ni-Cr-Fe	Alloy 601	14.0	23.0	-	-	-	-	1.3	0.4
Ni-Cr-Fe	Hastelloy X	18.5	22.0	1.5	9.0	0.6	-	-	-
Ni-Cr-Mo	Alloy 625	2.5	21.5	-	9.0	-	3.6	0.2	0.2
Ni-Cr-Mo	Hastelloy S	1.0	15.5	-	14.5	-	-	0.3	-
Ni-Cr-W	Haynes 230	1.5	22.0	2.5	2.0	14.0	-	0.3	-

Table 2.1: Classification of Ni-base alloys on the basis of the main compositional elements [10, 98]

2.3.1 Phases and Hardening Mechanisms

The phases occurring in Ni-base alloys are commonly differentiated into strengthening and damaging phases, whereas on the other side these phases can be distinguished by its crystal topology, e.g. closed packed phases and carbides or carbonitrides. The closed packed phases can in turn be differentiated into geometrically closed packed (GCP) and topologically closed packed (TCP) phases [98]. In the fcc γ-matrix all the alloying elements are soluted, whereby the solid solution hardening is featured by the elements Co, Cr, Fe, Mo, W, Nb and Ta, with increasing lattice misfit parameter in the given order. Additional effective solid solution hardening elements are Ti, Al, Hf and Zr, whereby these elements are only soluble in small concentrations. The most effective solid solution elements with practicable content generally are Mo and W, with larger atomic radii and hence sufficiently high lattice misfit parameters, and Cr, caused by its high solubility in the γ-matrix. Furthermore the elements B and Zr are added in various alloys in order to reduce the grain boundary diffusion coefficient, since these elements tend to concentrate at LAGB. This effectively reduces grain boundary sliding and delays intergranular creep damage formation [10].

Alloys with sufficiently high Ni content tend to form GCP phases with an ordered crystal structure of the composition A_3B, where the metallic components A and B feature atomic radii $r_A < r_B$. The most important precipitation hardening effect in Ni-base alloys is featured by the γ'-phase, which is constituted as the Ni-richest phase in the binary Ni-Al phase diagram, Ni_3Al. The lattice structure of the fcc γ'-phase exhibit a small misfit parameter δ compared to the fcc γ-matrix, resulting in coherent interfacial boundaries. The nucleation of the γ'-phase is homogeneous, leading to an equal distribution throughout the grains of the material. There exist various substitute elements, where Ni is mainly substituted by Co and Al by Ti, Ta and Nb, where the γ'-phase can be given as $Ni_3(Al,Ti,Nb)$ or $(Ni,Co)_3(Al,Ti,Nb)$. The volume fraction of the γ'-phase can exceed levels of approximately 60% for cast single crystal turbine blade alloys, but is generally reduced in wrought alloys in order to ensure an acceptable processability, e.g. low forming forces and sufficient ductility. The shape and size of the γ' precipitated particles is dependent on the heat treatment of the material, whereby the structure of these particles is generally characterised by the particle size. Very fine particles with sizes of 0.05 to 0.1μm typically precipitate spherically, whereas larger γ' particles show a cubic shape. Specific alloys may exhibit bimodal particle populations, i.e. simultaneous existence of both precipitate particle shapes [10].

At higher Al/Ti-ratios the η-phase might precipitate by transformation from the γ'-phase at long ageing times. The η-phase, consisting of $Ni_3(Ti,Nb)$, is characterised by an hexagonal close-packed (HCP) lattice structure and hence constitutes an incoherent interface towards the γ-matrix. The η-phase precipitates as coarse plates or as *Widmannstätten*-formations and generally adversely affects the ductility, toughness, notch sensitivity and fatigue endurance of the material [10].

In Ni-base alloys with sufficiently high Nb content the γ''-phase Ni_3(Nb,Al,Ti) is precipitated next to the standard γ' hardening. The γ''-phase is characterised by a lamellar formation, which can be explained by its fcc lattice structure and the semi-coherent interface with the γ-matrix. In the medium temperature range the γ''-phase leads to increased strengthening effects, but at higher temperatures the γ''-phase tends to accelerated coarsening and thermal instability. A commercial Ni-base alloy exhibiting the γ''-phase is the wrought Ni-Fe Alloy 718, which is used for turbine rotor discs, and which long term operation temperature is limited to 650°C. Another undesirable phase in Ni-base alloys is the orthorhombic δ-phase Ni_3Nb, which transforms further from the γ''-phase. The δ-phase is incoherent with respect to the γ-matrix and precipitates in coarse lamellar structures, which excessively limits the notch sensitivity and fatigue endurance of the affected material [10, 98].

In contrast to geometrically closed packed (GCP) phases, topologically closed packed (TCP) phases are characterised by an arrangement of closed packed planes and intervening layers of larger atoms. These TCP phases generally are undesirable, because of their hardness and low ductility due to a decreased amount of slip systems, resulting in low toughness and fatigue endurance properties. Also the creep properties are affected by the precipitation of TCP phases, leading to a considerable embrittlement of the material and hence to a decreased creep rupture strength and creep ductility. The TCP phases feature a complex crystalline structure with relatively large unit cells. *Laves*-phases $(Fe,Cr,Mn,Si)_2(Mo,W,Nb,Ti)$ can only precipitate in Ni-base alloys with high Fe content, especially in the presence of Si. Another TCP precipitated phase is constituted by the σ-phase, which covers a broad spectrum of compositions $(Fe,Ni,Co)_x(Cr,Mo,W)_y$ and $x \approx y$. The σ-phase is characterised by a complex body centred structure with strong tetragonal distortion and precipitates lamellarly or spearly. The hexagonal rhombohedral μ-phase is constituted by a $(Co,Fe)_7(Mo,W)_6$ structure, where the μ-phase competes with the σ-phase and primarily depends on the Cr/Mo-ratio and secondarily on the temperature and ageing time [10, 98].

Another particle strengthening effect is featured by the precipitation of carbides, which tend to nucleate heterogeneously at grain boundaries and dislocations. The pinning of dislocations is effectively achieved by a fine distribution of the carbides among the grains. Additionally the carbides feature a comparable strong thermal stability even at high temperatures and precipitate primarily during the casting process of the alloy. Ni-base alloys principally exhibit carbides of the structure MC and $M_{23}C_6$, at higher Mo or W contents also M_6C. MC carbides are primary carbides, i.e. created during solidification during the casting process. Since the metallic partners Ti, Ta, Nb of these MC carbides tend to segregate strongly interdendritically, the relatively coarse MC carbides typically form at dendrite interstices. During high temperature ageing the MC carbides transform to $M_{23}C_6$ carbides, which is the more important carbide type in Ni-base alloys and its metallic partner is mainly Cr. $M_{23}C_6$ carbides largely dissolve during the solution treatment and are precipitated during subsequent ageing treatments mainly at grain boundaries, where they increase the resistance against grain boundary sliding. Globular carbides are regarded as the most favourable, whereas continuous smooth film of carbides tend to embrittle the material. In Ni-base alloys with high Mo or W content, M_6C constitutes the main carbide type. Typically, at the presence of sufficient high Cr content, $M_{23}C_6$ carbides tend to form first, which is subsequently transformed gradually into the more thermodynamically stable carbide M_6C [10].

2.3.2 Alloy 617

Alloy 617 (NiCr22Co12Mo9) is a solid solution strengthened Ni-base alloy which was originally developed to be used as thin walled material for gas turbine combustion chambers and pipes for service duty at temperatures above 750°C. In contrast it is now being widely used for lower temperature power generation and petrochemical applications involving thicker section product forms, e.g. in the temperature range 650-750°C. Apart from high strength properties at elevated temperatures, Alloy 617 shows good long term microstructural stability, very good oxidation and corrosion resistance and excellent processability, i.e. castability, forgeability, weldability.

Its creep strength at high temperatures is attributed to solid solution strengthening due to Mo and Co, and particle strengthening by carbides $M_{23}C_6$, M_6C and carbonitrides Ti(C,N), which precipitate in the solution treated austenitic γ-matrix. Microstructural investigations [27] on crept Alloy 617 samples at 700°C revealed the vast majority of carbides to be of type $(Cr,Mo,Fe)_{23}C_6$, both along grain boundaries and grain interior, and minor amounts of (Cr,Mo,Fe)C and $(Cr,Mo,Fe)_6C$. During long term exposure the amount of carbides was found to increase, especially discontinuously precipitated $(Cr,Mo,Fe)_{23}C_6$ at the grain boundaries and within twinning structures. The discrete and discontinuous distribution of these grain boundary carbides improves the mechanical properties of the material, specifically the creep resistance, by effectively reducing grain boundary sliding mechanisms. Prolonged exposure at 800°C induced a significant dissolution and coalescence of $(Cr,Mo,Fe)_{23}C_6$ carbides, which eventually formed a intergranular film morphology. This film morphology was observed to reduce the effect of grain boundary pinning and the possibility of intergranular embrittlement [27]. Also the microstructural investigations on aged Alloy 617 samples at 870°C revealed the abundance of a relatively uniform distribution of $M_{23}C_6$ carbides [103].

Furthermore the Mo-rich δ-phase Ni_3Mo has been observed at specimen exposed to 700°C, characterised by a plate-like morphology at grain and twin boundaries, which extend from these regions into the γ-matrix. These δ-phase particles were mainly responsible for the occasionally observed grain boundary waviness and were reported to from directly from the supersaturated solid solution γ-matrix during ageing at high temperatures. Additionally relatively rare and homogeneously distributed carbonitrides Ti(C,N) were observed, with a size in the range of 4-10μm.

The addition of $\approx$1% Al results in further matrix strengthening through the formation of γ'-phase Ni_3Al, which significantly improves the mechanical properties at 650-760°C. In forged Alloy 617, creep rupture strength is enhanced by increasing the content of Ti and Al to encourage the additional precipitation of γ'-phase $Ni_3(Al,Ti)$ spheroidal or cuboidal particles, with a measured diameter of about 60nm for long-term exposure at 700°C [27, 103]. At crept samples at 800°C the amount of γ' particles was drastically reduced with their diameter exceeding 200nm as a consequence of the higher temperature exposure, that induced a partial coalescence in favour of the initially larger particles. The coalescence of γ' particles was observed to be faster in the load-bearing regions of the crept specimen, which could be interpreted by means of a stress-enhanced diffusion rate or dislocation-driven coarsening mechanism respectively. It was therefore agreed that the dissolution temperature of the γ'-phase is about 800°C, which was also observed at aged Alloy 617 samples at 870°C [103]. This microstructural instability of Alloy 617, e.g. the large differences in size and distribution of γ' precipitates at 700 and 800°C, account for the relatively improved creep resistance at the lower temperature and hence should be carefully considered in extrapolating creep strength at 700°C, since it should lead to a substantial underestimation of creep life [27].

2.4 Heat Resistant Steels and their Weldments

2.4.1 Heat Resistant Steels

Heat resistant steels are typically divided into ferritic, martensitic and austenitic steels. Whereas ferritic and martensitic steels exhibit a bcc α-lattice structure, austenitic steels feature a fcc γ-lattice, which shows a larger amount of slip planes and a smaller diffusion coefficient. Hence austenitic steels are superior towards ferritic and martensitic steels with respect to their creep resistance but also with respect to their corrosion resistance. Ferritic steels on the other side feature a smaller thermal expansion coefficient and a higher heat conductivity and are for this reason favourable for the use as materials for large section components, where the high heat conductivity is reducing thermal induced stresses due to transient temperature changes. Low alloyed ferritic heat resistant steels are, due to its relatively low corrosion resistance, not applicable above 550°C. A considerable increase of the operation temperature can be achieved by the application of higher alloyed ferritic-martensitic steels, which feature higher Cr content exceeding 12%. The application limit of modern ferritic-martensitic 9-12%Cr steels could have been increased to approximately 600°C for the use in steam turbine applications. For temperatures above 600°C only austenitic steels can be applied, since they feature an entirely austenitic lattice structure. These so called Fe-based superalloys exhibit very beneficial properties, e.g. lower stacking fault energy, lower diffusion coefficients and hence higher creep resistance, higher Cr and Ni contents for increased oxidation resistance and improved solid solution hardening compared to ferritic CrMoV steels.

Low alloy ferritic-bainitic steels

Bainitic steels show a beneficial balance of strength, toughness and creep properties at high temperatures and are typically used as heavy forgings in nuclear reactors, pressure vessel components (CrMo steels) and steam turbine rotors (NiCrMoV, NiMoV and CrMoV).

Bainite is a non-lamellar aggregate of ferrite plates or laths and carbide and/or cementite and forms from a decomposition of austenite generally between the martensite and paerlite transformation temperature according to the alloy specific time-temperature transformation diagram. During the bainite reaction fine ferrite plates grow in clusters from the prior austenite grain boundaries. These clusters form sheaves or packets, where the plates are parallel and feature the same crystallographic orientation. These bainitic sheaves tend to lengthen at a much slower rate than during the formation of martensite and feature an irrational habit-plane. After the growth of the bainitic sheaves, cementite and carbides precipitate from the untransformed austenite layers between the ferrite sub-units. Thereby one distinguishes two main configurations of bainite, e.g. upper bainite and lower bainite. Whereas upper bainite is formed at higher transformation temperatures and its sheaves consist of sub-units that are separated by cementite particles, lower bainite forms at lower transformation temperatures featuring a fine dispersion of precipitated cementite and/or carbides within the ferritic sub-units [61]. Lower bainite often exhibit a higher strength and toughness than upper bainite, which is mainly caused by the distribution of fine cementite particles. After the forging process in the austenitisation temperature regime and subsequent quenching, forged components are usually subjected to a quality heat-treatment, which consist of a hardening and a tempering phase. During hardening the component is entirely austenitised and subsequently cooled at a specified cooling rate. The speed of cooling determines the final transformation product of the steel, i.e. martensite (fast cooling), bainite (intermediate cooling) and paerlite (slow cooling). Fig. 2.30 shows the continuous cooling transformation diagram of a 1%CrMoV rotor steel with the accordant hardness measures indicating the strength level. Hence for voluminous components, such as large turbine rotor forgings, different transformation products result in locations with different cooling rates, e.g. rotor rim and core. During the tempering process of bainitic steels both the microstructure and the mechanical properties are changing. Depending on the exposure time, excess solid solution C segregates at defects or forms clusters by precipitation of cementite (low-carbon alloys) or transition Fe-carbides (high-carbon alloys). Secondarily at longer exposure times precipitation of excess C leads to transformation of carbides into more stable cementite and decomposition of retained austenite [61].

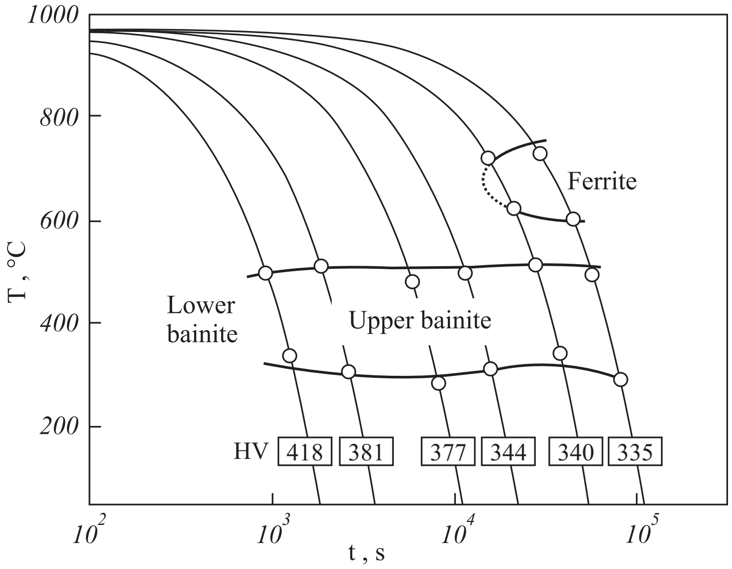

Figure 2.30: Continuous cooling transformation diagram for 1%CrMoV steel at an austenitisation temperature of 970°C, after [97]

The high-temperature strength of bainitic steels is mainly attributed to solid solution strengthening of the matrix and the hardening effects of carbides, e.g.

carbide type, stability and dispersion in the matrix. Thereby interstitial hardening by C and N create a tetragonal distortion of the crystal lattice, which is generally more effective than substitutional hardening by e.g. P, Si, Mn and Mo. The ductility of bainitic steels is increased by the addition of Mn and Cr, while Mo and P have a detrimental effect. Concerning the creep strength the addition of Mo for solid solution hardening and carbide precipitation is most beneficial. The most influential effect on the mechanical properties during high-temperature operation of bainitic steels is constituted by the type and dispersion of carbides. The crystal structure of these carbides typically depends on the alloying elements, e.g. cubic carbides $M_{23}C_6$, M_4C_3 (formed by Ti, Zr, V, Nb), close-packed hexagonal carbides M_2C, M_7C_3 (formed by Ta, Mo, W) and orthorhombic carbides M_3C (formed by Mo, Cr, Mn). The dispersion of carbides is a further important factor that determines the ductility and strength and may also impede recovery by reducing dislocation mobility. For high-temperature operation the carbides should essentially remain stable so that particles with enhanced resistance to growth are preferred. The stability of carbides decreases in the order M_4C_3, M_2C, $M_{23}C_6$, M_7C_3 and M_3C [61].

SENIOR [85] reviewed the precipitation condition in a 1%CrMoV rotor steel. Thermodynamically unstable Fe_3C mainly precipitates on grain boundaries during bainite formation and is further enriched by Mo, Cr and Mn or transforming to stable M_7C_3 or $M_{23}C_6$ during tempering. Simultaneously acicular M_2C and fine dispersed M_4C_3 particles precipitate in the matrix, preferentially at matrix dislocations, contributing to increased creep resistance. An optimum dispersion of V_4C_3 carbides is critically influenced by the content of C, Cr, Mo and V and the transformation product after hardening heat-treatment, which is why the chemical composition and the quality heat-treatment are to be specified in an accurate manner. Additionally the amount of Mn and Ni has to be limited in order to ensure the thermodynamic stability of V_4C_3 and therefore of the matrix strength. The most promising dispersion of V_4C_3 carbides is attained during upper bainite transformation with respect to steam turbine rotor forgings. This requires adequate control of cooling rates during the hardening of large rotor forgings to provide appropriate uniformity through the component. While various preliminary heat-treatments are applied in order to adjust the austenite grain size, the quality heat-treatment for rotor steels contains a final austenitisation treatment at 970-975°C / 12h / oil-quenching and a tempering heat-treatment at 700°C / 18h / furnace cooling [61, 67].

Higher alloyed ferritic-martensitic steels

In contrast to low alloyed bainitic steels, whose high-temperature application is limited to 550°C, higher alloyed martensitic CrMoV steels can be operated at temperature levels exceeding 600°C. In international research projects, like the European COST program [45, 90], ferritic-martensitic 9-12%CrMoV steels have been developed and optimised for the application in steam turbines. The advanced steels of this type feature higher creep strength for temperatures of above 600°C and allow for the engineering of steam power plants with steam inlet temperatures in excess of 600°C and corresponding inlet pressures of 300 bar.

On the basis of the high Cr content the 9-12%CrMoV steels feature a martensitic structure also for low cooling rates. During heat-treatment the austenitic γ-lattice is transformed into the tetragonal distorted martensitic structure with a fine sub-grain structure and free dislocations in the interior of the sub-grains or cells. The lower bound of Cr content for this group of 9-12%CrMoV steels is regarded as minimum Cr content for sufficient carbide formation, whereas a Cr content of 12% constitutes the limit of complete austenitisation and subsequent martensitic transformation in the binary Fe-Cr phase diagram. The austenitisation temperature of about 1050°C is therefore to be kept exactly, depending on the chemical composition of the alloy. Fig. 2.31 shows the continuous cooling transformation diagram of a 12%CrMoVNbN rotor steel with the accordant hardness measures indicating the strength level. The tempering of the 9-12%CrMoV steels is accomplished slightly above 700°C, where carbides precipitate at former austenite grain boundaries, and depending on the N content also carbonitrides [10]. After heat-treatment the 9-

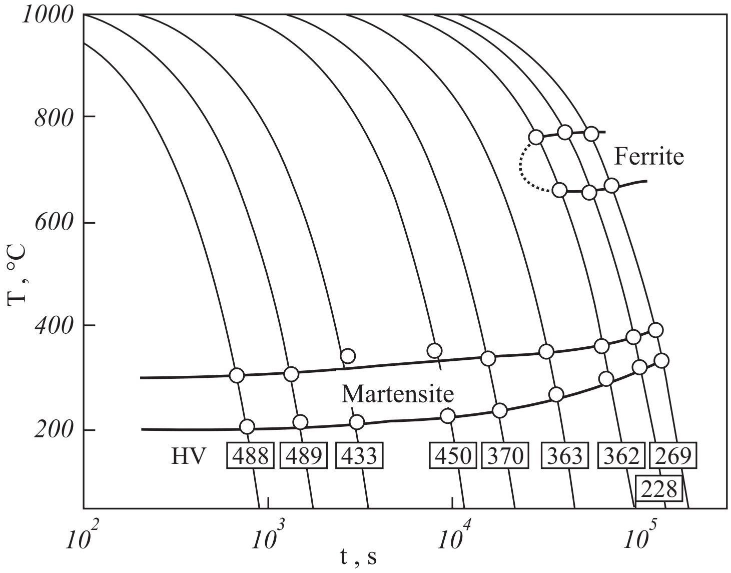

Figure 2.31: Continuous cooling transformation diagram for 12%CrMoVNbN steel at an austenitisation temperature of 1050°C, after [97]

12%CrMoV steels feature a tempered martensitic structure with sub-grains, that are fixed by the precipitated carbides. The stabilisation of the substructure of the tempered martensite is of particular importance during alloy development, since it influences the long term creep properties [10, 84].

The higher content of Cr, Mo, V and possibly Nb and W in the higher alloyed 9-12%CrMoV steels lead to an increased carbide hardening with basically the same type of carbides as the low alloyed bainitic steels with additional precipitation of Cr_7C_3 carbides. The 9-12%CrMoV steels additionally contain amounts of Nb and depending on steel type also W, B and N. Thereby the ferrite formers, especially Mo and W might form δ-ferrite, which influences the creep properties negatively and hence represents a undesirable phase. The balance of the alloying elements with respect to the formation of δ-ferrite is therefore one of the main difficulties in 9-12%CrMoV steels, since low contents of austenite formers benefit the weldability and toughness and high amounts of ferrite formers benefit creep properties [84]. The addition of W furthermore favours the formation of *Laves*-phase $Fe_2(W,Mo)$, whose influence on the creep strength is controversially discussed, since it binds W and Mo out of the solid solution matrix, leading to softening at long operation times. Also the Z-phase Cr(V,Nb)N plays an important role in 9-12%CrMoV steels, which occurs during long-term high-temperature operation. Since the Z-phase tends to coarsen excessively compared to MX-particles like V(C,N) and Nb(C,N), it leads to a dissolution of fine dispersed carbides and nitrides and hence to a decreasing of creep strength and hardness [84].

The higher application temperatures of higher alloyed martensitic 9-12%Cr-MoV steels result from an increased strength as well as an enhanced oxidation resistance compared to the low alloyed bainitic steels. Although a pure Cr_2O_3 oxide layer is not developed, layers of Fe_2O_3, Fe_3O_4 and the spinel $FeCr_2O_4$ feature much lower growth constants compared to the Fe oxides of low alloyed steels with comparatively low Cr content [10].

Representatives of these higher alloyed 9-12%CrMoV steels are X22CrMoV12-1 as well as X10CrMoVNb9-1 (T91, P91). Further developments aiming at increasing the operation temperature above 600°C, and hence avoiding the use of thermo-mechanical sensitive austenitic steels, is accomplished by W-alloyed variants X12CrMoWVNbN10-1-1 and P92/NF616 [10]. The 10%CrMoV steels of type X12CrMoWVNbN10-1-1 have been developed aiming at a compromise between long-term creep properties and acceptable producibility and processability. They contain austenite forming Ni and N as well as ferrite formers Cr, Mo, V and Nb. The δ-ferrite content in X12CrMoWVNbN10-1-1 steel is restricted by limiting the amounts of Ni and Mn. The austenitisation temperature is specified at between 1050-1130°C / 12h / forced air cooling and the subsequent tempering treatment is conducted at 730°C / 12h / air cooling [33, 84]. For large turbine components, which require high creep rupture strength properties, the tempering treatment is typically conducted in two steps at 570°C and 650-720°C featuring relatively long hold times.

Fig. 2.32 shows a comparison of the 10^5h creep rupture strength of low alloy bainitic 1%CrMoV and higher alloyed martensitic 9-12%CrMoV steam turbine rotor steels as a function of temperature. The chemical compositions of the materials tested are given as well. As observed, the X12CrMoWVNbN10-1-1 steel features a temperature gain of approximately 40°C with respect to 100 MPa creep rupture strength. The X18CrMoVNbB9-1 steel, which features additional alloying with 0,01% B, is an onward development of the Japanese TAF steel and shows about 20% higher creep rupture strength compared to X12CrMoWVNbN10-1-1 [62].

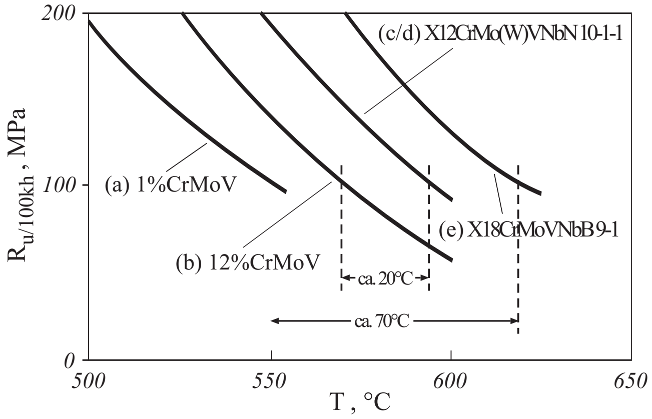

Figure 2.32: 100000h creep rupture strength of steam turbine rotor steels, after [62]. Chemical composition in weight %
C, Cr, Mo, W, V, Nb, N, B:
(a) 0.28, 1.0, 0.9,-,0.3,-,-,-
(b) 0.21, 12.0, 1.0,-,0.3,-,-,-
(c) 0.12, 10.0, 1.5,-,0.20, 0.05, 0.05,-
(d) 0.12, 10.0, 1.0, 1.0,-
0.20, 0.05, 0.05,-
(e) 0.18, 9.0, 1.5,-
,0.25, 0.05, 0.02, 0.01

2.4.2 High Temperature Weldments

Welding with all its varieties constitutes an important joining and repairing technology for power plant components. The application of fabrication welds, connecting components with small or large cross sections and joints of similar or dissimilar materials, e.g. tube to tube, pipe to pipe or pipe to casting, as well as repair welds of casting defects imposes considerable awareness to the structural integrity of such components in the thermal power generation industry. During the welding process the microstructure of the joined materials is strongly influenced and thereby their mechanical properties are altered. Long-term experience of creep exposed welded structures has revealed that the heat affected zone (HAZ), a narrow zone of base material (BM) adjacent to the weld fusion line altered by the weld thermal cycle, is often regarded as the weakest link with respect to the creep strength.

Low alloy ferritic/bainitic steels for boiler components like waterwalls or for subcritical steam piping and headers as well as higher alloyed 9-12%Cr steels for ultra super critical power plants are of great interest. Awareness of the importance of knowledge of the creep behaviour in welded structures has increased during the last few decades, backed by several partly catastrophic failures of welded steam piping systems in the 1990s. These failures acted as a driving force for increased research activities of manufacturers, operators as well as academics on failure mechanism characterisation, non-destructive testing methods, remaining life prediction methods, repair technology as well as the development of improved steel grades and welding procedures [13].

During fusion welding the BM microstructures and properties are changed locally and inhomogeneously within the HAZ by the applied weld thermal cycle. These altered BM properties might differ substantially from the optimized ones adjusted by the BM manufacturer through accurate melting techniques, exact production process control and proper heat treatment. In Fig. 2.33 the basic influences of the fusion welding process on metallurgy in the HAZ is schematically presented and compared to the calculated equilibrium phase diagram of X10CrMoVNb9-1 (P91) steel [13]. The resulting microstructure is governed by the prevailing welding process parameters such as the heating rate of the weld thermal cycle, the experienced peak temperature, the dwell time, the cooling rate, the effect of multilayer welding and finally by the adjusted post weld heat treatment (PWHT) parameters. The HAZ can be divided into a number of sub-zones, featuring a continuous gradient from the fusion line between the deposited weld metal (WM) to the unaffected BM since often no distinct border between the different regions is recognisable. The *grain growth zone* adjacent to the fusion line experiences peak temperatures far exceeding the A_{c3} transformation temperature. At these high temperatures precipitates dissolve entirely resulting in excessive grain growth and hence coarse grains of austenite. Thereby the considerably high heating rates during the welding process tendentially lead to a shift of the phase transformation and recrystallisation temperatures to higher levels as well as the solution temperatures of carbides and nitrides. During cooling low alloy CrMoV steels form a bainitic/martensitic microstructure and 9-12%CrMoV steels form a martensitic microstructure. The coarse-grained zone (CGHAZ) features the highest hardness of the HAZ and generally low toughness properties are expected. Additionally the CGHAZ may be vulnerable to reheat cracking during creep loaded service [13]. Lower peak temperatures of about 1100°C just above A_{c3} result in an incomplete

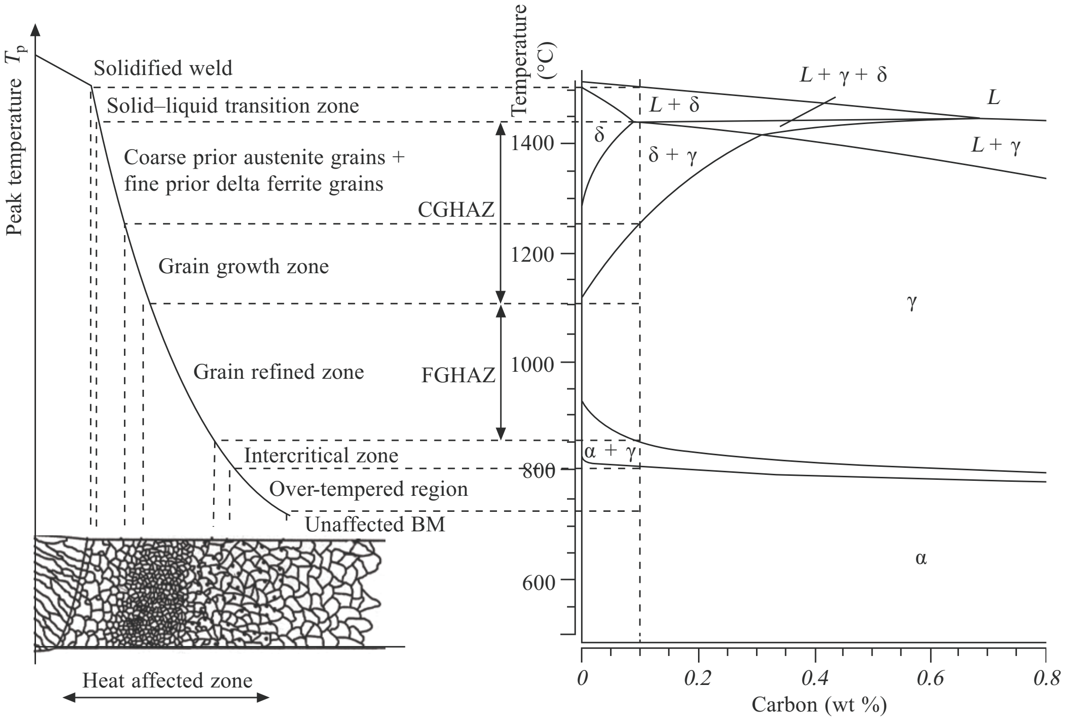
Peak temperature T_p
Solidified weld
Solid–liquid transition zone
Coarse prior austenite grains + fine prior delta ferrite grains
CGHAZ
Grain growth zone
Grain refined zone
FGHAZ
Intercritical zone
Over-tempered region
Unaffected BM
Heat affected zone
Temperature (°C)
1400
1200
1000
800
600
L + γ + δ
L
L + δ
δ
δ + γ
L + γ
γ
α + γ
α
0
0.2
0.4
0.6
0.8
Carbon (wt %)

Figure 2.33: Schematic of the sub-zones of the HAZ corresponding to the calculated equilibrium phase diagram of X10CrMoVNb9-1 (P91) steel, after [13]

α-γ-transformation during heating, producing an austenitic fine-grained zone (FGHAZ). In addition the peak temperature may not be high enough for complete precipitate dissolving, limiting the grain growth by pinning the austenite grain boundaries. During cooling either a fine-grained bainitic/martensitic microstructure for low alloy CrMoV steels or a martensitic microstructure for 9-12%CrMoV steels is formed. During long-term creep loading the FGHAZ is regarded as the weakest link in weldments of creep-resistant ferritic steels, caused by the so-called Type IV cracking mechanism. Peak temperatures between A_{c1} and A_{c3} lead to a partial transformation of α into γ phase during heating, indicating the intercritical heat affected zone (ICHAZ). While new austenite grains nucleate at favoured positions, e.g. prior austenite grain boundaries or martensitic lath boundaries, the untransformed bainitic or tempered martensitic microstructure is simply tempered a second time by the weld thermal cycle. Partial dissolution of precipitates may occur in the ICHAZ as well as coarsening of undissolved precipitates especially during subsequent PWHT. After cooling a twofold microstructure of newly formed bainite for low alloy CrMoV steels, or virgin martensite for 9-12%CrMoV steels respectively, and the tempered original microstructure before welding coexist. The ICHAZ features a small grain size and exhibits the lowest hardness values across the weldment. It shows a similar susceptibility to Type IV cracking as the FGHAZ [13]. With peak temperatures below A_{c1} the microstructure does not undergo any phase transformations, but the temperature level in this locally *over-tempered region* is still above that of the annealed base material. Due to the higher diffusion coefficient at this temperature the coarsening of precipitates may be enhanced in this zone. The zone of unchanged material, usually constituted by peak temperatures up to 700°C, features no changes in morphology of the constituents. Nevertheless, in this region over-tempering effects may occur, which may weaken the creep strength of low alloyed quenched and tempered steels, e.g. 1%CrMoV steels [13].

During the recent decades intense effort has been spent on the development of weld filler materials for modern creep-resistant steel grades. Of particular importance has been the simultaneous development of matching filler materials, primarily with respect to the creep rupture properties, compared to the base materials. Thereby special deoxidation practices, additions of micro alloying elements, improvement of weldability and handling often remain the detailed knowledge of the individual manufacturers. Especially the formation of δ-ferrite during solidification and cooling constitutes an important issue, since this phase detrimentally influences the toughness and creep rupture properties of the particular weldment. The chemical composition of the weld filler material has to be balanced in order to limit the retention of δ-ferrite during the welding process.

Ferritic steel weldments exposed to creep loading exhibit tendentially a very similar behaviour irrespective of their chemical composition as well as various other parameters such as particular welding procedure and weld geometry. Creep tests on cross-weld samples have revealed that at higher stress levels and lower temperatures the failure location is rather randomly distributed between BM, WM and HAZ, indicating no significant difference of creep rupture strength. The difference becomes more prominent when the stress level is lowered and the temperature is increased. The time of deviation of the cross-weld creep strength from the BM creep rupture characteristics varies with the creep testing conditions, e.g. stress level, temperature, material grade, welding process parameters and PWHT. At lower stress levels and higher testing temperatures the HAZ of creep-resistant steels appears to be the weakest link, exhibiting creep strength reduction factors of weldments exceeding 50%. Fig. 2.34 compares the creep rupture strength of cross-welds with the mean BM characteristics of 9%Cr steel E911. Considering the implications for industries using welded creep-resistant steels, a weld strength factor (WSF) or a weld strength reduction factor (WSRF) have been recommended by the European Creep Collaborative Committee [21] in order to be applied dur-

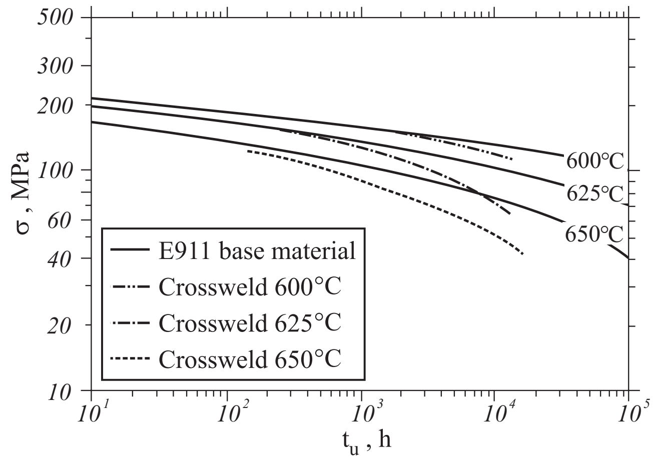

Figure 2.34: Comparison of cross-weld with mean BM creep rupture strength of E911 steel at different temperatures, after [13, 52]

ing the design stage of new components and the residual life evaluation of existing structures:

$$WSF = \frac{R_{u(w)/t/T}}{R_{u/t/T}} \quad \text{and} \quad WSRF = \frac{R_{u/t/T} - R_{u(w)/t/T}}{R_{u/t/T}}. \tag{2.42}$$

In contrast to earlier assumptions of constant WSRFs independent of time and temperature, investigations by many researchers have proved the dependency on material grade, stress level, temperature and time to rupture with significant variation [94]. Especially the extrapolation from short-term creep rupture tests holds the risk of severe overestimation of long-term creep properties. Therefore long-term creep rupture testing of cross-welds, base metals and weld metals for a reliable material selection is inevitable [13].

The damage mechanisms and related types of cracking observed in weldments of heat-resistant steels can be classified by their location and orientation. Fig. 2.35 categorises schematically the cracking modes in weldments. Cracks in the deposited weld metal correspond to Type I and II and are mainly associated with the weldment process itself or stress relief during PWHT. While Type I cracks mainly arrest in the WM, Type II cracks may propagate into the HAZ or even in the BM mostly in transversal direction. Both crack types appear as hot cracks during solidification of the weld metal and are of great concern in austenitic and Ni-base weld metals. In ferritic steels solidification cracking could have been restrained by development of improved weld metals and cleanliness of the weld deposit. Additionally the weld metal deposit during multilayer welding may exhibit a non-uniform microstructure due to repeated sub-critical tempering of the solidified weld beads from subsequent weld thermal cycles. These zones in the WM, similar to the HAZ in the BM, may therefore show susceptibility to various forms of creep damage [13].

Type III reheat or stress relief cracking is defined as the intergranular cracking in the HAZ during PWHT or high temperature operation up to 20000 h. While

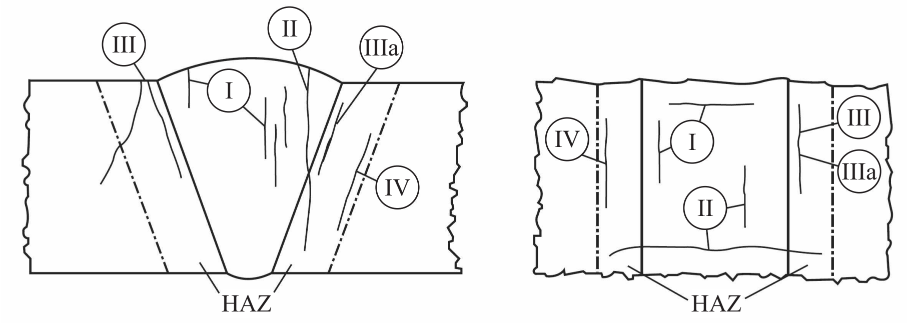

Figure 2.35: Schematic of cracking modes in weldments of heat-resistant steels, after [13]

9-12%Cr steels show almost no susceptibility to reheat cracking, lower alloyed ferritic CrMoV steel weldments as well as some Ni-base alloys were found to exhibit occasional Type III cracking. Generally reheat cracking is related to relaxation strains due to residual stresses exceeding the local ductility of the material. In the CGHAZ the majority of the precipitates dissolve during the applied weld thermal cycle. During high temperature exposure reprecipitation of carbides and carbonitrides occurs in the grain interior as well as at the grain boundaries. Whereas the grain interior is significantly strengthened by fine dispersed coherent carbonitrides, the prior austenite grain boundaries (PAGB) are favourable to the precipitation of incoherent carbides. Due to diffusion processes the PAGB carbides coarsen, leading to a depletion of solid solution strengthening elements in the vicinity of the PAGB. This weakened PAGB areas concentrate the deformation during the reduction of welding residual stresses, leading to macroscopic intergranular cracking [13].

The most important failure mechanism of ferritic steel weldments exposed to long-term creep loading is constituted by Type IV cracking, i.e. the formation of cracks in the FGHAZ and the ICHAZ. Type IV cracking has been reported for various low alloy ferritic/bainitic CrMo(V) steels as well as higher alloyed 9-12% CrMoV steel grades [13, 30, 68, 93]. The failure mechanism of Type IV cracking is generally associated with creep cavitation, where creep voids initiate at the subsurface and grow by diffusion in a rather narrow band in the FGHAZ or ICHAZ region. Preferred nucleation sites of creep voids are particle/matrix interfaces associated with inclusions or second phase particles. In the FG/ICHAZ region of weldments, carbides and carbonitrides are only partially dissolved by the applied weld thermal cycle. In order to decrease interfacial energy, precipitation on retained large particles, such as $M_{23}C_6$, is favoured instead of fine reprecipitation on grain boundaries and therefore retained particles coarse more rapidly than those in the BM. LETOFSKY [52] investigated the evolution of microstructural changes in the ICHAZ of cast G-X12CrMoWVNbN10-1-1 steel at different stages of creep testing, with much faster coarsening of precipitates and formation of *Laves*- and Z-phase in the ICHAZ compared to other regions of the weldment. Furthermore the fine subgrain microstructure of IC/FGHAZ tend to coarsen considerably during high-temperature creep exposure compared to other regions of the weldment, leading to much lower dislocation densities and hence to enhanced weakening of this specific region with respect to the creep rupture strength. A fundamental factor in clarification of creep induced Type IV cracking is the role of constraint in the thin creep weak IC/FGHAZ region from the adjacent stronger CGHAZ and BM. As a result, a triaxial stress state predominates, leading to higher vacancy diffusion, formation and creep void growth in the centre of cross-weld specimens compared to surface areas and finally to an enhancement of damage accumulation [13, 52, 93].

Dissimilar Metal Welded Joints

In contrast to similar metal welded (SMW) joints, dissimilar metal welded (DMW) joints comprise base materials and weld filler metals with different characteristics. In modern thermal power and process plant development DMWs between low alloy ferritic and high alloy ferritic as well as austenitic steels are used depending on the specific desired material behaviour, such as creep properties, corrosion resistance, cost effectiveness and other design parameters. Accordingly the application of DMW joints inherits a major challenge in design and fabrication, since such weldments are characterised by sometimes very sharp transitions in microstructure, physical properties, chemical compositions and, as a result, mechanical properties [13].

Besides the typical Type IV cracking during long-term creep exposure in the FG/ICHAZ region of the BM, various other failure mechanisms have to be considered during the design of DMW joints. The mismatch of physical properties of the BMs, most importantly the thermal expansion and heat conductivity coefficients, have to be compensated by an appropriate weld metal filler in order to reduce the danger of thermal fatigue cracking in service and during temperature transients [55]. This especially applies to DMWs between ferritic steels and austenitic steels or Ni-base alloys. Another major failure mechanism is related to the diffusion of chemical elements, especially C and Cr, in the transition zone due to a gradient in chemical composition and potential. Investigations on a DMW between a low alloy 1%CrMoV (G-S 17CrMoV5-11) and a higher alloyed 12%CrMoV steel (X20CrMoV12-1) [102] have shown the formation of a carbide seam in the vicinity of the fusion line in the higher alloyed weld metal due to carburisation. In contrast the decarburisation in the lower alloyed 1%CrMoV steel HAZ lead to a carbon depleted zone with a decreased creep strength, resulting in localised premature damage. This carbon migration was not apparent initially after welding and PWHT but occurred during long-term high-temperature exposure.

In order to overcome the problems of carbon migration in DMWs between ferritic and austenitic steels, Ni-base weld filler metals have been used instead of austenitic fillers because of the lower diffusivity of C in Ni-base alloys and reduced C activity gradient. Nevertheless studies on DMW between low alloy 2.25%CrMo steel (P22/T22) and Alloy 800 using Inconel 182 weld metal [9] revealed the presence of interfacial carbide precipitation and the formation of decarburised ferritic band adjacent to the fusion line even after short ageing times of about 100 h. Investigations on the microstructure of a very similar DMW joint between 2.25%CrMo steel (P22/T22) and Type 316 austenitic steel using Inconel 182 weld metal [72] have shown that samples extracted from the pipe weldment and subsequently aged up to 6000 h at 625°C exhibited precipitation at the weld interface. SEM investigations revealed a line of spherical $M_{23}C_6$ and M_6C carbide particles at a distance of about 1 μm from the fusion line and a lath like structure, about 5-8 μm in width parallel to the interface in the HAZ of the steel. The above indications were described as Type I and II carbides respectively. Results from Type I carbide measurements indicated particle growth with increasing ageing time and formation of a lenticular morphology, whereas Type II carbides tended to dissolve completely during ageing treatment. Uniaxial cross-weld creep testing on the same DMW joint [73] revealed cavity development associated with carbides at the weld metal interface with preferential nucleation at the surface of laboratory specimens. The fracture appeared in a rather low ductile manner for lower stress creep rupture experiments, with extensive cracking developing initially at the weld fusion boundary by linkage of adjacent cavities. The final rapid propagation of the defect was observed to be in the low alloy steel HAZ.

Investigations on a DMW joint between modified X10CrMoVNb9-1 steel (P91) and Alloy 800 with Inconel 182 weld filler [86] respectively revealed the presence of a precipitate layer with the width of 2 μm only after an extended ageing period of 5000 h. A carbon depleted zone on the other hand was not observed in the steel HAZ. Several factors have been determined to be responsible for the reduced tendency of C migration, such as the lower C content of grade 91 steel matching the one of Inconel 182 weld filler, higher Cr content in P91 reducing the C activity gradient between ferritic steel and weld filler as well as the presence of strong carbide formers Nb and V, binding C in $M_{23}C_6$ carbides and MX carbonitrides [86].

Studies on a DMW joining a higher alloyed martensitic X10CrMoVNb9-1 steel (P91) and an austenitic X3CrNiMoN 17-13 steel using a Ni-based weld filler NiCr20Nb on tube experiments, featuring combined loading of inner pressure and superimposed axial loading, have revealed no damage related to microstructural changes in the vicinity of the weld metal interface [26]. These results further indicated that thermal cyclic loading does not encourage diffusion processes leading to migration of alloying elements in the investigated DMW since only minor carbide precipitation at the fusion line was observed for low stress experiments. The results from the welded tube experiments on the other side have to be assessed concerning the specific geometrical constraints imposed by the DMW, consisting of an austenitic-martensitic-austenitic steel arrangement, leading to extensive bulging of the middle martensitic steel region. All the experiments failed by longitudinal creep induced cracks in the parent P91 steel far away from the HAZ and not due to Type IV cracking in the P91 steel HAZ nor by fusion line cracking due to Type I carbide creep cavitation.

Chapter 3

Materials and Testing Procedure

This chapter provides an overview about the details of the materials, e.g. the chemical composition, product form, adopted heat treatment, which have been provided for material testing and evaluation to the present research project. Furthermore information is given on the testing procedures and the scope of the testing program, which has been conducted in order to achieve the project objectives.

3.1 Materials

3.1.1 Alloy 617

Alloy 617 has been selected as the most promising candidate rotor material for 700°C steam turbines. An important reason is the excellent weldability of the alloy, because a welded construction is being favoured due to limitations in the capabilities of forgemasters to produce monobloc rotors. The main reason is the difficulty to uniformly forge the required very large material pieces. The properties of two full size IP-rotor production forgings of Alloy 617 have been evaluated within the THERMIE AD700 collaborative project [99, 100]. The dimensions of the two Alloy 617 forgings, both prepared by Saarschmiede, were respectively 700 mm diameter x 800 mm long (Heat designation L617F2, Heat No. 933255) and 1000 mm diameter x 1500 mm long (Heat designation L617F3, Heat No. 930680). The production process for both forgings comprised vacuum induction melting and electro-slag remelting. Material from the outer section of a ring of the L617F3 forging was made available to the present research collaboration. Subsequently the material was additionally aged. This ageing treatment was responsible for an initial carbide precipitation phase and hence to material hardening relative to the solution annealed condition (see 2.3.2). Following this ageing treatment, the heat was referred to as MMS-036. The nominal chemical composition of Alloy 617 is given in Table 2.1 in section 2.3.

In addition to the Alloy 617 property evaluations performed on material from the two Saarschmiede production forgings, there were existing data available from the MARKO DT5 project [98] on a heat of Alloy 617 referred to as DT5/d2A, which have also been reviewed within the present research project. This material has been produced by electro-slag remelting and has been delivered as forged block with dimensions 100 x 200 x 360 mm. Additionally a second heat of Alloy 617 has been investigated in the present research project, originating from a full ring production weldment comprising a similar metal Alloy 617 - Alloy 617 weld and a dissimilar metal Alloy 617 - 1% CrMoV weld (see 3.1.2). This DMW has been designated as MMS-069, with the Alloy 617 part being designated as MMS-069a.

Available data on L617F2 and L617F3 heats comprised results on solution annealed material as well as for different aged conditions, whereas the product form and the heat treatment of DT5/d2A heat of Alloy 617 were non-standard with respect to material specification. Next to heat specific differences in strength values the effect of ageing is noticeable, with increasing yield and tensile strength properties for the aged material. Also decreasing fracture ductility as well as impact toughness properties can be identified due to ageing treatment of Alloy 617.

3.1.2 Dissimilar Metal Welded Joints

Two dissimilar metal welded joints have been investigated within the present research project, i.e. weldments between Alloy 617 and a) a 1% CrMoV low alloy bainitic rotor steel and b) a higher alloyed 10% Cr martensitic rotor steel.

The Alloy 617 - 1% CrMoV DMW originated from a full size production ring weld, comprising a similar metal Alloy 617 - Alloy 617 weld and a dissimilar metal Alloy 617 - 1% CrMoV weld. This DMW has been designated as MMS-069, with the Alloy 617 part being designated as MMS-069a. The two forged Alloy 617 discs (Heat designation MMS-069a, Heat No. 933796) with the dimensions of 1100 mm diameter x 250 mm length have been prepared by Saarschmiede. The production process for both forged discs comprised vacuum induction melting and electro-slag remelting and the discs were subsequently aged. The Alloy 617 - 1% CrMoV DMW contained an Alloy 617 disc forging welded to a 1% CrMoV forged steel ring, which was prepared by Buderus Edelstahl (Heat No. 80708) and has been designated as MMS-069b in the present project. The dimensions of the forged ring were 1000/600 mm diameter x 250 mm length and the production process comprised VIM and ESR. The welding process of the ring weldment comprised narrow-gap TIG welding using Alloy 617 weld filler. After the welding process the ring weldment was post weld heat treated for 10 h at 670°C. Sections cut from this full size production ring weldment have been available to the present research project.

The Alloy 617 - 10% Cr DMW joints were procured as laboratory produced weld blocks, whereas the material originated from a THERMIE AD-700 full production weld ring [99, 100] comprising two joints; an Alloy 625 forged disc welded to a 10% Cr forged steel ring and the 10% Cr ring welded to an Alloy 617 ring forging with 980 / 780 mm diameter. Two Alloy 617 - 10% Cr weld ring sections were delivered for testing purposes to the present research activity. The Alloy 617 material originated from the L617F3 heat, whereas the 10% Cr forged steel ring has been supplied by Böhler. There was no information available to the present research project on the exact chemical composition, heat treatment details and room temperature mechanical properties of the 10% Cr material. The Alloy 617 - 10% Cr weld had been cut and the Alloy 617 material had been aged. Following this treatment the material was referred to as MMS-036 accordingly. After this treatment two Alloy 617 - 10% Cr weld blocks with dimensions of 190 x 80 mm, referred to as MMS-052, were manufactured by narrow-gap TIG welding using weld geometries and process parameters corresponding to full size production weldments. After post weld stress relief treatment the weld blocks were inspected by ultrasonic testing and shown to be free of defects.

3.2 Testing Procedure

In order to achieve the objectives of the present research project an extensive testing campaign has been conducted. Thereby it was attempted to limit the amount of material testing with respect to testing time and the number of individual tests in order to accommodate the limited testing capabilities. For existing material data, which has been available to the present research collaboration, spot tests have been conducted to ensure the compatibility of the generated results with previous data and also to investigate heat specific differences as well as the material characteristics for different heat treatment conditions. For missing material data, particularly in the low to medium temperature range, experiments have been conducted in order to determine the material characteristics. The focus has primarily been on the determination of creep, fatigue and creep-fatigue properties both with respect to deformation and endurance.

3.2.1 LCF/TMF Testing

The present research project comprised a number of low cycle fatigue (LCF), cyclic/hold creep-fatigue (CF) as well as thermo-mechanical fatigue (TMF) experiments in order to determine the necessary material properties for the creep-fatigue assessment of Alloy 617 parent material and the Alloy 617 - 1% CrMoV and Alloy 617 - 10% Cr DMW joints respectively. These experiments have been conducted on a 100 kN MTS uniaxial servohydraulic material testing machine with inductive heating, see Fig. 3.1. The tests were executed under strain control using a class 0.5 extensometer, attached to the specimen surface with an effective gauge length of 15 mm according to the relevant standards [6, 40]. The load cell and the alignment of the testing machine have been regularly checked and calibrated to ensure reliable and repeatable results.

Of particular importance during high temperature material testing is the accurate control and observance of the testing temperature since it represents a substantial influence on the deformation and damage behaviour of the material and hence on the obtained results. The temperature measurement was determined by type K thermocouples which have been spot welded on the specimen surface. Thermocouples are widely used in high temperature material testing since they feature a high insensitivity to any variation of mechanical boundary conditions. In order to observe the temperature profile across the gauge section as accurately as possible 3 thermocouples were used; one control thermocouple in the centre and 2 thermocouples at the upper and lower ends of the gauge section. At the beginning of the testing campaign the process parameters for thermocouple spot welding have been optimized for each contacting material, e.g. to minimize the amount of heat input into the specimen surface in order to exclude the probability of premature crack initiation at the spot weld location due to locally altered

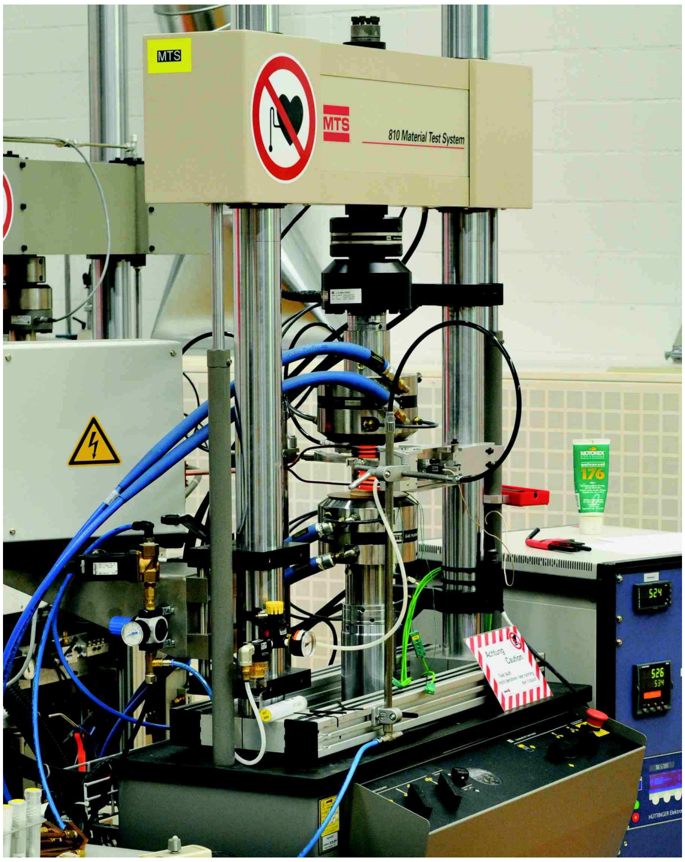

Figure 3.1: 100KN MTS uniaxial servohydraulic testing machine

material properties. This task has been successfully achieved for the Ni-base Alloy 617 (both parent material and weld metal) and the constituent steels in the DMW joints. The temperatures were continuously acquired throughout the test duration.

For continuous cycling LCF, creep-fatigue experiments with hold times at peak strains in tension and/or compression, TMF testing as well as tensile tests on Alloy 617 parent material, a short LCF specimen geometry has been adopted, see Fig. A.1. This was necessary because the delivered material blocks cut from the prototype rotor were too short in the rotor axial direction to apply the normally used LCF/TMF specimen geometry, see. Fig. A.2. It was decided to extract the specimens in axial direction from the rotor blocks in order to optimize the arrangement and to maximize the amount of available specimens with particular respect to the most relevant orientation in steam turbine rotor operation.

The second main objective of the present research work was the identification of the maximum application temperatures of dissimilar metal welded joints between the Ni-base Alloy 617 and a 1% CrMoV low alloy bainitic rotor steel as well as a higher alloyed 10% Cr martensitic rotor steel, with respect to their creep rupture and fatigue properties. For this purpose LCF and CF experiments have been conducted on these DMW joints using specimens extracted from across the weld with the LCF/TMF geometry, see Fig. A.2. Thereby the specimen has been positioned in such a way, that the interface between the Alloy 617 weld filler and the steel HAZ coincides with the centre plane of the specimen gauge length, see Fig. 3.2. Since the parallel length of the LCF/CF test specimen is only 20 mm the gauge length comprises only Alloy 617 weld filler material and steel HAZ as well as some part of steel base material.

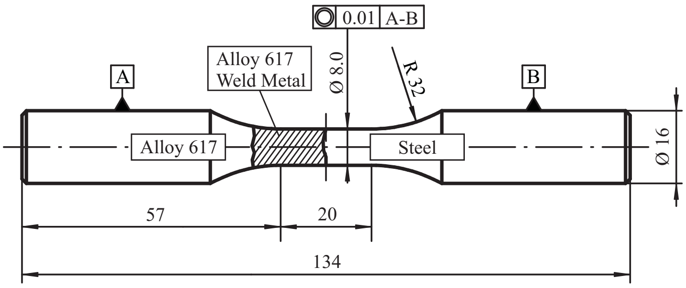
0.01
A-B
A
Alloy 617
Weld Metal
Ø 8.0
R 32
B
Alloy 617
Steel
Ø 16
57
20
134

Figure 3.2: DWM cross-weld specimen geometry arrangement for LCF and CF testing. The interface weld filler - steel HAZ is positioned in the centre of the gauge length.

A serious problem which had to be overcome was the induction coil heating of the DMW joint specimen. Due to very different electro-magnetic properties of the Ni-base Alloy 617 and the ferritic steels, e.g. electrical resistivity and conductivity as well as magnetic permeability, the electromagnetic field would have been distorted when placing a bi-metallic specimen into a common alternating magnetic field. Different surface power densities and hence temperature non-uniformities would

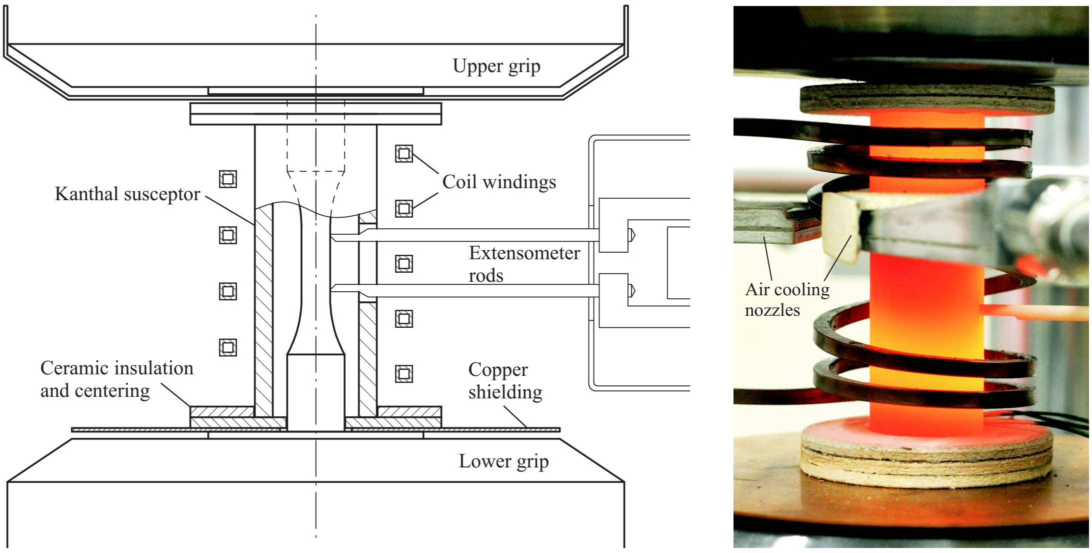
Upper grip
Kanthal susceptor
Coil windings
Extensometer
rods
Ceramic insulation
and centering
Copper
shielding
Lower grip
Air cooling
nozzles

(a) Schematic drawing of the susceptor arrangement. The susceptor is centred and hold in position by ceramic insulation slices.

(b) Photograph of operating induction heating with the use of a susceptor

Figure 3.3: Susceptor concept for induction heating of DMW

have been expected along the parallel length of the specimen and especially in the vicinity of the interface between the Alloy 617 weld filler material and the ferritic steel HAZ, leading to undesirable thermal stress gradients in the dissimilar metal weld. In order to overcome this problem a susceptor concept has been developed, see Fig. 3.3. The susceptor constitutes a coupling agent made of a highly thermally and electrically conductive material, the FeCrAl heatsealing alloy Kanthal, surrounding the specimen with a cylindrical arrangement. The susceptor is slotted in order to grant access for the extensometer legs onto the specimen surface and features also an exit slot for the thermocouple wires, which are guided in the gap between specimen and susceptor walls. With this solution the bi-metal specimen is heated uniformly by radiant heat from the surrounding susceptor which is heated directly by the induction coil. Kanthal, next to its supreme conductive properties, also features very good oxidation resistance since the susceptor temperatures may well exceed more than 900°C for applied DMW specimen test temperatures up to 625°C. Considering this fact the susceptor is held in a central position with ceramic isolation pads to minimize heat transport towards the machine grips. In order to achieve an acceptable temperature gradient along the specimen gauge length it was necessary to invoke forced convection air cooling at the susceptor outer surface which was accomplished by surrounding air nozzles, see Fig. 3.3b. With this susceptor heating arrangement the LCF and CF experiments on the Alloy 617 - 1% CrMoV and Alloy 617 - 10% Cr DMW joints have been successfully conducted, with even the option of performing future anisothermal TMF experiments on such bi-metallic specimen.

3.2.2 Creep Rupture Testing

A considerable number of creep rupture (CR) experiments have been conducted on Alloy 617 parent material and on Alloy 617 - 1% CrMoV and Alloy 617 - 10% Cr DMW joints to achieve the objectives of the present research project. In order to perform the high amount of experiments within the present project, it was necessary to restrict the planned durations of the creep experiments to approximately 5000 h.

For Alloy 617 parent material MMS-036 a number of high stress CR experiments were conducted to investigate the influence of the ageing treatment on the material creep characteristics, since a considerable amount of existing CR data on solution treated Alloy 617 has been available to the present project from the industrial partner originating from previous research activities. The CR experiments have been performed on motor controlled spring loaded testing machines and continuous recording of the specimen elongation according to the accordant standard [1]. The CR specimens were 8 mm in diameter and featured measuring ridges for the attachment of the extensometer, see Fig. A.3. The temperature measurement and control was implemented by Type N thermocouples which have been placed at the specimen centre and at the upper and bottom ends of the gauge length. The CR testing machines were equipped with resistance heated furnaces featuring 3 independent heating zones in order to optimally adjust the temperature profile along the specimen gauge length.

The CR experiments on the Alloy 617 - 1% CrMoV (MMS-069) and Alloy 617 - 10% Cr (MMS-052) DMW joints have been conducted on dead weight loaded lever CR testing machines with a 3 zone resistance heated furnace. The CR specimens have been extracted across the weld using a specimen geometry following a review of weldment creep testing practices of ECCC [22] and ALSTOM, see Fig. A.4. Since the welds were only 15 mm wide it was possible to include the weld metal, both HAZs and sections of both parent materials in the 60 mm CR specimen parallel lengths, see Fig. 3.4. The temperature measurement has been made using 3 Type K thermocouples at the specimen centre and at the upper and bottom end of the gauge length accordingly. The specimen elongation has been derived by measures of the total elongation of the load train. Since the creep deformation occurs non-uniformly across the weldment, the local creep deformation could only be reliably measured as reduction of area value after creep rupture during post-test inspection.

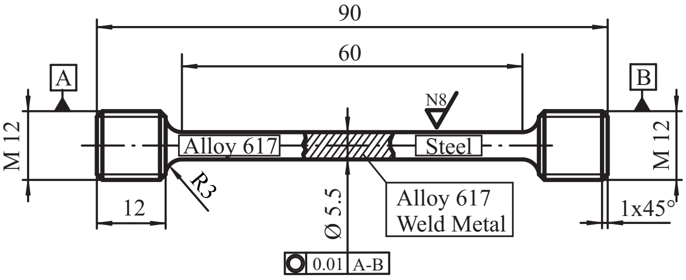

Figure 3.4: DWM cross-weld specimen geometry arrangement for creep rupture testing. The centre of the weld is positioned in the centre of the parallel gauge length.

Chapter 4

High Temperature Mechanical Behaviour of Alloy 617

This chapter covers the work performed on the first objective of the present research project on the development and verification of the effectiveness of advanced creep-fatigue lifetime assessment methodologies and determination of the required material input parameters for the accurate and reliable evaluation of Alloy 617 steam turbine rotor features at maximum steam turbine application temperatures.

In the first part of this chapter the experimental results of the material testing program are presented. An overview is given on the material behaviour observed during tensile tests, continuous cycling LCF experiments, CR experiments as well as CF experiments including hold periods at peak strains. Concurrently the accordant damage mechanisms occurring in the material are discussed on the basis of post test metallurgical investigations.

The second part of this chapter contains an overview on the modelling activities of the observed material behaviour. The constitutive equations for modelling the material response and deformation behaviour during cyclic and static loading conditions are presented. The model equations for fatigue damage as well as creep damage are introduced and subsequently the creep-fatigue interaction mechanism is discussed with the help of results obtained during post-test microstructural investigations.

The third part of this chapter provides an overview on the creep-fatigue lifetime assessment of Alloy 617 steam turbine rotor features. The thermo-mechanical cycle definition is presented on which basis the service cycle TMF testing has been performed in order to determine the material behaviour under realistic operation conditions. In the last part the creep-fatigue assessment procedure for Alloy 617 rotor features is introduced and discussed.

4.1 Experimental Determination of Material Behaviour

4.1.1 Tensile Properties

Important short-term experiments for the determination of the tensile strength R_m, the yield strengths $R_{p0.2}$, $R_{p0.5}$, $R_{p1.0}$, the fracture deformation properties A_u, Z_u and the Young's modulus E are constituted by tensile tests at ambient conditions and elevated temperatures. For this purpose tensile tests have been conducted at different temperature levels on a servohydraulic testing machine, controlling the total elongation of the specimen according to [41]. The tests have been performed under strain control with a rate of 0.3 %/min up to 3.0 % total strain and subsequently in stroke control to final rupture with an equivalent strain rate of 6.0 %/min. Since the determined properties are dependent on the deformation rate an experimental procedure according to the standard is decisive for the comparability of the results. The tensile results indicate a good strength level of the investigated forged Alloy 617 with considerable high rupture ductility properties. Fig. 4.1 compares the 0.2 % yield strength $R_{p0.2}$ and the tensile strength R_m of the investigated Alloy 617 heat MMS-036 to values of the reviewed material data obtained in previous research activities. The results show a significant influence of the ageing treatment on the strength properties with particular low yield strength for the solution treated material. The considerable strengthening effect is related to additional precipitation of carbides and γ'-phase particles, see section 2.3.2.

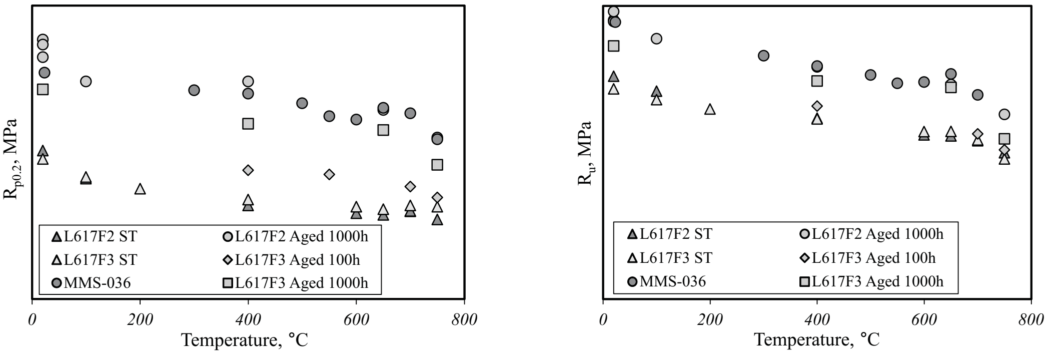

(a) Yield strength $R_{p0.2}$ of reviewed heats and investigated Alloy 617 heat MMS-036 showing influence of heat treatment

(b) Tensile strength R_m of reviewed heats and investigated Alloy 617 heat MMS-036 showing influence of heat treatment

Figure 4.1: Tensile and yield strength properties of reviewed and investigated heats of Alloy 617

4.1.2 Creep

A significant quantity of existing creep rupture data on Alloy 617 has been available to the present project from previous research activities [99, 100]. These data were mainly for temperatures ≥650°C and have been entirely based on material in the solution treated condition. Consequently the focus of the present research project was to determine the creep behaviour at lower temperatures and to examine the influence of an ageing heat treatment on the creep characteristics compared to the solution treated condition. Therefore a number of creep rupture experiments were planned in the accordant temperature regime with durations not exceeding 2000 h. CR experiments which would clearly not have failed within an acceptable test duration have been stopped after reaching a sufficient large creep strain. Fig. 4.2 shows by example the determined creep curves for the experiments conducted at 600 and 700°C. Except for the high stress tests, which exhibit considerable instantaneous plastic strains due to exceeding the yield strength of the material on loading, only very small amounts of primary creep have been observed. Furthermore there were no distinctive secondary creep regimes with constant creep strain rate visible, but instead monotonic increasing creep rates were observed. Additionally, the material features considerable creep ductility for the higher temperatures. The creep rupture strengths of the reviewed and investigated heats of Alloy 617 for the temperatures 600, 650, 700 and 750°C are compared in Fig. 4.3. For lower temperatures and short testing durations the strengthening effect of the ageing treatment is observable, whereas at higher temperatures no difference is distin-

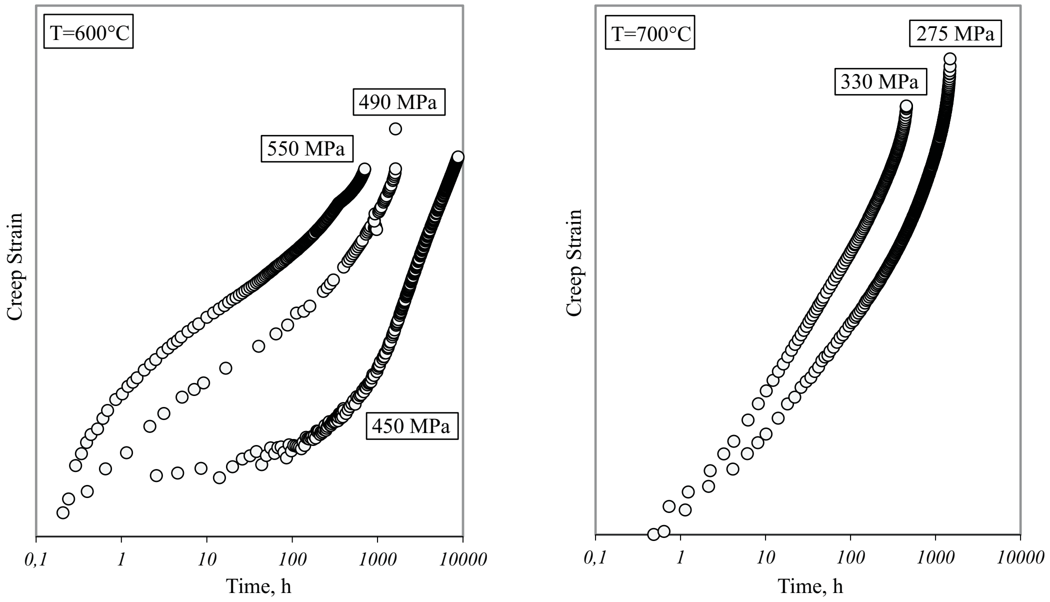

Figure 4.2: Creep curves of Alloy 617 heat MMS-036 for 600°C and 700°C

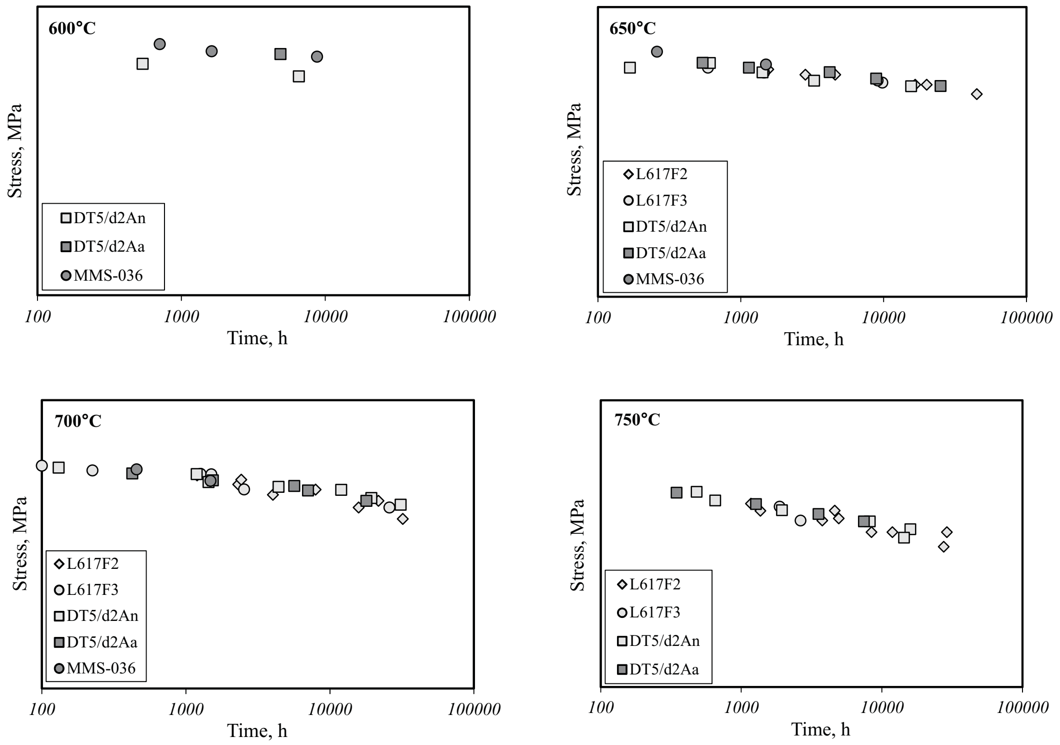

Figure 4.3: Creep rupture strength of Alloy 617 heats

guishable between the heat treatment conditions. The evaluation of the creep rupture strength and creep strain strength will be addressed in section 4.2.2.

Important information for damage analysis is the knowledge of the mechanisms leading to crack development. Consequently creep damage has been characterised through the post-test examination of ruptured specimens from the present research activity and additionally of selected specimens of long duration creep rupture experiments conducted in previous activities [99, 100]. The appearance of creep damage in Alloy 617 specimen for a comparably high stress of 550 MPa and medium temperature of 600°C is by example shown in Fig. 4.4. Even under these loading conditions, leading to creep rupture at times below 1000 h, creep damage is generated in the form of cavities and micro-cracking at grain boundaries. Despite the high rupture ductilities of Alloy 617 under these conditions, the appearance of damage seem to be more consistent with creep brittle behaviour. Additionally the existence of twinning structures has been observed, particularly in the larger grains of the section, which seems to be a typical feature in high-stress creep deformation for this alloy. The creep damage appearance in Alloy 617 specimen of a creep rupture test at high temperature of 700°C and medium stress of 275 MPa is presented in Fig. 4.5. Even with a relatively short rupture time of 1485 h creep damage is generated as cavities and cracks predominantly at grain boundaries in a more distributed and volumetric manner. The very high creep ductility under

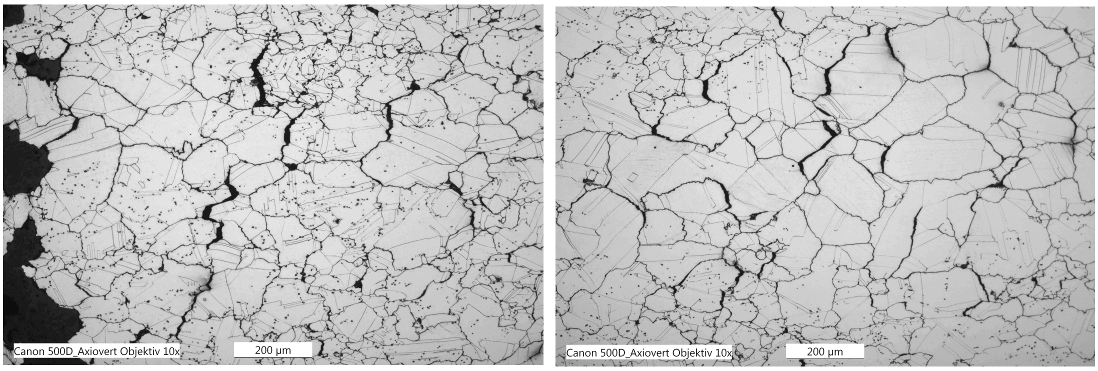
Canon 500D_Axiovert Objektiv 10x
200 µm
Canon 500D_Axiovert Objektiv 10x
200 µm

(a) Position adjacent to the fracture surface (b) Position in the centre section of the specimen

Figure 4.4: Appearance of creep damage in Alloy 617 heat MMS-036: T=600°C, σ=550 MPa, Z_u=20.7%

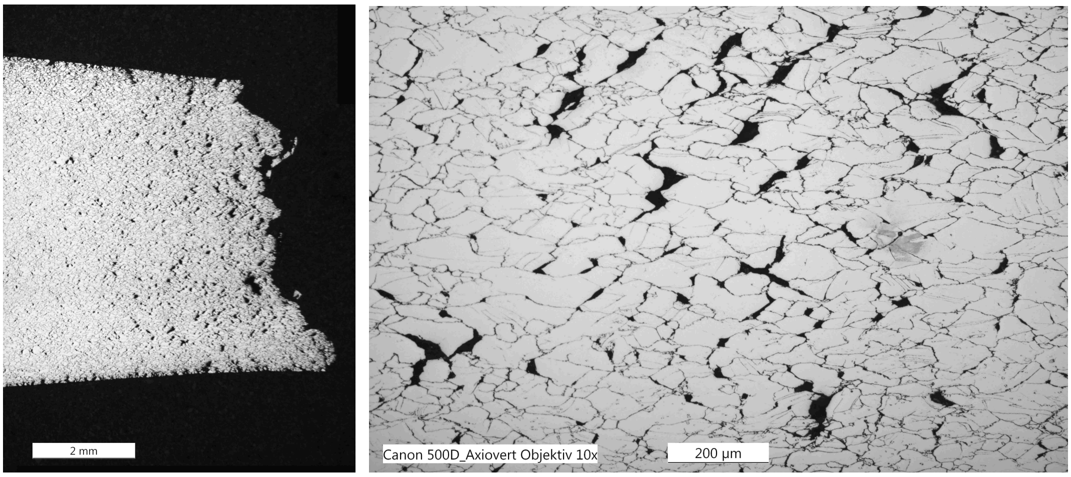
2 mm
Canon 500D_Axiovert Objektiv 10x
200 µm

(a) Specimen fracture surface (b) Position in the centre section of the specimen

Figure 4.5: Appearance of creep damage in Alloy 617 heat MMS-036: T=700°C, σ=275 MPa, Z_u=48.9%

these conditions is presented in Fig. 4.5a with extensive reduction of fracture area. The same creep damage appearance has been observed in specimens of long-term duration creep rupture experiments at 650 and 700°C with lower stresses responsible for rupture in ~32-45 kh.

4.1.3 Low Cycle Fatigue

LCF experiments have been conducted on the Alloy 617 heat MMS-036 in order to determine the endurance characteristics of the material and to establish a constitutive deformation model for the entire range from ambient to maximum application temperatures. Since a considerable amount of previously generated fatigue experiments ([99, 100]) have been available to the present research collaboration, these data have been reviewed and used for scatter band analysis. The performed LCF experiments have all been conducted under strain control and a total strain rate of 0.1 %/s.

In Fig. 4.6 the low cycle fatigue endurance data of the reviewed and investigated heats of Alloy 617 is by example given for test temperatures 700 and 750°C. Generally a small amount of scatter can be observed independent of the heat treatment condition of the tested specimen. A more extensive overview on the LCF endurance data and calculated endurance curves based on a fatigue damage model for the entire temperature range is given in section 4.2.1.

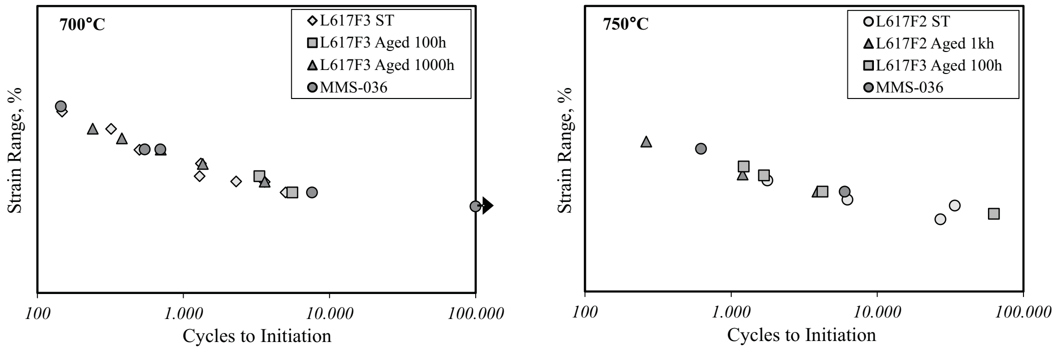

Figure 4.6: LCF endurance data of Alloy 617 heats at 700 and 750°C

Like austenitic steels and other solution strengthened Ni-base alloys, Alloy 617 exhibits significant hardening during cyclic loading conditions. The hardening rate and the magnitude of peak hardening during cyclic loading were strongly dependent on the applied strain amplitude. Nevertheless the material characteristics feature a stabilised response after initial hardening, which is in contrast to precipitation strengthened ferritic steels, that exhibit continuous softening during cyclic loading. Fig. 4.7 shows by example the stress amplitude profiles and the hysteresis loops of the first and mid-life cycle obtained from a LCF experiment with 1.0 % total strain range at 600°C. The peak stress profiles show a distinctive stabilised plateau, with the mid-life cycle representative for the major part of total lifetime. Fatigue failure due to crack initiation has been defined as a 2 % load-drop in the tensile peak stress profile, see Fig. 4.7a.

Low cycle fatigue damage in Alloy 617 appeared to be predominantly transgranular, although there seems to be a small tendency to follow conveniently placed grain boundaries, see Fig. 4.8. The development of fatigue damage is similar to that of ferritic steels, with many short cracks first developing along the surface of the gauge section, before one becomes dominant and propagates preferentially, extending to a size responsible for failure.

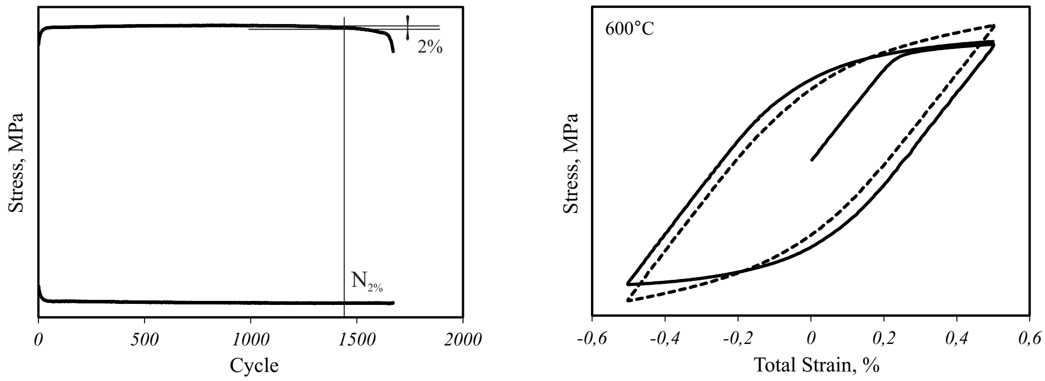

Figure 4.7: Cyclic hardening shown in peak stress profiles (a) and hysteresis loop for first and mid-life cycle (b) of Alloy 617 heat MMS-036 - LCF test: T=600°C, $\Delta\varepsilon_t$=1.0%

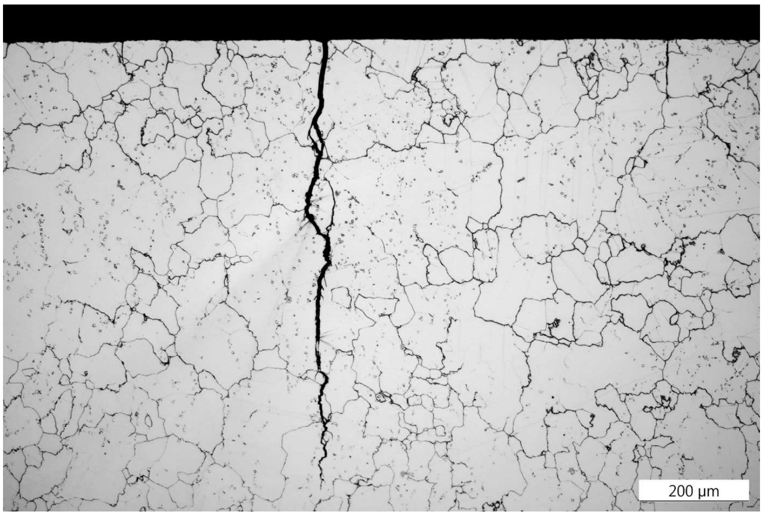

Figure 4.8: Appearance of LCF damage in Alloy 617 heat MMS-036: T=700°C, $\Delta\varepsilon_t$=1.0 %

4.1.4 Creep-Fatigue

Isothermal CF experiments with different hold periods at peak strains have been conducted on the Alloy 617 heat MMS-036 in order to determine the endurance characteristics of the material and to establish a constitutive deformation model for the temperature regime relevant for time-dependent creep deformation. Since a considerable amount of previously generated creep-fatigue experiments ([99, 100]) have been available to the present research collaboration, these data have been reviewed and used for scatter band analysis. The performed CF experiments have all been conducted under strain control and a total strain rate of 0.1 %/s. A preliminary analysis of the 0.2 % yield strength and 100 kh creep rupture data had shown that the insignificant creep temperature for forged Alloy 617 heat MMS-036 is likely to be ≤470°C and hence CF experiments were performed starting at 500°C. At higher temperatures 650, 700 and 750°C cyclic hold tests have been continued until failure, whereas for lower temperatures 500, 550 and 600°C the tests were prematurely terminated after reaching a stabilised peak stress cyclic hardening response condition.

In Fig. 4.9 the cyclic/hold endurances are compared with the low cycle fatigue endurance data of the reviewed and investigated heats of Alloy 617 for test temperatures 700 and 750°C. At 700°C the influence of hold times on LCF endurances is not significant for strain ranges ≤0.5 %, although the tests performed on MMS-036 heat with hold times of ±10 min and ±60 min at strain ranges of 1.0 % do indicate a small influence of increasing hold time within the endurance data scatterband collated for Alloy 617. At 750°C there is apparently a greater influence of hold time, increasingly with reducing strain amplitude and with increasing hold duration.

Fig. 4.10 provides by example the cyclic hardening characteristic and a comparison of the first and mid-life cycle hysteresis loops of a cyclic/hold test of Alloy 617 heat MMS-036 at test temperature 700°C and a strain range of 1.0 %. After initial hardening early in life, the material subsequently softens and descends into a stabilised response for the major part of lifetime. The first and mid-life cycle peak stresses almost coincide, see Fig. 4.10b. On the other hand, the material exhibits a considerable decrease in creep resistance during peak strain hold periods as the relaxed stresses indicate.

For the cyclic/hold experiments the introduction of considerably long 60 min hold periods at peak strains in tension and compression appears to have little influence on the mechanism of fatigue crack development in Alloy 617 at 700 and 750°C, see Fig. 4.11. Surface crack initiation and propagation is entirely transgranular at 700°C with many micro-cracks distributed at the specimen surface. At test temperature of 750°C fatigue crack propagation appears to occur partially along creep damaged grain boundaries, whereas almost no creep cavitation has

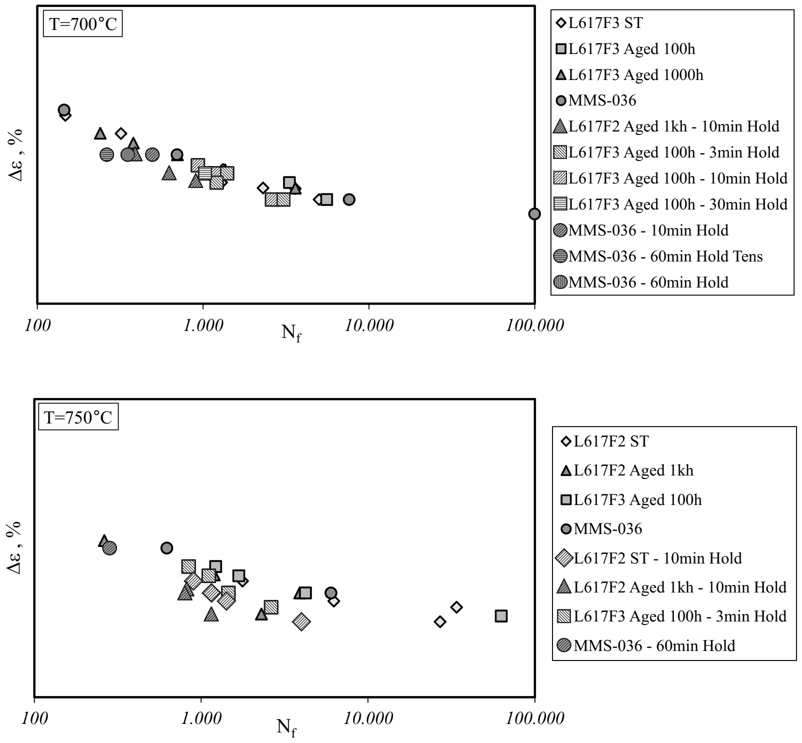

Figure 4.9: CF endurance data of Alloy 617 heats at 700 and 750°C

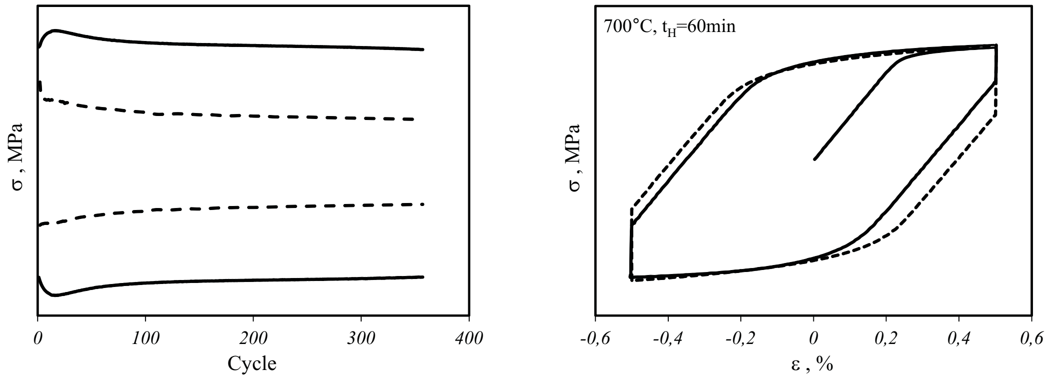

Figure 4.10: Cyclic hardening characteristic with peak and relaxation stress profile (a) and hysteresis loop for first and mid-life cycle (b) of Alloy 617 heat MMS-036 - CF test: T=700°C, $\Delta\varepsilon_t$=1.0%, t$_h$=60 min

been observed in the interior region of the specimen under these test conditions. In contrast, the appearance of damage in a 700°C isothermal cyclic/hold test with a 60 min hold time at peak strain in tension is concentrated at the grain boundaries, see Fig. 4.12. The predominantly intergranular damage associated with creep cavities and grain boundary cracking is consequently comparable to that observed in creep rupture experiments, see Fig. 4.4 and 4.5. The comparison of the dam-

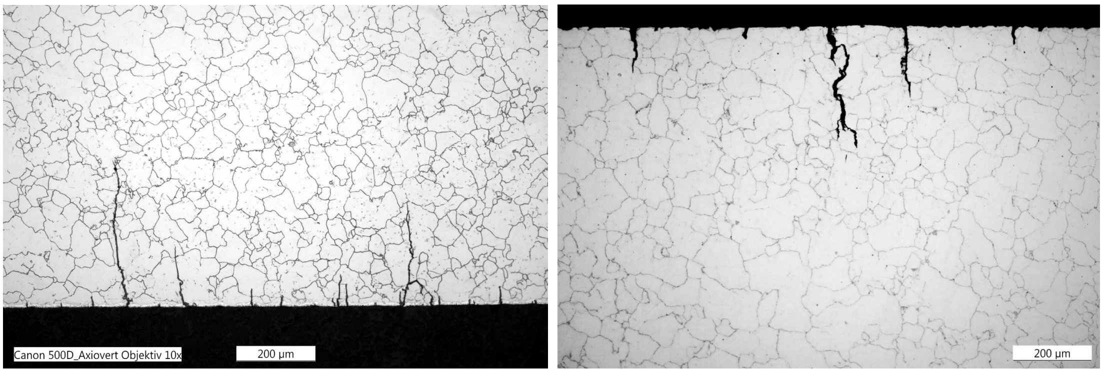

(a) T=700°C, $\Delta\varepsilon_t$=1.0%, t_h=60 min symmetric hold periods in tension and compression

(b) T=750°C, $\Delta\varepsilon_t$=1.0%, t_h=60 min symmetric hold periods in tension and compression

Figure 4.11: Damage appearance in symmetric cyclic/hold tests of Alloy 617 heat MMS-036 at 700 and 750°C

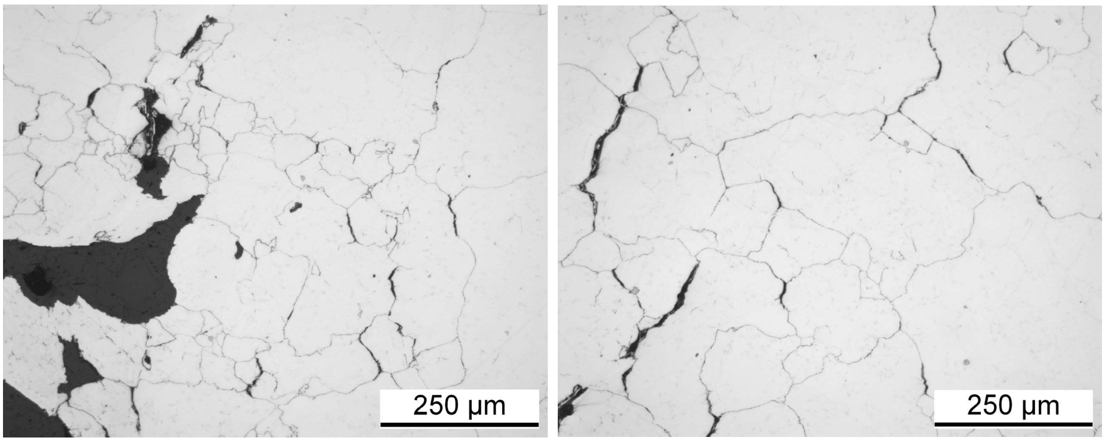

(a) Position adjacent to the fracture surface

(b) Position in the centre section of the specimen

Figure 4.12: Damage appearance in asymmetric cyclic/hold tests of Alloy 617 heat MMS-036: T=700°C, $\Delta\varepsilon_t$=1.0%, t_h=60 min hold periods in tension

age appearance of cyclic/hold experiments with symmetric hold periods and those of tests with hold times exclusively in tension gives rise to the assumption, that the hold periods at peak strain in compression appear to have no contributing effect to the creep damage occurring during tensile hold periods, resulting in almost exclusive fatigue damage and transgranular crack development in cyclic/hold experiments with symmetric hold periods.

4.2 Modelling of Material Behaviour

4.2.1 Cyclic Plasticity

For modelling the deformation response of Alloy 617 parent material the adopted strategy was to formulate a non-unified constitutive material model for which time independent (cyclic plasticity) and time dependent (creep) deformation are treated separately. The cyclic plasticity formulation is based on a multiple backstress model, featuring the superposition of three non-linear kinematic hardening components, see eqn. (2.25) and (2.28). With respect to the stabilised hardening characteristics observed for Alloy 617 during LCF experiments, a fitting procedure of the mid-life cyclic stress strain curves (CSS) was conducted in order to obtain a consistent behaviour of the constitutive cyclic plasticity model throughout the temperature and strain amplitude range. Fig. 4.13 shows an overview about the experimentally obtained CSS results of reviewed and investigated Alloy 617 heats for various temperatures and the Chaboche multiple backstress model fit for mid-life condition according to eqn. (2.29). Thereby the curve fit has been adjusted to represent aged Alloy 617 characteristics, in particular the heat MMS-036 results. For higher temperatures the ageing condition appears not to influence the cyclic flow characteristics, at medium temperature of 500°C the aged material exhibits

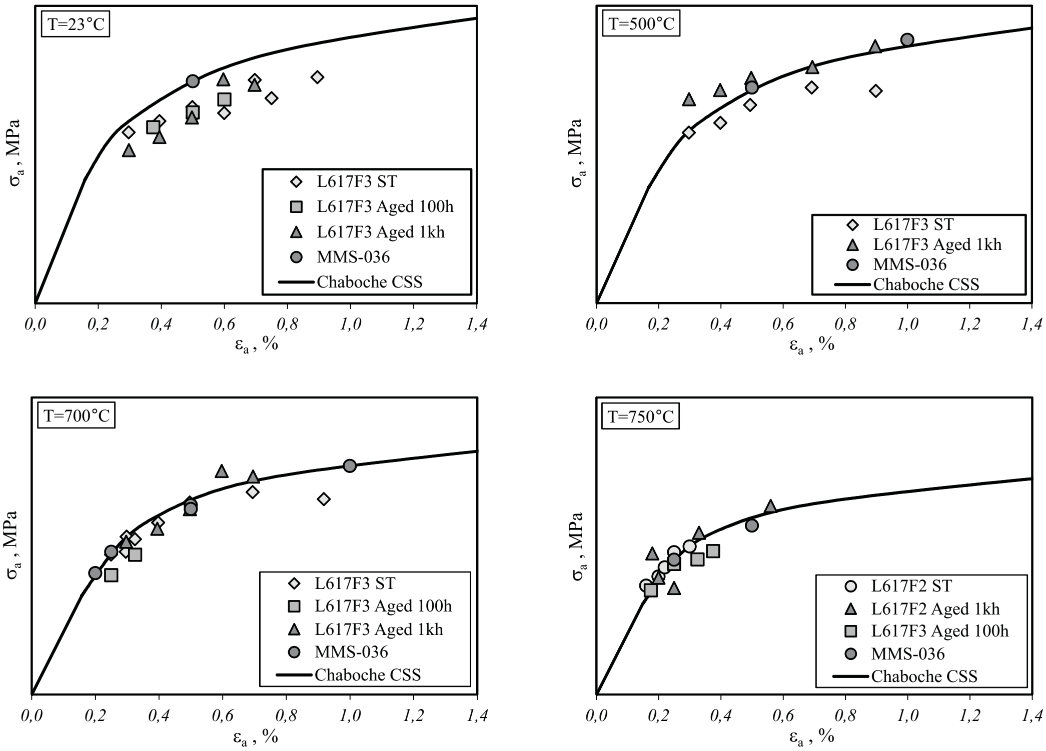

Figure 4.13: Cyclic stress-strain curves for mid-life condition of Alloy 617 heats for temperatures 23, 500, 700 and 750°C

more hardening than solution treated material. Fig. 4.14 shows the CSS curve family throughout the temperature range, indicating a good temperature consistency. The Chaboche multi-term backstress model can be selected as an implemented standard material model in the commercial FE analysis software ABAQUS, which has been used within the present research project.

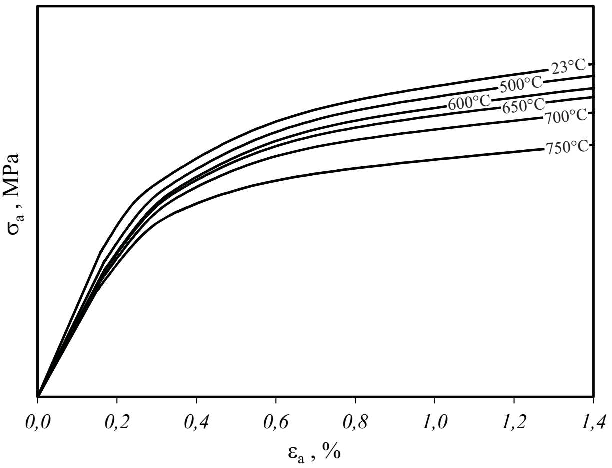

Figure 4.14: Modelled CSS curves of Alloy 617 heat MMS-036 using Chaboche multiple non-linear kinematic backstress model for various temperature conditions.

The comparison between measured and calculated mid-life cycle hysteresis loops of LCF experiments with various strain amplitudes and temperatures is presented in Fig. 4.15. The flow characteristics are modelled very accurately consistently throughout the entire temperature range, in particular the transition between elastic behaviour and small scale yielding. This results in exact modelling of even low strain hysteresis loops, which correspond to those occurring during operation of steam turbine components in service.

Fatigue damage modelling

For the determination of fatigue damage, reference was made to the general formulation of the fatigue criterion based on the dissipated energy during cyclic loading. The dissipated energy $W_{pl} = \int \sigma d\varepsilon_{pl}$, see eqn. (2.36), has been obtained by numerical calculation within ABAQUS as the standard output variable PENER. The energy dissipated within the mid-life cycle $W_{pl,cyc}$ as well as the total dissipated energy $W_{pl,tot} = N_{2\%} W_{pl,cyc}$ have been determined for the LCF experiments conducted on Alloy 617 heat MMS-036. The values of the accumulated plastic strain per cycle p_{cyc} and the total accumulated plastic strain $p_{tot} = N_{2\%} p_{cyc}$ have been calculated for comparison as well for the LCF experiments, using the ABAQUS standard output variable PEEQ. Thereby it was assumed that the mid-life hysteresis loop is representative throughout the whole lifetime, which is valid for Alloy 617 with sufficient accuracy, see Fig. 4.7 for example. The calculated results for $W_{pl,tot}$ appear to exhibit a temperature consistent trend with only minor dependence on the strain amplitude for a given temperature. This is not the case for the results

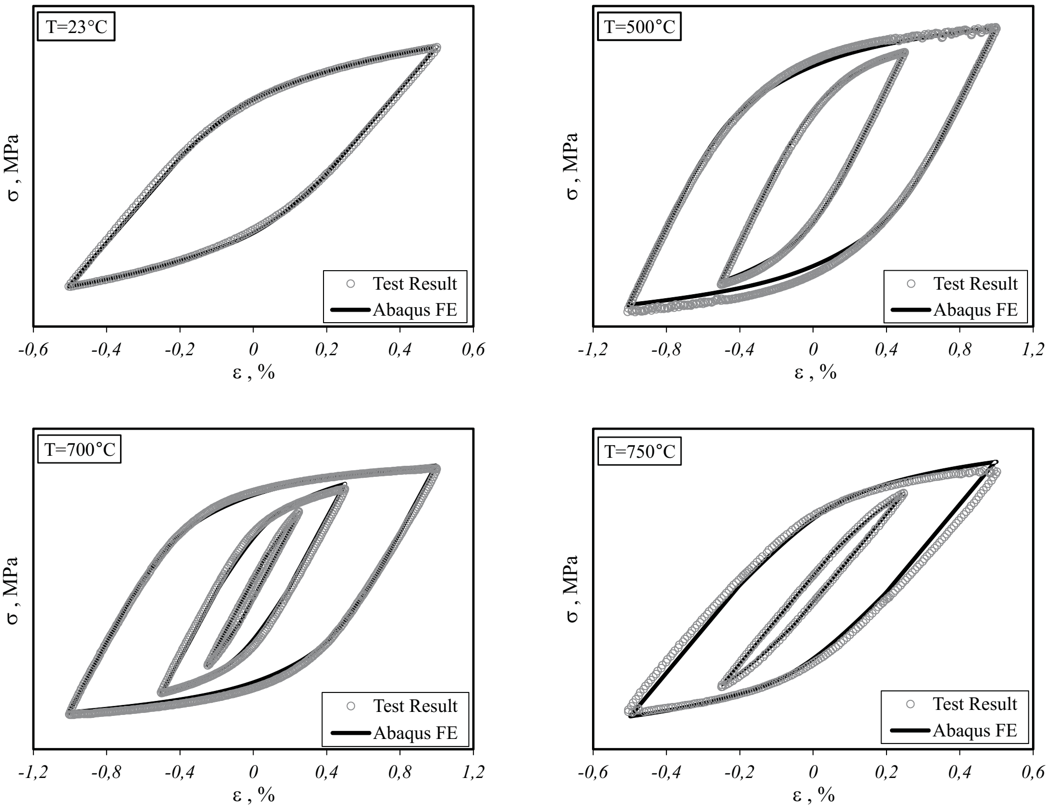

Figure 4.15: Comparison of measured and calculated mid-life cycle hysteresis of Alloy 617 heat MMS-036 for various strain amplitudes and temperatures 23, 500, 700 and 750°C

of accumulated plastic strain p_{tot}, which show temperature and strain amplitude dependence. The calculated values of $W_{pl,tot}$ of the performed LCF experiments are plotted against temperature in Fig. 4.16 together with the critical dissipated energy for fatigue failure $W_{pl,crit}(T)$, which has been fitted using the following equation:

$$W_{pl,crit}(T) = A_{W_{pl},0} - \frac{A_{W_{pl}}}{1 + e^{\frac{T_{TW_{pl}} - T}{K_{W_{pl}}}}} \,. \tag{4.1}$$

The curve fit of $W_{pl,crit}$ in Fig. 4.16 represents the calculated values $W_{pl,tot}$ of the test results in a satisfactory manner, in particular with respect to the normal scatter observed within fatigue endurance tests of materials. For the definition of the critical dissipated energy $W_{pl,crit}$ a 2% load drop in the tensile peak stress profiles has been used as crack initiation criterion, see Fig. 4.7a.

With the function of the critical dissipated energy for fatigue failure $W_{pl,crit}(T)$ the LCF endurance curves can be determined. For this purpose mid-life cycle hysteresis loops have been calculated for various strain amplitudes and temperatures using the constitutive cyclic plasticity model, the fatigue endurances have been de-

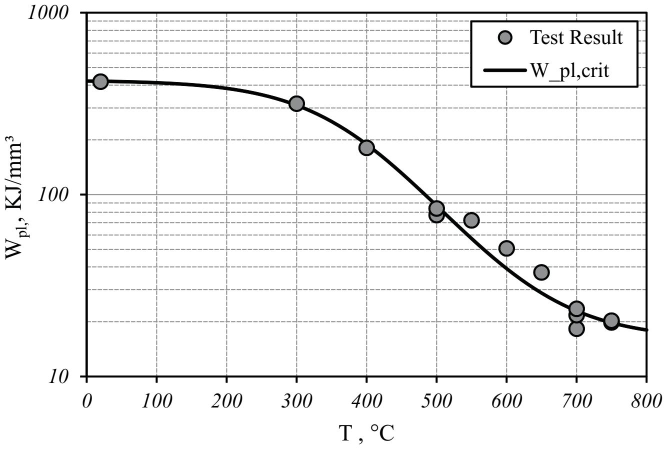

Figure 4.16: Total dissipated energy $W_{pl,tot}$ of LCF experiments on Alloy 617 heat MMS-036 for different temperatures and strain amplitudes. Curve fit of critical dissipated energy $W_{pl,crit}$ assuming strain amplitude independence.

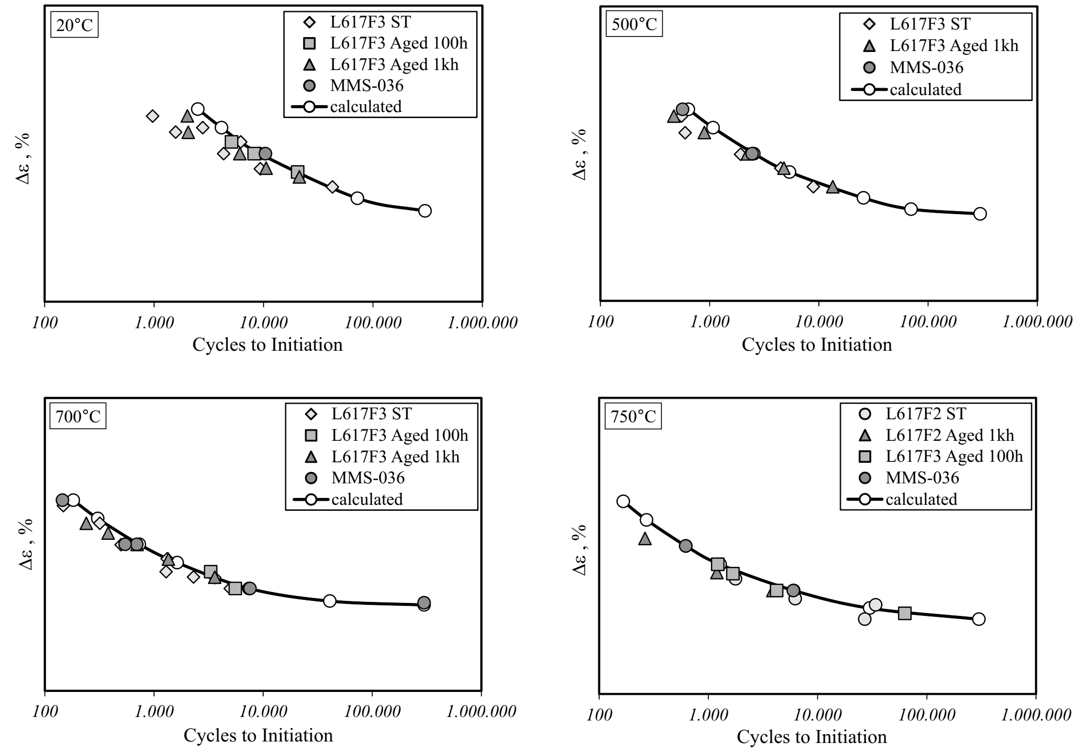

Figure 4.17: Comparison of measured and calculated LCF endurance data of Alloy 617 heat MMS-036 for temperatures 23, 500, 700 and 750°C

termined by the relation of calculated dissipated energy $W_{pl,cyc}$ and $W_{pl,crit}$. The results are presented in Fig. 4.17, where the experimental data is compared to the calculated fatigue endurance curves for representative temperatures. The prediction quality is astonishingly accurate throughout the temperature range. Only at room temperature the endurance curve appears to lay at the upper range of the scatterband, which can be explained by the CSS curve adjusted for the MMS-036 heat of Alloy 617, see Fig. 4.13a, which shows generally a higher strength at room temperature compared to the other heats reviewed. For all the other temperatures the curve fit is well acceptable, with particular respect to the normal data scatter observed in fatigue endurance tests. The dissipated energy approach for the determination of fatigue damage clearly shows a very good accuracy for Alloy 617 for a broad range of temperatures and strain amplitudes.

4.2.2 Creep

The investigation of the time-dependent creep deformation of materials constitutes an important basis for the analysis of the deformation behaviour of high temperature components. For the design of steam turbine components the mean alloy creep characteristics are often of particular importance, since an average description of various alloy heats is obtained. With data scatter band analysis accordant low confidence intervals can be determined and corresponding minimum expected creep strain and rupture strength curves can be estimated as a basis of a possible safety margin.

For the determination of the mean Alloy 617 creep behaviour mean creep curves had to be identified on the basis of a scatter band analysis. For this purpose curve families for creep rupture strength $R_{u/t/T}$ and datum strain strengths $R_{\varepsilon/t/T}$ have been estimated for the reviewed and investigated heats of Alloy 617. Instead of time-temperature-parametric equations, e.g. (2.12) and (2.13), algebraic equations of type Soviet Model 1 (SM1) have shown to deliver the best results and were adopted. The SM1 algebraic creep rupture model equation is defined by:

$$\log(t_u) = B_0 + B_1 \log(T) + B_2 \log(\sigma) + \frac{B_3}{T} + B_4 \frac{\sigma}{T}\,. \tag{4.2}$$

For each datum strain strength curve $R_{\varepsilon/t/T}$, for ε_c=0.1%, 0.2%, 0.5%, 1.0%, 2.0%, 5.0%, 10.0%, 20.0% and creep rupture strength curve $R_{u/t/T}$ optimised parameter sets have been determined in order to obtain a curve family without overlaps.

Fig. 4.18 shows by example the curve fit of the creep strain strength $R_{0.2\%/t/T}$, which is of great importance to the design of high-temperature components, and the creep rupture strength $R_{u/t/T}$ to the experimental results. A comprehensive overview on the curve fits for the entire range of datum strains is given in Fig. B.1 in the appendix. The isotherms of the different creep strain strengths are well representing the measured data for Alloy 617, where for the lower temperatures 550-650°C the results for aged material were weighted higher in order to represent the MMS-036 specified heat treatment condition. As reference, the experimental results obtained during tensile tests were used to construct the curve fits at very short times whenever possible, whereas problems encountered for high stress creep rupture experiments on solution treated Alloy 617 because of attaining static yield

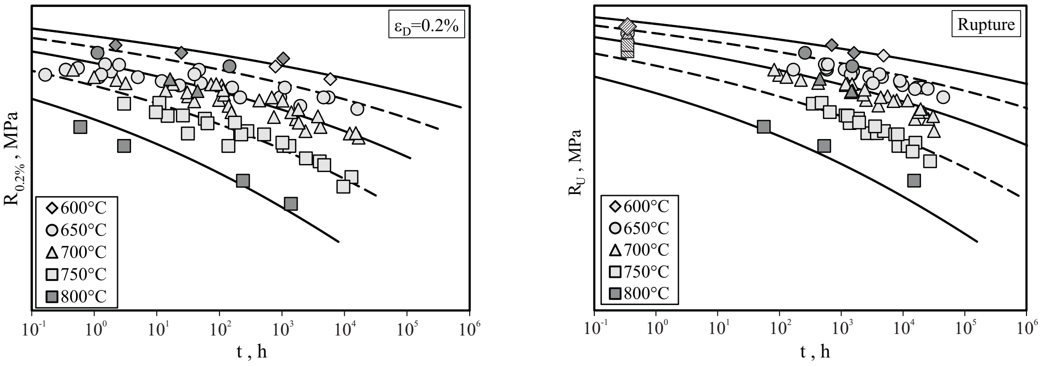

Figure 4.18: Comparison of measured creep data and calculated strength curves of Alloy 617 for datum strain ε_f=0.2% and creep rupture. Dark grey symbols indicate results on aged material condition.

strength of the material resulting in considerable initial plastic strains. Additionally the results for 800°C are based on test results on aged Alloy 617 material with non-standard heat treatment condition and can only be treated as reference. Nevertheless a consistent description of the mean creep behaviour for short-term as well as long-term durations was achieved covering the broad temperature range. The presented creep description can only be seen as preliminary, since for reliable prediction of the creep strength of Alloy 617 additional CR experiments for different alloy heats are required, exceeding rupture times of approximately the planned operation period of more than 100 kh. For further information on the creep strain and rupture assessment, the reader is referred to the recommendation and guidance given in [23].

The modelled curve families of datum creep strain strengths of Alloy 617, by example for temperatures 650 and 750°C, are presented in Fig. 4.19. A comprehensive overview on the datum creep strain strength curve families of the entire temperature range 550-800°C is given in Fig. B.2 in the appendix. With the optimised SM1 algebraic model parameters in eqn. (4.2) a consistent set of curve families has been obtained without overlapping of individual curves. With these parameter sets basis points of mean creep curves can be determined for stresses within the data range. Fig. 4.20 shows a representation of Alloy 617 mean creep curves for various stresses at a temperature of 700°C. A good description of the mean alloy creep behaviour substantially depends on the optimisation of the creep datum strain and rupture strength family. Analogously to Fig. 4.20 mean creep curves of Alloy 617 have been constructed for the entire temperature and stress range. The optimised and smoothed mean creep curves formed the basis of the modelling of a Alloy 617 creep equation, whose foundation and parameter identification are explained in the following.

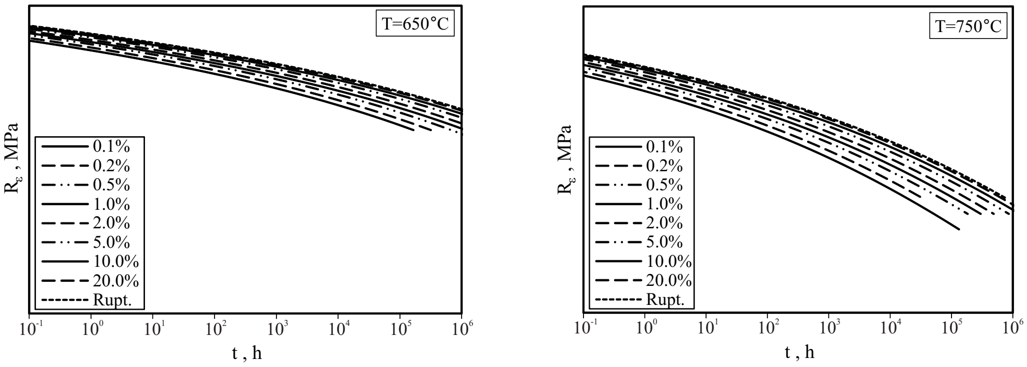

Figure 4.19: Modelled curve family of datum creep strain and rupture strength curves of Alloy 617 for temperatures 650 and 750°C.

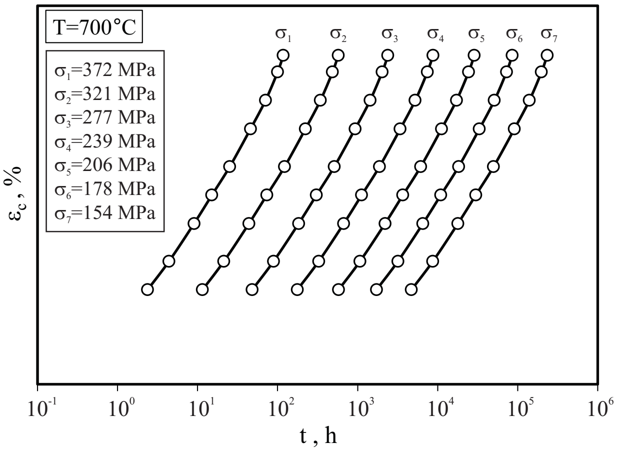

Figure 4.20: Calculated mean creep curves of Alloy 617 for various stresses at 700°C. The marked points represent the datum creep strains, for which the datum creep strain strength curve families have been fitted and the solid black line has been obtained by interpolation.

Creep model equation

For the description of Alloy 617 creep behaviour the modified Graham-Walles creep law has been used, whose constitutive formulation is as follows:

$$\dot{\varepsilon}_c = A_1 \sigma_e^{n_1} \varepsilon_{c,e}^{m_1} + A_2 \sigma_e^{n_2} \varepsilon_{c,e}^{m_2} \, . \tag{4.3}$$

The underlying strain based formulation $\dot{\varepsilon}_c = f(\varepsilon_c, \sigma)$ incorporates the strain hardening assumption, which was found to give more realistic results under variable loads, compared to the time hardening assumption, for most materials. Furthermore the Graham-Walles creep law is relatively easy to implement into commercial FE analysis programs, which for the present research project was performed as a creep subroutine in ABAQUS.

In eqn. (4.3) the creep strain exponent $m_1 < 0$ describes primary creep strain evolution with the transition to secondary creep regime, whereas the exponent $m_2 > 0$ represents secondary to tertiary creep with progressively increasing creep strain rates until failure. On the basis of the significantly less complex creep behaviour of Alloy 617, compared to low and high alloyed steel grades, a third term in the creep law could be omitted, which was originally present in the standard Graham-Walles creep law. The creep model equation (4.3) has been fitted to the mean creep curves of Alloy 617, where in order to consider the complex stress and temperature dependence the parameters A_1, A_2, n_1, n_2, m_1 and m_2 have been modelled as polynomials of second order. With this purpose a consistent and continuous trend of the creep model parameters have been accomplished, which is important in complex numerical calculations with varying temperature and stress conditions. Fig. 4.21 shows by example the model fits to the Alloy 617 mean creep curves for various stresses at temperatures of 600 and 700°C. The Graham-Walles creep model fit to the Alloy 617 mean creep curves shows good quality for the entire stress and temperature range. As mentioned before the material exhibits only very small amounts of primary creep strain in the range of less than 0.1%. The creep curves were fitted accordingly with respect to the experimental creep behaviour observed at very low creep strains within the present research activity, see Fig. 4.2. Unfortunately the quality of the creep data for Alloy 617 from previous experimental observations were not accurate enough in the relevant strain region in order to be considered within the assessment. Furthermore the Graham-Walles creep model fit well represents the observed progressive increasing creep strain rate for Alloy 617, with no significant secondary creep regime present.

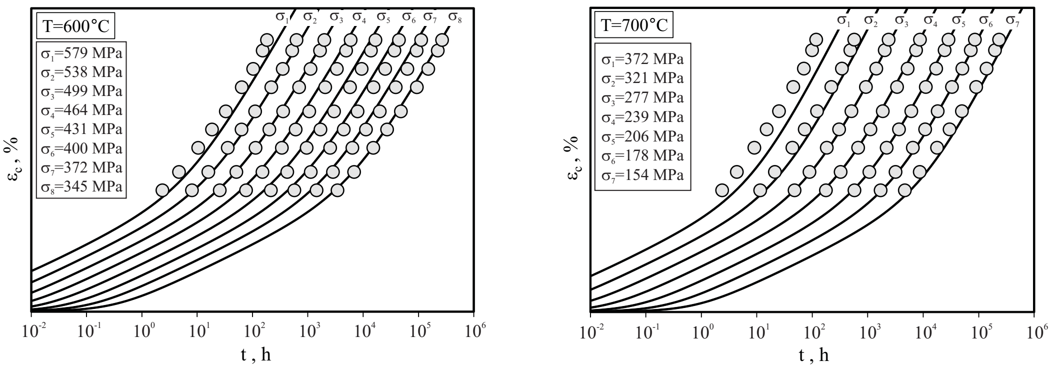

Figure 4.21: Graham-Walles creep model fit to mean creep curves of Alloy 617 for various stresses at temperatures 600 and 700°C.

With the successfully accomplished adjustment of the modified Graham-Walles creep model equation to the determined mean creep curves the creep behaviour of Alloy 617 can be predicted with sufficient accuracy. With respect to the longest achieved rupture times of creep experiments of ~32-45 kh for the relevant application temperatures sufficient care must be taken in extrapolation of creep rupture times and hence in the accuracy of the derived creep deformation model.

4.2.3 Creep-Fatigue Interaction

The cyclic/hold experiments conducted on Alloy 617 reveal, next to the creep-fatigue damage mechanisms prevailing in the material, the influence of creep processes during the relaxation periods on cyclic plasticity. Generally the CSS curve of LCF experiments with hold time features lower strength compared to continuous LCF tests, with decreasing strength for longer hold periods, see Fig. 2.20. Furthermore the cyclic flow characteristics are influenced by creep strain accumulations during the hold periods, depending on temperature and hold time. Fig. 4.22 compares the mid-life cycle hysteresis loops of LCF experiments and cyclic/hold CF tests for Alloy 617 heat MMS-036. At a temperature of 500°C the peak stresses at the strain reversals of the LCF test coincide with the values of the cyclic/hold experiment featuring a hold period of 60 min. For temperatures above 600°C the flow characteristics are significantly different with lower peak stresses for the CF cyclic/hold experiments. As indicated in Fig. 4.22c at 700°C the peak stresses and flow characteristics appear to be identical for hold periods of 10 and 60 min, which gives evidence that the influence of creep strain accumulation during hold periods on cyclic plasticity is apparent even at short durations and seems to stabilise at longer hold periods.

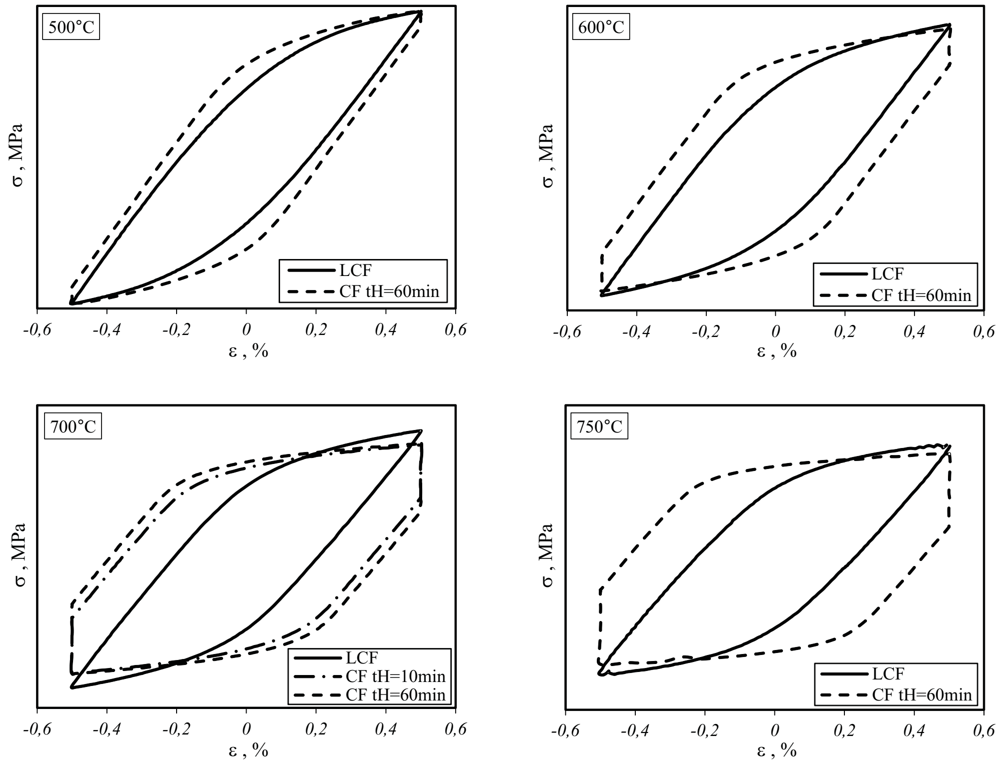

Figure 4.22: Comparison of measured LCF and CF mid-life hysteresis loops of Alloy 617 heat MMS-036 for temperatures 500, 600, 700 and 750°C

The Chaboche constitutive cyclic plasticity model has been adjusted to incorporate the effect of relaxation during hold periods of CF experiments. Fig. 4.23 shows the model fit to the CSS curves of cyclic/hold experiments on various heats of Alloy 617. The optimised CSS curves for continuous LCF tests, see also Fig. 4.13, is shown for comparison, indicating the considerable softening effect of the relaxation phases in cyclic/hold CF experiments. Additionally the test results on heat L617F3 at 700°C proof the observation that the softening effect on cyclic plasticity is stabilised even for short hold periods of 3 min. Whereas at 700°C there appears to be a slight different characteristic dependent on the heat treatment condition of Alloy 617, this is not observable at 750°C, where the test data shows supposed experimental scatter with no clear visible heat treatment influence nor heat variability.

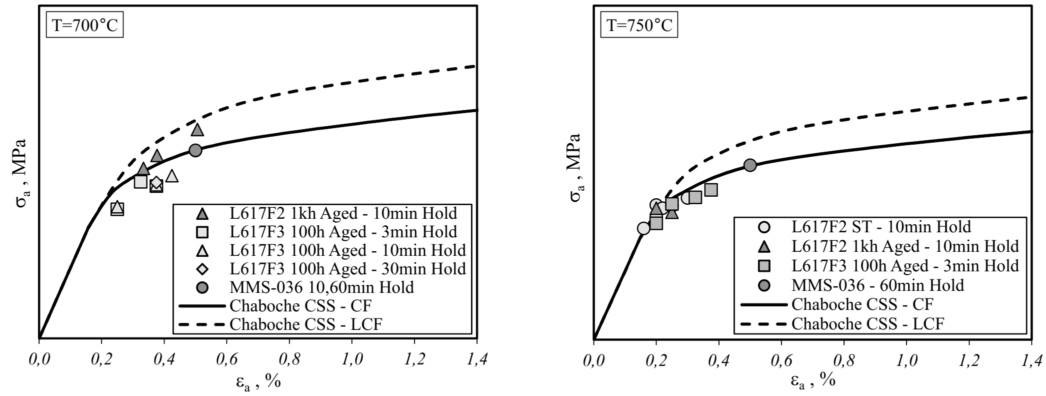

Figure 4.23: Mid-life CSS curves for cyclic/hold experiments of Alloy 617 heats for temperatures 700 and 750°C

In order to account for the considerable decrease in creep resistance as a consequence of stress relaxation in the peak strain hold periods of cyclic/hold experiments, see Fig. 4.10 by example for test temperature of 700°C, modifications of the constitutive creep deformation model have been introduced. A correction factor Z_c' was included into the modified Graham-Walles creep law (4.3) to account for the effect of cyclic plastic deformation on the creep deformation response of Alloy 617:

$$\dot{\varepsilon}_c = A_1 \left(\frac{\sigma_e}{1 - Z_c'} \right)^{n_1} \varepsilon_{c,e}^{m_1} + A_2 \left(\frac{\sigma_e}{1 - Z_c'} \right)^{n_2} \varepsilon_{c,e}^{m_2} \, . \tag{4.4}$$

The stress term in eqn. (4.4) is similar to the effective stress in eqn. (2.32), whereas Z_c' is not strictly related to physical damage D but describes phenomenologically the influence of prior plastic strain accumulation on subsequent creep deformation. This might certainly be related to changes in the microstructure of the material, which occur very early in life and manifest in the observed fast decrease in creep resistance. In Fig. 4.10 this is recognizable even for the second hold period, where a significant larger stress relaxation is evident. A similar approach for consideration of prior plastic deformation on the decreased creep resistance of low alloyed 1-2% CrMoV as well as 9% Cr steam turbine rotor steels have been introduced in preceding collaborative research projects [20, 78].

An investigation on the relaxation characteristics of various cyclic/hold experiments at different temperatures has revealed that the values for correction factor Z_c' correspond to $Z_c' = 0.0 - 0.1$ for the first cycle tensile relaxation and rapidly increase during subsequent hold periods. In Fig. 4.24 the evolution of Z_c' depending on the normalized dissipated plastic energy $W_{pl}/W_{pl,crit}$ is shown for the investigated CF experiments on Alloy 617 heat MMS-036. The results indicate that the evolution characteristics of Z_c' appear to show no dependence on temperature nor on the hold time of the experiments with respect to the supposed data scattering. Hence a fitting function $Z_c' = f(W_{pl}/W_{pl,crit})$ has been introduced which can be formulated by the following expression:

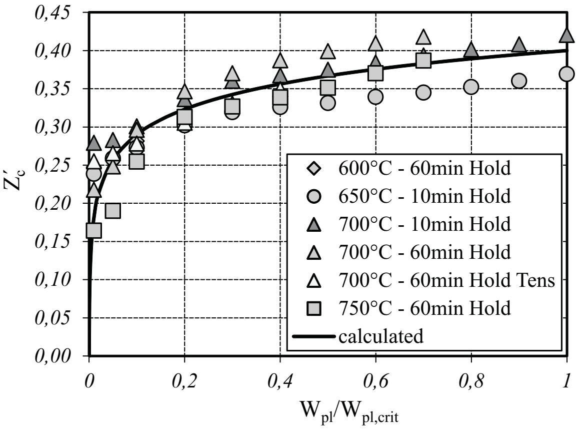

Figure 4.24: Calculated correction factor Z_c' in creep deformation model to accommodate for the decrease in creep resistance during cyclic/hold experiments based on normalized dissipated plastic energy $W_{pl}/W_{pl,crit}$ for Alloy 617 heat MMS-036

$$Z_c' = a_{Z_c'} \log\left(\frac{W_{pl}}{W_{pl,crit}} + b_{Z_c'}\right) + c_{Z_c'} \,. \tag{4.5}$$

Equation (4.5) represents the evolution of the correction factor Z_c' sufficiently accurate for different temperature conditions. A comparison to CF data on different heats of Alloy 617 from previous research activities [99, 100] revealed that the calculated values of Z_c' can also be applied to experimental data obtained for various strain ranges and hold periods, whereas here only mid-life cycle results data has been available.

Fig. 4.25 shows the constitutive deformation model fit to the measured mid-life cycle hysteresis loop of a cyclic/hold experiment with 60 min hold period at peak strains at a temperature of 700°C. The adjusted parameter for this condition was $Z_c' = 0.37$, resulting in the accurate description of stress relaxation during the

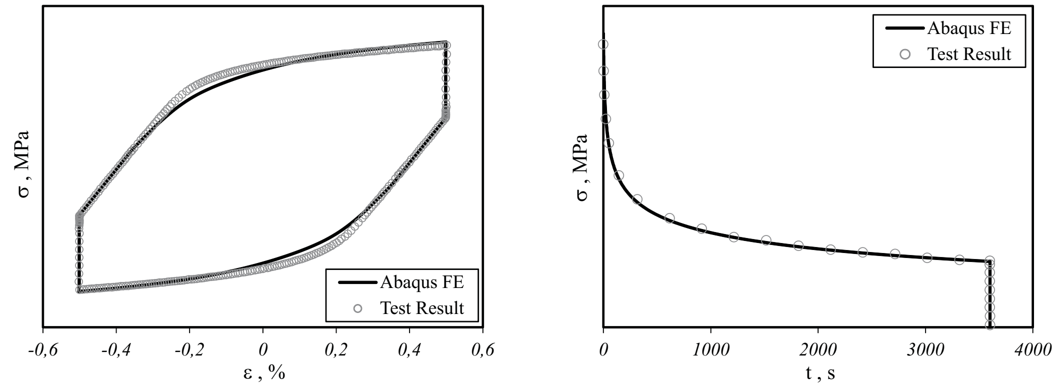

Figure 4.25: Comparison of measured and calculated mid-life cycle hysteresis of Alloy 617 heat MMS-036 for CF experiment with 60 min hold periods at peak strains at temperature 700°C (a) and detailed relaxation stress profile during hold period at tensile peak strain (b)

hold period. With the Chaboche cyclic plasticity model and the adjusted Graham-Walles creep equation (4.4), (4.5) an effective constitutive deformation model for Alloy 617 has been determined. During an extensive calculation campaign this deformation model has been verified on comprehensive experimental data on Alloy 617 heats investigated within this project and from previous research activities [99, 100]. In the following, the fatigue and creep damage fractions of the CF experiments are characterised and an assessment procedure of creep-fatigue damage interaction is introduced.

Creep-fatigue damage modelling

The fatigue damage fractions of CF experiments have been assessed based on the dissipated plastic energy approach described in chapter 4.2.1. The fatigue damage D_f can be determined by incremental summation of the ratio of dissipated plastic energy $\mathrm{W}_{pl} = \int \sigma d\varepsilon_{pl}$ and critical dissipated energy for fatigue failure $\mathrm{W}_{pl,crit}(\mathrm{T})$ (4.1), or by calculation of the integral respectively:

$$D_f = \sum_i \frac{W_{pl,i}}{W_{pl,crit}(T)} = \int \frac{\sigma}{W_{pl,crit}(T)} d\varepsilon_{pl} \,. \tag{4.6}$$

The determination of the creep damage fraction is referenced to the creep strain energy exhaustion approach (2.41), e.g. the analogous ratio of dissipated creep energy $\mathrm{W}_c = \int \sigma d\varepsilon_c$ and a critical dissipated energy for creep failure $\mathrm{W}_{c,crit}$:

$$D_c = \sum_i \frac{W_{c,i}}{W_{c,crit}} = \int \frac{\sigma}{W_{c,crit}} d\varepsilon_c \,. \tag{4.7}$$

The values for $\mathrm{W}_{c,crit}$ have been derived by determination of the true creep rupture strain from reduction of area Z_u measures of creep rupture specimen, since Z_u gives a reliable value of the local creep rupture ductility. Fig. 4.26 shows by example the distribution of $W_{c,crit}$ dependent on stress for creep rupture experiments conducted at 650 and 700°C. Despite the experimental scatter one clearly can distinguish heat specific characteristics in the $W_{c,crit} - \sigma$ plot. Especially the non-standard heat treatment condition of the DT5-d2Aa heat of Alloy 617 appears to result in higher values of $W_{c,crit}$. A reasonable description of the critical dissipated creep energy was determined by a power law on stress:

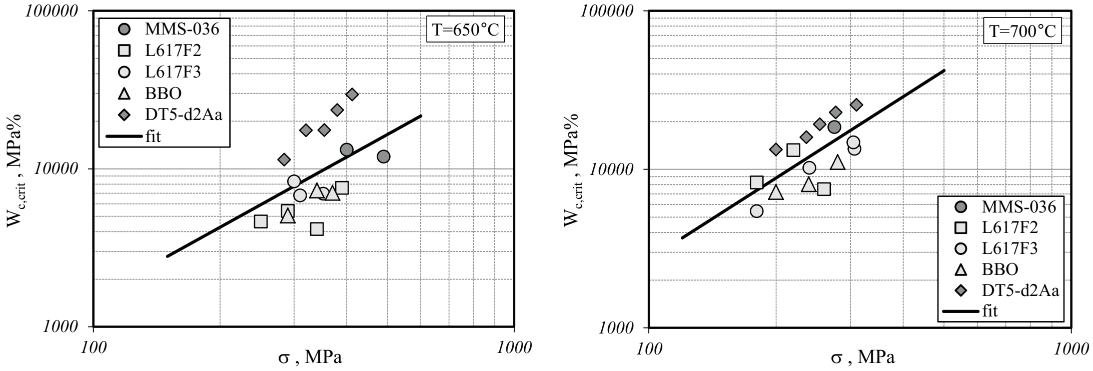

Figure 4.26: Critical dissipated creep energy derived from reduction of area measures Z_u of Alloy 617 heats for temperatures 650 and 700°C

$$W_{c,crit}(T,\sigma) = A_{W_c}(T)\sigma^{n_{W_c}(T)}\,, \tag{4.8}$$

with $A_{W_c}(T)$ and $n_{W_c}(T)$ polynomials of second order to obtain a temperature consistent equation fit on the experimental results.

For the consideration of combined creep and fatigue damage fractions, damage accumulation hypothesis have been proposed, first by Taira [95] with the linear accumulation of fatigue cycle ratios (2.35) and creep time fractions (2.38). By summation of the relative fatigue life fraction D_f=N/N_f and the relative creep life fraction D_c=Δt/t_u, the creep-fatigue damage fraction D is determined, which constitutes a material dependent parameter. An extension of this linear damage accumulation hypothesis has been developed by a generalisation of the approach, where the fatigue damage is calculated based on a reference fatigue endurance N_{f0}. The reference fatigue endurance N_{f0} is determined by cyclic experiments with a specific hold period at maximum strain, depending on the material affected [46, 47, 56, 83, 84]. Therefore only the remaining part of the relaxation period larger than the reference hold time is attributed to creep damage, whereas the beginning part of the relaxation period is covered by N_{f0}. The concept of the generalised damage accumulation hypothesis has been successfully adapted for a series of low alloyed 1% Cr as well as higher alloyed 10-12% Cr steels [83, 84].

Applied to the dissipated energy failure criteria pursued within the present work, a linear damage accumulation hypothesis with the superposition of fatigue damage D_f (4.6) and creep damage D_c (4.7) is proposed:

$$D = D_f + D_c = \int \frac{\sigma}{W_{pl,crit}(T)} d\varepsilon_{pl} + \int \frac{\sigma}{W_{c,crit}(T)} d\varepsilon_c \,. \tag{4.9}$$

For the determination of the combined creep-fatigue damage D the CF experiments on Alloy 617 heats conducted within the present research project as well as in previous activities have been analysed and the fatigue and creep damage fractions have been calculated. Fig. 4.27 shows the creep-fatigue damage interaction diagram with calculated D_f and D_c values for various CF experiments on Alloy 617 heats for different strain ranges, hold periods and temperatures. The calculated values of the creep-fatigue damage D are in the range of D=0.8-1.2. For the estimation of D_c a strategy similar to the generalised damage accumulation hypothesis has been followed, where the dissipated creep energy in the initial part of the relaxation phase has been attributed to the dissipated plastic energy. Thereby temperature specific stress levels have been estimated for Alloy 617, at which the association into fatigue and creep damage is separated. The investigation on the CF experiments conducted on Alloy 617 heats revealed these stress levels to be optimal in the range of 260 MPa for temperatures of 700°C and 230 MPa for 750°C respectively. Following this approach, the damage appearances of the CF experiments with hold periods ≤ 10 min and medium to large strain amplitudes were explainable, showing major transgranular cracking and no evidence of characteristic creep damage, see Fig. 4.27. This gives rise to the assumption that the deformation mechanisms during the relaxation phases for stresses above these transition levels are comparable to those apparent during plastic deformation, which are considered by the dissipated plastic energy exhaustion within the damage evaluation. The results of the damage assessment in Fig. 4.27 show the expected distribution, with increasing

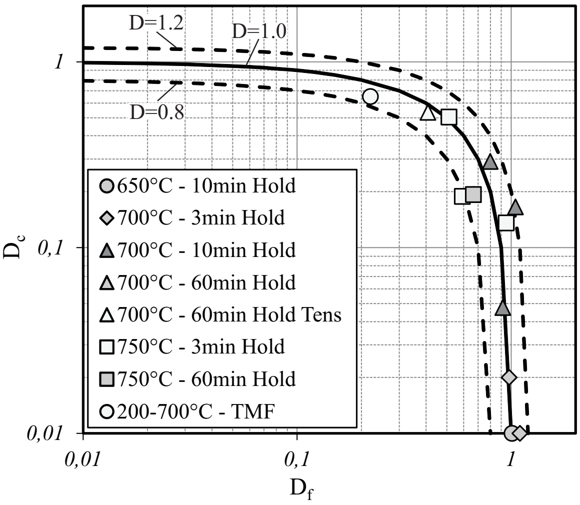

Figure 4.27: Calculated fatigue damage D_f and creep damage D_c fractions from various CF experiments for different strain ranges, hold periods and temperatures for investigated and reviewed Alloy 617 heats. Each symbol may comprise experiments with different strain amplitudes. For comparison the damage locus for D=0.8, 1.0, 1.2 are plotted also.

creep damage fraction with increasing hold duration and temperature and decreasing total strain range. With respect to normal experimental data scattering the adopted method of determination of creep-fatigue damage by consideration of dissipated plastic and creep energy for Alloy 617 seems to deliver sufficiently accurate results. Furthermore the calculated damage fractions correlate with the observations from metallurgical investigations performed on various test specimens. For the asymmetric hold experiment with 60 min hold duration in tension and $\Delta\varepsilon$=1.0, the calculated creep damage fraction of D_c=0.53 well corresponds to the damage appearance in the specimen, e.g. the percentage of cracked grain boundaries, see Fig. 4.12. For the symmetric hold experiments with 60 min hold duration in tension and compression at test temperatures of 700 and 750°C and $\Delta\varepsilon$=1.0 the calculated creep damage fractions are D_c=0.32 and D_c=0.23 respectively. The observed damage appearances in these specimens, see Fig. 4.11, show much less creep damage in the form of grain boundary cavitation and cracking, and primarily exhibit transgranular fatigue crack propagation.

In order to further verify the proposed creep-fatigue damage accumulation method, endurance curves for CF cyclic/hold experiments of Alloy 617 featuring 10 min and 60 min hold periods at peak strains in tension and compression for temperatures of 700 and 750°C have been calculated for mean creep-fatigue damage D=1.0. Fig. 4.28 shows the calculated CF endurances compared to experimental results obtained on various Alloy 617 heats. The cyclic endurances show a considerable hold time influence on the cyclic lifetime. For 700°C and 10 min hold durations the calculated cyclic endurance curve well represents the average experimental data, in particular with respect to heat specific scatter. For 60 min hold periods at 700°C only experimental evidence at large strain ranges can be used for verification. At test temperatures of 750°C the calculated endurances for 10 min hold durations exhibit a high quality fit to the experimental results for the whole strain range, whereas the same comments hold for experiments with 60 min hold compared to test temperature of 700°C. In Fig. 4.29 the creep-fatigue damage interaction diagram is plotted for the base points of the calculated cyclic endurance curves. For hysteresis with decreasing strain range and increasing hold duration, increasing creep dominated damage is predicted.

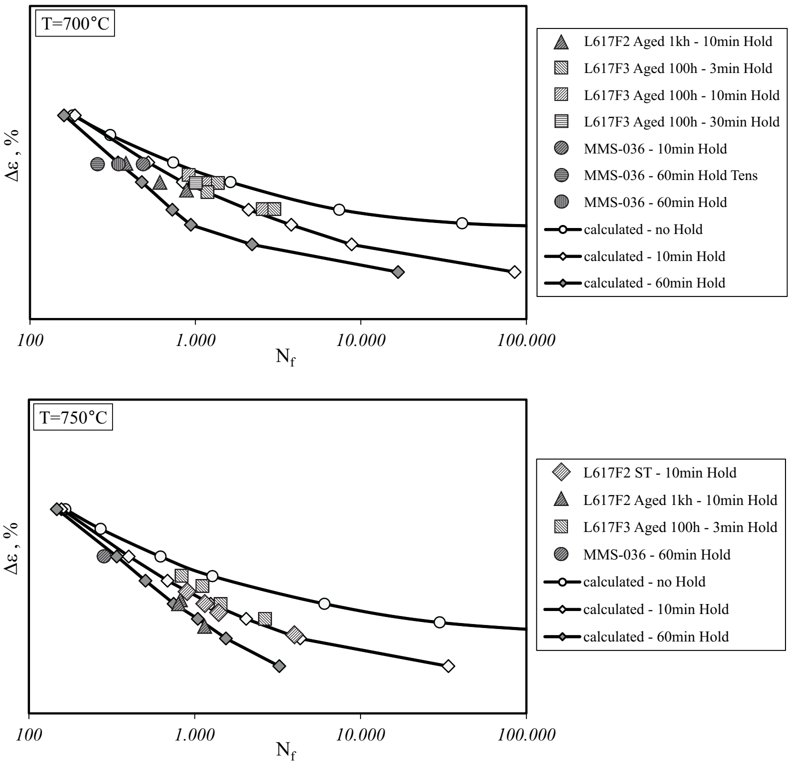

Figure 4.28: Calculated CF endurance curves for cyclic/hold experiments with 10 min and 60 min hold durations compared to experimental data of Alloy 617 heats at 700 and 750°C. The determined fatigue and creep damage fractions of the experimental data are shown in the associated damage interaction diagram Fig. 4.27.

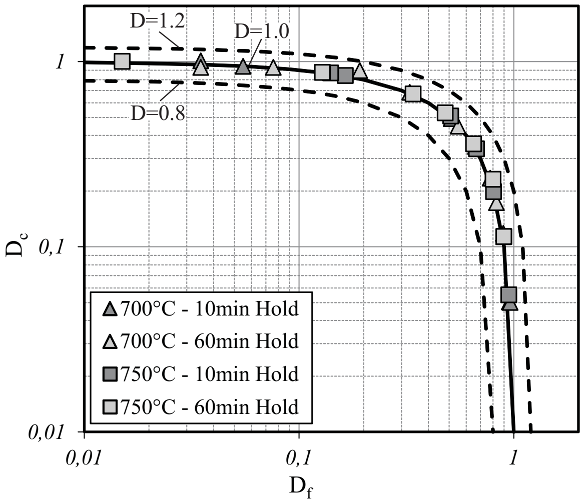

Figure 4.29: Calculated fatigue damage D_f and creep damage D_c fractions for estimated endurance curves for CF cyclic/hold experiments at various strain ranges with 10 min and 60 min hold duration at 700 and 750°C, see Fig. 4.28. Each symbol may comprise experiments with different strain amplitudes. For comparison the damage loci for D=0.8, 1.0, 1.2 are plotted also.

4.3 Lifetime Assessment of Alloy 617 Rotor Features

4.3.1 Thermo-mechanical Cycle Definition

One main objective of the present research project is the verification of the effectiveness of the developed analytical creep-fatigue lifetime assessment procedures with the results obtained from rotor-feature specimen thermo-mechanical fatigue tests, in which the consequential creep-fatigue damage is consistent with that which would be generated during service operation at critical locations of 700°C steam turbine rotors. In order to provide an optimum representation of the creep-fatigue damage, the rotor feature specimen design was to be determined to represent the surface and sub-surface stress-strain state at the life limiting steam turbine rotor location in a rigorous way. This was to be achieved by the determination of the profiles of the axial mechanical strain range $\Delta\varepsilon_m$, the multiaxiality factor H (2.30) or triaxiality factor $t_\sigma=\sigma_1/\sigma_e$ and the accumulated creep strain per cycle at and below the appropriate groove root surface. This method was successfully adopted during the steam turbine rotor-feature assessment for low alloyed 1-2% CrMoV as well as 9% Cr steel grades in preceding collaborative research projects between ALSTOM Power Switzerland and the Swiss Federal Laboratories for Materials Science and Technology EMPA and ETH Zurich respectively [20, 78].

To achieve an optimal service-cycle TMF feature-specimen representation, the assessment of target rotor features was necessary. Two candidate life limiting locations were identified at surface regions of a 700°C steam turbine rotor, both during start-up conditions. The most critical of these was to be assessed for standard start-up as well as start-up conditions with artificially increased heating gradients, and the results were to be compared with those of various configurations of candidate circumferential notched round tensile (CNRT) specimen subjected to service-type TMF cycles. The proposal for the service-cycle TMF benchmark test was for a crack initiation endurance to be of the order of 4-6 weeks, and for this a strain range $\Delta\varepsilon=1.0\%$ was judged to be required. In order to achieve such strain amplitude conditions in a way which was representative of service operation, a rotor simulation was performed assuming artificially increased heating rates throughout the entire start-up thermal transient. A corresponding rotor simulation has been performed for this operation cycle in order to determine the loading conditions at the critical location of the 700°C steam turbine rotor. Fig. 4.30 shows the resulting mid-life cycle stress-strain hysteresis loop and the transient temperature and mechanical strain profiles. In order to comply with the requirement on the overall test duration the transients of mechanical strain and temperature evolutions had to be adapted to laboratory testing conditions and a start-up service-type TMF cycle shape featuring artificially increased heating rates had been formed, which is presented in Fig. 4.31. Thereby it was attempted to

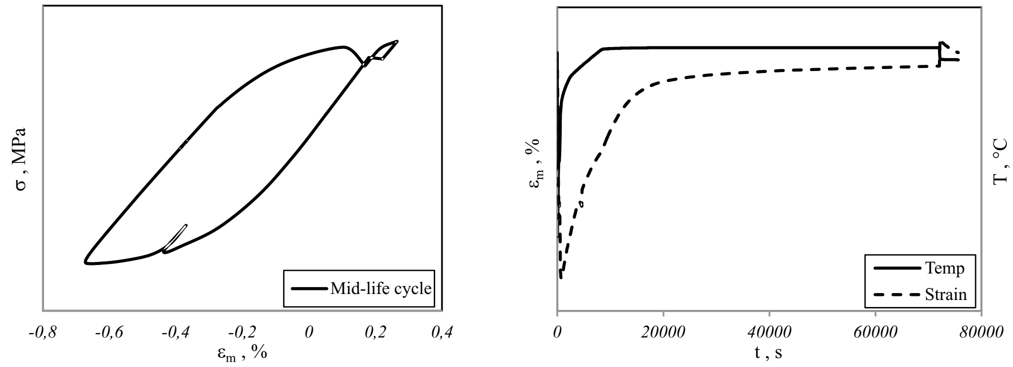

Figure 4.30: Loading conditions at critical location of 700°C steam turbine rotor during fast warm start scenario: (a) Stress-strain hysteresis loop for mid-life cycle, (b) Mechanical strain and temperature profiles

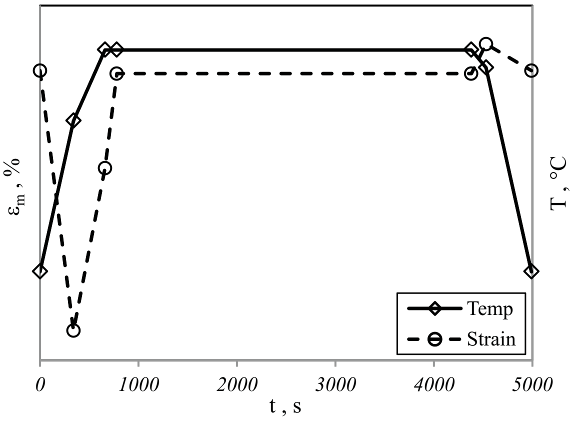

Figure 4.31: Cycle shape adopted to represent service conditions in service-cycle TMF benchmark test. The mechanical strain and temperature profiles represent fast warm start conditions for the critical location of the 700°C steam turbine rotor.

adopt the heating rates and mechanical strain rates during heating and cooling phases consistent with the conditions at the surface of the 700°C steam turbine rotor. A hold period of 1 h at maximum temperature in the cycle, at peak strain in tension, was adopted to represent the steady state phase during operation, recognising that in practice this would last for at least 16 h. For the definition of the TMF rotor feature specimen geometry representative of the surface and sub-surface stress-strain state of the critical location of the 700°C steam turbine rotor a parametric study has been performed to identify the optimal geometry of the CNRT specimen. The methodology adopted to devise the component-feature representative specimen geometry was similar to the one proposed earlier by RADOSAVLJEVIC ET. AL. [78, 79]. Fig. 4.32 shows the example of an axialsymmetric FE model of such a CNRT specimen with notch radius R. During simulation the displacement of the nodes in the upper loading plane are controlled in such a way to impose the desired deformation in the elements in the notch root. The calculated results for the evolutions of equivalent mechanical strain range and triaxiality factor dependent on the distance from notch root surface for the steam turbine rotor groove and for various CNRT geometries are shown in Fig. 4.33.

Generally the surface gradient at the surface region of the critical location of the 700°C steam turbine rotor is comparatively small, with the equivalent mechanical strain range reducing only minor sub-surface. A CNRT geometry with a considerable large radius of R=40 mm best represents these sub-surface conditions. Furthermore the calculated triaxiality factor close to unity indicates that the stress-strain state in the surface and sub-surface region of the critical location is almost uniaxial, which is also best represented with very large CNRT notch radii. Consequently it was decided to perform the benchmark TMF service cycle rotor feature experiments on standard plain specimens, since the required CNRT notch radius would be so large, that the relative notch effect would be negligible with particular respect to the limited notched specimen diameter of approximately 10 mm. Experience on high-alloyed martensitic rotor steels shows a comparatively small notch effect, which is mainly attributed to early redistributions of the stress field in the notched region [84, 78, 79]. For Alloy 617 on the other hand, only experimental evidence on CNRT specimens would show the notch sensitivity of the material at high temperatures of 700°C. The high creep ductility of Alloy 617, see Fig. 4.5, is expected to be an indication of low notch sensitivity.

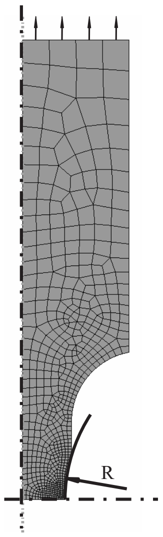

Figure 4.32: Axialsymmetric FE model of a circumferentially notched round tensile (CNRT) specimen with notch radius R

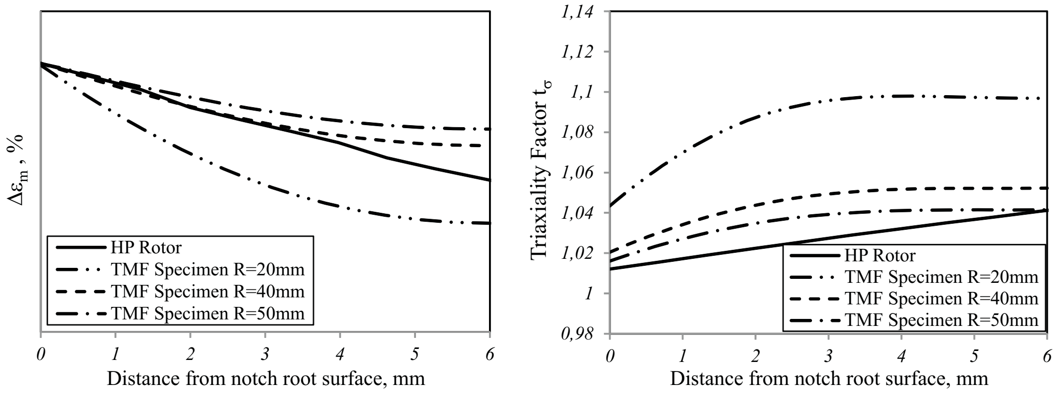

Figure 4.33: Comparison of stress-strain state criteria for 700°C steam turbine rotor feature and different CNRT specimen geometries: (a) Equivalent mechanical strain range and (b) Triaxiality factor depending on the distance from notch root surface. Concept similar to [78, 79].

4.3.2 Service Cycle TMF Testing

With the definition of the service-type TMF benchmark cycle, see Fig. 4.31, a strain-controlled TMF experiment has been conducted on Alloy 617 using the plain short standard LCF/TMF test specimen geometry, see Fig. A.1. Thereby significant effort was spent on complying with the recommendations of the code of practice on TMF testing [35], which is based on TMF testing experience of some 20 European material testing laboratories involved within the TMF standardisation project. Particular attention has been made to the accuracy of dynamic temperature measurement and control, to permissible deviations from nominal temperature profiles and to temperature gradients along the specimen gauge length. As described in section 3.2.1, the observation of the specimen temperature profile has been accomplished by attaching one control thermocouple in the centre and 2 thermocouples at the outer sections of the gauge length of the specimen. With respect to the moderate cooling rates of the service-type TMF cycle there was no need to use forced air cooling, since the impact of convective specimen cooling and the heat transfer through the specimen into the cooled grips of the testing machine was sufficient.

In Fig. 4.34 a the cyclic hardening characteristics of the service-type TMF experiment, e.g. the tensile and compressive peak stress profiles as well as the evolution of the relaxed stress at the end of the hold period, is presented. Similar to the hardening characteristics observed in isothermal CF cyclic/hold experiments on Alloy 617, see Fig. 4.10, the material shows initial hardening early in life followed by subsequent softening of the tensile stress. The relaxed stress evolution shows a similar decrease in creep resistance respectively. In Fig. 4.34 b the first cycle and mid-life cycle hysteresis of the service-cycle TMF experiment are presented, showing the hardening of the compressive peak stress and almost identical values

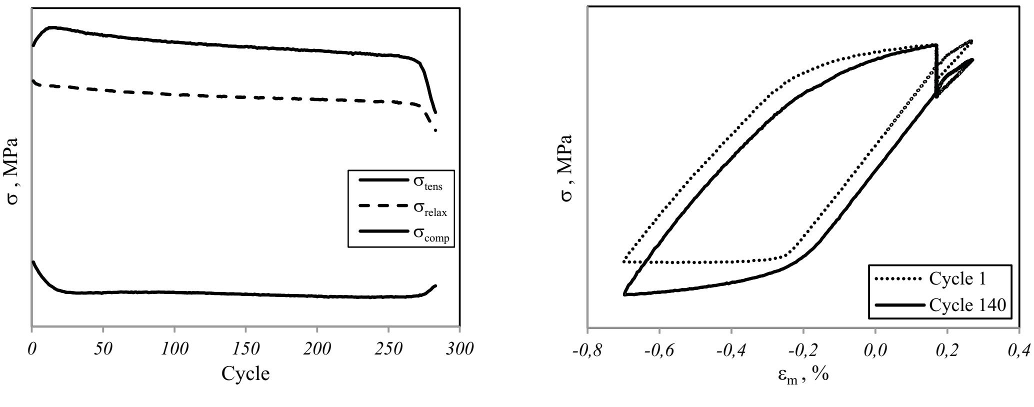

Figure 4.34: Cyclic hardening shown in peak stress profiles (a) and hysteresis loop for first and mid-life cycle (b) of Alloy 617 heat MMS-036 - TMF test: T=200-700°C, $\Delta\varepsilon_t$=1.0%

of the peak tensile stress.

The metallurgical investigations conducted on the service-type TMF cycle specimen reveal clearly highly creep-dominated creep-fatigue cracking. Fig. 4.35 shows the damage appearance for a specimen surface region and in the interior of the specimen respectively. Subjected to TMF loading with a temperature transient between 200 and 700°C, a mechanical strain range of $\Delta\varepsilon_m = 1.0\%$ and a 1 h hold period at peak strain in tension at maximum temperature, induced damage is predominantly and dramatically intergranular. Creep damage associated with creep cavitation and grain boundary cracking is observed at preferably oriented grain boundaries in the entire specimen cross-section similar to specimens of creep rupture experiments, Fig. 4.5, and CF specimen with asymmetric hold period in tension, Fig. 4.12.

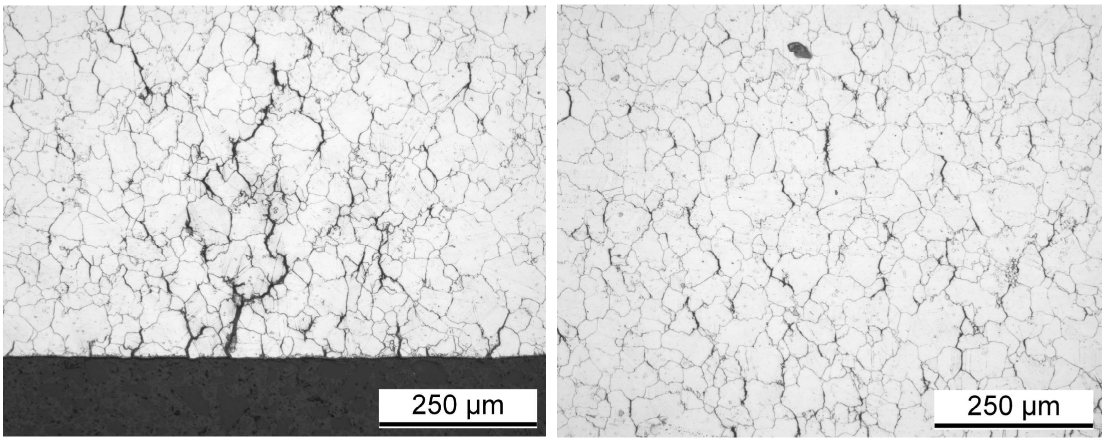

Figure 4.35: Damage appearance in service cycle TMF test of Alloy 617 heat MMS-036: (a) Intergranular cracking due to creep-fatigue damage at specimen surface, (b) Creep damage in the interior of the specimen

For the determination of creep and fatigue damage fractions and the resulting combined creep-fatigue damage, the service-type TMF mid-life cycle has been simulated using the constitutive deformation model described in section 4.2. Thereby, in contrast to the calculated hysteresis of CF cyclic/hold experiments, the Chaboche cyclic plasticity model parameters derived for continuous cycling LCF experimental data have shown to best represent the measured data. Fig. 4.36 presents a comparison of measured and calculated service-type TMF mid-life cycle data, e.g. the stress-strain hysteresis, the transient stress profile, the mechanical strain and temperature profiles. For the incorporation of reduced creep resistance due to plastic deformation into the Graham-Walles creep law (4.4) a correction factor Z_c consistent with the trend shown in Fig. 4.24 and the accordant fitting function (4.5) has been adapted. As mentioned earlier, the test control parameters ε_m and T are in strict accordance to the nominal profiles of the service-type TMF cycle,

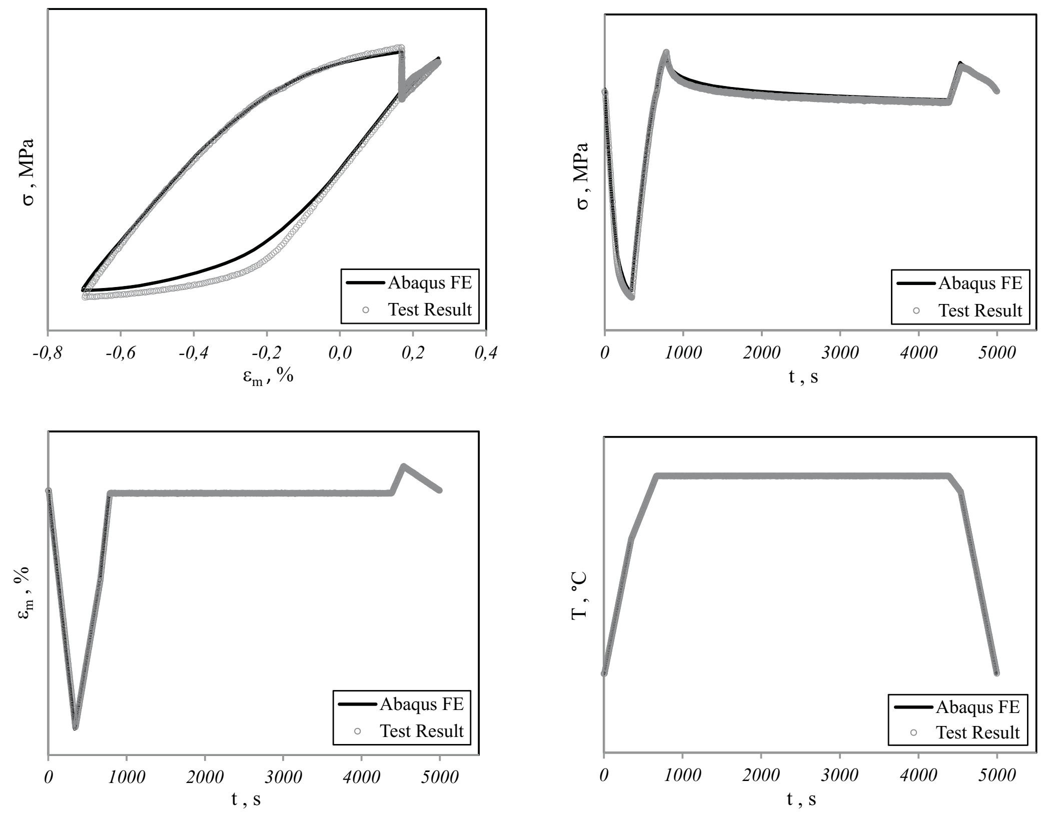

Figure 4.36: Comparison of measured and calculated TMF mid-life cycle parameters: (a) Stress-strain hysteresis, (b) Stress profile, (c) Mechanical strain profile, (d) Temperature profile

see Fig. 4.36 c,d. Especially the moderate heating and cooling rates in the range of 1°C/s clearly have a beneficial effect in order to comply with the TMF testing recommendations [35]. The calculated stress response of the mid-life cycle shows, except for small deviations in the compression going branch during heating up of the TMF cycle, a very good correspondence to the measurements, see Fig. 4.36 a,b. Especially the material response in the tension going part of the hysteresis, the stress relaxation during the hold period and the shut down phase of the TMF cycle are well represented by simulation. This is of particular importance, since it verifies the effectiveness of the constitutive deformation model of Alloy 617 in terms of significantly different mechanical strain rates of the service-type TMF experiment compared to those applied in standard LCF/CF tests.

For the determination of the fatigue damage fraction D_f (4.6), the advantages of the definition of the fatigue damage as ratio of dissipated plastic energy W_{pl} and critical dissipated plastic energy $W_{pl,crit}(T)$ (4.1) for fatigue failure can be exploited. Since the incremental damage during the anisothermal cycle can be calculated with the estimation for $W_{pl,crit}(T)$, the definition of a reference temperature is unnecessary. Such a reference temperature T_{ref} would have to be defined for anisothermal loading conditions when using the conventional approach in determining the fatigue damage fraction as accumulation of cycle ratios $N_i/N_{fi}(T_{ref})$ (2.35). The creep damage fraction D_c (4.7) is respectively defined as the ratio of dissipated creep energy W_c and critical dissipated creep energy $W_{c,crit}(T,\sigma)$ (4.8), which can be calculated incrementally for the anisothermal service-type TMF cycle accordingly. For the service-type TMF mid-life cycle, see Fig. 4.36, a fatigue damage fraction $D_f=0.22$ and a creep damage fraction $D_c=0.65$ have been determined, which is plotted in the creep-fatigue damage interaction diagram Fig. 4.27 in addition to the results of conventional CF cyclic/hold experiments for Alloy 617. The comparatively high value of D_c very well represents the observed damage appearance in the TMF specimen, see Fig. 4.35, which is clearly highly creep dominated and exhibits a large percentage of cracked grain boundaries. Thereby the calculated dissipated creep energy during the compressive phase of the cycle has been attributed to the dissipated plastic energy, since compressive stress states are expected not to contribute to the observed creep damage evolution but certainly have to be considered as dissipated plastic energy associated with fatigue damage, in particular at the prevailing stress levels. The calculated moderate fatigue damage fraction of $D_f=0.22$ also well represents the conditions observed during microstructural investigation of the service-type TMF specimen, which entirely shows intergranular creep-fatigue cracking along creep damaged grain boundaries. An explanation for the relatively small calculated fatigue damage is constituted by the fact, that a major part of plastic deformation in the compressive phase during start-up is performed at moderate temperatures below 500°C, where the corresponding critical dissipated plastic energy $W_{pl,crit}(T)$ exhibits larger values than for maximum cycle temperature, see Fig. 4.16.

With the performed service-type TMF experiment the effectiveness of the developed analytical creep-fatigue assessment procedures could be successfully verified. This benchmark test could prove the applicability of the constitutive deformation model for Alloy 617 for service-type operation conditions, with mechanical strain rates different from conventional experiments and under anisothermal conditions. Furthermore the effectiveness of the developed dissipated energy approach for determination of fatigue and creep damage fractions could be demonstrated, which very well corresponds to the observed damage appearance in the service-type TMF specimen.

A further method of verification of prediction method effectiveness is a comparison of predicted and experimentally observed number of cycles to crack initiation. In Fig. 4.37 the predicted and experimentally observed cycles to crack initiation are compared for the conducted service-cycle TMF experiment and various CF cyclic/hold experiments with different strain ranges and hold periods at various temperatures for investigated and reviewed heats of Alloy 617, see also Fig. 4.28. Thereby a mean creep-fatigue damage $D=1.0$ was assumed in the linear damage accumulation hypothesis, see eqn. (4.9), for the prediction of cycles to crack initiation. As shown in Fig. 4.37, the predicted and observed values for N_f correlate in a narrow band within $N_{f,pred}/N_{f,obs}=0.7$ and 1.3, which appears to be a very accurate prediction capability of the proposed dissipated energy failure criteria, with respect to normal scattering of experimental endurance data, in particular for different alloy heats.

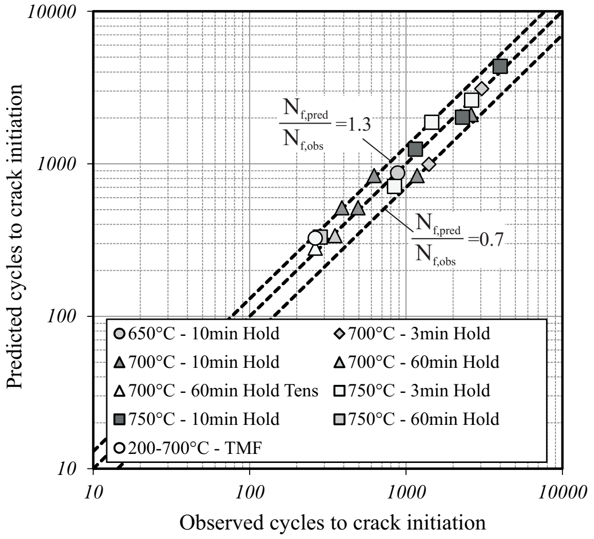

Figure 4.37: Comparison of predicted and experimentally observed cycles to crack initiation for the TMF experiment and various CF experiments with different strain ranges and hold periods at various temperatures for investigated and reviewed Alloy 617 heats. For comparison the locus for $N_{f,pred}/N_{f,obs}=0.7$, 1.3 are plotted also

Chapter 5

High Temperature Behaviour of Dissimilar Metal Welded Joints

This chapter covers the work performed on the second main objective of the present research project on the identification of the maximum application temperatures of dissimilar welded joints between the Ni-base Alloy 617 and a 1% CrMoV low alloy bainitic rotor steel as well as a higher alloyed 10% Cr martensitic rotor steel with respect to both their creep and creep-fatigue properties.

In the first part of this chapter the experimental results of the material testing campaign are presented. An overview is given on the material behaviour observed during CR experiments, continuous cycling LCF experiments as well as CF cyclic/hold experiments on both dissimilar metal welded joints. Concurrently the accordant damage and failure mechanisms occurring in the DMWs are discussed on the basis of post test metallurgical investigations.

The second part of this chapter contains an overview on the modelling activities of the observed DMW joint behaviour. The model equations for endurance properties under cyclic loading conditions are presented as well as for creep rupture properties under static loading conditions for both DMW joints. Subsequently the creep-fatigue interaction mechanisms are discussed with the help of results obtained during post-test metallurgical investigations on DMW CF test specimens. Finally recommendations are given on the maximum application temperatures of both DMW joints on the basis of the obtained test results and evidence from post-test microstructural observations.

5.1 Experimental Determination of Material Behaviour

5.1.1 Creep

For the determination of creep rupture strength properties and for identification of the prevailing damage mechanisms creep rupture experiments have been conducted on the Alloy 617 - 1% CrMoV (MMS-069) and Alloy 617 - 10% Cr (MMS-052) DMW joints at target temperatures, which have been determined on experience on accordant similar metal welds of the corresponding steels. Details on the applied CR testing procedure and the DMW cross-weld specimen geometry arrangement are given in section 3.2.2 of the document.

Alloy 617 - 1% CrMoV

For the Alloy 617 - 1% CrMoV DMW joint creep rupture experiments at temperatures 500, 525 and 550°C have been conducted. The stresses have been selected on the basis of experience on similar 1% CrMoV weldments and with the requirement of creep rupture times of maximum 4000-5000 h, since the limited research project duration and testing capabilities did not allow for longer testing times. Based on information of the prevailing damage mechanisms and fracture locations, obtained from laboratory cross-weld specimens, estimations for the maximum application temperatures of the DMWs were to be estimated.

Due to the fact that only the total elongation of the cross-weld specimen could be measured, nominal displacement values constitute integral measures over the whole specimen gauge length, see Fig. 3.4. For this reason and in order to account for local creep strain accumulation, the reduction of area measures Z_u of the fracture surface have been determined. The creep rupture ductilities of the Alloy 617 - 1% CrMoV DMW joint are considerably low, indicating brittle like creep rupture behaviour of the welded joint. Also the integral creep displacement data exhibit only very small values due to creep strain localisation within the steel HAZ. The total elongation of the specimen featuring a 60 mm gauge length were only in the range of 0.2-0.6 mm, and hence the equivalent integral strains provide inadequate measures for characterisation of the inhomogeneous creep strain distribution along the DMW cross-weld specimen gauge length.

Fig. 5.1 shows the micrographs of Alloy 617 - 1% CrMoV DMW creep rupture specimen, tested at a temperature of T=500°C and a stress of σ=240 MPa. The specimen section has been etched with a 2% Nital solution [1], leading to the desired etching of the 1% CrMoV steel but leaving the Ni-base Alloy 617 unaffected. Creep failure at these loading conditions occurred predominantly from the speci-

---

[1] The composition of the Nital etchant is: 2 ml HNO_3, 100 ml C_2H_5OH

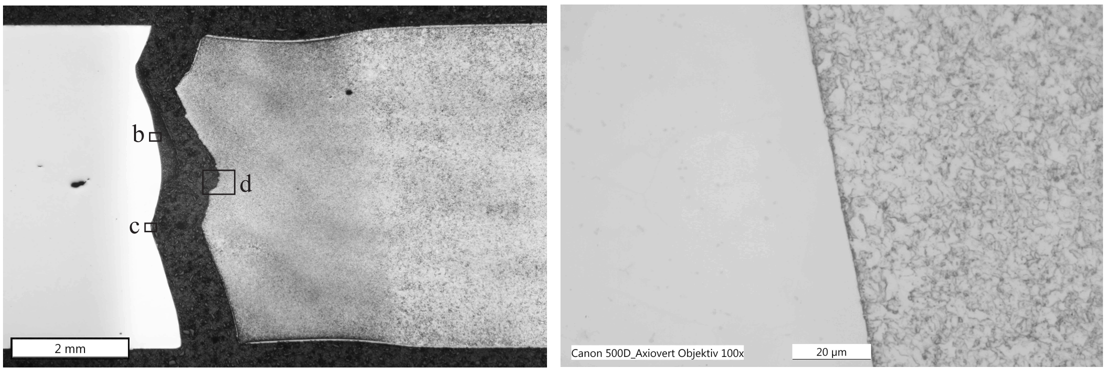

(a) Macroscopic view on the ruptured specimen cross section indicating positions of detailed micrographs

(b) Type I carbide formation in 1% CrMoV steel adjacent to interface between Alloy 617 weld metal and steel

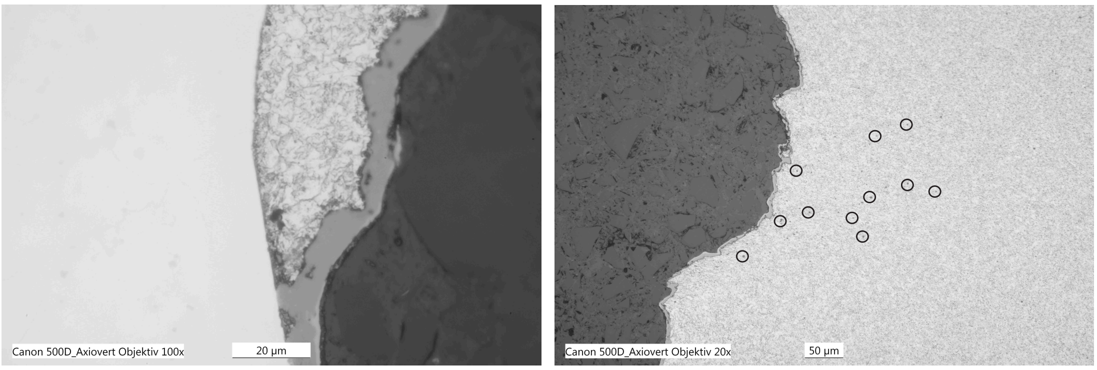
Canon 500D_Axiovert Objektiv 100x
20 µm
Canon 500D_Axiovert Objektiv 20x
50 µm

(c) Interface cracking adjacent to Type I carbide layer

(d) Creep cavitation in 1% CrMoV steel FGHAZ in the centre of the specimen

Figure 5.1: Micrographs of Alloy 617 - 1% CrMoV DMW creep rupture specimen: T=500°C, σ=240 MPa, t_u>1000 h

men surface at the fusion line between Alloy 617 weld metal and the 1% CrMoV steel HAZ and is associated with Type I precipitate formation, see Fig. 5.1 b,c. The Type I carbide precipitate condition is already existing after PWHT and relatively short duration testing at the steel side of the fusion line and forms a layer with the width of only a few μm. This was despite high local creep deformation and gauge section reduction associated with the FGHAZ. The location of final rupture was provided by subsurface creep cavity formation in the FGHAZ at the specimen axis, whereas at a test temperature of T=500°C only a small creep cavity density has been observed, see Fig. 5.1 d. The apparent Type I carbide formation in the 1% CrMoV steel adjacent to the interface is very similar to that observed by Nicholson [65, 66] in dissimilar metal welds between a 2% CrMo steel and Inconel 182 weld metal.

The micrographs of the damage appearance of Alloy 617 - 1% CrMoV DMW cross-weld CR specimen tested at T=550°C and σ=140 MPa are shown in Fig. 5.2. These loading conditions result basically in similar creep failure mechanism, but due to the increased temperature a significantly larger content of creep cavity formation was observed in the axis centre of the specimen, see Fig. 5.2 c,d, despite of a comparatively short creep rupture time of ~1000 h. The shown creep damage appearances in Fig. 5.1 and 5.2 are representative for all the conducted creep rupture experiments on the Alloy 617 - 1% CrMoV DMW joint. Fig. 5.3 gives an overview about the experimental determined creep rupture strength of the Alloy 617 - 1% CrMoV DMW joint (MMS-069).

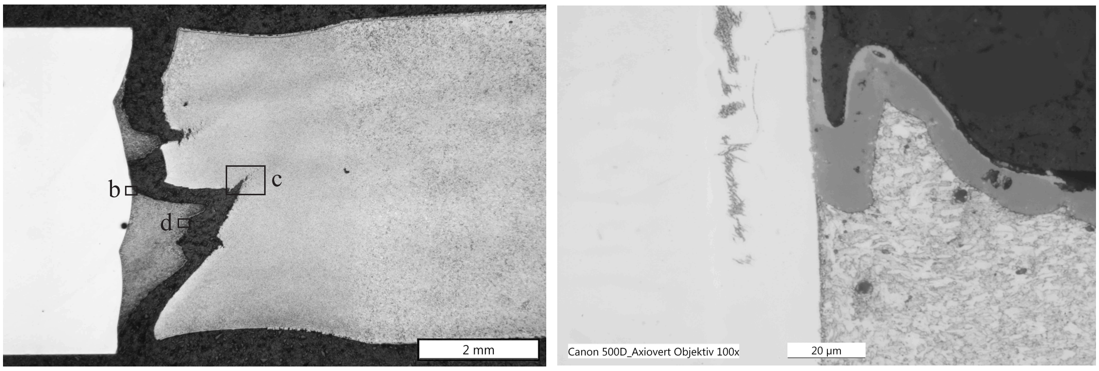

(a) Macroscopic view on the ruptured specimen cross section indicating positions of detailed micrographs

(b) Interface cracking adjacent to Type I carbide layer at interface between Alloy 617 weld metal and 1% CrMoV steel

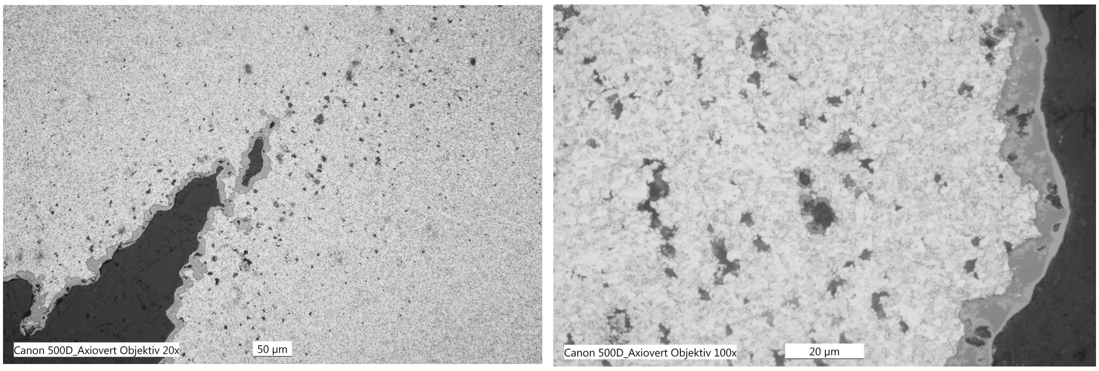
Canon 500D_Axiovert Objektiv 20x
50 µm
Canon 500D_Axiovert Objektiv 100x
20 µm

(c) Creep damage appearance in the FGHAZ of the 1% CrMoV steel in the centre of the specimen

(d) Creep cavitation and cracking in 1% CrMoV steel FGHAZ close to fracture surface

Figure 5.2: Micrographs of Alloy 617 - 1% CrMoV DMW creep rupture specimen: T=550°C, σ=140 MPa, t_u ~1000 h

Alloy 617 - 10% Cr

For the Alloy 617 - 10% Cr DMW joint, creep rupture experiments at temperatures 550, 575 and 600°C have been conducted. The stresses have been selected

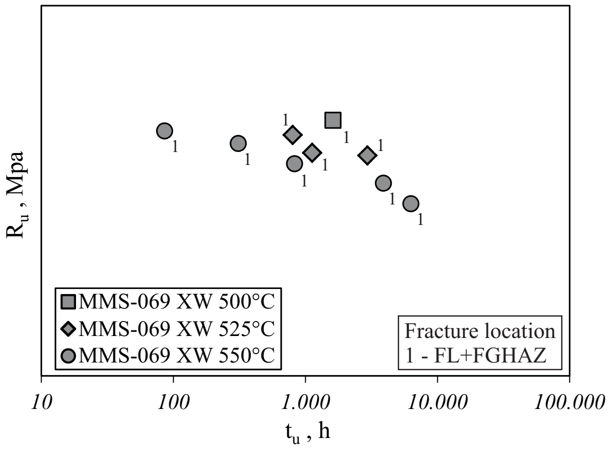

Figure 5.3: Creep rupture strength of Alloy 617 - 1% CrMoV DMW joint (MMS-069). Numbers to the symbols indicate creep failure location.

on the basis of experience on similar 10% Cr weldments and with the requirement of creep rupture times of maximum 4000-5000 h, since the limited research project duration and testing capabilities did not allow for longer testing times. The reduction of area measures Z_u indicate the same low ductility creep failure mechanisms observed for the Alloy 617 - 1% CrMoV DMW joint, whereas short duration creep rupture experiments exhibit higher ductilities, suggesting a possible change in the prevailing damage mechanism. Fig. 5.4 shows the micrographs of Alloy 617 - 10% Cr DMW cross-weld creep rupture specimen tested at T=550°C and σ=250 MPa. For the higher alloyed 10% Cr martensitic steel the etchant V2A[2] has been used, which also has been applied to etch the Ni-base Alloy 617, but with considerable less exposure time, resulting again in unaffected Alloy 617 parts

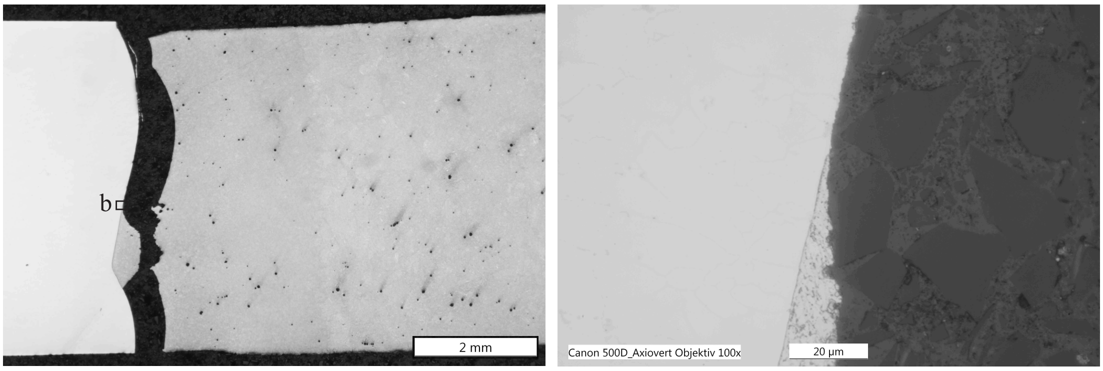

(a) Macroscopic view on the ruptured specimen cross section indicating positions of detailed micrographs

(b) Interface cracking adjacent to Type I carbide layer at interface between Alloy 617 weld metal and 10% Cr steel

Figure 5.4: Micrographs of Alloy 617 - 10% Cr DMW creep rupture specimen: T=550°C, σ=250 MPa, t_u ~6000 h

of the specimen section. Creep failure at these loading conditions occurred adjacent to the fusion line initiated at the specimen surface, see Fig. 5.4 a. It could not be verified if the interface cracking is associated with Type I carbide formation, because at these particular loading conditions at moderate temperatures of T=550°C this carbide formation was not clear from post-test inspection, see Fig. 5.4 b. From other experience on dissimilar metal welded joints it is possible to anticipate the appearance of Type I carbide formation at longer exposure times during high temperature duty [65, 66, 81]. The gauge section reductions associated with 10% Cr HAZ at Alloy 617 - 10% Cr DMW CR test specimens were not as pronounced as observed in corresponding Alloy 617 - 1% CrMoV DMW CR specimens, but were still a characteristic feature. Additionally at the moderate temperature of 550°C no visible creep damage in the form of cavity formation was observed in the 10% Cr steel HAZ.

---

[2] The composition of the V2A etchant is: 100 ml HCl, 10 ml HNO_3, 100 ml H_2O and 0.3 ml Vogel's pickling inhibitor

For test conditions leading to shorter rupture times Alloy 617 - 10% Cr DMW CR test specimens show a different damage appearance. Fig. 5.5 shows the micrographs of Alloy 617 - 10% Cr DMW cross-weld creep rupture specimen tested at T=600°C and σ=180 MPa. Creep failure occurred consistently in the ICHAZ and over-tempered parent material (PM) of the 10% Cr steel, caused by creep cavity formation in these regions approximately 2 mm from the fusion line, see Fig. 5.5 c,d. The same failure location was observed for the high stress CR experiment at T=550°C and σ=300 MPa, indicating that the short term creep rupture properties and ultimately the tensile strength properties are determined by the ICHAZ/PM characteristics of the 10% Cr steel. The high temperature exposure to T=600°C for ~1000 h also lead to visible formation of Type I precipitates, which were observed for a CR test specimen adjacent to the fusion line, see Fig. 5.5 b. The Type I precipitate condition could not be detected for longer test conditions at this temperature, since creep failure occurred consistently along the fusion line and oxide formation at the fracture surface prevented clear identification.

Fig. 5.6 gives an overview about the experimental determined creep rupture strength data of the Alloy 617 - 10% Cr DMW joint (MMS-052). The locations of creep failure are also presented for each test specimen, indicating a shift of fracture location from ICHAZ/PM for short test durations to FL/FGHAZ failure and finally consistent FL cracking with increasing test duration, thereby not exhibiting Type IV creep damage. In contrast creep rupture in matching 9-12% Cr steel similar metal weldments typically occurs in the IC/FGHAZ for longer creep rupture times with significant Type IV damage. For lower stresses and longer creep rupture times respectively, comparable to service conditions of components containing dissimilar metal weldments, consistent FL cracking associated with Type I precipitates is expected.

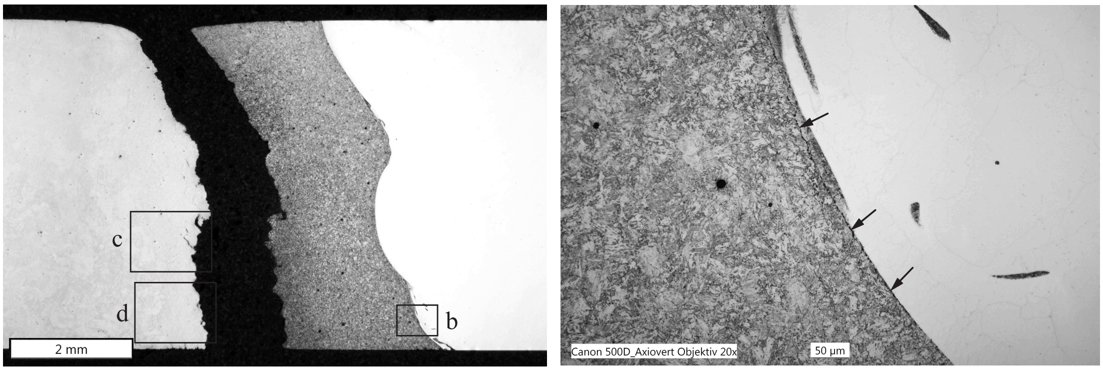
c
d
b
2 mm
Canon 500D_Axiovert Objektiv 20x
50 µm

(a) Macroscopic view on the ruptured specimen cross section indicating positions of detailed micrographs

(b) Type I carbide layer formation at interface between Alloy 617 weld metal and 10% Cr steel

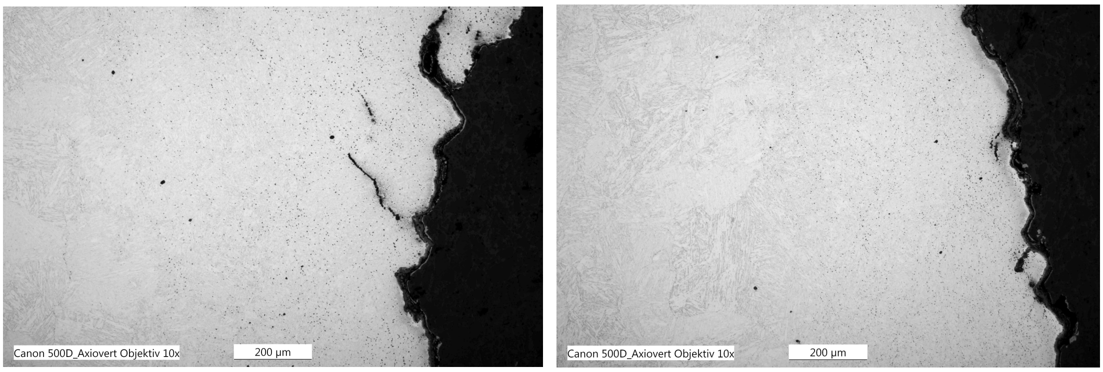
Canon 500D_Axiovert Objektiv 10x
200 µm
Canon 500D_Axiovert Objektiv 10x
200 µm

(c) Creep cavity formation and cracking in the HAZ of the 10% Cr steel in the centre of the specimen

(d) Creep cavity formation and cracking in the HAZ of the 10% Cr steel in the outer section of the specimen

Figure 5.5: Micrographs of Alloy 617 - 10% Cr DMW creep rupture specimen: T=600°C, σ=180 MPa, t_u ~1000 h

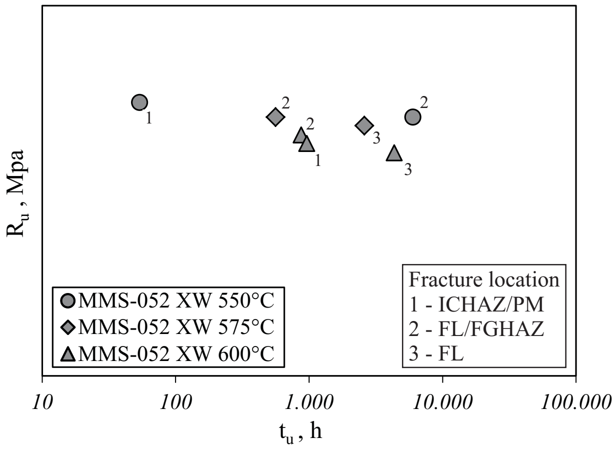

Figure 5.6: Creep rupture strength of Alloy 617 - 10% Cr DMW joint (MMS-052). Numbers to the symbols indicate creep failure location.

5.1.2 Low Cycle Fatigue

Low cycle fatigue experiments without hold periods have been conducted on cross-weld specimens extracted from the Alloy 617 - 1% CrMoV (MMS-069) and Alloy 617 - 10% Cr (MMS-052) DMW joints. The specimen geometry arrangement has been chosen in a way that the interface between the Alloy 617 weld metal and the steel HAZ coincides with the centre plane of the standard size specimen gauge length, see Fig. 3.2. The 20 mm parallel length of the specimen hence comprises Alloy 617 weld metal, the steel HAZ and parts of the steel parent material. During LCF testing of the cross-weld DMW joint specimens the integral strain along the 15 mm gauge length was controlled. For detailed information on the induction heating of the dissimilar metal joints, please refer to section 3.2.1. The continuous cycling LCF experiments were conducted in order to determine the LCF endurance characteristics and the prevailing damage mechanisms and locations of fatigue failure of the DMW joints.

Alloy 617 - 1% CrMoV

For the Alloy 617 - 1% CrMoV DMW joint continuous cycling LCF experiments have been conducted at temperatures of 500, 525 and 550°C and total strain ranges of $\Delta\varepsilon$ ~0.5, 1.0% with an applied strain rate of $\dot{\varepsilon}$=0.1%/s. During the course of LCF testing of the Alloy 617 - 1% CrMoV DMW joint it became obvious from a fractured cross-weld specimen that the tensile strength of the welded joint might be achieved during first cycle tensile loading. Hence, the tensile peak strain of the experiments with total strain range of $\Delta\varepsilon$=1.0% was set to 0.35% for the first 3 cycles, in order to prevent premature rupture. This was possible because of considerable cyclic softening early in life of the DMW joint during strain controlled LCF loading, which by example is presented in Fig. 5.7 for the LCF experiment with $\Delta\varepsilon$=1.0% at temperature T=500°C. Typically for particle strengthened fer-

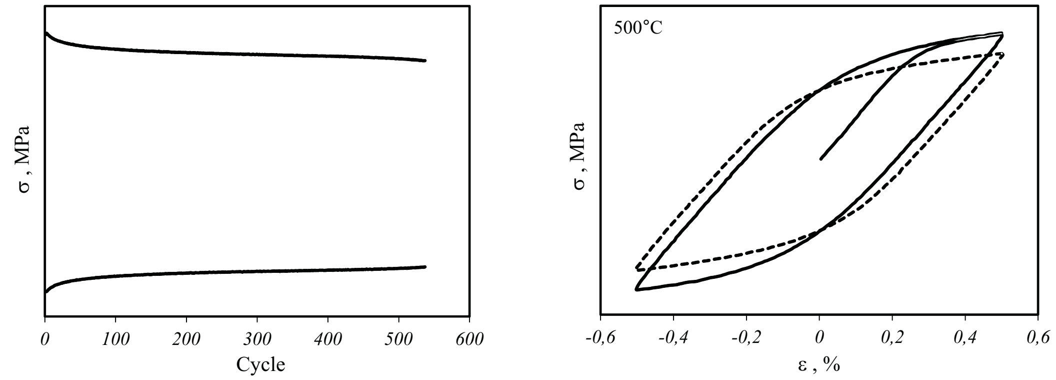

Figure 5.7: Cyclic softening shown in peak stress profiles (a) and hysteresis loops for first and mid-life cycles (b) of Alloy 617 - 1% CrMoV DMW (MMS-069) cross-weld joint - LCF test: T=500°C, $\Delta\varepsilon_t$ ~1.0%

ritic bainitic and martensitic steels, the peak stress profiles show cyclic softening behaviour, with fast decreasing peak stresses at the beginning of the experiment and following steady decline until macroscopic crack development. The first and mid-life cycle hysteresis show the corresponding shape for cyclic softening materials, see Fig. 5.7 b. The observed material response during Alloy 617 - 1% CrMoV DMW joint LCF testing is thereby almost exclusively controlled by the properties of the 1% CrMoV steel HAZ and parent material, since the Alloy 617 weld metal show firstly significantly larger yield strength at these temperatures and secondly a cyclic hardening characteristic. Hence it can be assumed that based on the test results the deformation of Alloy 617 weld metal is approximately elastic.

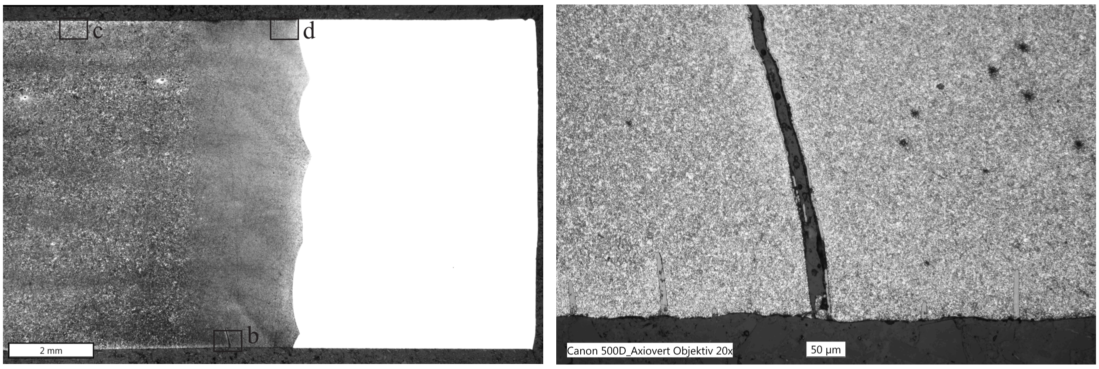

(a) Macroscopic view on the specimen cross section indicating positions of detailed micrographs

(b) Dominant and smaller fatigue cracks in the FGHAZ of the 1% CrMoV steel

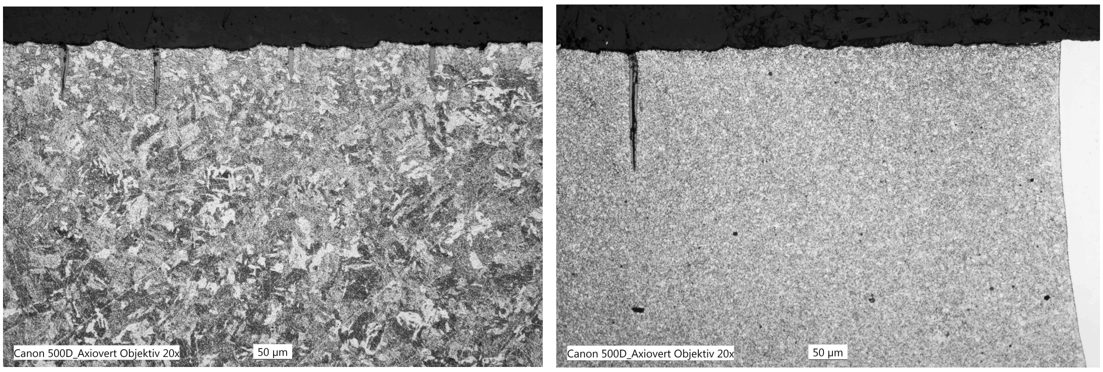
Canon 500D_Axiovert Objektiv 20x
50 µm
Canon 500D_Axiovert Objektiv 20x
50 µm

(c) Collection of small fatigue cracks in 1% CrMoV parent steel region

(d) FGHAZ fatigue crack and absence of Type I associated FL cracking

Figure 5.8: Micrographs of Alloy 617 - 1% CrMoV DMW joint LCF specimen: T=550°C, $\Delta\varepsilon \sim$1.0%, $N_{f2\%}$<1000 cycles

Fig. 5.8 shows the damage appearance in a specimen, tested at $\Delta\varepsilon \sim$1.0% and T=550°C. Fatigue failure was identified by dominant transgranular cracking in the FGHAZ of the 1% CrMoV steel, see Fig. 5.8 b. Thereby crack initiation was at the specimen surface in the FGHAZ region and subsequently crack propagation tended into the ICHAZ and over-tempered parent 1% CrMoV material, which was the tendency observed in all the LCF experiments conducted on the Alloy 617 - 1% CrMoV DMW joint. At these particular testing conditions, e.g. high temperature T=550°C and comparable high strain range $\Delta\varepsilon_t$ ~1.0%, collections of distributed small transgranular fatigue cracks were also observed in the parent 1% CrMoV steel section of the specimen, see Fig. 5.8 c. This gives rise to the assumption that fatigue endurance properties of parent 1% CrMoV steel are close to the Alloy 617 - 1% CrMoV DMW joint at these loading conditions. Furthermore no fusion line cracking associated with Type I precipitates was observed in continuous cycling LCF experiments, indicating that this cracking mechanism is almost entirely creep related, see Fig. 5.8 d. The experimental determined fatigue endurance data of the continuous cycling LCF experiments on the Alloy 617 - 1% CrMoV DMW joint are shown in Fig. 5.9.

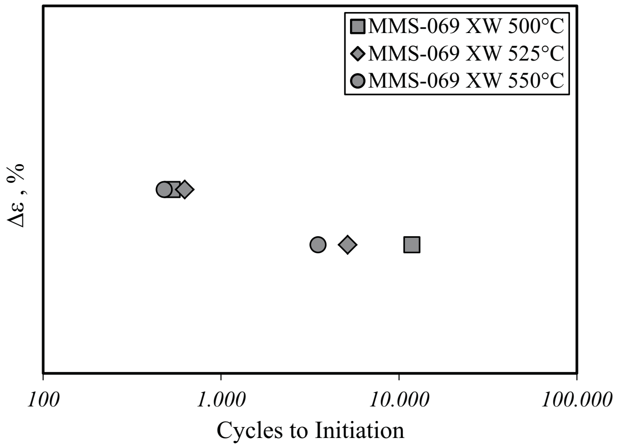

Figure 5.9: LCF experimental endurance data for Alloy 617 - 1% CrMoV DMW joint (MMS-069).

Alloy 617 - 10% Cr

For the Alloy 617 - 10% Cr DMW joint, continuous cycling LCF experiments have been conducted at temperatures of 550, 575 and 600°C and total strain ranges of $\Delta\varepsilon$ ~0.5, 0.7, 1.0% with an applied strain rate of $\dot{\varepsilon}$=0.1%/s. Similar to LCF testing of the Alloy 617 - 1% CrMoV DMW joint, experiments with $\Delta\varepsilon$ ~1.0% were driven to only 0.35% tensile strain for the first 3 cycles in order to prevent premature rupture. Cyclic softening observed during LCF testing of the Alloy 617 - 10% Cr DMW joint is presented by example for the experiment with total strain range of $\Delta\varepsilon$ ~0.7% at temperature T=600°C in Fig. 5.10. Similar to the softening characteristics of the DMW comprising low alloy bainitic steel 1% CrMoV, the Alloy 617 - 10% Cr DMW joint shows fast softening in the early stages of life and subsequent steady decline of the peak stresses until macroscopic crack development. Therefore it can be concluded that, similar to the Alloy 617 - 1% CrMoV DMW joint, the observed material response during Alloy 617 - 10% Cr DMW joint LCF testing is almost exclusively controlled by the properties of the 10% Cr steel HAZ and parent material sections contained within the DMW joint cross-weld

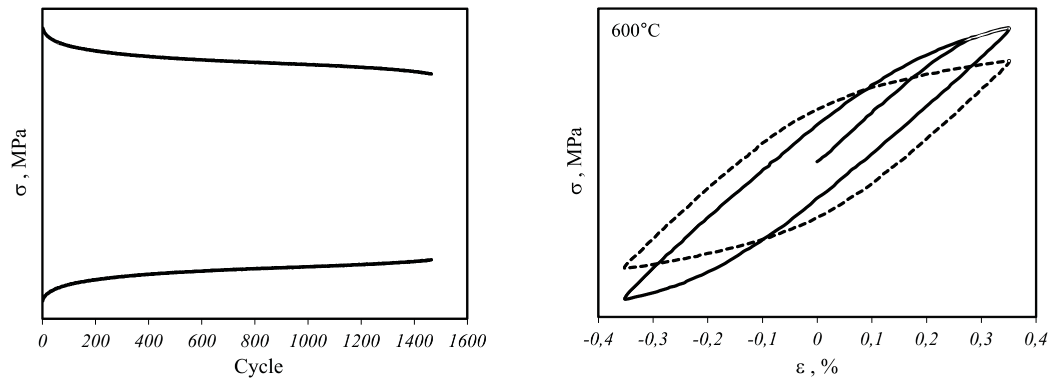

Figure 5.10: Cyclic softening shown in peak stress profiles (a) and hysteresis loops for first and mid-life cycles (b) of Alloy 617 - 10% Cr DMW (MMS-052) cross-weld joint - LCF test: T=600°C, $\Delta\varepsilon_t$ ~0.7%

specimen gauge length, with apparent elastic Alloy 617 weld metal deformation.

The fatigue damage appearance observed in Alloy 617 - 10% Cr DMW joint LCF testing is by example shown in Fig. 5.11 for a specimen tested at $\Delta\varepsilon$ ~0.5% and T=600°C. Fatigue failure is associated with dominant transgranular cracking in the ICHAZ of the 10% Cr steel, see Fig. 5.11 a,b. Simultaneously fatigue cracking was observed in the FGHAZ of the steel, closer to the weld interface, see Fig. 5.11 c. Furthermore transgranular fatigue cracking was observed also in the over-tempered parent 10% Cr material, even for experiments with comparable small strain ranges, see Fig. 5.11 d. This is in contrast to the Alloy 617 - 1% CrMoV DMW joint, where collections of distributed fatigue cracks were observed along the steel gauge section only at specimen tested at large strain ranges, see Fig. 5.8. Hence it can be concluded that the fatigue endurance properties of parent 10% Cr steel are close to the Alloy 617 - 10% Cr DMW joint, at least for the experimentally covered strain ranges. Similar to the Alloy 617 - 1% CrMoV DMW joint, there was no occurrence of FL cracking associated with Type I precipitate condition observed in continuous cycling LCF experiments on the Alloy 617 - 10% Cr DMW joint. The experimental determined fatigue endurance data of the continuous cycling LCF experiments on the Alloy 617 - 10% Cr DMW joint are shown in Fig. 5.12.

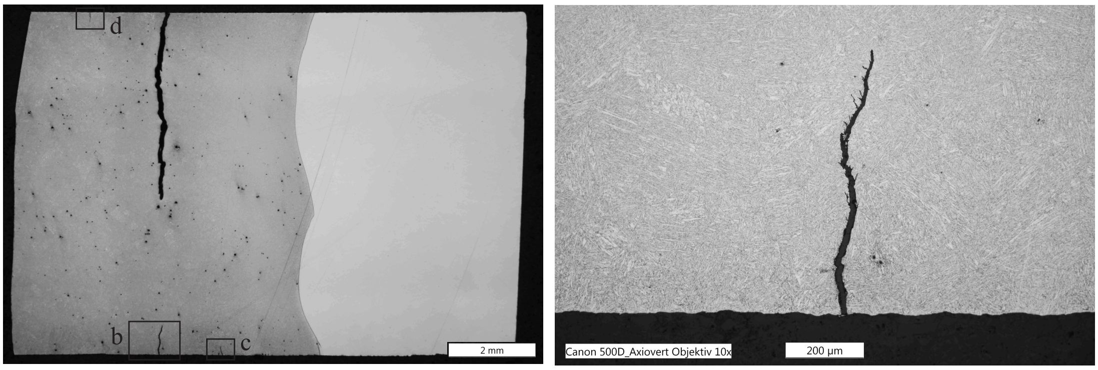
d
b
c
2 mm
Canon 500D_Axiovert Objektiv 10x
200 µm

(a) Macroscopic view on the specimen cross section indicating positions of detailed micrographs

(b) Fatigue crack analogical to dominant crack in the ICHAZ of the 10% Cr steel

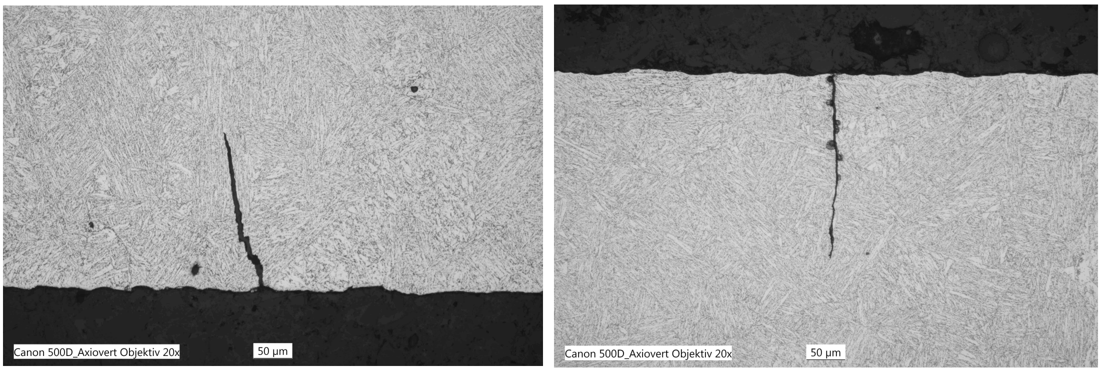
Canon 500D_Axiovert Objektiv 20x
50 µm
Canon 500D_Axiovert Objektiv 20x
50 µm

(c) Small fatigue crack in the FGHAZ of the 10% Cr steel

(d) Small fatigue crack in the over-tempered parent 10% Cr steel

Figure 5.11: Micrographs of Alloy 617 - 10% Cr DMW joint LCF specimen: T=600°C, $\Delta\varepsilon \sim 0.5\%$, $N_{f2\%} \sim 3000$ cycles

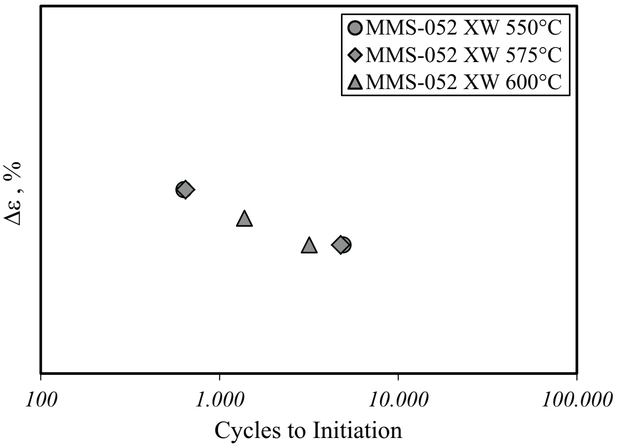

Figure 5.12: LCF experimental endurance data for Alloy 617 - 10% Cr DMW joint (MMS-052).

5.1.3 Creep-Fatigue

For investigation of the prevailing damage mechanisms under combined creep-fatigue loading, CF cyclic/hold experiments have been conducted on the Alloy 617 - 1% CrMoV (MMS-069) and Alloy 617 - 10% Cr (MMS-052) DMW joints. The test temperatures were identical to those applied in creep rupture and continuous cycling LCF experiments in order to ensure the classification of the creep and fatigue damage fractions under CF loading. The cross-weld specimen geometry arrangement was identical to those in continuous cycling LCF experiments and is explained together with the testing procedure in detail in section 3.2.1.

Alloy 617 - 1% CrMoV

For the Alloy 617 - 1% CrMoV DMW joint strain controlled CF cyclic/hold experiments have been conducted at temperatures of 500, 525 and 550°C and total strain ranges of $\Delta\varepsilon$ ~0.5, 0.7, 1.0% with an applied strain rate of $\dot{\varepsilon}$=0.1%/s. 20 min hold periods at peak strain in tension were included in order to account for creep loading and resulting creep damage development. The CF cyclic/hold experiments conducted on the Alloy 617 - 1% CrMoV DMW joint show, similar to continuous cycling experiments, considerable softening with fast decreasing peak stresses at the beginning of life and a steady decline until macroscopic crack development, see Fig. 5.13 by example for the experiment, tested with $\Delta\varepsilon$ ~0.7% at maximum test temperature T=550°C. Fig. 5.13 b shows the first cycle and mid-life cycle stress-strain hysteresis of the experiment accordingly. The shown cyclic softening behaviour in Fig. 5.13 is representative for all the CF cyclic/hold experiments performed on the Alloy 617 - 1% CrMoV DMW joint.

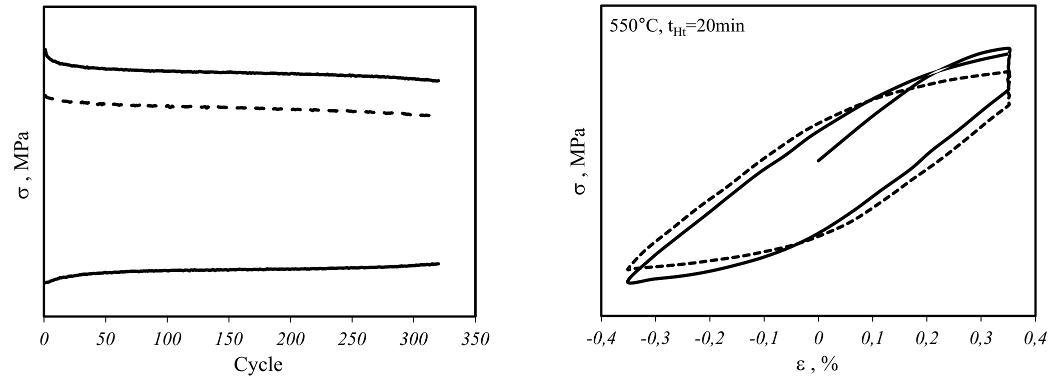

Figure 5.13: Cyclic softening shown in peak stress profiles (a) and hysteresis loops for first and midlife cycles (b) of Alloy 617 - 1% CrMoV DMW (MMS-069) cross-weld joint - CF cyclic/hold test: T=550°C, $\Delta\varepsilon_t$ ~0.7%, t_{Ht}=20 min

Fig. 5.14 shows the micrographs of Alloy 617 - 1% CrMoV DMW CF cyclic/hold test specimen, tested at T=550°C and $\Delta\varepsilon \sim 0.7\%$. The specimen exhibits significant gauge section reduction associated with high creep deformation in the 1% CrMoV steel HAZ. Originating from the surface, transgranular fatigue crack development was observed generally for CF experiments with comparable high strain ranges $\Delta\varepsilon \sim 0.7$, 1.0%, whereas at high temperatures T=550°C moderate creep cavity formation was apparent in the HAZ subsurface regions, see Fig. 5.14 b. Fig. 5.14 c represents the conditions at the dominant crack tip region close to the centre of the specimen, where a significant creep cavity density was observed. Although the crack initially appeared to be transgranular close to specimen surface, crack propagation was more creep dominated following creep damaged grain boundaries towards the centre region. In parallel, creep induced cracking associated with Type I precipitate condition at the interface between Alloy 617 weld metal and 1% CrMoV steel HAZ occurred, see Fig. 5.14 d. These cracks initiated

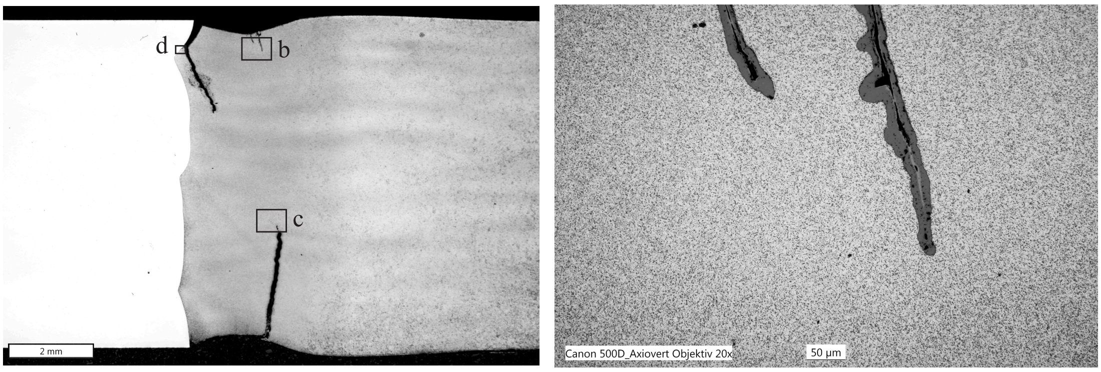

(a) Macroscopic view on the specimen cross section indicating positions of detailed micrographs

(b) Transgranular fatigue surface cracking in the FGHAZ of the 1% CrMoV steel

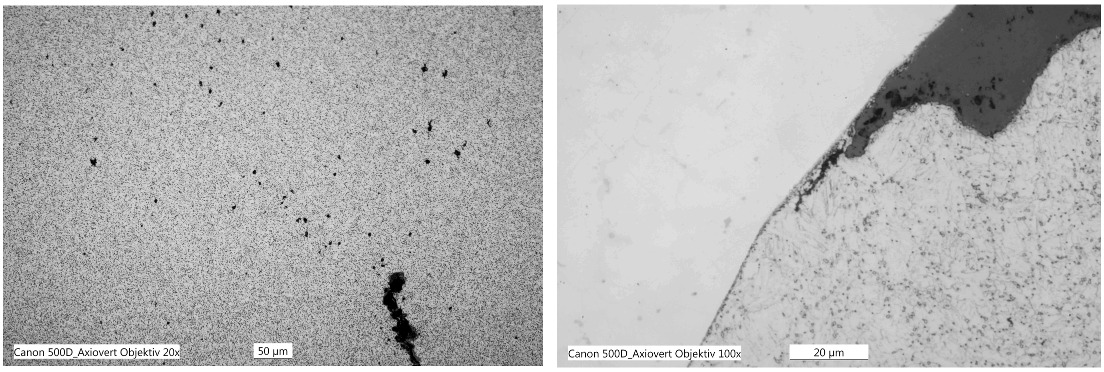
Canon 500D_Axiovert Objektiv 20x
50 µm
Canon 500D_Axiovert Objektiv 100x
20 µm

(c) Dominant fatigue crack tip region near the FG/ICHAZ centre of the specimen showing creep cavity formation

(d) FL cracking associated with Type I precipitates at interface between Alloy 617 weld metal and 1% CrMoV steel HAZ

Figure 5.14: Micrographs of Alloy 617 - 1% CrMoV DMW joint CF specimen: T=550°C, $\Delta\varepsilon \sim 0.7\%$, $N_{f2\%} \sim 300$ cycles

at the specimen surface and appeared to branch off into the 1% CrMoV CGHAZ region of the specimen. Furthermore Fig. 5.14 d shows the exact location of the interface cracking a few μm away from the Type I carbide layer just on the steel side, which is sometimes hard to identify due to formation of oxidation layers at the free fracture surface.

In Fig. 5.15 the damage appearance of Alloy 617 - 1% CrMoV DMW CF cyclic/-hold test specimen is presented, tested at T=550°C and $\Delta\varepsilon$ ~0.5%. Generally at CF cyclic/hold experiments with moderate strain ranges of $\Delta\varepsilon$ ~0.5% no crack initiation at the surface of the significant reduced gauge section region was observed, despite the fact that the apparent notched geometry would act as a stress raiser and encourage fatigue crack initiation. Similar to test specimen in Fig. 5.14 the damage appearance was twofold. FL cracking initiated on the entire circumference of the cross-weld specimen surface and occurred adjacent to a Type I carbide

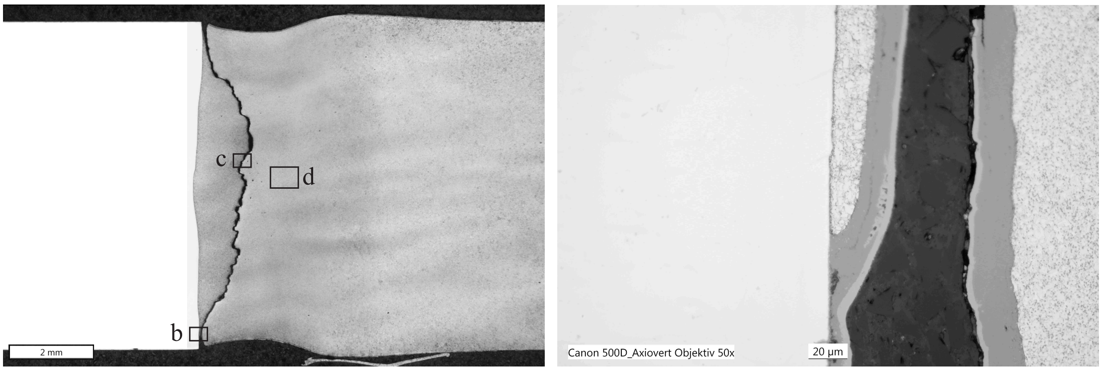

(a) Macroscopic view on the specimen cross section indicating positions of detailed micrographs

(b) FL cracking adjacent to Type I carbide layer at interface between Alloy 617 weld metal and 1% CrMoV steel HAZ

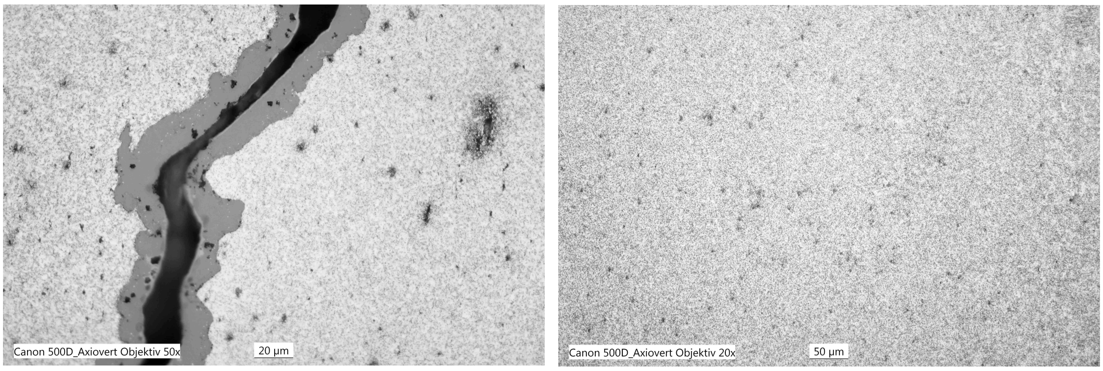
Canon 500D_Axiovert Objektiv 50x
20 µm
Canon 500D_Axiovert Objektiv 20x
50 µm

(c) Extensive creep cavity formation and cracking in the steel FGHAZ near fracture surface in the specimen centre

(d) Creep damage associated with cavity formation in the FG/ICHAZ of the steel in the specimen centre

Figure 5.15: Micrographs of Alloy 617 - 1% CrMoV DMW joint CF specimen: T=550°C, $\Delta\varepsilon$ ~0.5%, $N_{f2\%}$ ~700 cycles

layer between Alloy 617 weld metal and the steel HAZ. The cracks subsequently propagated into the 1% CrMoV CGHAZ, where significant creep damage in the form of extensive creep cavity formation and associated cracking was observed, see Fig. 5.15 c. The appearance of creep damage in the centre axis region of the specimen, see also Fig. 5.15 d for the FG/ICHAZ region, gives rise to the assumption that this apparent Type IV creep damage condition developed independent of the Type I associated creep cracking at the fusion line. This could not be definitely verified on the corresponding specimen in Fig. 5.15, since it was tested until rupture. The investigated creep damage appearance of the CF cyclic/hold experiment in Fig. 5.15 was entirely consistent with the one observed in a creep rupture specimen tested at an identical temperature with a comparable time to creep rupture, see Fig. 5.2. It should be noted, when comparing the respective micrographs, that different specimen gauge section diameter have to be considered, e.g. d=5.5 mm for CR cross-weld specimen and d=8.0 mm for LCF/CF cross-weld specimen.

Fig. 5.16 shows the damage condition of Alloy 617 - 1% CrMoV DMW CF cyclic/-hold test specimen, tested at T=500°C and $\Delta\varepsilon \sim 0.5\%$. This experiment has been stopped before rupture and hence the separate creep damage mechanisms could be investigated in more detail. Apparently the registered stress drop has been caused by the dominant FL crack adjacent to the interface between Alloy 617 weld metal and 1% CrMoV steel HAZ. The FL cracking occurred along the entire circumference of the cross-weld specimen and constitutes an obvious feature, see Fig. 5.16 b,e. Similar to the condition in Fig. 5.14,5.15 the FL crack subsequently propagated into the 1% CrMoV CGHAZ, where considerable creep damage in the form of creep cavity formation was observed, see Fig. 5.16 c. In parallel significant Type IV creep damage has been developed in the FGHAZ at the centre axis of the specimen, see Fig. 5.16 a,d. A dense field of single creep cavities and resulting creep cracking was apparent. This was in contrast to the damage appearance observed in creep rupture specimens at equal temperature and comparable creep rupture time, see Fig. 5.1, which showed only a minor amount of individual creep cavities in the CGHAZ close to the fusion line and apparently no visible Type IV creep damage in the FGHAZ of the 1% CrMoV steel.

The experimental determined cyclic endurance data of the CF cyclic/hold experiments with 20 min hold periods at peak strain in tension on the Alloy 617 - 1% CrMoV DMW joint (MMS-069) are shown in Fig. 5.17.

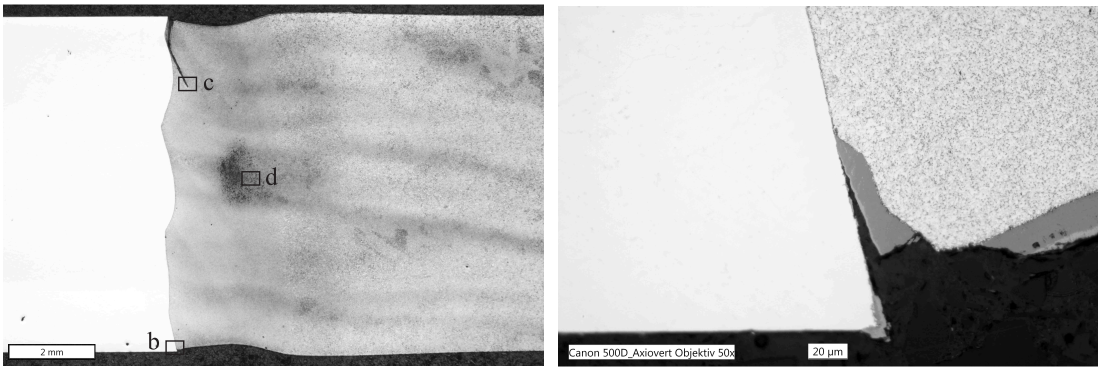
c
d
b
2 mm
Canon 500D_Axiovert Objektiv 50x
20 µm

(a) Macroscopic view on the specimen cross section indicating positions of detailed micrographs

(b) Fusion line cracking adjacent to Type I carbide layer at interface between Alloy 617 weld metal and 1% CrMoV steel HAZ

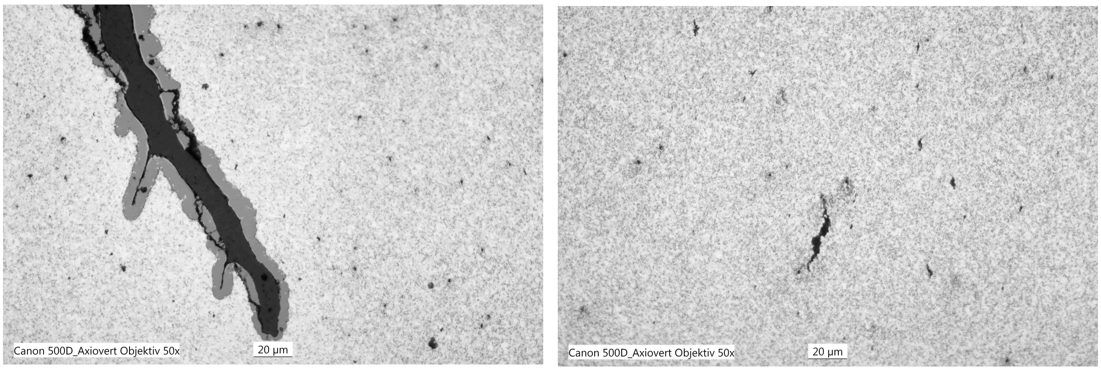
Canon 500D_Axiovert Objektiv 50x
20 µm
Canon 500D_Axiovert Objektiv 50x
20 µm

(c) FL crack branches off into creep damaged CGHAZ/FGHAZ of the 1% CrMoV steel

(d) Creep damage associated with cavity formation and cracking in the FGHAZ of the steel in the specimen centre

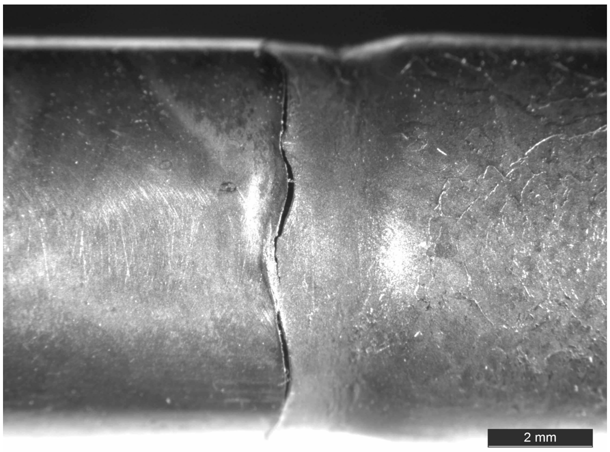

(e) Circumferential FL cracking of the specimen after testing and before section cutting

Figure 5.16: Micrographs of Alloy 617 - 1% CrMoV DMW joint CF specimen: T=500°C, $\Delta\varepsilon \sim 0.5\%$, $N_{f2\%} > 1000$ cycles

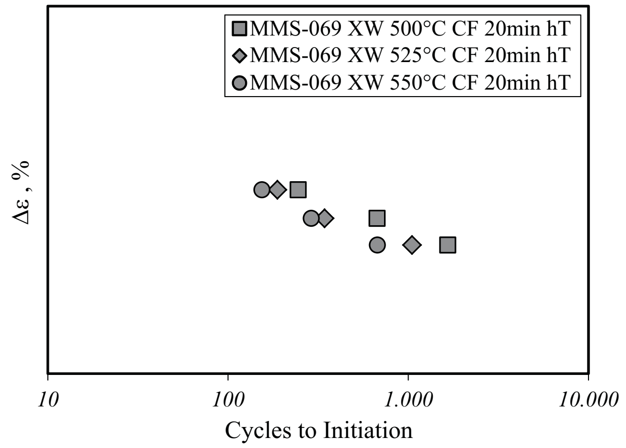

Figure 5.17: Experimental CF cyclic/hold endurance data for Alloy 617 - 1% CrMoV DMW joint (MMS-069). The cycles included 20 min hold periods at peak strain in tension.

Alloy 617 - 10% Cr

For the Alloy 617 - 10% Cr DMW joint, strain controlled CF cyclic/hold experiments have been conducted at temperatures of 550, 575 and 600°C and total strain ranges of $\Delta\varepsilon$ ~0.5, 0.7, 1.0% with an applied strain rate of $\dot{\varepsilon}$=0.1%/s. 20 min hold periods at peak strain in tension were included in order to account for creep loading and resulting creep damage development. The CF cyclic/hold experiments conducted for the Alloy 617 - 10% Cr DMW joint show, similar to continuous cycling experiments considerable softening with fast decreasing peak stresses at the beginning of life and a steady decline until macroscopic crack development, see Fig. 5.18 by example for the experiment tested with $\Delta\varepsilon$ ~0.7% at maximum test temperature T=600°C. Compared to the response of the accordant CF cyclic/hold experiment on the Alloy 617 - 1% CrMoV DMW joint at T=550°C, see Fig. 5.13, the steady decline of the peak stresses for the Alloy 617 - 10% Cr DMW joint appears to be larger. Additionally, similar to the Alloy 617 - 1% CrMoV DMW joint the amount of stress relaxation appears to be approximately constant during the

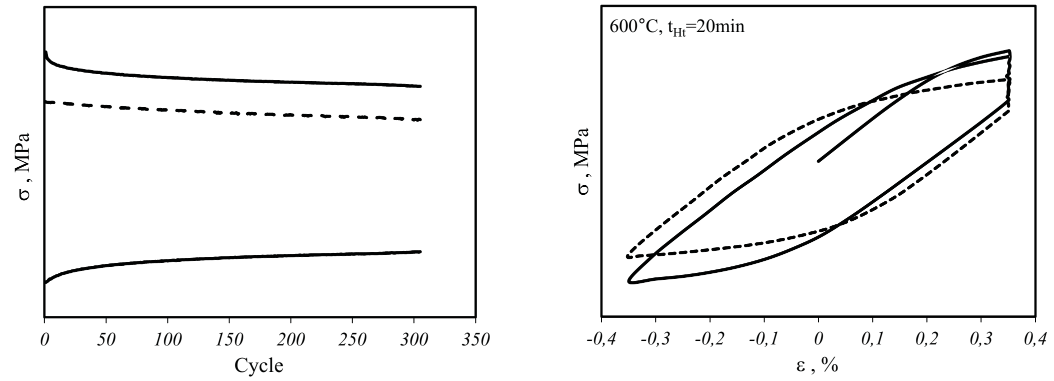

Figure 5.18: Cyclic softening shown in peak stress profiles (a) and hysteresis loops for first and mid-life cycles (b) of Alloy 617 - 10% Cr DMW (MMS-052) cross-weld joint - CF cyclic/hold test: T=600°C, $\Delta\varepsilon_t$ ~0.7%, t_{Ht}=20 min

course of testing. Fig. 5.18 b shows the first cycle and mid-life cycle stress-strain hysteresis of the experiment accordingly. The shown cyclic softening behaviour in Fig. 5.18 is representative for all the CF cyclic/hold experiments performed on the Alloy 617 - 10% Cr DMW joint.

In Fig. 5.19 the damage appearance of Alloy 617 - 10% Cr DMW CF cyclic/hold test specimen is presented, which was tested at T=575°C and $\Delta\varepsilon_t$ ~0.7%. Although the specimen exhibits gauge section reductions associated with higher local creep deformation in the region of the FG/ICHAZ of the 10% Cr steel, this local necking is not as pronounced as observed in the Alloy 617 - 1% CrMoV DMW joint under CF loading. The damage condition in the specimen is mainly characterised by intense creep damage in the over-tempered (OT) parent 10% Cr steel, see Fig. 5.19 b, where significant grain boundary cracking occurred in the centre region of the specimen. Apparently the resulting weakening of the specimen cross-section was responsible for the registered load drop as adopted test termination criterion. The

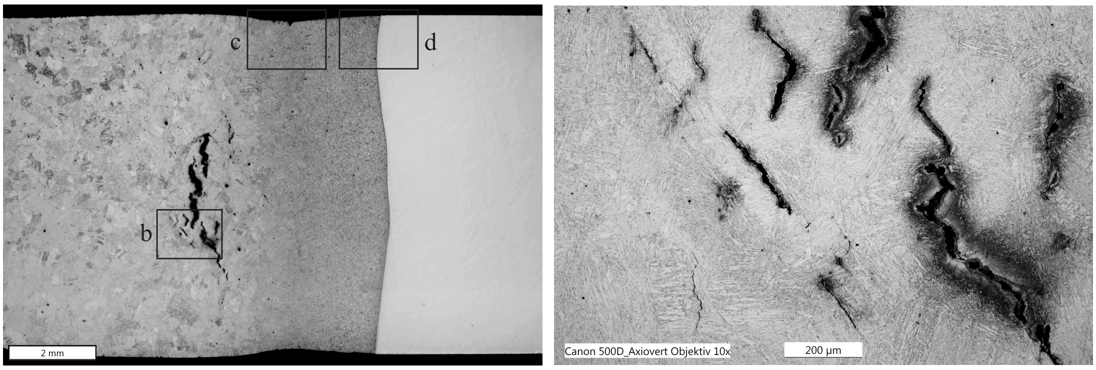

(a) Macroscopic view on the specimen cross section indicating positions of detailed micrographs

(b) Extensive creep associated grain boundary cracking in the over-tempered parent 10% Cr steel at the axis of the specimen

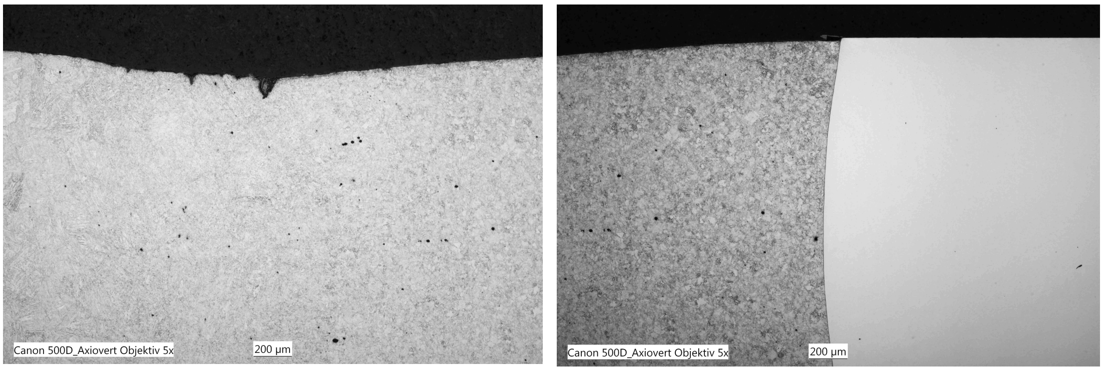
Canon 500D_Axiovert Objektiv 5x
200 µm
Canon 500D_Axiovert Objektiv 5x
200 µm

(c) Fatigue crack initiation at the surface of the 10% Cr steel FGHAZ

(d) Minor indication of FL cracking associated with Type I precipitate condition

Figure 5.19: Micrographs of Alloy 617 - 10% Cr DMW joint CF specimen: T=575°C, $\Delta\varepsilon$ ~0.7%, $N_{f2\%}$ ~700 cycles

creep damaged region in the OT parent 10% Cr was approximately 4-5 mm away from the weld fusion line, see Fig. 5.19 a. In parallel fatigue crack initiation was observed for this particular loading condition at the stress concentration at the surface of the gauge section reduction in the FGHAZ region, see Fig. 5.19 c. In experiments with a higher total strain range of $\Delta\varepsilon_t$ ~1.0%, fatigue dominated cracking in the FGHAZ of the 10% Cr steel was identified as the cause of specimen failure, whereas at higher temperatures T=575 and 600°C the crack propagation was enhanced by creep associated damage along convenient placed grain boundaries. Furthermore microstructural evidence on test specimen in Fig. 5.19 shows only a minor indication of FL cracking associated with the Type I precipitate condition, see Fig. 5.19 d. Evidence from post-test inspections on various other specimens even at comparable high imposed strain ranges on the other side clearly showed the existence of FL cracking, very similar to the damage appearance observed in Alloy 617 - 1% CrMoV DMW joint specimen under CF loading. The damage appearance observed in test specimen in Fig. 5.19 is similar to the conditions investigated in comparable short term creep rupture specimen, see Fig. 5.5, but with a shift of the creep failure location from the FG/ICHAZ towards the OT parent 10% Cr steel.

Fig. 5.20 shows the damage condition of Alloy 617 - 10% Cr DMW CF cyclic/hold test specimen, which was tested at T=600°C and $\Delta\varepsilon_t$ ~0.5%. The major reason for termination at this experiment was the development of a FL crack, which consistently followed the weld interface between Alloy 617 weld metal and 10% Cr HAZ, see Fig. 5.20 a,b. Additionally the high temperature loading at T=600°C resulted in the accumulation of significant creep damage in the form of cavity formation and creep associated cracking in the FGHAZ and ICHAZ of the 10% Cr steel, see Fig. 5.20 c,d respectively. Generally, for the CF cyclic/hold experiments with moderate strain ranges conducted on the Alloy 617 - 10% Cr DMW joint, there appears to be a shift of Type IV creep damage location present, with the failure location in the over-tempered parent 10% Cr steel for temperatures up to 575°C, see Fig. 5.19, and creep damage formation entirely in the FG/ICHAZ for test temperatures of 600°C. The apparent complexity of creep associated damage mechanisms is even extended with the occurrence of FL cracking associated with Type I precipitates adjacent to the interface between Alloy 617 weld metal and 10% Cr steel HAZ. With respect to the evidence from creep rupture experiments on the Alloy 617 - 10% Cr DMW joint it has to be expected, that the FL cracking becomes increasingly dominant during combined creep-fatigue loading with increased hold durations and lower strain ranges. This is particularly important for the loading conditions of these DMW joints during service operation in 700°C steam turbine rotors.

The experimentally determined cyclic endurance data of the CF cyclic/hold experiments with 20 min hold periods at peak strain in tension for the Alloy 617 - 10% Cr DMW joint (MMS-052) are shown in Fig. 5.17.

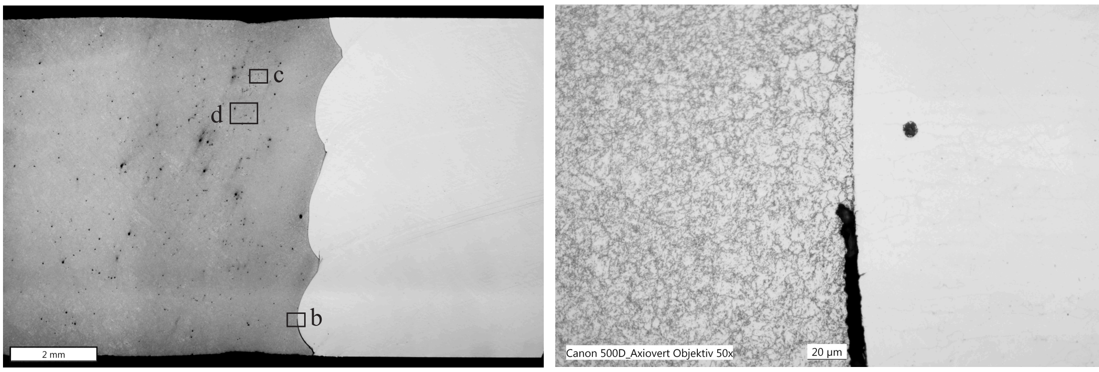
c
d
b
2 mm
Canon 500D_Axiovert Objektiv 50x
20 µm

(a) Macroscopic view on the specimen cross section indicating positions of detailed micrographs

(b) FL cracking adjacent to Type I carbide layer at interface between Alloy 617 weld metal and 10% Cr steel HAZ

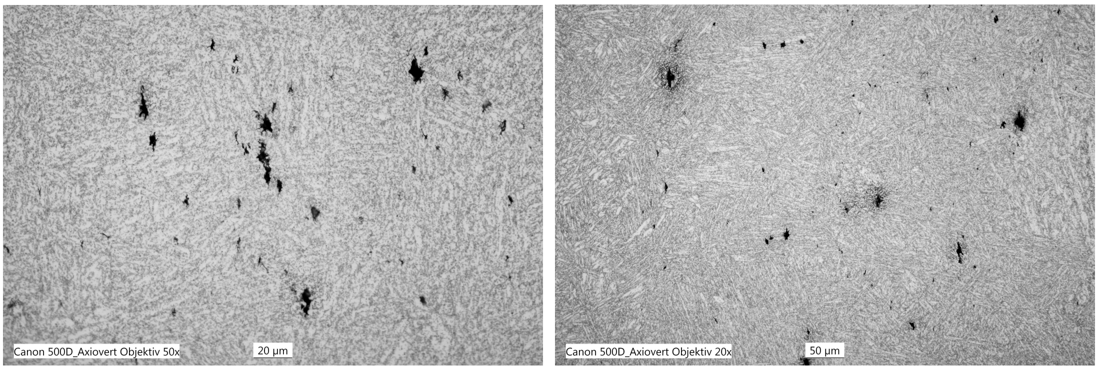
Canon 500D_Axiovert Objektiv 50x
20 µm
Canon 500D_Axiovert Objektiv 20x
50 µm

(c) Extensive creep cavity formation and cracking in the 10% Cr steel FGHAZ

(d) Creep damage associated with cavity formation in the FG/ICHAZ of the 10% Cr steel

Figure 5.20: Micrographs of Alloy 617 - 10% Cr DMW joint CF specimen: T=600°C, $\Delta\varepsilon$ ~0.5%, $N_{f2\%}$ ~660 cycles

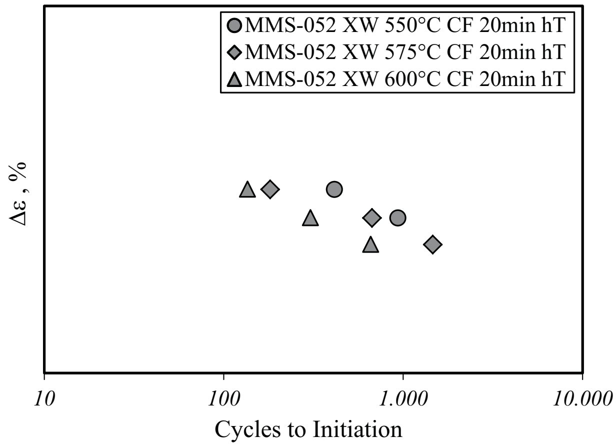

Figure 5.21: Experimental CF cyclic/hold endurance data for Alloy 617 - 10% Cr DMW joint (MMS-052). The cycles included 20 min hold periods at peak strain in tension.

5.2 Modelling of Material Behaviour

5.2.1 Creep Rupture Strength

For the determination of the creep rupture strength of the Alloy 617 - 1% CrMoV and Alloy 617 - 10% Cr DMW joints a creep rupture data assessment has been conducted on each DMW joint on the basis of the test results from section 5.1.1. Since the creep rupture result data set was rather limited, the present scatter band analysis can only be seen as preliminary and constitutes a basis for further CR testing of the accordant DMW joints. In particular, results from long-term CR experiments are yet to be generated.

Alloy 617 - 1% CrMoV

Similar to the creep rupture data assessment of Alloy 617 parent material an algebraic equation type Soviet Model 1 (SM1), see equation (4.2), has been used to fit the experimental creep rupture data on the Alloy 617 - 1% CrMoV DMW joint. A comparison of the experimental data and the modelled creep rupture strength of the Alloy 617 - 1% CrMoV DMW joint for the temperatures 500, 525 and 550°C are presented in Fig. 5.22. On the basis of achieved experimental creep rupture times of approximately t_u=6500 h extrapolations of rupture times up to 20 kh are reasonable, which has been implemented in Fig. 5.22. An important observation on the evolution of the creep rupture strength of the Alloy 617 - 1% CrMoV DMW joint is constituted by the fact that at T=550°C the creep rupture strength shows a considerable decrease, especially for rupture times relevant to service operation of steam turbine components. An acceptable value for the 100 kh creep rupture strength of the Alloy 617 - 1% CrMoV DMW joint, which constitutes an important reference in the design of steam turbine components, appears to be achievable only for temperatures of maximum 500°C. From microstructural investigations on the damage appearance observed on the Alloy 617 - 1% CrMoV DMW joint, it became obvious that creep damage associated with Type I precipitate condition and

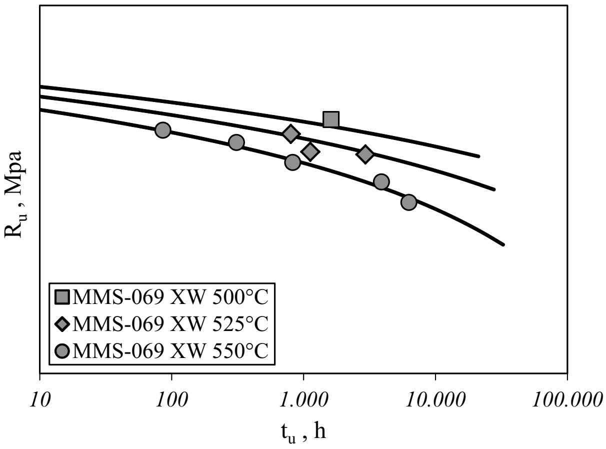

Figure 5.22: Creep rupture strength of Alloy 617 - 1% CrMoV DMW joint (MMS-069). Experimental data points and modelled trend according to creep rupture model SM1 eqn. (4.2).

related weld interface cracking appeared to be the dominant failure mechanism for longer testing times. Since enhanced diffusion processes in the vicinity of the interface between the low alloyed 1% CrMoV steel and the Ni-base Alloy 617 weld metal cannot be excluded during long-term high temperature operation, caution has to be taken in the extrapolation of creep rupture strength.

Alloy 617 - 10% Cr

The creep rupture data assessment of the Alloy 617 - 10% Cr DMW joint comprised CR result data of the current work, see Fig. 5.3, and additionally experimental data from previous research activity [99, 100] on a DMW joint between Alloy 617 (heat L617F2) and a similar 10% Cr steel. Despite this apparent shortcoming the overall creep rupture characteristics are expected to be very similar for both 10% Cr steels. For fitting the experimental data again the algebraic SM1 creep rupture model eqn. (4.2) was used. Fig. 5.23 shows the comparison of the experimental CR data on Alloy 617 -10% Cr DMW joints and the modelled creep rupture strength for temperatures 500, 550, 575 and 600°C. For the Alloy 617 - 10% Cr DMW joint the achieved experimental creep rupture times of roughly 10 kh permit extrapolations to approximately 30 kh. Hence, also for this DMW joint long-term creep rupture experiments are necessary in order to obtain reliable creep rupture strength values and to ensure safe service operation of the joint.

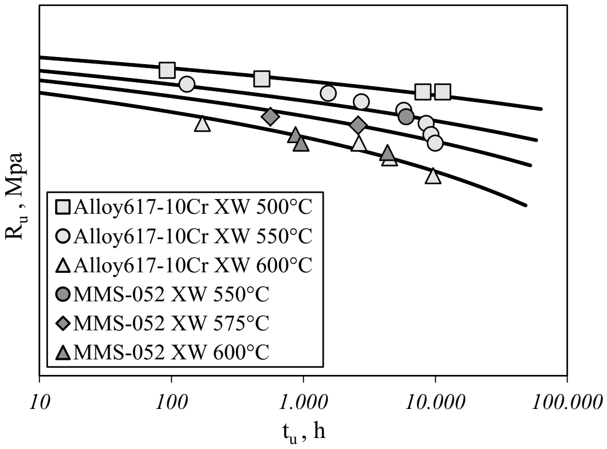

Figure 5.23: Creep rupture strength of Alloy 617 - 10% Cr DMW joint (MMS-052). Experimental data points and modelled trend according to creep rupture model SM1 eqn. (4.2).

5.2.2 Fatigue Endurance

For determination of the fatigue endurance characteristics of the Alloy 617 - 1% Cr-MoV and Alloy 617 - 10% Cr DMW joints the conventional equation proposed by COFFIN-MANSON (2.15), see also section 2.1.3, was used:

$$\Delta\varepsilon = \frac{\sigma_f}{E} \cdot N_f^{-b_1} + \varepsilon_f \cdot N_f^{-b_2} \, . \tag{5.1}$$

The fatigue failure criterion for N_f was identified as a 2% load drop from the peak stress response for strain controlled testing, see by example Fig. 5.7 and 5.10 for the peak stress profiles of Alloy 617 - 1% CrMoV and Alloy 617 - 10% Cr DMW joints respectively. Thereby the elastic and plastic strain contributions of the mid-life cycle hysteresis of the continuous cycling LCF experiments were determined and the parameters of the elastic and plastic parts of (5.1) were optimised with particular respect to temperature consistency of the individual endurance curves.

Alloy 617 - 1% CrMoV

For the Alloy 617 - 1% CrMoV DMW joint (MMS-069) the experimentally derived fatigue endurances and the modelled endurance curves for temperatures T=500, 525, 550°C are compared in Fig. 5.24. As already mentioned for the creep rupture strength data assessment of the DMW joints, the experimental LCF data set is comparatively small and comprises only data from specimens extracted from one weldment. Only further testing activity can result in a more reliable fatigue endurance assessment. Nevertheless the modelled curves well represents the fatigue endurance data on the Alloy 617 - 1% CrMoV DMW joint.

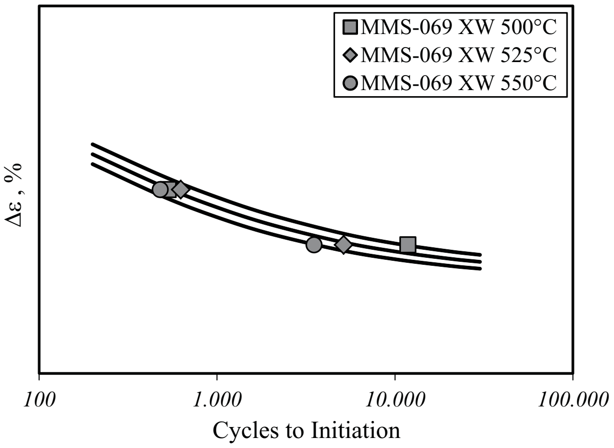

Figure 5.24: LCF experimental result data and modelled fatigue endurance curves for Alloy 617 - 1% CrMoV DMW joint (MMS-069).

Alloy 617 - 10% Cr

For the Alloy 617 - 10% Cr DMW joint (MMS-052) the experimentally derived fatigue endurances and the modelled endurance curves for temperatures T=550, 575, 600°C are compared in Fig. 5.25. Similar to the Alloy 617 - 1% CrMoV DMW joint the endurance dataset was rather limited and hence a more reliable fatigue endurance assessment of the Alloy 617 - 10% Cr DMW joint can only be achieved on the basis of extended testing activity in particular on different DMW weldments in order to investigate the extend of weld to weld scatter. The modelled endurance curves show an acceptable fit to the experimental results. Furthermore the location of the modelled curves is almost coincident to the endurance curves of the Alloy 617 - 1% CrMoV DMW joint in Fig. 5.24, giving rise to the assumption that the Alloy 617 - 10% Cr DMW joint features comparable fatigue endurance characteristics at approximately 50°C higher temperatures than the Alloy 617 - 1% CrMoV DMW joint.

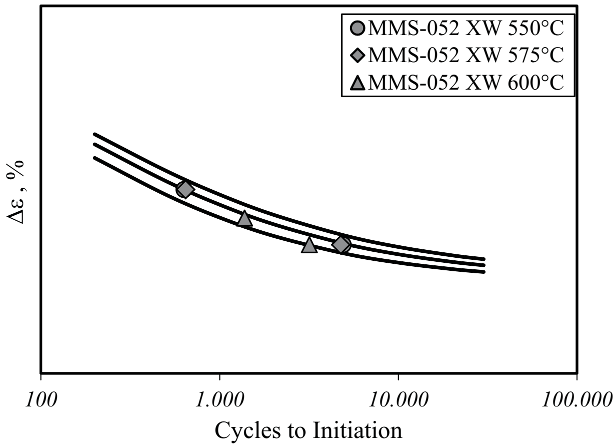

Figure 5.25: LCF experimental result data and modelled fatigue endurance curves for Alloy 617 - 10% Cr DMW joint (MMS-052).

5.2.3 Creep-Fatigue Interaction

For the determination of creep-fatigue endurances the conventional COFFIN-MANSON equation (5.1) was fitted to the results of the CF cyclic/hold experiments conducted on the Alloy 617 - 1% CrMoV and Alloy 617 - 10% Cr DMW joints. The crack initiation criterion was identified as a 2% load drop from the peak stress response for strain controlled testing, see by example Fig. 5.13 and 5.18 for the peak stress profiles of the Alloy 617 - 1% CrMoV and Alloy 617 - 10% Cr DMW joints respectively.

A creep-fatigue damage assessment of the CF cyclic/hold experiments on the Alloy 617 - 1% CrMoV and Alloy 617 - 10% Cr DMW joints has been performed. The fatigue damage fraction D_f was determined by the cycle ratios N/N_f, see eqn. (2.35) in section 2.2.2:

$$D_f = N/N_f \,. \tag{5.2}$$

The crack initiation endurances $\Delta\varepsilon = f(N_f)$ determined for continuous cycling LCF experiments for the Alloy 617 - 1% CrMoV and Alloy 617 - 10% Cr DMW joints formed the basis of the fatigue damage assessment, see Fig. 5.24 and 5.25 respectively. For the determination of the creep damage fraction during combined creep-fatigue loading of the cross-weld DMW joint specimens the conventional *Time fraction* approach eqn. (2.38) has been adopted:

$$D_c = N \int_0^{t_h} \frac{dt}{t_u(\sigma, T)} \,. \tag{5.3}$$

For the estimation of the required creep rupture strength $t_u(\sigma, T)$ the modelled curves for the Alloy 617 - 1% CrMoV and Alloy 617 - 10% Cr DMW joints shown in Fig. 5.22 and 5.23 respectively were used.

For the creep-fatigue damage assessment of both DMW joints it has to be mentioned, that the fatigue crack initiation endurances $\Delta\varepsilon = f(N_f)$ and creep rupture strength $t_u(\sigma, T)$ are based on results from specimens with different gauge section lengths, see Fig. 3.2 and Fig. 3.4 respectively. Although the geometry of continuous cycling LCF specimen and CF cyclic/hold specimen is identical for both DMW joints, the creep rupture strength $t_u(\sigma, T)$ of the DMWs has been obtained from cross-weld specimens with much longer sampling length and smaller gauge section diameter.

Alloy 617 - 1% CrMoV

For the Alloy 617 - 1% CrMoV DMW joint (MMS-069) the creep-fatigue crack initiation endurances of CF cyclic/hold experiments, including 20 min hold periods at peak strain in tension, and the corresponding modelled creep-fatigue endurance curves for temperatures T=500, 525, 550°C are compared in Fig. 5.26. The modelled curves well represent the experimental data, whereas again the comparatively small dataset has to be noted, consisting of a total of 9 experiments with specimens originating from one single dissimilar metal weldment. The obtained results show a significant influence on the crack initiation endurance compared to data of continuous cycling LCF experiments, see Fig. 5.24. During the fitting procedure of the CF cyclic/hold endurances attention was spent on deriving temperature consistent endurance curve trends in the creep-fatigue area as well as in the fatigue area.

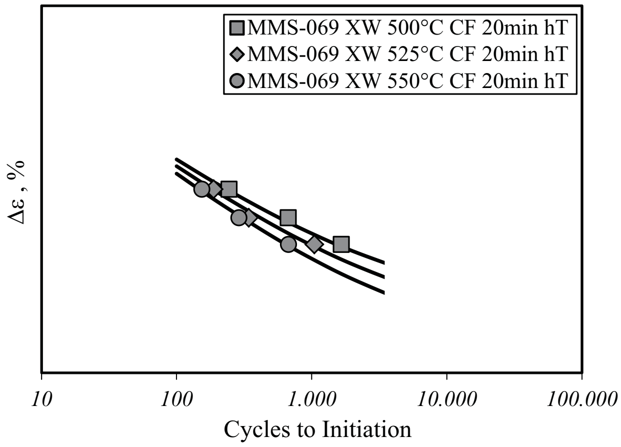

Figure 5.26: CF cyclic/hold experimental result data and modelled creep-fatigue endurance curves for Alloy 617 - 1% CrMoV DMW joint (MMS-069). The cycles included 20 min hold periods at peak strain in tension.

The calculated fatigue damage D_f and creep damage D_c fractions of CF cyclic/-hold experiments conducted on the Alloy 617 - 1% CrMoV DMW joint are shown in the creep-fatigue damage interaction diagram in Fig. 5.27. Thereby, for each temperature, decreasing fatigue damage fractions D_f were determined with decreasing total strain ranges of the experiments. Whereas the values of D_f were in the expected range, the calculated creep damage fractions D_c show significant large values exceeding unity and hence total damage accumulations $D=D_f+D_c$ larger than one were obtained. This was the case despite the fact, that during the calculation of the creep damage during the hold period the initial part of stress relaxation was not considered for creep damage accumulation. The transition hold time after the fast stress relaxation, where creep damage contribution was considered, was identified to ~5-6 min for the CF cyclic/hold experiments on the Alloy 617 - 1% CrMoV DMW joint for temperatures 525 and 550°C. The short-term deformation occurring during the initial relaxation phase at peak strain in tension is thereby regarded as plastic deformation and not to contribute to the observed creep damage. With consideration of the whole hold period for contribution

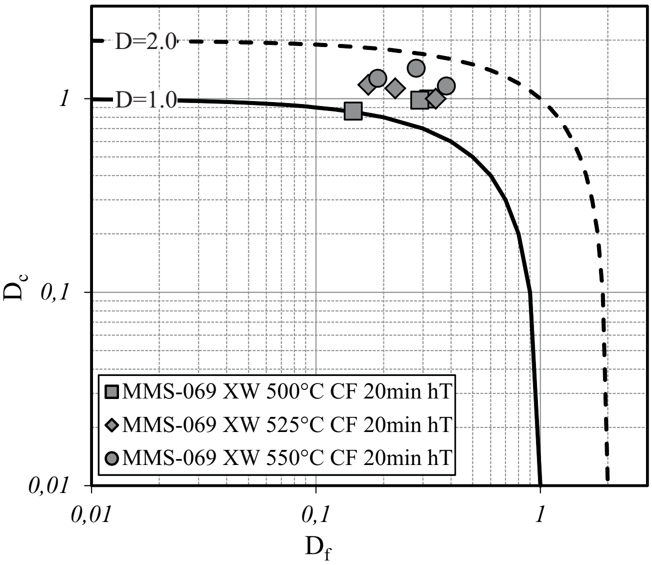

Figure 5.27: Calculated fatigue damage D_f and creep damage D_c fractions of CF experiments on Alloy 617 - 1% CrMoV DMW joint (MMS-069). For comparison the damage loci for D=1.0, 2.0 are plotted also.

to creep damage development the calculated creep damage would otherwise show unrealistic high values. The *Time fraction* approach, eqn. (5.3), for determination of creep damage for combined creep-fatigue loading of the Alloy 617 - 1% CrMoV DMW joint appears to be conservative, at least for the total strain ranges and hold durations covered within the present investigation. Additional CF cyclic/hold experiments, in particular for smaller strain ranges representative for Alloy 617 - 1% CrMoV dissimilar metal weldments in 700°C steam turbine rotors, are necessary to verify these assumptions. Furthermore the influence of significantly larger hold durations is yet to be investigated in order to verify the applicability of the *Time fraction* approach for the creep-fatigue damage assessment of Alloy 617 - 1% CrMoV DMW joints.

Alloy 617 - 10% Cr

For the Alloy 617 - 10% Cr DMW joint (MMS-052) the creep-fatigue crack initiation endurances of CF cyclic/hold experiments, including 20 min hold periods at peak strain in tension, and the corresponding modelled creep-fatigue endurance curves for temperatures T=550, 575, 600°C are compared in Fig. 5.28. The modelled curves well represents the experimental data, whereas again the comparatively small dataset has to be noted, consisting of a total of 8 experiments with specimens originating from one single dissimilar metal block weldment. Similar to the results on the Alloy 617 - 1% CrMoV DMW joint, the obtained CF crack initiation endurances of the Alloy 617 - 10% Cr DMW joint show a significant reduction compared to data of continuous cycling LCF experiments, see Fig. 5.25. Furthermore the CF cyclic/hold endurances appear to more strongly dependent on the temperature compared to the endurance curves obtained for the Alloy 617 - 1% CrMoV DMW joint, which show less variation within the covered temperature span, see Fig. 5.26. Eventually only further testing activity can clarify these observed char-

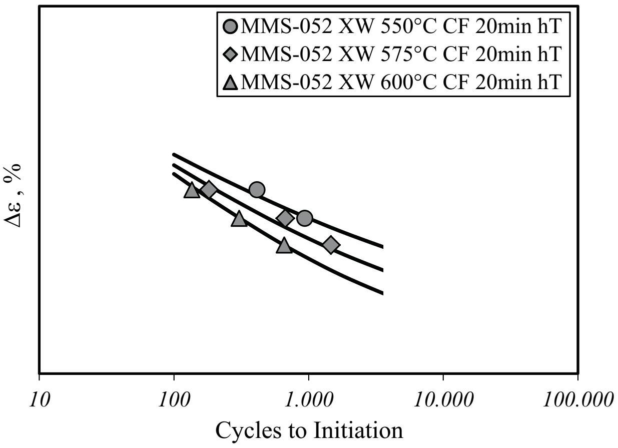

Figure 5.28: CF cyclic/hold experimental result data and modelled creep-fatigue endurance curves for Alloy 617 - 10% Cr DMW joint (MMS-052). The cycles included 20 min hold periods at peak strain in tension.

acteristics. The calculated fatigue damage D_f and creep damage D_c fractions of CF cyclic/-hold experiments conducted on the Alloy 617 - 10% Cr DMW joint are shown in the creep-fatigue damage interaction diagram in Fig. 5.29 respectively. Similar to the Alloy 617 - 1% CrMoV DMW joint the calculated values for D_f of the Alloy 617 - 10% Cr DMW joint show reasonable values, exhibiting decreasing fatigue damage fractions D_f at decreasing total strain ranges for each temperature. Interestingly, the calculated creep damage fractions D_c show significant low values, even for the low strain range experiment at maximum temperature T=600°C a value of only 0.24 was determined. This was apparent despite the fact that, in contrast to the assessment of the Alloy 617 - 1% CrMoV DMW joint, the whole deformation occurring within the relaxation phase was regarded to contribute to creep damage development for the Alloy 617 - 10% Cr DMW joint in order to exclude any possible non-conservatism. Therefore the total damage accumulations $D=D_f+D_c$ result in significant lower values than one. As described by the dashed damage locus in Fig. 5.29 the CF cyclic/hold experiments on the Alloy 617 - 10% Cr DMW joint show values of D=0.35-0.6. This indicates a considerable creep-fatigue interaction in the damage mechanism leading to failure in the Alloy 617 - 10% Cr DMW joint. With respect to the observed damage appearance in the cross-weld Alloy 617 - 10% Cr DMW joint specimens, the apparent strong creep-fatigue interaction might be explained by enhanced FL crack propagation due to fatigue cycling as well as accelerated creep cavity consolidation and cracking in the FGHAZ of the 10% Cr steel, see Fig. 5.20. Additionally, the damage appearance of the test specimen in Fig. 5.19 could be explained by accelerated grain boundary cracking along creep damaged grain boundaries in the over-tempered parent 10% Cr steel. The preferential cracking along grain boundaries with 45° inclination towards the loading direction gives rise to the assumption of enhanced grain boundary sliding due to superimposed alternating strain cycling apparent in the CF cyclic/hold experiments.

Hence the conservatism of the *Time fraction* approach, eqn. (5.3), for determination of creep damage for combined creep-fatigue loading of the Alloy 617 - 10% Cr

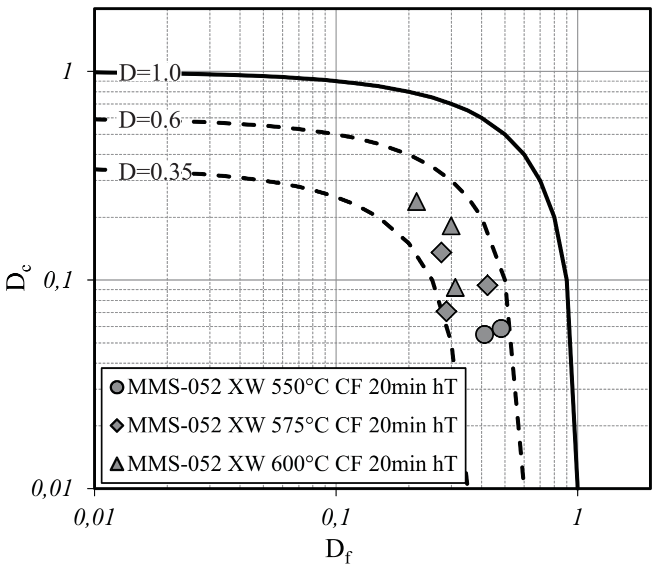

Figure 5.29: Calculated fatigue damage D_f and creep damage D_c fractions of CF experiments on Alloy 617 - 10% Cr DMW joint (MMS-052). For comparison the damage loci for D=0.35, 0.6, 1.0 are plotted also.

DMW joint is drastically discriminated by the observed intense creep-fatigue interaction on the steel side of the joint. Additional CF cyclic/hold experiments on Alloy 617 - 10% Cr DMW joints with considerable lower total strain ranges, representative to 700°C steam turbine rotor weldment features, are proposed in order to verify the existence of the apparent strong creep-fatigue interaction under such conditions.

5.2.4 Maximum Application Temperatures

The maximum application temperatures of both Alloy 617 - 1% CrMoV and Alloy 617 - 10% Cr dissimilar metal welded joints appear to be strongly dominated by their creep rupture properties. For both DMW joints the conducted CR and CF experiments at the selected target temperatures were sufficiently useful for the identification of the maximum application temperatures.

For the Alloy 617 - 1% CrMoV DMW joint the modelled trend of the creep rupture strength, see Fig. 5.22, and accordant creep-fatigue endurances, see Fig. 5.26, reveal a maximum application temperature of 500°C, whereas a definite statement can only be achieved by long-term verification of the creep-rupture strength of this joint.

For the Alloy 617 - 10% Cr DMW joint the determined creep rupture strength extrapolation, see Fig. 5.23, and the CF endurance characteristics, see Fig. 5.28, show an achievable maximum application temperature of around 575°C.

Chapter 6

Conclusion and Outlook

The findings of the present research work clearly show that the Ni-base Alloy 617 is an appropriate material for the use in advanced 700°C steam turbine applications. The combination of good creep rupture, fatigue and creep-fatigue properties together with excellent ductility even for long-term loading conditions underpin the selection of Alloy 617 for the use in large steam turbine components with complex geometries. Thus with the adoption of Alloy 617 in future steam turbine technology, the scope of operation can be significantly enhanced to higher steam inlet parameters exceeding temperatures of 700°C and simultaneously higher thermal efficiencies.

The required input parameters for the development of an advanced lifetime assessment methodology of Alloy 617 steam turbine rotor features have been generated within an extensive material testing campaign. For the characterisation of the material behaviour under static loading conditions creep rupture experiments for medium and target application temperatures have been conducted in order to investigate the influence of ageing treatment on the properties of Alloy 617. Taking into account material property data from previous research activities a constitutive creep deformation equation has been developed on the basis of the modified Graham-Walles law, which well represents the mean creep behaviour of the investigated and reviewed Alloy 617 heats. In order to determine the time-independent plastic flow as well as the fatigue endurance characteristics continuous cycling LCF experiments have been performed for the entire temperature range. On this basis a constitutive plasticity model of Chaboche type has been developed, which accurately describes the observed material response under cyclic loading. Furthermore cyclic/hold experiments have been conducted on Alloy 617 in order to investigate the occurring creep-fatigue damage mechanism and to determine the CF endurance characteristics. Thereby a modification on the creep law has been introduced for description of the materials decreased creep resistance under combined creep-fatigue loading. For the assessment of creep and fatigue damage fractions a very promising approach considering plastic and creep dissipated energy as failure criteria has been developed. The effectiveness of this energy exhaustion method has been verified with the calculation of endurance curves for continuous cycling LCF and CF cyclic/hold conditions over a broad range of temperatures, strain ranges and hold periods. The effectiveness of the developed constitutive deformation model has been further verified with the results of a service-type TMF experiment, the cycle definition for which had been determined from a life-limiting location in a 700°C high-pressure steam turbine rotor under realistic loading conditions featuring significantly different strain ranges within an anisothermal cycle. The developed creep-fatigue lifetime assessment methodology for Alloy 617 has been verified with the help of post test microstructural investigations, where the accordant damage appearances could reliably be represented.

For further characterisation of Alloy 617 and accordant verification of applicability of the material in future steam turbine technology, with particular respect to the planned long-term operation in steam turbine rotors, additional creep-rupture experiments are necessary for a reliable creep rupture strength prediction. Additionally creep-fatigue experiments, preferably also thermomechanical experiments with representative strain ranges and sufficiently long hold durations, are recommended in future research activities to further investigate the apparent creep-fatigue damage mechanism. The post-test metallographic investigation on the TMF test conducted within the present work has revealed, despite the comparable large strain range of the experiment, extensive creep damage development under the imposed thermomechanical cycle.

The presented constitutive deformation models for Alloy 617 provide a substantial capability to describe the materials short- and long-term behaviour under complex thermomechanical loading conditions. In an outlook a more sophisticated approach could be proposed, using unified viscoplastic material models featuring a coupling of phenomenological deformation equations and constitutive damage parameters in order to describe the damage evolution within the material. Such material models are inherently associated with larger material testing campaigns as well as increased material modelling and calculation efforts for providing efficient FE-models for structural calculations of steam turbine components.

The second main objective of the present research work was the identification of the maximum application temperatures of dissimilar metal welded joints between the Ni-base Alloy 617 and a 1% CrMoV low alloy bainitic rotor steel as well as a higher alloyed 10% Cr martensitic rotor steel with respect to both their creep and creep-fatigue properties. A testing procedure for the static creep and cyclic testing of the DMW joints has been developed and an extensive testing campaign has been conducted comprising creep rupture, continuous cycling LCF as well as CF cyclic/hold experiments for target temperatures defined on experience with similar metal weldments. Based on the experimental results the fatigue and creep-fatigue endurance characteristics have been determined and corresponding models have been developed for their description. Accordingly the creep rupture strength curves have been determined, whereas CR strength extrapolations are only possible to maximum rupture times of 30 kh, due to the limited test duration of available DMW joint creep data. On this basis, information could be obtained on the maximum achievable application temperatures of the investigated DMW joints. Post-test metallographic investigations revealed a complexity of apparent damage mechanisms for representative creep and creep-fatigue conditions. Next to Type IV creep damage in the FGHAZ of the steels, which constitutes the main creep failure observed during creep loading of similar metal weldments, fusion line cracking associated with a Type I precipitate condition at the interface between Alloy 617 weld metal and the steel HAZ is observed in the investigated Alloy 617 - 1% CrMoV and Alloy 617 - 10% Cr DMW joints. Whereas the Type I carbide layer is apparent in Alloy 617 - 1% CrMoV DMW joint specimens even after short duration high temperature exposure, the situation is not clearly visible within the Alloy 617 - 10% Cr DMW joint. One major reason for the development of these Type I precipitates is the chemical composition gradients, mainly for the constituents C and Cr, which is obviously larger for the low alloyed 1% CrMoV steel compared to the 10% Cr steel with respect to the chemical composition of Alloy 617. For long-term creep loading conditions, representative of service condition existing in steam turbine rotors, the predominant failure mechanism for both DMW joints appears to be FL cracking associated with the Type I precipitate condition. Since additional element diffusion is to be expected during long-term high temperature exposure, the experimental verification of long-term creep rupture strength is absolutely essential in order to guarantee the safe operation of the dissimilar metal weldments under service conditions. Additionally it should be noted that the presented experimental results have been obtained by uniaxial loaded cross-weld specimens with relatively small cross-sections that have been extracted from the weldments. On the one hand possible welding residual stresses have been reduced by the cutting out of the specimens and on the other hand no experience has been obtained on the effect of multiaxial stress states on the creep behaviour of the investigated DMW joints.

In an outlook, further research on the Alloy 617 - 1% CrMoV and Alloy 617 - 10% Cr dissimilar metal welded joints is necessary the provide information on the long-term situation of the Type I precipitate condition. Therefore long-term heat treatments of these DMW joints are proposed in order to investigate the diffusion properties adjacent to the weld interface, whereas ageing temperatures above the target application temperature of the joints may be applied in order to accelerate the element diffusion process. Furthermore, in order to improve the material modelling of these DMW joints and to generate accordant detailed properties for the most significant zones of the steel HAZs, test specimen featuring simulated grain structures similar to those generated during the welding process may be prepared. With this effort, next to the deformation characteristics, information could be gathered concerning the relevant damage evolution within the particular zones of the steel HAZs. To further underpin the observed damage appearance in the dissimilar metal welded joints a FE based analysis of the non-homogeneous stress-strain state in the weldment might be proposed. With absolute priority the experimental verification of long-term creep rupture strength of the Alloy 617 - 1% CrMoV and Alloy 617 - 10% Cr DMW joints is recommended.

Appendix

A Specimen Geometries

This appendix contains the technical drawings of the test specimen geometries used within the present research project. The test specimen geometry used for parent Alloy 617 LCF, CF and TMF experiments is shown in Fig. A.1. The specimen geometry for experiments on cross-weld DMW joints is shown in Fig. A.2.

For Alloy 617 parent material creep rupture testing the specimen geometry shown in Fig. A.3 was adopted, whereas for CR experiments on cross-weld DMW joints the specimen geometry shown in Fig. A.4 was used.

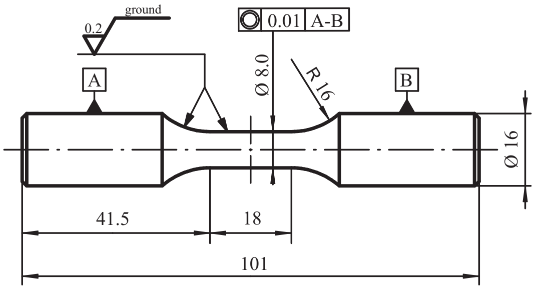
ground
0.2
0.01 A-B
A
Ø 8.0
R 16
B
Ø 16
41.5
18
101

Figure A.1: LCF/TMF short specimen

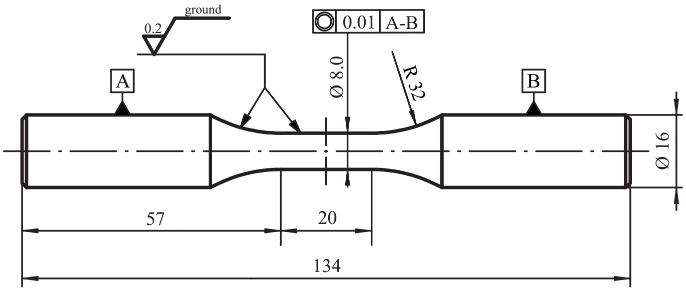
ground
0.2
0.01 A-B
A
Ø 8.0
R 32
B
Ø 16
57
20
134

Figure A.2: LCF/TMF standard specimen

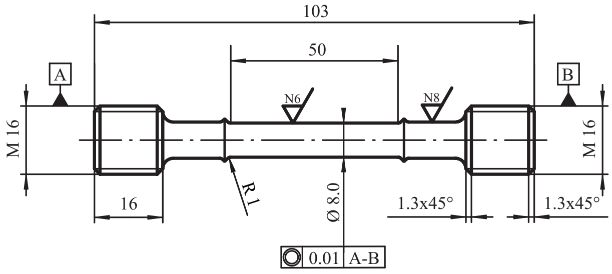

Figure A.3: Creep specimen adopted for parent material according to ISO 204

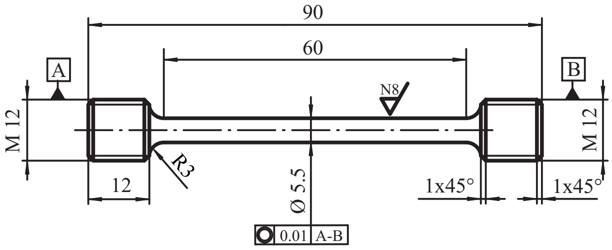

Figure A.4: Creep specimen adopted for dissimilar metal welded joint testing according to ISO 204

B Alloy 617 - Creep Model Parameters

The appendix contains the results of the scatterband analysis for the determination of the mean Alloy 617 creep behaviour. As described in detail in section 4.2.2 the curve families for creep rupture strength $R_{u/t/T}$ and datum strain strengths $R_{\varepsilon/t/T}$ for various datum strain have been obtained by SM1 algebraic creep rupture model equations. Fig. B.1 shows a comprehensive overview about comparisons of measured creep data and calculated strength curves for the reviewed and investigated heats of Alloy 617 for various creep datum strains. In Fig. B.2 the modelled curve families of datum creep strain strength curves for Alloy 617 are shown.

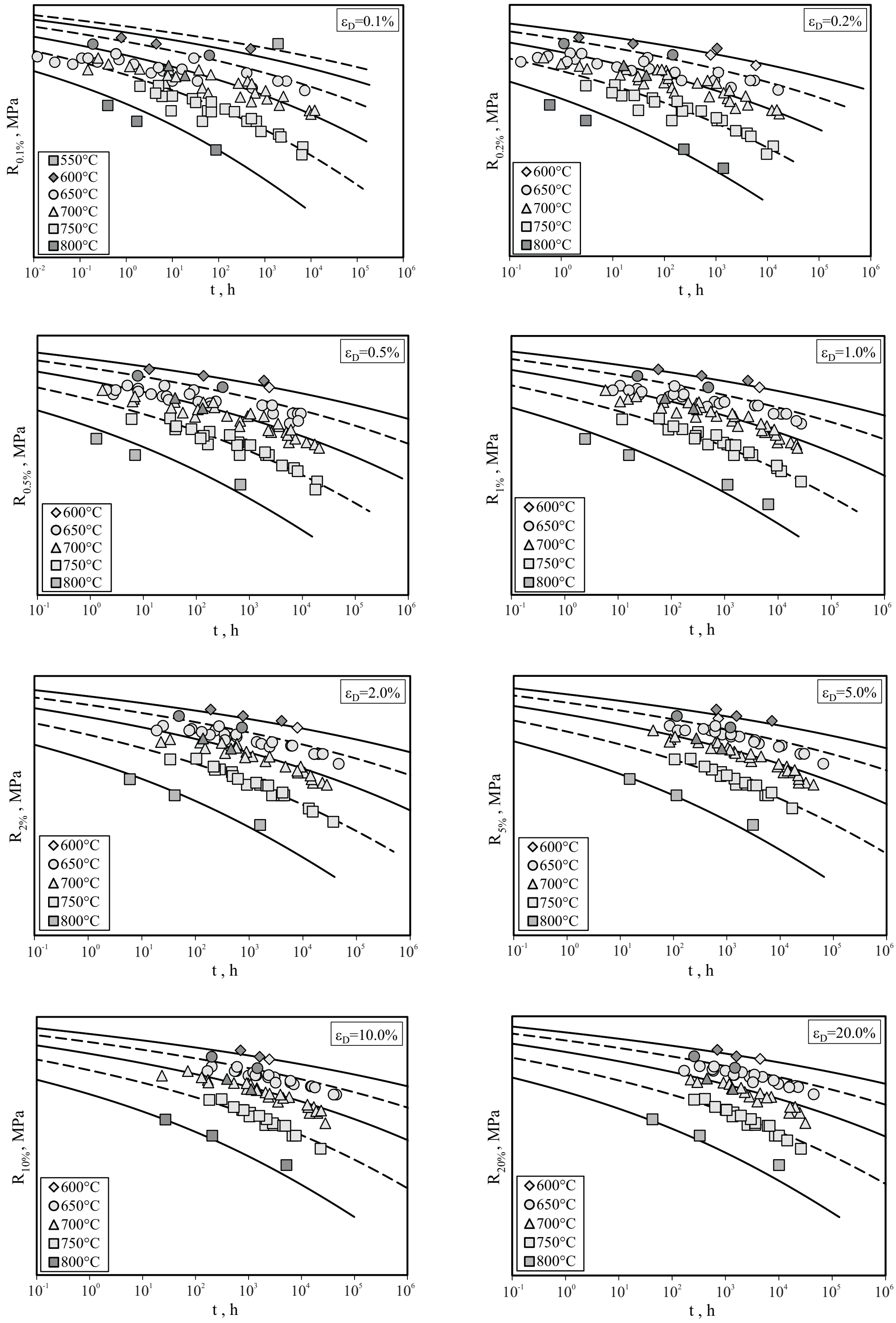

Figure B.1: Comparison of measured creep data and calculated strength curves of Alloy 617 for various datum strains

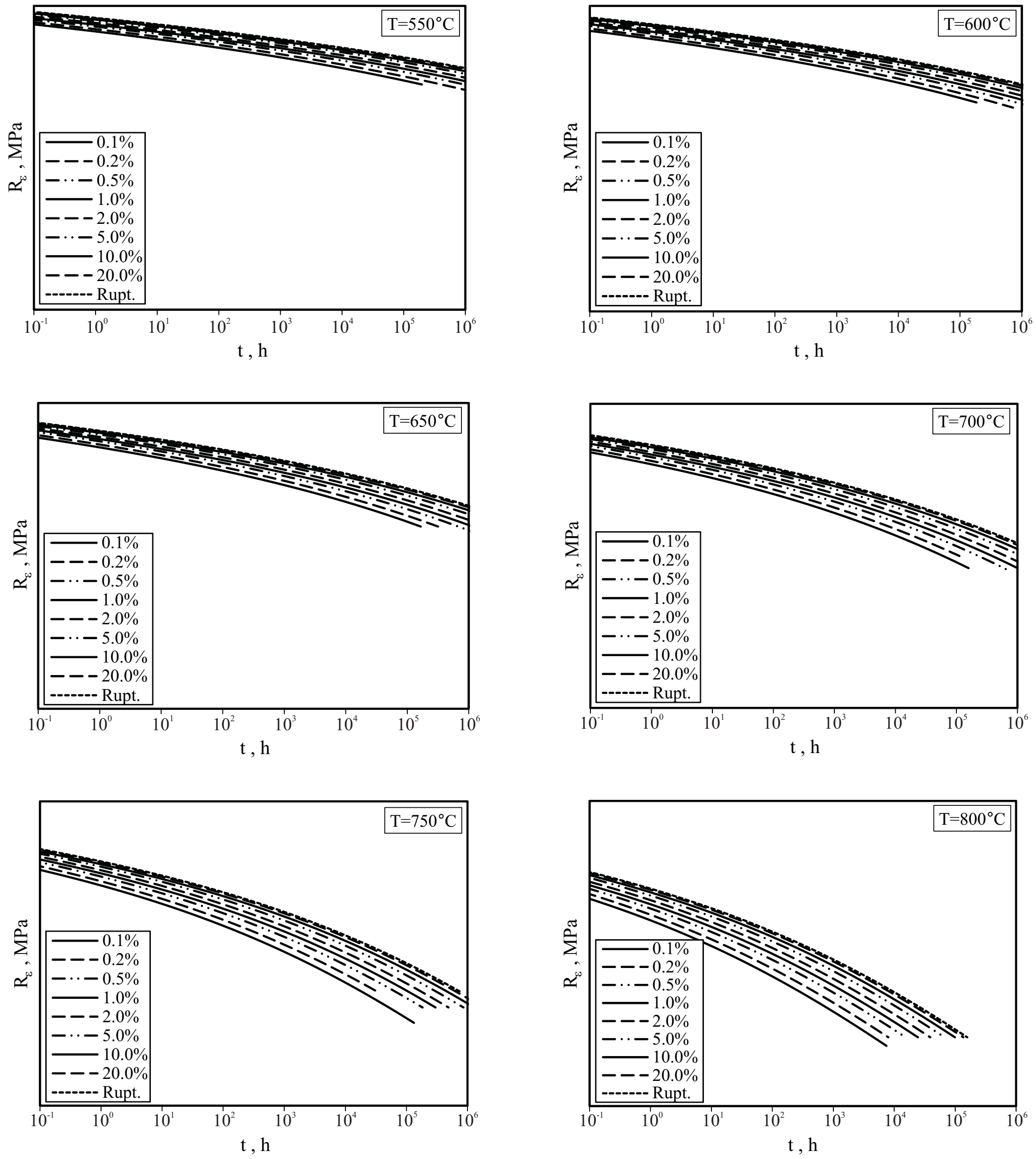

Figure B.2: Modelled curve families of datum creep strain strength curves for Alloy 617.

List of Figures

2.1 Unit cell for bcc and fcc crystal lattice structure 6
2.2 Edge and screw dislocations in the crystal lattice 7
2.3 Microstructural alteration during recovery and recrystallisation 8
2.4 Twin formation in a crystal 10
2.5 Solid solution hardening 11
2.6 Interaction of point defects and dislocations 12
2.7 Interfaces between precipitated particles and matrix 12
2.8 Interactions of dislocations passing through precipitated particles 13
2.9 Deformation and fracture mechanism maps 15
2.10 Creep strain and creep strain rate for different engineering alloys 16
2.11 Evolution of dislocation substructures during creep deformation 17
2.12 Correlation between diffusion-creep and lattice self diffusion 19
2.13 Minimum creep rate of strengthened steels 19
2.14 Scatterband analysis using time-temperature parameter 21
2.15 Master curve families for creep strain strength 22
2.16 σ-ε-hysteresis loop and designations of important measures 23
2.17 Cyclic softening and hardening of a material 24
2.18 Reduction of $\Delta\sigma$ in ε-controlled LCF tests 25
2.19 Schematic partition of the endurance curve for LCF and HCF 26
2.20 Cyclic stress-strain curves under LCF testing 27
2.21 Isotropic and kinematic hardening 29
2.22 Multiple backstress approach 31
2.23 Multiaxial stress state in a circumferentially notched specimen 32
2.24 Evolution of creep damage 35
2.25 Dislocation substructures in cyclic loaded fcc metals 36
2.26 Fatigue crack initiation due to PSBs - Schematic 37
2.27 Fatigue crack initiation due to PSBs in Cu 38
2.28 Formation of PSBs in precipitation hardened alloys 39
2.29 Micro-damage mechanism due to fatigue and creep-fatigue loading 42
2.30 Continuous cooling transformation diagram for 1%CrMoV steel 50
2.31 Continuous cooling transformation diagram for 12%CrMoVNbN steel . . . 52
2.32 100000h creep rupture strength of steam turbine rotor steels 54
2.33 Schematic of the sub-zones of the HAZ of P91 steel 56
2.34 Comparison of cross-weld with mean BM creep rupture strength of E911 steel 58
2.35 Schematic of cracking modes in weldments of heat-resistant steels 59

3.1 100KN MTS uniaxial servohydraulic testing machine 67
3.2 DWM cross-weld LCF/CF specimen geometry arrangement 68
3.3 Susceptor concept for induction heating of DMW 68
3.4 DWM cross-weld CR specimen geometry arrangement 70

4.1 Tensile and yield strength properties of heats of Alloy 617 72
4.2 Creep curves of Alloy 617 heat MMS-036 for 600°C and 700°C 73
4.3 Creep rupture strength of Alloy 617 heats 74
4.4 Creep damage in Alloy 617 heat MMS-036 75
4.5 Creep damage in Alloy 617 heat MMS-036 75
4.6 LCF endurance data of Alloy 617 heats at 700 and 750°C 76
4.7 Peak stress profiles and hysteresis loops of LCF test 77
4.8 LCF damage in Alloy 617 heat MMS-036 77
4.9 CF endurance data of Alloy 617 heats at 700 and 750°C 79
4.10 Peak stress profiles and hysteresis loops of CF test 79
4.11 Damage appearance in symmetric cyclic/hold tests of Alloy 617 heat MMS-036 80
4.12 Damage appearance in asymmetric cyclic/hold tests of Alloy 617 heat MMS-036 80
4.13 Mid-life CSS curves of the Alloy 617 heats 81
4.14 Modelled CSS curves of Alloy 617 for various temperature conditions . . . 82
4.15 Comparison of measured and calculated LCF hysteresis of Alloy 617 heat MMS-036 83
4.16 Total dissipated energy W$_{pl,tot}$ of LCF experiments on Alloy 617 84
4.17 Comparison of measured and calculated LCF endurance data of Alloy 617 heat MMS-036 84
4.18 Comparison of measured creep data and calculated datum strain strength curves of Alloy 617 86
4.19 Modelled curve family of datum creep strain strength curves of Alloy 617 for temperatures 650 and 750°C. 87
4.20 Calculated mean creep curves of Alloy 617 for various stresses at 700°C. . 87
4.21 Graham-Walles creep model fit to mean creep curves of Alloy 617 88
4.22 Comparison of measured LCF and CF mid-life hysteresis loops of Alloy 617 89
4.23 Mid-life CSS curves of CF tests of Alloy 617 heats 90
4.24 Calculated correction factor Z_c' for cyclic/hold experiments 91
4.25 Comparison of measured and calculated mid-life cycle CF hysteresis of Alloy 617 heat MMS-036 92
4.26 Critical dissipated creep energy of Alloy 617 heats 93
4.27 Creep-fatigue damage fractions for CF experiments on Alloy 617 heats . . 94
4.28 Calculated CF endurance curves compared to experimental data of Alloy 617 heats at 700 and 750°C 96
4.29 Creep-fatigue damage fraction for CF endurance curves for Alloy 617 . . . 96
4.30 Loading conditions at critical location of 700°C steam turbine rotor 98
4.31 Cycle shape adopted to represent service conditions in service-cycle TMF benchmark test 98
4.32 FE model of a circumferentially notched round tensile (CNRT) specimen . 99

4.33 Comparison of stress-strain state criteria for different CNRT specimen geometries . . . 99
4.34 Peak stress profiles and hysteresis loops of TMF test . . . 100
4.35 Damage appearance in service cycle TMF test of Alloy 617 heat MMS-036 101
4.36 Comparison of measured and calculated TMF mid-life cycle parameters . 102
4.37 Comparison of predicted and experimentally observed N_f for CF experiments on Alloy 617 . . . 104

5.1 Micrographs of Alloy 617 - 1% CrMoV DMW creep rupture specimen . . . 107
5.2 Micrographs of Alloy 617 - 1% CrMoV DMW creep rupture specimen . . . 108
5.3 Creep rupture strength of Alloy 617 - 1% CrMoV DMW joint (MMS-069) . 109
5.4 Micrographs of Alloy 617 - 10% Cr DMW creep rupture specimen . . . 109
5.5 Micrographs of Alloy 617 - 10% Cr DMW creep rupture specimen . . . 111
5.6 Creep rupture strength of Alloy 617 - 10% Cr DMW joint (MMS-052) . . . 111
5.7 Peak stress profiles and hysteresis loops of Alloy 617 - 1% CrMoV DMW LCF test . . . 112
5.8 Micrographs of Alloy 617 - 1% CrMoV DMW joint LCF specimen . . . 113
5.9 LCF endurance data for Alloy 617 - 1% CrMoV DMW joint (MMS-069). . 114
5.10 Peak stress profiles and hysteresis loops of Alloy 617 - 10% Cr DMW LCF test . . . 115
5.11 Micrographs of Alloy 617 - 10% Cr DMW joint LCF specimen . . . 116
5.12 LCF endurance data for Alloy 617 - 10% Cr DMW joint (MMS-052). . . . 116
5.13 Peak stress profiles and hysteresis loops of Alloy 617 - 1% CrMoV DMW CF cyclic/hold test . . . 117
5.14 Micrographs of Alloy 617 - 1% CrMoV DMW joint CF specimen . . . 118
5.15 Micrographs of Alloy 617 - 1% CrMoV DMW joint CF specimen . . . 119
5.16 Micrographs of Alloy 617 - 1% CrMoV DMW joint CF specimen . . . 121
5.17 Cyclic endurance data for Alloy 617 - 1% CrMoV DMW joint (MMS-069). 122
5.18 Peak stress profiles and hysteresis loops of Alloy 617 - 10% Cr DMW CF cyclic/hold test . . . 122
5.19 Micrographs of Alloy 617 - 10% Cr DMW joint CF specimen . . . 123
5.20 Micrographs of Alloy 617 - 10% Cr DMW joint CF specimen . . . 125
5.21 Cyclic endurance data for Alloy 617 - 10% Cr DMW joint (MMS-052). . . 125
5.22 Creep rupture strength of Alloy 617 - 1% CrMoV DMW joint (MMS-069). 126
5.23 Creep rupture strength of Alloy 617 - 10% Cr DMW joint (MMS-052). . . 127
5.24 LCF endurance data for Alloy 617 - 1% CrMoV DMW joint (MMS-069). . 128
5.25 LCF endurance data for Alloy 617 - 10% Cr DMW joint (MMS-052). . . . 129
5.26 CF endurance data for Alloy 617 - 1% CrMoV DMW joint (MMS-069). . . 131
5.27 Creep-fatigue damage fractions for CF experiments on Alloy 617 - 1% CrMoV DMW joint (MMS-069). . . . 132
5.28 CF endurance data for Alloy 617 - 10% Cr DMW joint (MMS-052). 133
5.29 Creep-fatigue damage fractions for CF experiments for Alloy 617 - 10% Cr DMW joint (MMS-052). . . . 134

A.1 LCF/TMF short specimen . . . 139
A.2 LCF/TMF standard specimen . . . 139
A.3 Creep specimen adopted for parent material according to ISO 204 140

A.4 Creep specimen adopted for DMW joint testing according to ISO 204 . . . 140
B.1 Comparison of measured creep data and calculated strength curves of Alloy 617 for various datum strains 141
B.2 Modelled curve families of datum creep strain strength curves for Alloy 617.142

List of Tables

2.1 Classification of Ni-base alloys 44

Bibliography

[1] *BS EN 10291:2000. Metallic materials - Uniaxial creep testing in tension - Methods of test, British - European standard*, 2000.

[2] Abe, F. Strengthening mechanisms in steel for creep and creep rupture. In *Creep-resistant steels*, K. F. Abe and R. Viswanathan, Eds. Woodhead Publishing Limited, 2008, pp. 279–304.

[3] AFCEN, Paris. *RCC-MR: Design and Construction Rules for Mechanical Components of FBR Nuclear Islands*, 1985.

[4] Armstrong, P.J, and Frederick, C.O. A mathematical representation of the multiaxial bauschinger effect. *Central Electricity Generating Board (CEGB) Berkeley, UK* (1966).

[5] ASME, New York. *ASME Boiler and Pressure Vessel Code, Section III, Division 1: sub-section NH, Class 1 Components in Elevated Temperature Service*, 2001.

[6] ASTM. *E 606-92: Standard Practice for Strain-Controlled Fatigue Testing*, 1998.

[7] Bailey, R.W. Note on the softening of strain-hardened metals and its relation to creep. *J. Inst. Met. 35* (1926).

[8] Berger, C., Granacher, J., and Haase, H. Mehrstufiges betriebsähnliches Langzeitdehnwechselverhalten der neuen martensitischen Hochleistungsstähle. Tech. rep., Institut für Werkstoffkunde, TU Darmstadt, 2000. Research report.

[9] Bhaduri, A.K., Seetharaman, V., and Venkadesan, S. Effect of ageing on the interfacial microstructure and mechanical properties of a Alloy 800 / 2.25Cr-1Mo steel. *Zeitschrift für Metallkunde 80* (1989), 630–634.

[10] Bürgel, R., Maier, H. J., and Niendorf, T. *Handbuch Hochtemperatur-Werkstofftechnik*. Springer, Berlin, 2011.

[11] British Energy, Gloucester. *R5: Assessment Procedures for the High Temperature Response of Structures, Procedure R5*, 3 ed., 2003.

[12] Bugge, J., Kjaer, S., and Blum, R. High-efficiency coal-fired power plants development and perspectives. *Energy 31*, 10-11 (2006), 1437–1445.

[13] Cerjak, H., and Mayr, P. Creep strength of welded joints of ferritic steels. In *Creep-resistant steels*, K. F. Abe and R. Viswanathan, Eds. Woodhead Publishing Limited, 2008, pp. 472–503.

[14] Chaboche, J.L. A review of some plasticity and viscoplasticity constitutive theories. *International Journal of Plasticity 24* (2008), 1642–1693.

[15] Chaboche, J.L., Dang-Van, K., and Cordier, G. Modelization of the strain memory effect on cyclic hardening of 316 stainless steel. *5th International Conference on Structural Mechanics in Reactor Technology, Berlin* (1979).

[16] Christ, H.J. *Wechselverformung von Metallen.* Springer-Verlag, Berlin Heidelberg, 1991.

[17] Christ, H.J. Materialermüdung und Werkstoffmikrostruktur. In *Ermüdungsverhalten metallischer Werkstoffe*, Christ, H.J., Ed. Wiley-VCH, 2009, pp. 35–51.

[18] Coffin, L.F.J. A complex subject - some simple approximations. *Experimental mechanics* (1965), 193–226.

[19] Coffin, L.F.J. Fatigue at high temperature - prediction and interpretation. *Proc. IME 188* (1994), 109–127.

[20] Colombo, F. *Service-like thermo-mechanical fatigue characteristics of 1CrMoV rotor steel.* PhD thesis, ETH Zurich, 2007.

[21] ECCC. *ECCC Recommendations Vol.2, Terms and terminology for use with stress rupture, creep rupture, creep and stress relaxation*, 2005.

[22] ECCC. *ECCC Recommendations Vol.3, Recommendations for data acceptability criteria and the generation of creep data*, 2005.

[23] ECCC. *ECCC Recommendations Vol.5, Guidance for the assessment of uniaxial creep data*, 2005.

[24] Ennis, P.J., and Quadakkers, W.J. Mechanisms of oxidation and the influence of steam oxidation on the service life of steam power plant components. In *Creep-resistant steels*, K. F. Abe and R. Viswanathan, Eds. Woodhead Publishing Limited, 2008, pp. 519–535.

[25] Evans, R.W., and Wilshire, B. *Creep of metals and alloys.* The Institute of Metals, London, 1985.

[26] FRIEDMANN, V. *Versagensverhalten von Austenit-Martensit Rohrmischverbindungen für 600°C-Dampfkraftwerke unter Kriechermüdungsbelastung.* PhD thesis, Karlsruhe Institute of Technology, 2011.

[27] GARIBOLDI, E., CABIBBO, M., SPIGARELLI, S., AND RIPAMONTI, D. Investigation on precipitation phenomena of Ni-22Cr-12Co-9Mo alloy aged and crept at high temperature. *International Journal of Pressure Vessels and Piping 85* (2008), 63–71.

[28] GAROFALO, F. *Fundamentals of creep and creep rupture in metals.* McMillan, New York, 1965.

[29] GOCMEZ, T., AWARKE, A., AND PISCHINGER, S. A new low cycle fatigue criterion for isothermal and out-of-phase thermomechanical loading. *International Journal of Fatigue 32* (2010), 769–779.

[30] GOOCH, D.J., AND KIMMINS, S.T. Type IV cracking in 0.5Cr0.5Mo0.25V / 2.25Cr1Mo weldments. In *Proc. of the 3rd Int. Conf. on Creep and Fracture of Engineering Materials and Structures* (Swansea, 1987), Maney Publishers.

[31] GRAHAM, A., AND WALLES, K.F.A. Relationships between long- and short-time creep and tensile properties of a commercial alloy. *Journal of The Iro and Steel Institute 179* (1955), 104–121.

[32] HAASE, H., SCHOLZ, A., GRANACHER, J., AND BERGER, C. Mehrstufiges betriebsähnliches Kriechermüdungsverhalten der neuen martensitischen Hochleistungsstähle. In *Tagungsband der 23. Vortragsveranstaltung der Arbeitsgemeinschaft für warmfeste Stähle und Hochtemperaturwerkstoffe* (2000), pp. 50–63.

[33] HALD, J., AND STRAUB, S. Microstructural stability of 9-12%CrMo(W)VNbN steels. In *Proc. COST Conf. on Materials for advanced power engineering 1998* (1998), pp. 155–169.

[34] HALES, R. A method of creep damage summation based on accumulated strain for the assessment of creep-fatigue endurance. *Fatigue of Engineering Materials and Structures 6* (1983), 121–135.

[35] HÄHNER, P., AFFELDT, E., BECK, T., KLINGELHÖFFER, H., LOVEDAY, M., AND RINALDI, C. *Validated Code-of-Practice for Strain-Controlled Thermo-Mechanical Fatigue Testing.* JRC, June 2006.

[36] HOLDSWORTH, S.R. Recent developments in the analysis of creep rupture data. *Key Engineering Materials* (2000), 171–174.

[37] HOLDSWORTH, S.R. Constitutive equations for creep curves and predicting service life. In *Creep-resistant steels*, K. F. Abe and R. Viswanathan, Eds. Woodhead Publishing Limited, 2008, pp. 403–420.

[38] Hull, D., and Bacon, D.J. *Introduction to Dislocations.* Butterworth-Heinemann, Oxford, 2001.

[39] Hunsche, A. *Untersuchungen zur Rissbildung in Ermüdungsgleitbändern.* PhD thesis, RWTH Aachen, 1982.

[40] International Organization for Standardization. *ISO 12106, Metallic materials - Fatigue testing - Axial-strain-controlled method*, 2003.

[41] International Organization for Standardization. *ISO 6892, Metallic materials - Tensile testing - Part 1 + 2*, 2011.

[42] Kachanov, L.M. On the creep rupture time. *zv. Akad. Nauk SSR, Otd. Tekhn. Nauk 8* (1958), 26–31.

[43] Kassner, M.E., and Hayes, T.A. Creep cavitation in metals. *International Journal of Plasticity 19* (2003), 1715–1748.

[44] Kern, T.U. Using creep resistant steels in turbines. In *Creep-resistant steels*, K. F. Abe and R. Viswanathan, Eds. Woodhead Publishing Limited, 2008, pp. 573–596.

[45] Kern, T.U., Staubli, M., Mayer, K.H., Escher, K., and Zeiler, G. The European Effort in Development of New High Temperature Rotor Materials up to 650°C - COST522. In *Proc. COST Conf. on Materials for advanced power engineering 2002* (Liege, 2002), pp. 1049–1064.

[46] Kloos, K.H., Granacher, J., and Scholz, A. Langzeitverhalten einiger warmfester Stähle unter betriebsähnlicher Kriechermüdungsbeanspruchung. *Mat.-wiss. u. Werkstofftech. 24* (1993), 409–417.

[47] Kloos, K.H., Granacher, J., and Scholz, A. Mehrstufige betriebsähnliche Dehnwechselbeanspruchung warmfester Stähle. *Mat.-wiss. u. Werkstofftech. 27* (1996), 331–337.

[48] Korsunsky, A.M., Dini, D., Dunne, F.P., and Walsh, M.J. Comparative assessment of dissipated energy and other fatigue criteria. *International Journal of Fatigue 29* (2007), 1990–1995.

[49] Larson, F.R., and Miller, J. A time-temperature relationship for rupture and creep stresses. *Trans. ASME 74* (1952), 765–775.

[50] Lemaitre, J., and Chaboche, J.L. *Mechanics of Solid Materials.* Cambridge University Press, 1990.

[51] Lemaitre, J., and Desmorat, R. *Engineering damage mechanics.* Springer, Berlin, Heidelberg, 2005.

[52] Letofsky, E. *Das Verhalten von Schweissverbindungen moderner Kraftwerksstähle.* PhD thesis, Graz University of Technology, 2001.

[53] Macha, E., and Sonsino, C.M. Energy criteria of multiaxial fatigue failure. *Fatigue Fract Engng Mater Struct 22* (1999), 1053–1070.

[54] Maier, H. Rissbildung bei zyklischer Beanspruchung. In *Ermüdungsverhalten metallischer Werkstoffe*, Christ, H.J., Ed. Wiley-VCH, 2009, pp. 69–85.

[55] Maile, K., Klenk, A., Bauer, M., and Roos, E. Consideration of weld behaviour in design of high temperature components. In *Proceedings of the 5th International Conference on Advances in Material Technology for Fossil Power Plants* (2007).

[56] Manson, S., and Halford, G. A method of estimating high-temperature low cycle fatigue behaviour of materials. In *Symposium on Thermal and High Strain Fatigue* (1967).

[57] Manson, S.S., and Haferd, A.M. NASA-TN-2890. Tech. rep., NASA, 1953.

[58] Manson, S.S., Halford, G.R., and Hirschberg, M.H. Creep-fatigue analysis by strain-range partitioning. In *Symposium on Design for Elevated Temperature Environment* (1971), Zamrik, S.Y., Ed., pp. 12–28.

[59] Mao, T.S., Granacher, J., and Berger, C. Zeitstandbruchverhalten bauteilähnlicher Rundkerbproben. In *Tagungsband der 21. Vortragsveranstaltung der Arbeitsgemeinschaft für warmfeste Stähle und Hochtemperaturwerkstoffe* (1998), pp. 140–152.

[60] Mao, T.S., Granacher, J., and Berger, C. Life Calculation of Creep Loaded. In *Proc. of the 14th International Forgemasters Meeting, Wiesbaden* (2001), pp. 221–227.

[61] Mayer, T. *Characterisation and Modelling of the Microstructural and Mechanical Evolution of a Steam Turbine Rotor Steel.* PhD thesis, ETH Zurich, 2012.

[62] Mayer, K.H., and Masuyama, F. The development of creep-resistant steels. In *Creep-resistant steels*, K. F. Abe and R. Viswanathan, Eds. Woodhead Publishing Limited, 2008, pp. 15–77.

[63] Mughrabi, H. Dislocation wall and cell structures and long-range internal stresses in deformed metal crystals. *Acta metall. 31*, 9 (1983), 1367–1379.

[64] Mughrabi, H., Ackermann, F., and Herz, K. Persistant slipbands in fatigued face-centred and body-centred cubic metals. In *ASTM-STP 675, Proc. of an ASTM-NBS-NSF symposium, Kansas City* (1979), J.T. Fong, Ed., pp. 69–105.

[65] Nicholson, R.D. Effect of aging on interfacial structures of nickel-based transition joints. *Metals Technology 11* (1984), 115–124.

[66] Nicholson, R.D. Creep rupture properties of nickel-base transition joints after long-term service. *Materials Science and Technology 2* (1986), 686–692.

[67] Norton, J.F., and Strang, A. Improvement of creep and rupture properties of large 1%crmov steam turbine rotor forgings. *Journal of the Iron and Steel Institute* (1969), 193–203.

[68] Oehmigen, H.G. *Das Verhalten von Schweissverbindungen des warmfesten Stahles X11CrMoWVNb 9-1-1 unter Zeitbeanspruchung.* PhD thesis, TU Darmstadt, 2000.

[69] Ohrndorf, A. Zyklisches Spannungs-Dehungs-Verhalten bei konstanter and variierender Beanspruchungsamplitude. In *Ermüdungsverhalten metallischer Werkstoffe*, Christ, H.J., Ed. Wiley-VCH, 2009, pp. 61–68.

[70] Oikawa, H., and Iijima, Y. Diffusion behaviour of creep resistant steels. In *Creep-resistant steels*, K. F. Abe and R. Viswanathan, Eds. Woodhead Publishing Limited, 2008, pp. 241–264.

[71] Orowan, E. The creep of metals. *Transactions of the West of Scotland Iron and Steel Institute 54* (1947).

[72] Parker, J.D., and Stratford, G.C. Characterisation of microstructures in nickel based transition joints. *Journal of Materials Science 35* (2000), 4099–4107.

[73] Parker, J.D., and Stratford, G.C. The high-temperature performance of nickel-based transition joints - ii. fracture bahviour. *Materials Science and Engineering A 299* (2001), 174–184.

[74] Payten, W.M., Dean, D.W., and Snowden, K.U. A strain energy density method for the prediction of creep-fatigue damage in high temperature components. *Materials Science and Engineering A* (2010), 1920–1925.

[75] Prager, W. Recent developments in the mathematical theory of plasticity. *Journal of Applied Physics 20* (1949).

[76] Priest, R.H., and Ellison, E.G. A combinded deformation map - ductility exhaustion approach to creep-fatigue analysis. *Material Science and Engineering 49* (1980).

[77] Rabotnov, Y.N. *Creep problems in structural members.* North Holland, 1969.

[78] Radosavljevic, M. *Creep-Fatigue Assessment of High Temperature Steam Turbine Rotors.* PhD thesis, ETH Zurich, 2011.

[79] Radosavljevic, M., Holdsworth, S.R., Grossmann, P., Ripamonti, L., and Mazza, E. Service-cycle component-feature specimen thermomechanical fatigue testing. *Materials at High Temperatures 30* (2013), 13–18.

[80] Ramberg, W., and Osgood, W.R. Description of stress-strain curves by three parameters. *NACA Technical Note 902* (1943).

[81] Roberts, D.I., Ryder, R.H., and Viswanathan, R. Performance of dissimilar welds in service. *Journal of Pressure Vessel Technology 107* (1985), 247–254.

[82] Robinson, R.L. Effect of temperature variation on the long time rupture strength of steels. *Transactions of ASME 74* (1952), 777–781.

[83] Scholz, A. *Beschreibung des zyklischen Werkstoffverhaltens bei betriebsähnlicher Langzeithochtemperaturdehnwechselbeanspruchung.* PhD thesis, TU Darmstadt, 1988.

[84] Schwienheer, M. *Statisches und zyklisches Hochtemperaturverhalten der 600°C-Dampfturbinenstähle (G)X12CrMoWVNbN10-1-1.* PhD thesis, TU Darmstadt, 2004.

[85] Senior, B.A. A critical review of precipitation behaviour in 1CrMoV rotor steels. *Materials Science and Engineering A 103* (1988), 263–271.

[86] Sireesha, M., Albert, S.K., and Sundaresan, S. Influence of high-temperature exposure on the microstructure and mechanical properties of dissimilar metal welds between modified 9Cr-1Mo steel and Alloy 800. *Metallurgical and Materials Transactions A 36A* (2005), 1495–1506.

[87] Skelton, R.P. Energy criterion for high temperature low cycle fatigue failure. *Materials Science and Technology 7* (1991).

[88] Skelton, R.P., Rees, C.J., and Webster, G.A. Energy damage summation methods for crack initiation and growth during block loading in high-temperature low-cycle fatigue. *Fatigue Fract Eng Mater Struct 19* (1996).

[89] Spindler, M.W. The multiaxial and uniaxial creep ductility of Type 304 steel as a function of stress and strain rate. *Materials at High Temperatures 21* (2004).

[90] Staubli, M., Scarlin, B., Mayer, K.H., Kern, T.U., Bendick, W., Morris, P., Gianfrancesco, A. D., and Cerjak, H. Materials for Advanced Steam Power Plants. In *in Parsons 2003 Engineering: issues in Turbine machinery, Power Plant and Renewables, Proc. 6th Intern. Charles Parsons Turbine Conference* (2003), pp. 305–324.

[91] Stouffer, D.C., and Dame, L.T. *Inelastic Deformation of Metalls.* John Wiley and Sons Inc., 1996.

[92] Suresh, S. *Fatigue of Materials.* Cambridge University Press, 2004.

[93] Tabuchi, M., Hongo, H., Li, Y., Watanabe, T., and Takahashi, Y. Evaluation of microstructures and creep damages in the HAZ of P91 steel weldment. *Journal of Pressure Vessel Technology 131* (2009).

[94] Tabuchi, M., and Takahashi, Y. Evaluation of creep strength reduction factors for welded joints of modified 9Cr-1Mo steel. *Journal of Pressure Vessel Technology 134* (2012).

[95] Taira, S. Lifetime of structures subjected to varying load and temperature. In *Creep in structures, Colloquium held at Stanford University, July 1960*, N.J. Hoff, Ed. Springer Berlin Heidelberg, 1962.

[96] Takahashi, Y., Dogan, B., and Gandy, D. Systematic evaluation of creep-fatigue life prediction methods for various alloys. In *Proceedings of the ASME 2009 Pressure Vessels and Piping Division Conference* (2009).

[97] Tanaka, Y. Production of creep-resistant steels for turbines. In *Creep-resistant steels*, K. F. Abe and R. Viswanathan, Eds. Woodhead Publishing Limited, 2008, pp. 174–214.

[98] Thoma, A. *Nickelbasis-Legierungen für den Einsatz als Rotorwerkstoff in Dampfkraftwerken oberhalb 700°C - Langzeitstandverhalten und Modellierung.* PhD thesis, TU Darmstadt, 2004.

[99] Vanstone, R.W. Advanced 700°C Pulverised Coal Fired Power Plant - Phase 1B: Steam Turbine Material Property Demonstration - Final Report . Tech. rep., ALSTOM Power Ltd, 2004.

[100] Vanstone, R.W. Advanced 700°C Pulverised Coal Fired Power Plant - Phase 2: Report on IP-rotor forging manufacture. Tech. rep., ALSTOM Power Ltd, 2005.

[101] VGB, Technische Vereinigung der Grosskraftwerksbetreiber e.V., Essen. *Richtlinien zur Bewertung der Gefügeausbildung und -schädigung zeitstandbeanspruchter Werkstoffe von Hochdruckrohrleitungen und Kesselbauteilen*, 1992. VGB-TW 507.

[102] Witwer, M. *Untersuchungen an Mischschweissverbindungen warmfester CrMoV-Stähle.* PhD thesis, Graz University of Technology, 1989.

[103] Wu, Q., Song, H., Swindeman, R.W., Shingledecker, J.P., and Vasudevan, V.K. Microstructure of long-term aged IN617 Ni-base superalloy. *Metallurgical and Materials Transactions A 39A* (2008), 2569–2585.

Curriculum Vitae

Frank Ehrhardt

born on June 27^{th} 1980 in Dohna, Germany

citizen of the Federal Republic of Germany

ehrhardt.frank@gmail.com

Education

10/2008 - 10/2012	**Doctoral studies** Empa Dübendorf / ETH Zurich, Switzerland
10/2000 - 05/2007	**Dipl. Ing. in Mechanical Engineering** Dresden University of Technology, Germany **Focus**: Applied Mechanics, Structural and Fluid Mechanics, Numerical Methods
09/1992 - 08/1999	**High School**, ”J.-G.-Herder-Gymnasium“ Pirna, Germany
08/1987 - 08/1992	Primary School Graupa, Germany

Professional Experience

10/2008 - 10/2012	**Research Assistant** Empa Dübendorf / ETH Zurich, Switzerland
02/2007 - 09/2008	**Stress Engineer** / Mechanical Integrity ALSTOM (Switzerland) AG Baden, Switzerland
05/2006 - 11/2006	**Industrial Internship** ALSTOM (Switzerland) AG Baden, Switzerland

Publications

Journal	Ehrhardt, F., Holdsworth, S.R., Kühn, I., and Mazza, E., Creep fatigue crack development in dissimilar metal welded joints between steels and nickel based alloy., *Materials Research Innovations*, Vol. 17, Nr. 5, August 2013, pp. 327-331
Proceedings	Ehrhardt, F., Holdsworth, S.R., Kühn, I., and Mazza, E., Creep fatigue crack development in dissimilar metal welded joints between steels and nickel based alloy., *Proc. IOMMM Conf. on Integrity of High Temperature Welds & Creep and Fatigue at Elevated Temperatures*, London, 25-27. September 2012